FIRST PRINCIPLES CALCULATIONS OF THERMODYNAMICS OF HIGH TEMPERATURE METAL HYDRIDES FOR NGNP APPLICATIONS

A Dissertation
Presented to
The Academic Faculty

By

Kelly M. Nicholson

In Partial Fulfillment
Of the Requirements for the Degree
Doctor of Philosophy in Chemical Engineering

Georgia Institute of Technology

August, 2014

FIRST PRINCIPLES CALCULATIONS OF THERMODYNAMICS OF HIGH TEMPERATURE METAL HYDRIDES FOR NGNP APPLICATIONS

Approved by:

Dr. David Sholl, Advisor
School of Chemical & Biomolecular Engineering
Georgia Institute of Technology

Dr. Michael Filler
School of Chemical & Biomolecular Engineering
Georgia Institute of Technology

Dr. Carson Meredith
School of Chemical & Biomolecular Engineering
Georgia Institute of Technology

Dr. Mo Li
School of Materials Science and Engineering
Georgia Institute of Technology

Dr. Mark Styczynski
School of Chemical & Biomolecular Engineering
Georgia Institute of Technology

Date Approved: June 16, 2014

ACKNOWLEDGEMENTS

There have been many hands in this thesis, my own and my advisor's, of course, but without a doubt those of my family members. Without their support, completing this work might have been lonely and unfulfilling. Instead, their gentle pushing kept me focused and enthusiastic. Thank you to my parents for putting education first and for feeding the curiosity that has brought me to this point. Thank you, in particular, to my mother, Malinda, for the late night conversations and unconditional faith. I must also thank my advisor, David Sholl, for maintaining a collaborative atmosphere while allowing me to work independently. I am grateful for his patience and for the example he lives with regards to work ethic and work-life balance.

TABLE OF CONTENTS

LIST OF TABLES

LIST OF FIGURES

NOMENCLATURE

Abbreviations

AIMD	*ab initio* molecular dynamics
bcc	body-centered cubic
bct	body-centered tetragonal
CTMH	complex transition metal hydride
DFT	Density Functional Theory
DOE	U.S. Department of Energy
EPA	U.S. Environmental Protection Agency
fcc	face-centered cubic
fct	face-centered tetragonal
f.u.	formula unit
GGA	Generalized Gradient Approximation
hcp	hexagonal close-packed
ICSD	Inorganic Crystal Structure Database
LDA	Local Density Approximation
NGNP	Next Generation Nuclear Plant
NRC	Nuclear Regulatory Commission
PAW	projector augmented wave
VASP	Vienna *Ab Initio* Simulation Package
VDOS	vibrational density of states
VHTR	Very High Temperature Gas-Cooled Reactor
ZPE	zero point energy

Symbols

B	bulk modulus
E_0	DFT ground state electronic energy
F	Helmholtz free energy
F^{anh}	anharmonic Helmholtz free energy
F^{qh}	quasiharmonic Helmholtz free energy

F^{vib}	vibrational Helmholtz free energy
G	Gibbs free energy
H	enthalpy
h	Planck's constant
k_B	Boltzmann constant
N_c	number of unique configurations
P	pressure
P_0	reference pressure, 1 bar
R	universal gas constant
S	entropy
S^{conf}	configurational entropy
T	temperature
T_d	hydrogen release temperature for P = 1 bar H_2 partial pressure
U	internal energy
V	volume
V_0	ground state volume
V_{0c}	ground state volume corrected for zero point energy effects
ΔE_0	Reaction energy based on DFT ground state electronic energies
ΔF	Helmholtz free energy of reaction
ΔG	Gibbs free energy of reaction
ΔH	Enthalpy of reaction
$\Delta S°$	Entropy of reaction at standard conditions, 1 bar, 298 K
$\Delta G°$	Gibbs free energy of reaction at standard conditions, 1 bar, 298 K
$\Delta H°$	Enthalpy of reaction at standard conditions, 1 bar, 298 K
ΔS	Entropy of reaction
ε	isotropic volumetric thermal expansion
μ	chemical potential
ω	phonon frequency
ϕ	grand potential

SUMMARY

In addition to their potential use at low to moderate temperatures in mobile fuel cell technologies, metal hydrides may also find application as high temperature tritium getterers in the U.S. DOE Next Generation Nuclear Plant (NGNP). We use Density Functional Theory to identify metal hydrides capable of sequestering tritium at temperatures in excess of 1000 K. First we establish the minimum level of theory required to accurately capture the thermodynamics of highly stable metal hydrides and determine that isotope effects can be neglected for material screening. Binary hydride thermodynamics are largely well established, and ternary and higher hydrides typically either do not form or decompose at lower temperatures. In this thesis we investigate anomalous systems with enhanced stability in order to identify candidates for the NGNP application beyond the binary hydrides. Methods implemented in this work are particularly useful for deriving finite temperature phase stability behavior in condensed systems. We use grand potential minimization methods to predict the interstitial Th−Zr−H phase diagram and apply high throughput, semi-automated screening methodologies to identify candidate complex transition metal hydrides (CTMHs) from a diverse library of all known, simulation ready ternary and quaternary CTMHs (102 materials) and 149 hypothetical ternary CTMHs based on existing prototype structures. Our calculations significantly expand both the thermodynamic data available for known CTMHs and the potential composition space over which previously unobserved CTMHs may be thermodynamically stable. Initial calculations indicate that the overall economic viability of the tritium sequestration system for the NGNP will largely depend on the amount of protium rather than tritium in the metal hydride gettering bed feed stream.

CHAPTER 1

INTRODUCTION

1.1 Tritium Management in the NGNP

The U.S. Energy Policy Act of 2005[1] authorized the creation of the Department of Energy (DOE) Next Generation Nuclear Plant (NGNP) Project with prototype start-up by September 2021 as part of the U.S. Generation IV Implementation Strategy.[2-4] The NGNP seeks to demonstrate advanced nuclear technologies and provide low carbon process heat and electricity to downstream users economically. The NGNP consists of a gas-cooled nuclear reactor, a gas-driven or steam-driven electrical generator, and heat transfer loops that transport process heat to industrial users. The DOE has selected the Very High Temperature Gas-Cooled Reactor (VHTR), which is a thermal neutron spectrum nuclear reactor moderated by graphite and cooled by helium with core outlet temperatures in the range $1000 \leq T\,(\mathrm{K}) \leq 1200$.[3,5 6] What sets the NGNP apart from conventional reactor plants, other than the choice of nuclear reactor, is the thermal connection between the nuclear plant and a non-nuclear user of the high temperature process heat such as a hydrogen production plant or coal-to-liquids plant without the intermediate conversion to electricity. This boosts the overall efficiency of the nuclear plant, but presents technical hurdles, particularly with regard to controlling migration of fission products such as tritium to the end user.

Tritium, $^{3}\mathrm{H}$, is mildly radioactive with a half-life of 12.33 years. It behaves chemically as hydrogen and can form tritiated water, which poses health risks if absorbed or ingested by humans. The emission of tritium into the environment is regulated by the

Nuclear Regulatory Commission (NRC) and the U.S. Environmental Protection Agency (EPA).[7] Tritium permeates easily through many materials, especially metals, at high temperatures. It has been known to cause hydrogen embrittlement and, since it behaves chemically as hydrogen, could become incorporated into the industrial end user's chemical products. Significant buildup of tritium in the heat transfer loops and downstream plants has maintenance implications since worker radiation dosage will have to be managed, and excessively high contamination could push these areas into the nuclear-regulated regime.[7] While there currently is no set tritium effluent limit for the NGNP, it is expected that it will be no higher than that allowed for tritium environmental emissions set by the NRC and EPA. For example, tritium may be vented to the atmosphere if its concentration in a gas stream is less than 10^{-12} bar (1 part per trillion).[5] Therefore, tritium control systems and technologies including dynamic migration modeling, high temperature sensors, permeation barrier materials, membranes, and absorbent gettering systems are being investigated to reduce or eliminate the tritium contamination in the downstream plants.[7]

In such a capture system, a side stream of the helium coolant between $1000 \leq T$ (K) ≤ 1200 with tritium contaminant at low partial pressures, assumed to be on the order of 10^{-10} bar, comes into direct contact with the metal hydride material, and tritium is removed from the fluid. In these systems, the normal form of hydrogen, $^1H_2$, is available in the coolant so tritium is most commonly encountered as $^1H^3H$ (HT).[5] Periodically, the metal hydride gettering material is replaced with fresh media, and the tritiated hydride can be disposed of as low-level radioactive waste.

In this thesis, we investigate metal hydride gettering materials for use in potential high temperature sequestration systems for the NGNP using computational methods. Computational studies based on Density Functional Theory (DFT) have made useful contributions to material screening for other applications involving formation of metal hydrides and development of metal membranes for hydrogen purification.[8-12] Due to the significant hazards and practical difficulties associated with performing experiments involving tritium at high temperature, computational methods provide an important tool for down-selecting interesting materials for the application.

1.2 Metal Hydride Gettering Materials

1.2.1 Background

Many metals, intermetallics, and alloys react exothermically with hydrogen to form metal hydrides with high hydrogen densities.[13,14] Additionally, metal tritides such as TiH_x and UH_x are the current preferred method for long term storage of tritium in nuclear operations.[15] Recent research efforts, including computational modeling, have focused on identifying and engineering the properties of metal hydride systems with moderate thermodynamic stability, i.e., those that operate close to ambient temperatures and pressures, for the onboard solid state storage of hydrogen in fuel cell vehicles.[13,16-23] Relatively less focus has been placed on the high temperature applications of metal hydrides, such as their role as neutron moderators in nuclear reactors[24-27] or as thermochemical media in solar energy storage systems.[28-31] However, metal hydrides such as Zr-H and LiH, stable to temperatures in excess of 1000 K, have found several uses in nuclear applications as components of nuclear fuels and as neutron moderators since the 1950s.[27,32-35]

Metal hydrides are typically composed of a parent metal lattice that expands and/or transforms upon hydrogenation.[13,36] Pure metals react with hydrogen gas through dissociative chemisorption to form metal hydrides until the phases reach thermal equilibrium. For dehydriding reactions of the type

$$aA + bB + \ldots \leftrightarrow mM + nN + \ldots + H_2 \tag{1.1}$$

in which all phases are solids except for H_2 gas, the hydrogen overpressure, P, is governed by the van't Hoff relation[20, 40 21,37]

$$\ln\left(\frac{P}{P_0}\right) = \frac{-\Delta H(T)}{RT} + \frac{\Delta S(T)}{R} = \frac{-\Delta G(T)}{RT} \tag{1.2}$$

where P_0 is a reference pressure defined as 1 bar, ΔG, ΔH, and ΔS are the Gibbs free energy, enthalpy, and entropy of reaction, respectively, and R is the universal gas constant. The corresponding van't Hoff plots provide a useful means for comparing theoretical and experimental metal hydride stabilities. A convenient measure of the relative thermodynamic stabilities of metal hydrides is the temperature at which a metal hydride is in thermodynamic equilibrium with 1 bar H_2 gas, T_d. If heated beyond this temperature, the metal hydride will begin to release hydrogen.

1.2.2 Binary vs. ternary hydrides

In this thesis, we are primarily concerned with increasing the thermodynamic stabilities of metal hydrides by combining different metal species. With this spirit, we refer to metal hydrides as binary, ternary, or quaternary to describe materials with one, two, or three metal constituents.

The binary hydrides have the general formula M_xH_y where M is the metal. The metal-hydrogen chemical bonding can be ionic such as with NaH or interstitial, i.e., metallic, such as ZrH_2 where hydrogen absorbs into the parent metal interstitial sites

typically without a change in lattice symmetry. The thermodynamics of these materials are relatively well characterized.[36,38,39] Figure 1.1 provides representative T_d's for the binary hydrides across the periodic table. The mid to late transition metals do not form stable hydrides under ambient conditions, but may form a hydride at very high P. AlH_3 and InH_3 form metastable solid hydrides, but most other main group elements do not form hydrides.[40] The hydrides of the rare earth elements are very stable, but may not be practical for industrial scale use due to the high cost and/or radioactivity of the metal. We wish to find hydrides that are more thermodynamically stable than those in Figure 1.1.

H														He
LiH 993 1184	BeH_2 523											B	C	N-Ne
NaH 698	MgH_2 600											Al	Si	P-Ar
KH 690	CaH_2 873	ScH_2 1369	TiH_2 916	VH_2 419	CrH 61	MnH 34	FeH	CoH	Ni_2H 23	CuH	Zn	Ga	Ge	As-Kr
RbH 636	SrH_2 948	YH_2 1551	ZrH_2 1154	NbH_2 466	MoH 47	TcH	Ru	Rh_2H 140	$PdH_{0.77}$ 420	Ag	Cd	In	Sn	Sb-Xe
CsH 662	BaH_2 948	LaH_2 1381	HfH_2 873	Ta_2H 302	W	Re	Os	Ir	Pt	Au	Hg	Tl	Pb	Bi-Rn
Fr	Ra	Ac	Rf	Db	Sg	Bh	Hs	Mt						

CeH_2 1339	PrH_2 1420	NdH_2 1448	Pm	SmH_2 1372	Eu	GdH_2 1464	TbH_2 1510	DyH_2 1464	HoH_2 1464	ErH_2 1456	Tm 1482	Yb	LuH_2 1466
ThH_2 1127	Pa	UH_3 705	Np	PuH_2 1212	Am	Cm	Bk	Cf	Es	Fm	Md	No	Lr

Figure 1.1: T_d (K) of binary hydrides. Values listed are either experimental, calculated from experimental standard enthalpies and entropies of formation, or estimated based on $T_d \sim \Delta H/\Delta S$ with ΔS=0.130 kJ (K mol H_2)$^{-1}$ if not given. Data from Refs. 36,41-47.

Ternary and quaternary metal hydrides have representative stoichiometries $M_xN_yH_z$ and $M_wN_xP_yH_z$. These materials can be classified as interstitial hydrides in which hydrogen is taken up by the parent metal lattice, either an alloy or an intermetallic,

without change in the crystal structure of the parent lattice or as complex hydrides. Complex hydrides are stabilized by charge transfer from a cationic species, typically an alkali, alkaline earth, or lanthanide element, to an anionic hydrido complex.[48,49] For most ternary hydrides of transition metals, the enthalpy of hydride formation, ΔH, is approximately a weighted sum of heats of formation of the binary hydrides.[50 51] For example, while binary Pd-based hydrides exist, alloys of Pd tend not to form stable metal hydrides. There are few materials for which it is known experimentally that the ternary hydride exhibits lower hydrogen equilibrium pressures at a given temperature, i.e., higher T_d, than the associated binary hydrides.

If a ternary hydride is metastable to the binary hydrides and there are no kinetic limitations, it will dissociate to form a mixture of the binary hydrides, binary alloys and/or intermetallics, and parent metals when heated. In these cases, the binary hydride defines the most thermodynamically stable hydride phase that forms in the element space. For the purposes of the NGNP application, this would indicate that binary hydrides with largely known thermodynamic properties form the upper boundary on the potential performance of metal hydrides for the gettering application.

However, there is at least one example of a ternary interstitial system, Th−Zr−H, for which the higher hydrides $ThZr_2H_x$ were found experimentally to be more thermodynamically stable than the parent binary hydrides ThH_2, Th_4H_{15}, and ZrH_2.[32] Additionally, several complex hydrides of the alkali and alkaline earth metals that form borohydrides such as $Na(BH_4)$ (T_d = 838 K) and $Cs(BH_4)$ (T_d = 933 K) have enhanced stability with respect to the binary hydrides (NaH T_d = 698 K, CsH T_d = 443 K) while the alanates complex hydrides are destabilized.[48,52]

Of the known complex hydrides, the homoleptic (i.e., metals with identical hydrogen ligands) complex transition metal hydrides (CTMHs) are the most thermodynamically stable, and several known ternary materials release hydrogen at higher temperature than the binary hydrides. Some examples are listed in Table 1.1. Due to the relatively high temperatures required to release hydrogen from CTMHs (most have $T_d > 570$ K)[48] and low gravimetric hydrogen capacity, CTMHs have largely been ignored for the purposes of fuel cell hydrogen storage, and little thermodynamic data for them is available. However, with their stability, CTMH materials like Mg_2FeH_6 that release hydrogen in the 500-700 K range may be useful in high temperature applications such as the NGNP or in concentrated solar plant chemical heat storage.[28] As of 2005, there were 127 known CTMH materials that form from a wide range of cations and transition metal combinations. The vast majority of these have little to no experimental data available beyond that of a crystal structure. Since many of these materials crystallize in high symmetry crystal structures, i.e., relatively small unit cells, without disorder, they offer a rich landscape for exploring the thermodynamic stabilities of complex ternary hydrides with respect to the binary hydrides using DFT.

Table 1.1: Sample comparison of T_d for known complex transition metal hydrides based on linear scaling of Gibbs free energy. $T_d \sim \Delta H/\Delta S$ with ΔS=0.130 kJ (K-mol H_2)$^{-1}$. Data for Mg_2FeH_6 is from Bogdanovic et al.[28] All others from Miedema et al.[51]

Binary Hydride	T_d (K)	CTMH	T_d (K)
MgH_2	570	Mg_2FeH_6	595
FeH	-	$Mg_6Co_2H_{11}$	>753
RuH	-	Mg_2CoH_5	553
RbH	443	Mg_3RuH_7	>673
CsH	443	Mg_3RuH_4	>673
Zn	-	Mg_2RuH_4	>673
		Rb_2ZnH_4	633
		Rb_3ZnH_5	633
		Cs_2ZnH_4	633
		Cs_3ZnH_5	628

1.2.3 DFT for studying metal hydride thermodynamics

Density Functional Theory is a useful quantum mechanics-based method for describing a system of electrons and nuclei based on the total electron density. In its pure form, DFT does this exactly for the ground state, but in practical terms, we rely on use of an assumed exchange-correlation functional, the exact form of which is unknown. This represents the largest source of error in DFT calculations. [53-60]

DFT has been utilized extensively to evaluate the properties of metal hydride systems. It has been used to predict stable crystal structures, binding energies, zero point energies, mechanical properties, band structures, the electronic density of states among others for metals and metal hydrides, typically for mobile applications.[20-23,28,36,43,61-83] Finite temperature properties such as the vibrational free energy and phase transitions of metal-hydrogen systems can also be predicted via *ab initio* methods.[41-44,84-88]

DFT studies within the Generalized Gradient Approximation (GGA) have found that ground state (T = 0 K) energies can predict thermodynamic properties such as heats of formation of metal hydride systems to within ~10-20 kJ mol^{-1} H_2 for most compounds. Additionally, GGA performance is superior to that of the Local Density Approximation (LDA) functionals.[89] Wolverton et al. found that including vibrational corrections reduced the root mean square error in calculated vs. experimental reaction enthalpies for alkali, alkaline earth, and early transition metal binary hydrides from 19.4 to 14.7 kJ/mol H_2.[23] Although the thermodynamics of metal hydrides at low to moderate temperatures have been successfully described with DFT calculations using 0 K total energies and simple harmonic models centered at the equilibrium volume at 0 K, it is unclear as to what level of theory is required to study the thermodynamics of metal hydride systems at the high temperatures of the NGNP application.

Akbarzadeh et al. developed a framework to compute the multicomponent phase diagram, and thus, decomposition reaction pathways for multicomponent hydride systems through the minimization of the grand-canonical Gibbs free energy, calculating the total electronic energy and vibrational free energy for each applicable solid phase with DFT.[43] Alapati et al. screened a library of metal hydrides for favorable thermodynamics based on ground state DFT energies and predicted reaction pathways including multistep pathways for metal hydride decomposition based on the grand potential approach of Wolverton et al. [20,21,67-69,89-92] Kim et al. adapted Alapati's methods to identify destabilization reaction pathways for a 13 element space based on a library of 359 compounds.[71]. Methods based on these prior works that compute the stable mixture of compounds at a given hydrogen chemical potential will be extensively applied in this thesis.

1.3 Thesis Summary

It is known that metal hydride systems can be destabilized through chemical reactions with other compounds,[20,21,67-71] through alloying with other metals,[93] through doping,[13] or by controlling the size of the metal hydride particles.[94] Relatively little effort has been expended on increasing the stability of metal-hydrogen systems. Therefore, the overarching theme for this thesis revolves around using DFT-based methods to identify ternary and higher metal hydrides that are more thermodynamically stable than the associated binary hydrides and that operate at the high temperatures of the NGNP application.

To aid the development of computationally efficient DFT methods, we will first determine the minimum level of theory required to accurately characterize the thermodynamics of highly stable metal hydride systems in Chapter 2. We explore the stabilities of ZrH_2, HfH_2, TiH_2, LiH, and NaH with four levels of theory with increasing computational expense. In Chapter 3, we investigate the effect of hydrogen isotope substitution on the stabilities of the same five binary hydrides from low to high temperature. This is done to determine if normal hydrogen, protium ^1H, can be used as a proxy for tritium in the computational studies and if experimental thermodynamic data based on metal protides can be expected to be similar to the performance of metal tritides.

In Chapter 4, we use first principles methods based on DFT, phonon calculations, and grand potential minimization to predict the isobaric phase diagram for $0\ K \leq T \leq 2000\ K$ for the Th-Zr-H element space, which is of interest given that $ThZr_2H_x$ ternary interstitial hydrides have been reported with enhanced stability relative to the binary hydrides. We develop a cluster analysis method to rigorously estimate the configurational

entropy of the $ThZr_2H_6$ system in order to determine its contribution to the stabilization of the ternary hydride.

In Chapter 5, we describe the high throughput screening methodologies utilized in Chapters 6 and 7 to investigate CTMH materials libraries for the NGNP application. In Chapter 6, we characterize the thermodynamic stabilities of all known, simulation ready CTMH materials to identify materials with "enhanced stability" or higher T_d relative to the associated binary hydrides. Candidates identified in this chapter will provide a useful upper boundary on the thermodynamic stabilities that can be reached at the NGNP operating temperatures based on known materials. In Chapter 7, we extend our studies to examine a set of "missing" or "proposed" CTMH materials that may form based on a simple survey of existing structure prototypes and charge balancing. Interesting materials that are predicted to be energetically stable based on initial DFT calculations are then subjected to the more rigorous screening methodology of Chapter 6 in order to identify "proposed" candidates that have high thermal stabilities appropriate for the NGNP application.

In Chapter 8, we extend our first principles methods developed in Chapter 2 to the elpasolite halide scintillator materials. Computational methods able to identify elpasolite halides that crystallize with cubic symmetry are desirable since the isotropic properties of these materials have attractive manufacturing and optical properties. We compare the performance of three levels of theory for four elpasolite halides, $Cs_2NaGdBr_6$, $Cs_2NaLaBr_6$, Cs_2LiLaI_6, and Cs_2LiScI_6, in order to determine the minimum level of theory required to accurately predict the equilibrium crystal structures at finite temperatures.

1.4 References

[1] in *42 USC 14801* (Federal Energy Regulatory Commission, United States of America, 2005).

[2] U.S. DOE Nuclear Energy Research Advisory Committee and Generation IV International Forum, *A Technology Roadmap for Generation IV Nuclear Energy Systems*, Dec. 2002.

[3] U.S. DOE Office of Nuclear Energy, *Next Generation Nuclear Plant Report to Congress*, 2010.

[4] U.S. DOE, *The U.S. Generation-IV Implementation Strategy*, DOE Office of Nuclear Energy, 2003.

[5] S. R. Sherman and T. M. Adams, *Tritium Barrier Materials and Separation Systems for the NGNP*, U. S. DOE Savannah River National Laboratory, Aiken, Nov. 2008.

[6] NGNP Project, *Next Generation Nuclear Plant Project: Preliminary Project Plan*, U. S. DOE Idaho National Laboratory, 2007.

[7] S. R. Sherman, *A Tritium Research and Collaboration Plan for the NGNP Project*, U. S. DOE Savannah River National Laboratory, Aiken, Aug. 2008.

[8] S. Hao and D. S. Sholl, *J. Membr. Sci.* **381**, 192 (2011).

[9] S. Kang, S. Hao, and D. S. Sholl, in *Membrane Science and Technology*, edited by S. T. Oyama and M. S.-W. Susan (Elsevier, 2011), Vol. 14, p. 309.

[10] C. Ling, L. Semidey-Flecha, and D. S. Sholl, *J. Membr. Sci.* **371**, 189 (2011).

[11] S. Hao and D. S. Sholl, *J. Membr. Sci.* **350**, 402 (2010).

[12] S. Hao and D. S. Sholl, *Energy Environ. Sci.* **1**, 175 (2008).

[13] B. Sakintuna, F. Lamari-Darkrim, and M. Hirscher, *Int. J. Hydrogen Energy* **32**, 1121 (2007).

[14] K. H. J. Buschow, P. C. P. Bouten, and A. R. Miedema, *Rep. Prog. Phys.* **45**, 937 (1982).

[15] *DOE Handbook: Tritium Handling and Safe Storage*, U. S. D. o. Energy, Washington, D.C., March 1999.

[16] L. Zhou, *Renewable Sustainable Energy Rev.* **9**, 395 (2005).

[17] L. Schlapbach and A. Zuttel, *Nature* **414**, 353 (2001).

[18] A. Züttel, *Mater. Today* **6**, 24 (2003).

[19] W. Grochala and P. P. Edwards, *Chem. Rev.* **104**, 1283 (2004).

[20] S. V. Alapati, J. K. Johnson, and D. S. Sholl, *J. Phys. Chem. C* **112**, 5258 (2008).

[21] S. V. Alapati, J. K. Johnson, and D. S. Sholl, *Phys. Chem. Chem. Phys.* **9**, 1438 (2007).

[22] K. C. Kim and D. S. Sholl, *J. Phys. Chem. C* **114**, 678 (2009).

[23] C. Wolverton, J. S. Donald, A. R. Akbarzadeh, and V. Ozoliņš, *J. Phys. Condens. Matter* **20**, 064228 (2008).

[24] R. van Houten and S. Bartram, *Metall. Trans.*, **2**, 527 (1971).

[25] W. Bartscher, J. Rebivant, A. Boeuf, R. Caciuffo, F. Rustichelli, J. M. Fournier, and W. F. Kuhs, *J. Less-Common Met* **121**, 455 (1986).

[26] K. A. Terrani, G. W. Chinthaka Silva, C. B. Yeamans, M. Balooch, and D. R. Olander, *J. Nucl. Mater.* **392**, 151 (2009).

[27] K. Konashi, B. A. Pudjanto, T. Terai, and M. Yamawaki, *J. Phys. Chem. Solids* **66**, 625 (2005).

[28] B. Bogdanović, A. Reiser, K. Schlichte, B. Spliethoff, and B. Tesche, *J. Alloys Compd.* **345**, 77 (2002).

[29] M. Felderhoff and B. Bogdanović, *Int. J. Mol. Sci.* **10**, 325 (2009).

[30] A. Gil, M. Medrano, I. Martorell, A. Lázaro, P. Dolado, B. Zalba, and L. F. Cabeza, *Renewable Sustainable Energy Rev.* **14**, 31 (2010).

[31] D. N. Harries, M. Paskevicius, D. A. Sheppard, T. E. C. Price, and C. E. Buckley, *Proc. IEEE* **100**, 539 (2012).

[32] W. Bartscher, J. Rebizant, and J. M. Haschke, *J. Less-Common Met* **136**, 385 (1988).

[33] W. Zhu, R. Wang, G. Shu, P. Wu, and H. Xiao, *J. Phys. Chem. C* **114**, 22361 (2010).

[34] H. F. Zhang, Y. Yu, Y. N. Zhao, W. H. Xue, and T. Gao, *J. Phys. Chem. Solids* **71**, 976 (2010).

[35] M. T. Simnad, *Nucl. Eng. Des.* **64**, 403 (1981).

[36] K. Miwa and A. Fukumoto, *Phys. Rev. B* **65**, 155114 (2002).

[37] J. J. Vajo, F. Mertens, C. C. Ahn, R. C. Bowman Jr., and B. Fultz, *J. Phys. Chem. B* **108**, 13977 (2004).

[38] P. C. P. Bouten and A. R. Miedema, *J. Less-Common Met* **71**, 147 (1980).

[39] L. George, R. Hrubiak, K. Rajan, and S. K. Saxena, *J. Alloys Compd.* **478**, 731 (2009).

[40] H. Smithson, C. A. Marianetti, D. Morgan, A. Van der Ven, A. Predith, and G. Ceder, *Phys. Rev. B* **66**, 144107 (2002).

[41] B. Grabowski, P. Söderlind, T. Hickel, and J. Neugebauer, *Phys. Rev. B* **84**, 214107 (2011).

[42] T. Kelkar, D. G. Kanhere, and S. Pal, *Comput. Mater. Sci.* **42**, 510 (2008).

[43] A. R. Akbarzadeh, V. Ozoliņš, and C. Wolverton, *Adv. Mater.* **19**, 3233 (2007).

[44] W. Rui, W. Shaofeng, W. Xiaozhi, L. Mingjian, and S. Tingting, *Phys. Scr.* **85**, 035705 (2012).

[45] J. Sangster and A. D. Pélton, *J. Phase Equilib.* **14**, 373 (1993).

[46] J. Sangster and A. D. Pélton, *J. Phase Equilib.* **1**, 84 (1994).

[47] J. Sangster and A. D. Pélton, *J. Phase Equilib.* **15**, 87 (1994).

[48] K. Yvon and G. Renaudin, in *Encyclopedia of Inorganic Chemistry, Second Edition*, edited by B. R. King (John Wiley & Sons, Chichester, 2005), Vol. III, p. 1814.

[49] B. Bogdanović and G. Sandrock, *MRS Bull.* **27**, 712 (2002).

[50] R. Griessen and A. Driessen, *J. Less-Common Met* **103**, 245 (1984).

[51] A. R. Miedema, K. H. J. Buschow, and H. H. Van Mal, *J. Less-Common Met* **49**, 463 (1976).

[52] L. George and S. K. Saxena, *Int. J. Hydrogen Energy* **35**, 5454 (2010).

[53] D. S. Sholl and J. A. Steckel, *Density Functional Theory: A Practical Introduction* (John Wiley & Sons, Hoboken, 2009).

[54] G. Kresse and J. Hafner, *Phys. Rev. B* **47**, 558 (1993).

[55] G. Kresse and J. Hafner, *Phys. Rev. B* **49**, 14251 (1994).

[56] G. Kresse and J. Furthmüller, *Phys. Rev. B* **54**, 11169 (1996).

[57] G. Kresse and J. Furthmüller, *Comput. Mater. Sci.* **6**, 15 (1996).

[58] G. Kresse and D. Joubert, *Phys. Rev. B* **59**, 1758 (1999).

[59] P. E. Blöchl, *Phys. Rev. B* **50**, 17953 (1994).

[60] A. Zangwill, *arXiv:1403.5164v1* (2014).

[61] C. H. Hu, D. M. Chen, Y. M. Wang, and K. Yang, *J. Alloys Compd.* **450**, 369 (2008).

[62] J. S. Hummelshøj, et al., *J. Chem. Phys.* **131** (2009).

[63] R. Caputo and A. Tekin, *J. Solid State Chem.* **184**, 1622 (2011).

[64] A. Jain, G. Hautier, C. J. Moore, S. Ping Ong, C. C. Fischer, T. Mueller, K. A. Persson, and G. Ceder, *Comput. Mater. Sci.* **50**, 2295 (2011).

[65] L. K. Wagner, E. H. Majzoub, M. D. Allendorf, and J. C. Grossman, *Phys. Chem. Chem. Phys.* **14**, 6611 (2012).

[66] J. Jiang, S. Zhang, S. Huang, P. Wang, and H. Tian, *Comput. Mater. Sci.* **74**, 55 (2013).

[67] S. V. Alapati, J. K. Johnson, and D. S. Sholl, *J. Alloys Compd.* **446–447**, 23 (2007).

[68] S. V. Alapati, J. K. Johnson, and D. S. Sholl, *J. Phys. Chem. B* **110**, 8769 (2006).

[69] S. V. Alapati, J. K. Johnson, and D. S. Sholl, *J. Phys. Chem. C* **111**, 1584 (2007).

[70] K. C. Kim, A. D. Kulkarni, J. K. Johnson, and D. S. Sholl, *Phys. Chem. Chem. Phys.* **13**, 21520 (2011).

[71] K. C. Kim, A. D. Kulkarni, J. K. Johnson, and D. S. Sholl, *Phys. Chem. Chem. Phys.* **13**, 7218 (2011).

[72] K. M. Nicholson and D. S. Sholl, *Phys. Rev. B* **86**, 134113 (2012).

[73] K. M. Nicholson and D. S. Sholl, *J. Chem. Eng. Data* (2014).

[74] Y. Nakamori, K. Miwa, A. Ninomiya, H. Li, N. Ohba, S.-i. Towata, A. Züttel, and S.-i. Orimo, *Phys. Rev. B* **74**, 045126 (2006).

[75] K. Miwa, N. Ohba, S. Towata, Y. Nakamori, A. Züttel, and S. Orimo, *J. Alloys Compd.* **446–447**, 310 (2007).

[76] K. Miwa, M. Aoki, T. Noritake, N. Ohba, Y. Nakamori, S. Towata, A. Züttel, and S. Orimo, *Phys. Rev. B* **74**, 155122 (2006).

[77] K. Miwa, S. Takagi, M. Matsuo, and S. Orimo, *J. Phys. Chem. C* **117**, 8014 (2013).

[78] V. Ozolins, A. R. Akbarzadeh, H. Gunaydin, K. Michel, C. Wolverton, and E. H. Majzoub, *J. Phys. Conf. Ser.* **180**, 012076 (2009).

[79] A. R. Akbarzadeh, C. Wolverton, and V. Ozolins, *Phys. Rev. B* **79**, 184102 (2009).

[80] V. Ozolins, E. H. Majzoub, and C. Wolverton, *Phys. Rev. Lett.* **100**, 135501 (2008).

[81] K. J. Michel, A. R. Akbarzadeh, and V. Ozolins, *J. Phys. Chem. C* **113**, 14551 (2009).

[82] C. Wolverton and V. Ozoliņš, *Phys. Rev. B* **75**, 064101 (2007).

[83] K. J. Michel and V. Ozoliņš, *MRS Bull.* **38**, 462 (2013).

[84] R. Weiyi, X. Pingchuan, and S. Weiguo, *Physica B* **405**, 2057 (2010).

[85] Z. Wu, *Phys. Rev. B* **81**, 172301 (2010).

[86] Z. Wu and R. M. Wentzcovitch, *Phys. Rev. B* **79**, 104304 (2009).

[87] Q. Xu and A. Van der Ven, *Phys. Rev B* **76** (2007).

[88] P. Carrier, R. Wentzcovitch, and J. Tsuchiya, *Phys. Rev. B* **76**, 064116 (2007).

[89] C. Wolverton, V. Ozoliņš, and M. Asta, *Phys. Rev. B* **69**, 144109 (2004).

[90] C. Wolverton, *Acta Mater.* **49**, 3129 (2001).

[91] C. Wolverton and V. Ozoliņš, *Phys. Rev. B* **73**, 144104 (2006).

[92] C. Wolverton, X. Y. Yan, R. Vijayaraghavan, and V. Ozoliņš, *Acta Mater.* **50**, 2187 (2002).

[93] M. A. Abbas, D. M. Grant, M. Brunelli, T. C. Hansen, and G. S. Walker, *Phys. Chem. Chem. Phys.* **15**, 12139 (2013).

[94] K. C. Kim, B. Dai, J. K. Johnson, and D. S. Sholl, *Nanotechnology* **20**, 204001 (2009).

CHAPTER 2

USING FIRST PRINCIPLES CALCULATIONS TO DESCRIBE METAL HYDRIDE THERMODYNAMICS[*]

2.1 Introduction

As discussed in Chapter 1, metal hydride systems have been studied extensively as potential hydrogen storage media for hydrogen-powered automobiles due to their high capacity and safety relative to gaseous or liquid storage options. [1-9] Thus, research efforts have focused predominately on identifying metal hydride systems that release appreciable hydrogen at or around room temperature rather than those that operate at conditions relevant for the NGNP reactor.[5,10] Although the thermodynamics of metal hydrides at low to moderate temperatures have been successfully described with DFT calculations using 0 K total energies and simple harmonic models, it is unclear if this approach is valid for hydrides that are stable at high temperatures.

In this chapter we determine the minimum level of theory that will allow for sufficient accuracy in describing the thermodynamic stability of metal hydrides using DFT for material screening purposes. We use T_d, defined in Chapter 1, to rank materials since metal hydrides with greater T_d can operate at higher temperatures, which is ideal for NGNP gettering applications. We assess the capabilities of our minimum level of theory in describing the relative stabilities of NaH, LiH, TiH_2, ZrH_2, and HfH_2. These systems form particularly stable metal hydrides and exhibit a range of metal-hydrogen bonding characteristics. LiH and NaH exhibit strong ionic bonding, whereas the transition metal

[*] The material in this chapter has been previously published as K. M. Nicholson and D. S. Sholl, Phys. Rev. B 86, 134113 (2012). Copyright 2012 by the American Physical Society.

hydrides form interstitial structures with metallic-type bonds.[4] This list also spans a wide range in metal atomic weights, from 6.941 g mol^{-1} for Li to 178.49 g mol^{-1} for Hf.

2.2 Theoretical Methods

2.2.1 Free Energy

The thermodynamic stability of a metal hydride can be described via the Gibbs free energy difference between the metal hydride and its decomposition products, ΔG. For dehydriding reactions of the type

$$aA_{(s)} \leftrightarrow bB_{(s)} + H_2 \tag{2.1}$$

where A and B are the metal hydride and pure metal phases, respectively,

$$\Delta G(T) = bG_B + G_{H_2} - aG_A \tag{2.2}$$

$\Delta G < 0$ indicates the reaction in Eq. (2.1) proceeds to the right. Assuming the activity coefficients for the solid phases are unity, the van't Hoff relation relates the free energy difference to the hydrogen pressure at equilibrium:[7,11]

$$\frac{P}{P_0} = \exp\left(\frac{-\Delta G(T)}{RT}\right) \tag{2.3}$$

where P_0 = 1 bar. We define T_d as the temperature at which P = 1 bar H_2, or equivalently, where $\Delta G(T) = 0$.

The Gibbs free energy is defined as

$$G = U - TS + PV = F + PV \tag{2.4}$$

where U, S, and F are the internal energy, entropy, and Helmholtz free energy, respectively. As noted by Ackland, it is usually computationally simpler to determine F rather than G for solids since the Hamiltonian can be constructed as a function of volume rather than of pressure.[12] For the system in Eq. (2.1) it is assumed that

$\Delta(PV)_{solids} << (PV)_{H_2}$.[7] F will be used when referring to the free energy of a metal hydride or metal, and G for the gas phases is determined from a combination of experimental and DFT data discussed below.

Using the form adopted by Grabowski, F can be written as a sum of electronic and vibrational contributions.[13,14] The vibrational contribution can be further divided into a quasiharmonic and anharmonic correction term, F^{qh} and F^{anh}, respectively. This gives

$$F(V,T) = E_0(V) + F^{qh}(V,T) + F^{anh}(V,T) \tag{2.5}$$

where $E_0(V)$ is the ground state total energy of a crystal determined using DFT. Finite temperature electronic excitations are neglected in these calculations.[15] In Eq. (2.5), the quasiharmonic free energy contribution accounts for volume-dependent zero point and finite temperature vibrational effects in solids within the harmonic approximation. For a given volume, the vibrational density of states (VDOS) is computed and integrated to give the temperature-dependent vibrational free energy within the harmonic approximation.[12] In this chapter, the VDOS is computed using the direct method as implemented by Parlinski and is hereafter referred to as a phonon calculation.[16] F^{anh} corrects for the fact that the phonon frequency ω is a function of both V and T. Wu's method[17] of determining F^{anh} using *ab initio* calculations within the framework developed by Wu and Wentzcovitch[18] is utilized to complete the definition of Eq. (2.5).

2.2.2 Levels of Theory to Predict $F(V,T)$

Several levels of theory are embedded in $F(V,T)$ as defined in Eq. (2.5). Each level makes assumptions regarding which phenomena are relevant, and the higher levels require significantly more computational effort than lower levels. Additionally, there are several methods for calculating terms within each level of theory. In this chapter, we

determine the free energy of metal hydrides and the corresponding pure metal phase with four levels of theory to assess the relative benefit of the added computational cost for higher levels.

The simplest level of theory based solely on ground state energy calculations neglects the temperature dependence of the free energy. The free energy approximated in this way may either neglect or include zero point vibrational energies:

$$F(V_0) \cong E_0(V_0) \tag{2.6}$$

$$F(V_0) \cong E_0(V_0) + F^{qh}(V_0, T = 0) \tag{2.7}$$

Computations at this level simply involve determining the total energy of the solid phases at their uncorrected ground state equilibrium volume V_0 using DFT. V_0 is uncorrected because it does not include the shift in equilibrium volume due to zero point vibrational effects.[19] We use phonon calculations to determine zero point energies. Since $\Delta G = \Delta H(T) - T\Delta S(T)$ and ΔG behaves largely linearly with respect to T beyond the low temperature regime, T_d can be approximated using

$$T_d = \frac{\Delta H}{\Delta S} \tag{2.8}$$

with $\Delta H \approx \Delta F(V_0)$ and assuming a constant entropy, $\Delta S \approx 0.130$ kJ K^{-1} mol^{-1}H$_2$, as proposed by Zuttel et al. for all metal-hydrogen systems.[20]

Ground state energy calculations have been widely applied to determine properties of metal hydrides at low to moderate temperatures. For example, Ackland used DFT to identify the bistable crystal structure of ε-ZrH$_2$ using ground state energy calculations.[21] Alapati et al. screened over 300 metal hydrides systems for use in reversible H$_2$ storage applications based on reaction enthalpies calculated via the relation $\Delta H(T) \approx \Delta E_0$ + a correction term.[7] They found that the zero point energies were partially

offset by the H_2 translational, rotational, and PV contributions to the free energy and that these terms could be approximated with an empirical correction term.

Simple harmonic models introduce finite temperature vibrational effects in solid phases through a single phonon calculation at either the uncorrected or corrected ground state volume. The key difference between this and higher levels of theory is that the phonon frequency dependence on volume and temperature and, thus, thermal expansion are neglected. The free energy of each solid in this approach is approximated by

$$F(V_0,T) \cong E_0(V_0) + F^{qh}(V_0,T) \tag{2.9}$$

$$F(V_{0c},T) \cong E_0(V_{0c}) + F^{qh}(V_{0c},T) \tag{2.10}$$

where the first (second) expression uses the uncorrected (corrected) ground state volume. Zhu et al. used this approach to study γ-ZrH, ζ-Zr_2H, ε-ZrH_2, and δ-$ZrH_{1.5}$.[22]

The third level of theory we consider is a quasiharmonic model in which the dependence of phonon frequencies on volume is included:

$$F(V,T) \cong E_0(V) + F^{qh}(V,T) \tag{2.11}$$

Quasiharmonic models involve significantly more computational effort than lower levels of theory because $\omega = \omega(V)$ must be calculated for a range of volumes rather than at a single volume. Since the free energy surface has both volume and temperature degrees of freedom, the equilibrium volume is that which minimizes $F(V)$ at a given temperature. Thus, this calculation predicts how the volume of the solid expands or contracts with temperature. The relative computational cost for computing the free energy for a solid within a simple harmonic or quasiharmonic model depends greatly on the symmetry of the crystal structure and the number of volumes sampled to describe the volume-dependent free energy.

There are two common approaches to sampling the volume in the quasiharmonic approximation. The full search method varies each lattice degree of freedom independently while simultaneously relaxing ionic positions and determines ω and $F(T)$ for each unique configuration. This method can be very computationally expensive for materials with multiple degrees of freedom, but has successfully been applied to simple materials such as hexagonal close-packed (hcp) Mg, Ti, and Zr to study anisotropic thermal expansion.[23] The volume-only stress-minimization method, referred to as the static quasiharmonic method here, is less demanding in that phonon frequencies are only computed at specific volumes in a selected range of volumes where the lattice parameters and atomic coordinates are those that minimize the electronic total energy $E_0(V)$. Carrier et al. found good agreement between predicted lattice constants and internal ion positions of $MgSiO_3$ from static quasiharmonic calculations and experimental results at high T and P.[24] Frankcombe and Kroes used both methods to compute the thermal expansion of orthorhombic $LiBH_4$ with three lattice degrees of freedom. They found that the full search method led to a 5% greater relaxation in the free energy minimum compared with the static method although the quasiharmonic method, in general, did not lead to better agreement with experimental results compared with DFT models neglecting lattice vibrations.[25]

The highest level of theory we consider includes explicit anharmonic corrections to the quasiharmonic free energy to specify the terms in Eq. (2.5) in full. Methods for accounting for anharmonic effects in materials due to temperature-dependent phonon-phonon interactions using first principles are still in their infancy and can be computationally expensive.[14,15,25-27] In this work, calculations at this level required over

an order of magnitude more computational effort than for models based on the ground state energy alone, and this relative effort would be larger for materials with more complex crystal structures. Wu and Wentzcovitch recently developed a semi-empirical method to compute the anharmonic contribution based on integration of a parameterized F^{anh} with a single constant that can be determined through comparison of predicted and experimental data of a volume-dependent thermodynamic property such as the thermal expansivity.[18] Wu later proposed a method determining this constant from a single canonical ensemble (NVT) *ab initio* molecular dynamics (AIMD) calculation in combination with the quasiharmonic free energy.[17] Due to its relative computational simplicity, Wu's approach is used to determine the magnitude of F^{anh} for the metal hydrides we consider.

In this chapter, $F(V,T)$ in Eq. (2.11) was determined using static quasiharmonic calculations for Li, LiH, Na, NaH, Zr, ZrH_2, Hf, HfH_2, Ti, and TiH_2. For comparison, a quasiharmonic calculation employing the full search method was completed for hcp Zr and body-centered tetragonal (bct) ZrH_2 since both crystal structures have two lattice degrees of freedom. In most cases, levels of theory based on ground state energies and simple harmonic models with or without zero point lattice corrections (Eqs. (2.6-2.10)) were determined from Eq. (2.11) and required no separate computation. Since calculation of the explicit anharmonic correction to the quasiharmonic free energy is computationally expensive, this level of theory was only applied to Zr, ZrH_2, and zirconium ditritide, ZrT_2.

2.3 Computational Details

Plane wave DFT calculations were carried out with the Vienna *Ab Initio* Simulation Package (VASP).[28-32] Electronic ground states were determined using the projector augmented wave (PAW) method with the PW91 GGA exchange-correlation functional.[33-35] Except where indicated, all calculations were performed on a 1 × 1 × 1 crystallographic unit cell with a 425 eV cutoff energy and 9 × 9 × 9 *k*-point Monkhorst-Pack mesh. 2 × 2 × 2 supercells were used to compute phonon frequencies, and this was found to be sufficient to reduce the force constant at the supercell surface to three orders of magnitude less than the force constants at the center. All hcp structures were transformed into a rhombohedral setting for the calculation of vibrational frequencies. Monkhorst-Pack meshes were adjusted to maintain the same density of *k*-points for the phonon calculations as used in the electronic total energy calculations.

Initial crystal structures for metals and metal hydrides were obtained from the Inorganic Crystal Structure Database (ICSD).[36,37] The elemental metals were treated as hcp Zr, Ti, Hf, and Li and body-centered cubic (bcc) Na based on the structures each adopts at 0 K. The crystal structures of the stoichiometric metal hydrides studied include bct ZrH_2 and HfH_2 and face-centered cubic (fcc) TiH_2, LiH, and NaH. For agreement with common literature values, the bct lattice parameters are reported in terms of the face-centered tetragonal (fct) unit cell with the *a* (bct) lattice parameter multiplied by a factor of $\sqrt{2}$. The temperature-dependent free energy for each volume in a range of volumes was determined to find $F(V,T)$ for each solid phase. Between 6 and 17 volumes were sampled with the largest set of volumes used to describe light materials. At each volume, the cell shape and ionic coordinates were relaxed until forces on each atom were

less than 10^{-4} eV $Å^{-1}$. The PHONON code developed by Parlinski was used to calculate the VDOS and vibrational contribution to the free energy using the direct method.[16] A displacement magnitude of ±0.03 Å was applied. At each T examined, a fourth order polynomial was fit to $F(V)$. The error associated with this curve fitting was less than 0.5 kJ mol^{-1} for HfH_2 and less than 0.1 kJ mol^{-1} for all other materials.

Since Na and Li melt at 371 K and 450 K, respectively, predicting equilibrium volumes at high temperatures for these materials using the quasiharmonic approximation is a mathematical exercise.[38-40] NaH and LiH were predicted to expand beyond the range of volumes sampled for $T > 630$ K. Since ΔG behaves largely linearly beyond the low temperature regime, T_d for the quasiharmonic model was determined via a linear fit of ΔG between 300 K and 630 K for these systems.

For comparison with the static quasiharmonic method, a full search method was used for anisotropic Zr and ZrH_2, varying both a and c lattice parameters independently and calculating the vibrational free energy at each unique configuration. In the case of hcp Zr, 26 combinations of a and c lattice constants with $\Delta a = 0.01$ Å and $\Delta c = 0.07$ Å were separately tested for $a = 3.2$ - 3.25 Å and $c = 5.1$ - 5.45 Å. Since the vibrational free energy behaves largely linearly with independent changes in a and c, the vibrational free energies were slightly extrapolated to extend the range of volumes to $a = 3.27$ Å. Including volumes beyond these bounds changes the predicted lattice constants by less than 0.001 Å. In the case of ZrH_2, a grid of 63 a and c combinations with $\Delta a = 0.03$ Å and $\Delta c = 0.05$Å were used for $a = 3.45 – 3.63$ Å and $c = 4.35$ - 4.75 Å. A fourth order polynomial surface was fit to $F(a,c)$ at each temperature. The lattice coordinates corresponding to the minimum of $F(a,c)$ were determined using MATLAB's constrained

nonlinear optimization functions implemented by a sequential quadratic programming method. The estimated error for this surface fitting is less than 0.1 kJ mol^{-1}.

Wu's method for determining $F^{anh}(V,T)$ as described in Eq. (2.5) from a single AIMD calculation is described in Reference 17. A single AIMD calculation with reciprocal space sampled at the Γ-point with a cutoff energy of 425 eV was performed for Zr, ZrH_2, and ZrT_2. A 2 × 2 × 2 48 atom supercell with volume 65 Å^3 unit cell^{-1} for ZrX_2 and a 24 atom supercell with volume of 58 Å^3 unit cell^{-1} for Zr were tested. Temperature was maintained at 800 K using a Nosé thermostat and Nosé mass corresponding to a period of 40 timesteps. The AIMD simulations were run for 6.3 ps including a 2 ps equilibration period with timestep of 0.2 fs. The volume-independent dimensionless constants in Wu and Wentzcovitch's model were determined to be -0.25, -0.36 and 5.25 for ZrH_2, ZrT_2, and Zr, respectively.

Diatomic hydrogen isotope free energies for were calculated using

$$G(T) = \left[G(T) - H_{298.15}\right] + H_{DFT,298.15} \tag{2.12}$$

where [$G(T)$ - $H_{298.15}$] values were referenced from the Thermodynamics Research Center thermodynamic tables for non-hydrocarbons.[41] These data tables were chosen specifically because they contain references for tritium, for which data is scarce, and they are in agreement with the JANAF tables for H_2 and D_2 within 2 kJ mol^{-1} over the temperature range studied.[42] $H_{\mathrm{DFT},298.15}$ was calculated for each hydrogen isotope using

$$H(T) = E_0 + U_{vib}(T) + U_{trans+rot}(T) + PV \tag{2.13}$$

The DFT total energy of a hydrogen molecule was found using a cubic supercell of length 10 Å, cutoff energy of 660 eV, and 2 × 2 × 2 *k*-point Monkhorst-Pack mesh. These parameters were sufficient to converge E_0 to within 0.1 kJ mol^{-1}. Finite differences with

0.01 Å displacements were used to compute the Hessian matrix and vibrational frequencies at the Γ-point of the isotope species in the same cubic supercell. This produced zero point energies of 26.1, 18.5, and 15.1 kJ mol^{-1} X_2 for X = H, D, and T, respectively. At 298.15 K, the zero point energy dominates $U_{vib}(T)$ with temperature-dependent contributions of less than 10^{-3} kJ mol^{-1}. We assume hydrogen behaves as an ideal gas with $U_{trans+rot}+PV = 7/2\ RT$.

While the quasiharmonic and explicit anharmonic corrections to the quasiharmonic free energy levels of theory provide estimates of thermal expansion in solid phases that are unavailable through ground state or simple harmonic free energies alone, it is unclear as to how much incorporating this dependency changes T_d. To assess these effects, we compare predictions of T_d for ZrH_2 using four levels of theory. First we determine the appropriate method for computing free energies within the quasiharmonic approximation for anisotropic Zr and ZrH_2.

2.4 Full Search vs. Static Quasiharmonic Calculation

The unit cells of Zr and ZrH_2 each have two degrees of freedom, a and c. Formally, $F = F(a,c,T)$, but the full search method, which varies each lattice parameter independently and computes the vibrational free energy for each configuration, requires much more computational effort than a static quasiharmonic calculation. Presumably, predictions of $a(T)$, $c(T)$, and $F(T)$ within the quasiharmonic approximation using the full search method are more accurate than those predicted via the static method. However, the full calculation required six times as many phonon calculations as the static treatment of the free energy based on the lattice grid sampling used in this work. Table 2.1 presents

the lattice properties of Zr and ZrH_2 determined using both quasiharmonic methods along with comparisons to published experimental and first principles results. For both Zr and ZrH_2 the full and static methods produce nearly identical ground state values for *a*, *c*, *V*, and the bulk modulus *B* where [19]

$$B = V\frac{\partial^2 F(V)}{\partial V^2} \tag{2.14}$$

The DFT results are within 2% of the experimental values for both Zr and ZrH_2, but accounting for thermal expansion does not bring the predicted values into better agreement with experimental values at 298 K.

Table 2.1: Lattice properties of hcp Zr and fct ZrH_2 at 0 K (298 K) predicted within the quasiharmonic approximation using both full search and volume-only (static) stress minimization methods.

	Zr				ZrH_2			
	a (Å)	*c* (Å)	*V* ($Å^3$)	*B* (GPa)	*a* (Å)	*c* (Å)	*V* ($Å^3$)	*B* (GPa)
Full	3.230 (3.235)	5.175 (5.180)	46.7 (46.9)	97.6 (94.7)	5.060 (5.058)	4.458 (4.475)	114.1 (114.5)	125.2 (122.1)
Static	3.231 (3.235)	5.174 (5.180)	46.8 (47.0)	97.8 (94.5)	5.045 (5.049)	4.479 (4.486)	114.0 (114.4)	126.4 (123.6)
Expt.	3.227[a]	5.137[a]	46.3[a]	97.2[b] 95.2[c]	4.976[d]	4.451[d]	110.0	--

[a] at 298 K[43]
[b,c] at 4 K and 298 K[44]
[d] at 297 K[45,46]

Figure 2.1 shows the predicted lattice expansion and isotropic volumetric thermal expansion, ε

$$\varepsilon = \frac{V - V_{ref}}{3V_{ref}} \tag{2.15}$$

for Zr and ZrH_2 using the full search and static quasiharmonic methods where V_{ref} is the volume at a reference temperature. This definition is consistent with References 23 and 47. For both Zr and ZrH_2, static calculations predict similar rates of expansion in *a* and *c* while using the full search method, *a* is largely held constant with increasing temperature and expansion in *c* drives the overall unit cell volume expansion. Skinner and Johnston calculate ε = 0.0051 at 950 K with $V_{ref} = V_{298}$ based on X-ray diffraction measurements of Zr lattice parameters.[43] In comparison, our calculations give ε = 0.0039 and ε = 0.0045 for the full and static methods, respectively, which indicate reasonable agreement with the experimental result. Skinner and Johnston also determine the average linear coefficient of expansion between 298 K and 1143 K as 5.5×10^{-6} K^{-1} and 10.8×10^{-6} K^{-1} for *a* and *c*, respectively. Our full search method gives 3.0×10^{-6} K^{-1} and 12.0×10^{-6} K^{-1} for *a* and *c*, respectively, for the same temperature range. The static calculation predicts 7.7×10^{-6} K^{-1} and 5.6×10^{-6} K^{-1} for *a* and *c*, respectively. Based on this result, the full search method more accurately predicts the anisotropic thermal expansion of Zr. Over the temperature range studied, the lattice parameters for Zr expand only 0.01 Å in *a* and 0.11 Å in *c*, which are on the same order as the grid spacing we used to sample lattice configurations for the full method. A more detailed study of the anisotropic thermal expansion of Zr would need to use finer grid spacing. Nie and Xie similarly used DFT to study the thermal expansion of hcp Zr using a full search quasiharmonic method.[23] While our predicted ε with $V_{ref} = V_{293}$ are in good quantitative agreement, the predicted lattice

parameter expansions agree only qualitatively. Our calculations predict slightly less expansion in *a* and more expansion in *c* than Nie and Xie. However, this may be due to differences in grid spacing.

The full search and static quasiharmonic calculations predict virtually identical volumetric thermal expansion for ZrH_2. Yakel studied the thermal expansion of $ZrH_{1.92}$ using X-ray diffraction and found that the linear coefficient of volumetric expansion based on the fct unit cell was 9.03×10^{-6} K^{-1} between 300 K and 700 K.[48] Our calculations are in excellent agreement with an average linear coefficient of volumetric expansion over the same temperature range of 10.0×10^{-6} K^{-1} and 9.6×10^{-6} K^{-1} for the full and static methods, respectively. In Yakel's work, *a* contracts slightly by about 0.01 Å and *c* expands by approximately 0.1 Å between 100 K and 800 K. The grid spacing in this work, Δa = 0.03 Å and Δc = 0.05 Å, is too coarse to perform detailed comparisons of the anisotropic expansion for ZrH_2. Our calculations indicate, however, that *a* tends to expand more slowly than *c*, and that the volume expansion is driven by changes in *c*.

The predicted free energies for both quasiharmonic methods agree to within 0.3 kJ mol^{-1} for ZrH_2 and to within 0.1 kJ mol^{-1} for Zr over the full temperature range studied. This corresponds to T_d = 1131 K and T_d = 1129 K for the full search and static methods, respectively. Thus, static calculations were used in the remainder of this work to calculate $F(V,T)$ for solid phases within the quasiharmonic approximation.

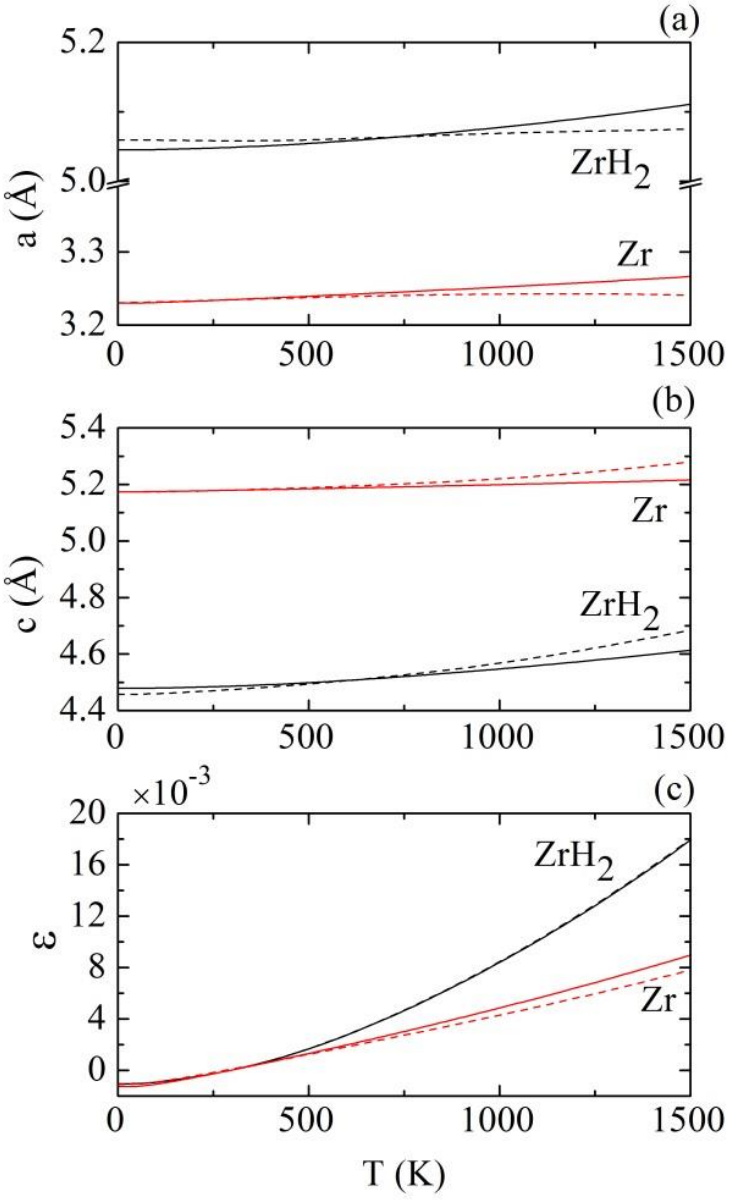

Figure 2.1: Predicted lattice constants and volume thermal expansion of hcp Zr and fct ZrH_2 within the quasiharmonic approximation using the volume-only (static) stress minimization (solid curves) and full search (dashed curves) methods: (a) lattice constant parallel to principal axis, (b) lattice constant perpendicular to principal axis, (c) volumetric thermal expansivity relative to lattice volume at 293 K.

2.5 Simple Harmonic Free Energies

As mentioned above, the computational effort associated with calculating ΔG with a simple harmonic calculation at V_0 in Eq. (2.9) is considerably less than using static quasiharmonic calculations, Eq. (2.11). However, simple harmonic calculations at V_{0c} in Eq. (2.10) raise the computational cost to the quasiharmonic level since both methods require computing volume-dependent vibrational energies. Figure 2.2 shows the slight correction in predicted ground state volume from 55.6 $Å^3$ to 57.0 $Å^3$ for ZrH_2 upon inclusion of zero point energies. The zero point energy lattice correction is even smaller for Zr, with a marginal expansion from 46.7 $Å^3$ to 46.8 $Å^3$.

The small corrections to the ground state volumes of Zr and ZrH_2 lead to a 0.7 kJ mol^{-1} H_2 difference in ΔH at 0 K including zero point energies and a difference in T_d of 15 K. The difference between these results is likely to be insignificant in terms of material screening. In terms of computational effort, it is, therefore, not cost-effective to calculate the volume-dependent zero point energy to compute $F(T)$ about the zero point energy corrected ground state volume.

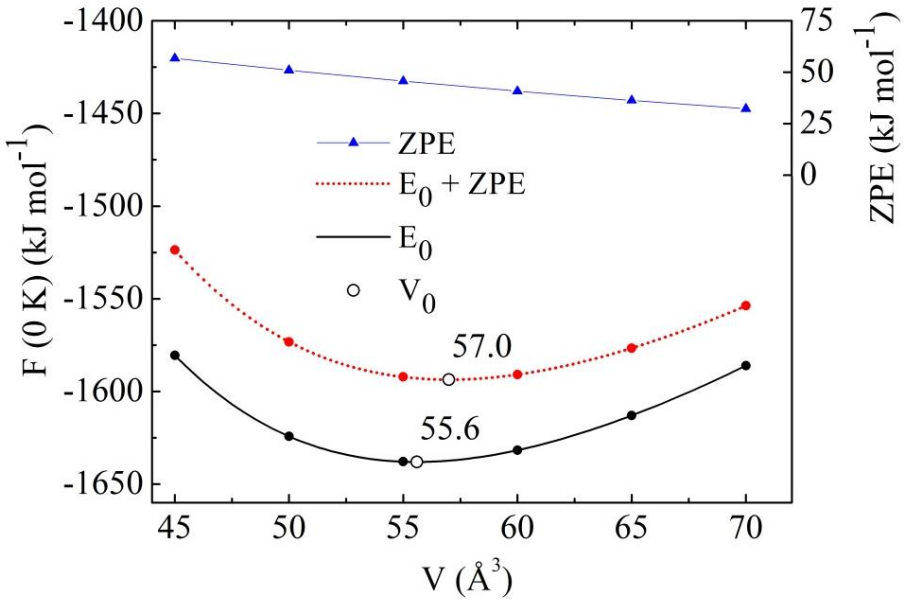

Figure 2.2: The shift in the ZrH_2 equilibrium unit cell volume (V_0) at 0 K upon addition of the volume-dependent zero point energy (ZPE) correction to the DFT electronic energy (E_0).

2.6 Explicit Anharmonic Correction

At temperatures greater than 1000 K, metals and metal hydrides may undergo significant thermal expansion due to temperature-dependent changes in vibrational properties. Often, in first principles thermodynamic studies of solids, anharmonic contributions are neglected such that $\omega \neq \omega(T)$ as in the quasiharmonic approximation. While calculations of $F(V,T)$ within the quasiharmonic approximation, Eq. (2.11), include an estimate of anharmonic effects through the temperature dependence of the equilibrium volume, it was unclear how large an error is introduced through not accounting for the explicit anharmonic correction as in Eq. (2.5). Figure 2.3 displays the computed anharmonic correction terms for Zr and ZrH_2. Incorporation of F^{anh} tends to decrease the total free energy of ZrH_2 and increase the free energy of Zr. However, adjustments are less than 1 kJ mol^{-1} H_2 between 0 K and 500 K, rising to about 5.0 kJ mol^{-1} H_2 and -2.4 kJ

mol^{-1} H_2 for Zr and ZrH_2, respectively, at 1500 K. Calculating ΔG via Eq. (2.5) leads to a predicted T_d of 1159 K compared with 1129 K computed with quasiharmonic free energies alone. At this temperature, ΔF^{anh} contributes approximately only 4.5 kJ mol^{-1} H_2 to ΔG. For ZrT_2, the magnitude of ΔF^{anh} at T_d is nearly the same as for the protiated material, and T_d similarly increases by 34 K relative to the T_d determined using only static quasiharmonic free energies.

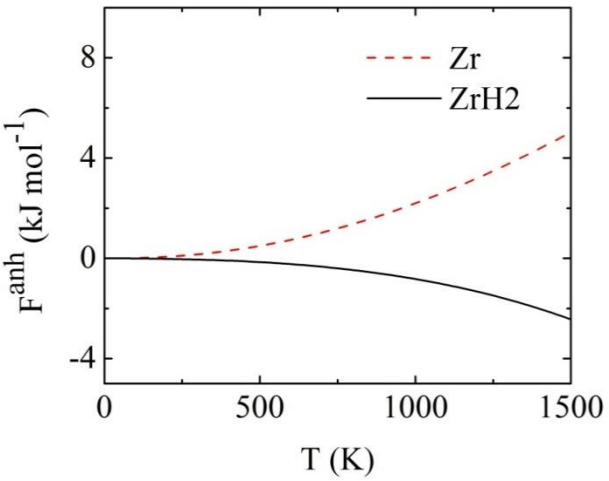

Figure 2.3: Contribution of the explicit anharmonic free energy term to the quasiharmonic free energies of Zr and ZrH_2 determined using the methods of Wu and Wentzcovitch.[17,18]

2.7 Level of Theory Comparison

Table 2.2 compiles the predicted T_d of ZrH_2 for 1 bar H_2 pressure for each of the four levels of theory studied in this work. For models based on ground state energies and simple harmonic calculations, two methods for each level of theory are presented. Of the models that include finite temperature vibrational effects, i.e., simple harmonic and higher, the difference between the lowest and highest level of theory is only about 50 K

which corresponds to an energy difference of about 7 kJ mol^{-1} H_2 based on $\Delta S \approx 0.130$ kJ K^{-1} mol^{-1} H_2. Alapati et al. calculated the enthalpy of formation for several metal hydride systems including MgH_2, LiH, CaH_2, AlH_3, $Ca(AlH_4)_2$, and $LiBH_4$ using both Ultrasoft Pseudopotentials and PAW methods with the PW91 functional (in supplementary information of Reference 49). Based on these systems the differences in calculated enthalpy of formation for these two methods range from 0 to 5 kJ mol^{-1} H_2. Similar calculations using the PAW method with PW91 and PBE functionals resulted in differences of 12 kJ mol^{-1} H_2 for LiH and 10 kJ mol^{-1} H_2 for MgH_2. Even larger differences are encountered when comparing USPP-PW91 and USPP-rPBE functionals. These results indicate that the predicted thermodynamic properties are more sensitive to the DFT functional than the level of theory used to include finite temperature vibrational effects.

The finite temperature models that include thermal expansion of the solid phases, quasiharmonic and the explicit anharmonic correction to the quasiharmonic free energies, exhibit only minor corrections to the simple harmonic models. In the case of the Zr-H system, the magnitude of the static quasiharmonic correction to the simple harmonic $F(V_0, 1000\ K)$ for ZrH_2 and Zr is only 3 kJ mol^{-1} H_2 and 0.2 kJ mol^{-1} H_2, respectively. Thus, the thermal expansion correction is negligible for this system. There is very little difference between the models that account for vibrational contributions to the free energy because ΔG largely behaves as a linear function of a constant ΔH and ΔS beyond the very low temperature regime. The models based on ground state energies rely on the choice of a constant ΔS. The good agreement between $T_d = 1154$ K, predicted for ground state energies including zero point energies, and the highest level of theory including

anharmonic corrections, T_d = 1159 K, is due to the fortuitous use of $\Delta S \approx 0.130$ kJ K^{-1} mol^{-1} H_2 recommended by Zuttel for all metal-hydrogen systems. The assumed value happens to be very close to that predicted for the anharmonic model with ΔS=0.133 kJ K^{-1} mol^{-1} H_2 based on linear regression of ΔG between 500 K and 1500 K. However, ΔS has been shown to be as low as 0.097 kJ K^{-1} mol^{-1} H_2 for complex metal hydrides such as $LiBH_4$.[49] Thus, use of the assumed $\Delta S \approx 0.130$ kJ K^{-1} mol^{-1} H_2 in ground state models may not yield results in as good agreement with higher levels of theory in cases where the entropy of reaction is significantly different than the assumed value.

Alapati et al. found that $-20 < \Delta E^*_{ZPE} + E_{ZPE,H_2} < -10$ kJ mol^{-1} H_2 for over 300 metal hydride decomposition reactions including reactions in which the metal hydride is destabilized by another compound where * indicates the change over the solid phases.[7] That is consistent with the finding for the Zr-H system studied here with computed $\Delta E^*_{ZPE} + E_{ZPE,H_2}$ of -16.9 kJ mol^{-1} H_2. Thus, with $\Delta S \approx 0.130$ kJ K^{-1} mol^{-1} H_2 the simplest calculation based only DFT ground state electronic energies can predict T_d to within approximately 150 K of the more rigorous computation that includes zero point energies. This is supported by the results shown in Table 2.3 for all five metal hydrides studied.

Table 2.2: Predicted temperature of dehydrogenation and reaction enthalpy at 0 K for ZrH_2 predicted using four levels of theory (V_0 and V_{0c} refer to ground state volumes not corrected and corrected for zero point vibrational effects, respectively).

Model Description	T_d (K)	ΔH_0 (kJ mol^{-1} H_2)
Ground state energies at V_0 – Eq. (2.6)	1284	166.9
Ground state energies including zero point energies at V_0 – Eq. (2.7)	1154	150.0
Simple harmonic calculation at V_0 – Eq. (2.9)	1108	150.0
Simple harmonic calculation at V_{0c} – Eq. (2.10)	1123	150.7
Quasiharmonic (static) – Eq. (2.11)	1129	150.7
Explicit anharmonic correction to quasiharmonic (static) free energy – Eq. (2.5)	1159	150.7

For the five metal hydrides studied in this work, the lowest level of theory predicts T_d to within approximately 150 K of the more rigorous quasiharmonic predicted value with the largest differences apparent for the heavy metal hydrides. With the exception of HfH_2, for which no experimental data could be found, the models including vibrational effects are within 70 K of the experimental values, and the simplest model predicts T_d to within 200 K of the experimental value. This suggests that material screening based on DFT calculations seeking to identify metal hydrides that are thermodynamically stable to the release of hydrogen at high temperatures could first screen a library of materials based on E_0 alone. As previously discussed, the simple harmonic and ground state energies including zero point vibration models require the same amount of computational effort with our method of computing vibrational energies.

Table 2.3: T_d (K) for metal hydrides predicted using both static quasiharmonic calculation of free energies and free energies based on ground state energies at volumes uncorrected for zero point energy vibrational effects with and without zero point energy. Published experimental values are included for comparison. ΔS=0.130 kJ K^{-1} mol^{-1} H_2.

	Quasiharmonic	$T_d = \frac{\Delta(E_0)}{\Delta S}$	$T_d = \frac{\Delta(E_0 + ZPE)}{\Delta S}$	Experiment
LiH	1118	1124	1075	1184 [38]
NaH	647	664	655	701 [50]
TiH_2	946	1088	941	916 [51,52]
ZrH_2	1129	1284	1154	1154 [52,53]
HfH_2	1003	1140	1001	--

For all materials tested, the quasiharmonic thermal expansion correction to the free energy was minor, and the zero point energy correction to the ground state volume shifted ΔH at 0 K by less than 1.5 kJ mol^{-1} H_2. TiH_2, ZrH_2, HfH_2, and NaH each had differences in the predicted T_d for the simple harmonic at the uncorrected ground state volume and the static quasiharmonic models of less than 30 K or 4 kJ mol^{-1} H_2 with the approximation ΔS = 0.130 kJ K^{-1} mol^{-1} H_2. The largest difference between the quasiharmonic and simple harmonic calculations at the uncorrected ground state volume was less than 70 K or 9 kJ mol^{-1} H_2 for LiH. The quasiharmonic approximation estimates the volume dependence of the vibrational frequency and, consequently, the volume expansion of the solid phases. LiH melts at 961 K, and above this temperature the appropriate phase system is a mixture of liquid LiH, liquid Li, and H_2 gas. The quasiharmonic approximation is not valid for temperatures approaching the melting point because anharmonic effects are no longer negligible.[54] In this two liquid region, H_2 reaches a pressure of 1 atm (≈1 bar) at 1184 K.[38,55] This is only slightly larger than the simple harmonic and quasiharmonic predicted values of 1053 K and 1118 K, respectively. Similarly, the predicted values of T_d for NaH are reasonably close to the

experimental value considering that Na melts at low temperature. The performance of the thermodynamic models used in this work in predicting dissociation temperatures for metal-hydrogen systems with solids that melt at temperatures lower than T_d is due to the linear nature of ΔG.

2.8 Conclusions

We have investigated the thermodynamic stabilities of five metal hydrides using four different levels of theory. These included predictions based solely on ground state energies, simple harmonic calculations at a single volume, quasiharmonic calculations, and inclusion of an explicit anharmonic correction to the quasiharmonic free energy. The two highest levels of theory include estimates of thermal expansion. Our aim was to determine the minimum amount of computational effort required to reliably predict $\Delta G(T)$ and T_d for metal hydride systems. Our calculations show that the levels of theory that account for volume expansion produce only a minor correction to the free energies of the metals and metal hydrides studied within the temperature range of interest. The simplest model based on DFT ground state electronic energies without zero point energy correction was shown to predict T_d within 200 K of the experimental values. Higher order models including vibrational free energies predicted T_d to within 70 K of the available experimental values. Since the simple harmonic calculation predicted stabilities within 70 K of the quasiharmonic values with largest differences for the lightest materials, an efficient screening method to identify very stable metal hydrides would first screen based on ΔE_0 and then investigate interesting materials more thoroughly with a simple harmonic calculation at the uncorrected ground state volume.

2.9 References

[1] L. Zhou, *Renewable Sustainable Energy Rev.* **9**, 395 (2005).

[2] L. Schlapbach and A. Zuttel, *Nature* **414**, 353 (2001).

[3] A. Züttel, *Mater. Today* **6**, 24 (2003).

[4] W. Grochala and P. P. Edwards, *Chem. Rev.* **104**, 1283 (2004).

[5] B. Sakintuna, F. Lamari-Darkrim, and M. Hirscher, *Int. J. Hydrogen Energy* **32**, 1121 (2007).

[6] S. V. Alapati, J. K. Johnson, and D. S. Sholl, *J. Phys. Chem. C* **112**, 5258 (2008).

[7] S. V. Alapati, J. K. Johnson, and D. S. Sholl, *Phys. Chem. Chem. Phys.* **9**, 1438 (2007).

[8] K. C. Kim and D. S. Sholl, *J. Phys. Chem. C* **114**, 678 (2009).

[9] C. Wolverton, J. S. Donald, A. R. Akbarzadeh, and V. Ozoliņš, *J. Phys. Condens. Matter* **20**, 064228 (2008).

[10] L. George and S. K. Saxena, *Int. J. Hydrogen Energy* **35**, 5454 (2010).

[11] J. J. Vajo, F. Mertens, C. C. Ahn, R. C. Bowman Jr., and B. Fultz, *J. Phys. Chem. B* **108**, 13977 (2004).

[12] G. J. Ackland, *J. Phys. Condens. Matter* **14**, 2975 (2002).

[13] B. Grabowski, T. Hickel, and J. Neugebauer, *Phys. Rev. B* **76**, 024309 (2007).

[14] B. Grabowski, P. Söderlind, T. Hickel, and J. Neugebauer, *Phys. Rev. B* **84**, 214107 (2011).

[15] T. Hickel, B. Grabowski, F. Körmann, and J. Neugebauer, *J. Phys. Condens. Matter* **24**, 053202 (2012).

[16] K. Parlinski, Software *PHONON*, 2005.

[17] Z. Wu, *Phys. Rev. B* **81**, 172301 (2010).

[18] Z. Wu and R. M. Wentzcovitch, *Phys. Rev. B* **79**, 104304 (2009).

[19] C. H. Hu, D. M. Chen, Y. M. Wang, and K. Yang, *J. Alloys Compd.* **450**, 369 (2008).

[20] A. Züttel, P. Wenger, S. Rentsch, P. Sudan, P. Mauron, and C. Emmenegger, *J. Power Sources* **118**, 1 (2003).

[21] G. J. Ackland, *Phys. Rev. Lett.* **80**, 2233 (1998).

[22] W. Zhu, R. Wang, G. Shu, P. Wu, and H. Xiao, *J. Phys. Chem. C* **114**, 22361 (2010).

[23] Y. Nie and Y. Xie, *Phys. Rev. B* **75**, 174117 (2007).

[24] P. Carrier, R. Wentzcovitch, and J. Tsuchiya, *Phys. Rev. B* **76**, 064116 (2007).

[25] T. J. Frankcombe and G. Kroes, *Phys. Rev. B* **73**, 174302 (2006).

[26] B. Grabowski, L. Ismer, T. Hickel, and J. Neugebauer, *Phys. Rev. B* **79**, 134106 (2009).

[27] L. Vočadlo and D. Alfè, *Phys. Rev. B* **65**, 214105 (2002).

[28] G. Kresse and J. Hafner, *Phys. Rev. B* **47**, 558 (1993).

[29] G. Kresse and J. Hafner, *Phys. Rev. B* **49**, 14251 (1994).

[30] G. Kresse and J. Furthmüller, *Phys. Rev. B* **54**, 11169 (1996).

[31] G. Kresse and J. Furthmüller, *Comput. Mater. Sci.* **6**, 15 (1996).

[32] D. S. Sholl and J. A. Steckel, *Density Functional Theory: A Practical Introduction* (John Wiley & Sons, Hoboken, 2009).

[33] P. E. Blöchl, *Phys. Rev. B* **50**, 17953 (1994).

[34] G. Kresse and D. Joubert, *Phys. Rev. B* **59**, 1758 (1999).

[35] J. P. Perdew, J. A. Chevary, S. H. Vosko, K. A. Jackson, M. R. Pederson, D. J. Singh, and C. Fiolhais, *Phys. Rev. B* **46**, 6671 (1992).

[36] G. Bergerhoff and I. D. Brown, in *Crystallographic Databases*, edited by F. H. Allen, G. Bergerhoff and R. Severs (International Union of Crystallography, Chester, 1987).

[37] FIZ Karlsruhe and NIST, *THE INORGANIC CRYSTAL STRUCTURE DATABASE (ICSD)*.

[38] J. Sangster and A. D. Pélton, *J. Phase Equilib.* **14**, 373 (1993).

[39] F. E. Pretzel, G. N. Rupert, C. L. Mader, E. K. Storms, G. V. Gritton, and C. C. Rushing, *J. Phys. Chem. Solids* **16**, 10 (1960).

[40] P. J. Linstrom and W. G. Mallard eds., *NIST Chemistry Webbook, NIST Standard Reference Database Number 69* (National Institute of Standards and Technology, Gaithersburg, MD.

[41] *TRC Thermodynamic Tables* (Thermodynamics Research Center, Texas A&M University System, College Station, TX, 1985).

[42] M. W. Chase, Jr., ed., *NIST-JANAF Thermochemical Tables, Fourth Edition* (J. Phys. Chem. Ref. Data, Monograph 9, 1998).

[43] G. B. Skinner and H. L. Johnston, *J. Chem. Phys.* **21**, 1383 (1953).

[44] E. S. Fisher and C. J. Renken, *Phys. Rev.* **135**, A482 (1964).

[45] E. Zuzek, J. P. Abriata, A. San-Martin, and F. D. Manchester, *J. Phase Equilib.* **11**, 385 (1990).

[46] C. P. Kempter, R. O. Elliott, and K. A. Gschneidner, *J. Chem. Phys.* **33**, 837 (1960).

[47] D. E. Gray ed., *American Institute of Physics Handbook* (McGraw Hill, New York, 1972).

[48] H. L. Yakel Jr., *Acta Crystallogr.* **11**, 46 (1958).

[49] S. V. Alapati, J. K. Johnson, and D. S. Sholl, *J. Phys. Chem. B* **110**, 8769 (2006).

[50] C. Qui, S. M. Opalka, G. B. Olson, and D. L. Anton, *Int. J. Mat. Res.* **97**, 845 (2006).

[51] W. M. Mueller, in *Metal Hydrides* (Academic Press, New York, 1968), p. 336.

[52] International Energy Agency, U.S Department of Energy, and Sandia National Laboratory, *Hydride Database*.

[53] R. L. Beck and W. M. Mueller, in *Metal Hydrides* (Academic Press, New York, 1968), p. 241.

[54] H. F. Zhang, Y. Yu, Y. N. Zhao, W. H. Xue, and T. Gao, *J. Phys. Chem. Solids* **71**, 976 (2010).

[55] E. Veleckis, *J. Nucl. Mater.* **79**, 20 (1979).

CHAPTER 3

HYDROGEN ISOTOPE EFFECTS IN METAL HYDRIDES*

3.1 Introduction

Polyatomic crystals, including metal hydrides, are known to experience isotope effects such as the contraction of the unit cell with substitution of ^{2}H (D) and ^{3}H (T) isotopes (deuterides and tritides) relative to ^{1}H (H)-substituted metal hydrides (protides).[1,2] Isotope effects in metal hydrides arise due to differences in vibrational frequencies of hydrogen isotopes in a crystal lattice. Isotope effects are known to cause changes in equilibrium lattice constants and thermal conductivities, as well as shifts in phase transition temperatures.[2,3] Zhernov and Inyushkin wrote a review article on changes in phonon modes due to isotope composition in crystals. They note that for a polyatomic crystal the frequency shift of a vibrational mode is inversely proportional to $M_c^{1/2}$, the average mass of the crystal, and proportional to the square of the modulus of the associated polarization vector.[2] Thus, metal hydrides with heavier isotopes will have smaller vibrational contributions to the free energy.

Thermodynamic models that account for temperature and/or volume-dependent lattice vibrations can predict structural changes due to isotope substitution. For example, Hu et al. quantified the zero point energy corrections to the lattice constants of TiX_2 (X = H, D, T) using a quasiharmonic approach to describe the vibrational properties of the solids.[4] Hu et al. and Zhang et al. studied the relative thermodynamic stabilities of TiH_2 and LiH substituted with hydrogen isotopes using Density Functional Perturbation

* The material in this chapter has been previously published as K. M. Nicholson and D. S. Sholl, Phys. Rev. B 86, 134113 (2012). Copyright 2012 by the American Physical Society.

Theory (DFPT).[4,5] Directly comparing the temperature-dependent free energies of the protide, deuteride, and tritide species, both authors concluded that the metal tritides are more stable than the corresponding metal hydrides over wide temperature ranges. This conclusion, however, did not account for isotope effects in the gas phase species (H_2, D_2, or T_2). In this chapter, we show that accounting for these effects leads to a revision of these earlier conclusions. In addition, we use different levels of theory to clarify the effect of hydrogen isotopes in the five representative metal hydride systems examined in Chapter 2, particularly the magnitude of the zero point energy correction to ground state unit cell volumes and relative hydride decomposition temperature to establish if isotope effects should be accounted for in material screening for the NGNP application. To this end, $F(V,T)$ in Eq. (2.11) was determined using static quasiharmonic calculations for Li, LiX, Na, NaX, Zr, ZrX_2, Hf, HfX_2, Ti, and TiX_2 with X = H, D, T following the computational methodology outlined in Chapter 2.

3.2 Temperature Dependence of H-Isotope Substituted Metal Hydride Relative Stability

Two papers investigating isotope effects in TiX_2 and LiX using first principles calculations have discussed the stability of isotope-substituted metal hydrides only in terms of the free energy of the metal hydride.[4,5] This led to the erroneous conclusion that metal hydrides substituted with heavier hydrogen isotopes are more stable over large temperature ranges. More correctly, however, the free energy of a metal hydride must be considered relative to that of other reaction products. For TiX_2 and LiX, these include the pure metal species and, critically, the hydrogen gas isotope. We show below the relative

stabilities of the isotope-substituted metal hydrides relative to the associated pure metal and hydrogen gas species are temperature dependent.

The thermodynamic stability of a metal hydride can be calculated with respect to formation of the pure metal phase and hydrogen gas. For TiX_2 where X = H, D, or T, the dehydrogenation reaction can be written as Ti$X_2 \leftrightarrow$Ti + X_2 and

$$\Delta G(T) = G_{\mathrm{Ti}} + G_{X_2} - G_{\mathrm{Ti}X_2} \tag{3.1}$$

Since

$$G = U + PV - TS = H - TS \tag{3.2}$$

we can write

$$\Delta G = \Delta H + \Delta(-TS) \tag{3.3}$$

where the enthalpy of each solid species is the summation of the DFT electronic total energy and the vibrational contribution to the free energy determined from phonon calculations. The entropies of the ordered solid species are the vibrational entropies from phonon calculations, and the thermodynamic properties of the gaseous hydrogen isotope species are calculated as discussed. As written, $\Delta H = -\Delta H_f$ for the metal hydride. As a reminder, $\Delta G > 0$ indicates that the formation of the metal hydride is favored.

Figure 3.1 compares the magnitudes of the ΔH and $\Delta(-TS)$ terms for protium relative to deuterium and tritium in the TiX_2 metal hydride system. These calculations were based on Eq. (2.10) using PAW(GGA-PW91) DFT calculations with a cutoff energy of 350 eV and 8 × 8 × 8 *k*-points for consistency with Hu et al.[4] Our calculations are similar to Hu et al. except for the use of PAW (GGA-PW91) rather than USPP (GGA-PW91). At low temperature, negative ($\Delta G_H - \Delta G_D$) and ($\Delta G_H - \Delta G_T$) indicate that the heavier isotopes are more thermodynamically stable to the pure metal and associated

hydrogen gas species than TiH_2. The hydrogen pressures in equilibrium with the solid species are ranked $TiT_2 < TiD_2 < TiH_2$ at low temperature. Above 360 K and 390 K for the tritide and deuteride, respectively, the relative stability ranking changes such that $TiH_2 < TiD_2 < TiT_2$ in terms of hydrogen pressures. Wiswall and Reilly determined a similar crossover point experimentally at 445 K for VH_2 and VD_2.[3] At 0 K, $\Delta H_H - \Delta H_X$ is dominated by the difference in zero point energies of the metal hydrides.

At high temperature, the difference in ΔG between the isotope-substituted systems is again controlled by the enthalpy terms. The differences in the entropy terms reach constant values at high temperature. This trend was seen for ZrX_2 and LiX up to 1500 K. It was found that the difference in entropy terms approach approximately constant negative values for protium relative to deuterium and tritium for both metal hydrides. Again, the enthalpy term dominates the difference in stability of the isotope-substituted species particularly for temperatures greater than 1000 K. However, $\Delta H_H - \Delta H_X$ is dominated by the difference in vibrational internal energies of the gaseous species rather than the metal hydrides at the high temperatures studied. While at both low and high temperatures the differences in ΔH dominate the stabilities of the hydrogen isotope-substituted metal hydrides relative to the pure metal and associated gas species, at intermediate temperatures, the stability is a balance between entropic and enthalpic terms.

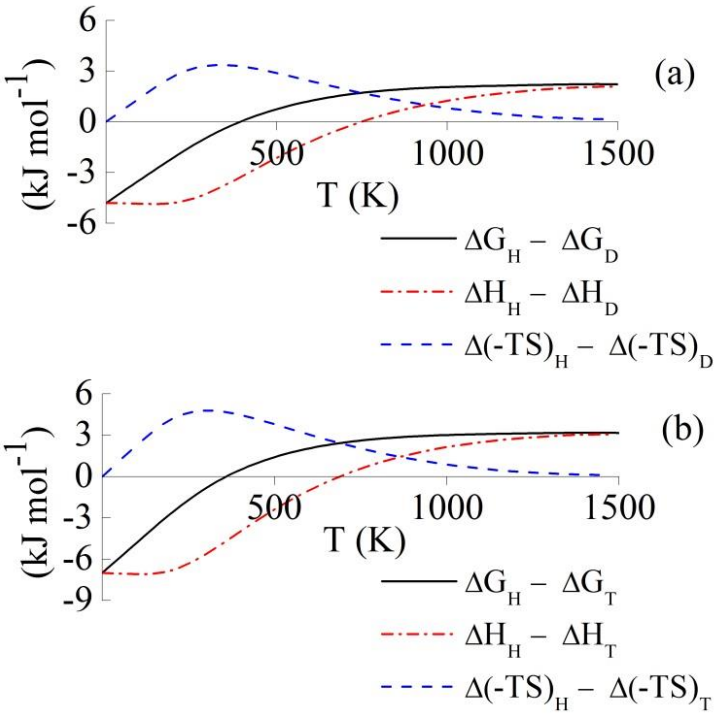

Figure 3.1: Temperature-dependent contributions of ΔH and $\Delta(-TS)$ to $\Delta G = \Delta H + \Delta(-TS)$ for isotope-substituted TiX_2 (X = D and T) relative to TiH_2 determined using a simple harmonic model of the free energy at the zero-point energy corrected ground state volume: (a) TiD_2 relative to TiH_2 and (b) TiT_2 relative to TiH_2.

3.3 Mass-Induced Volume Changes at T= 0 K

The quasiharmonic approximation corrects equilibrium volumes for lattice vibrations (see Section 2.2). The magnitude of the correction to the unit cell volume for various metal hydrides at 0 K due to isotopic mass is shown in Table 3.1. The volume changes are presented as percentages of the uncorrected volume. The magnitude of the zero point energy correction for a given metal hydride depends on the slope of the vibrational free energy curve $F^{qh}(V, 0\text{ K})$ and the shape of $E_0(V)$. The correction magnitude decreases for heavier isotopes and similarly decreases for heavier metal atoms.

Table 3.1: Zero point energy correction to ground state volume of metal hydrides due to hydrogen isotope mass $(V_{0c} - V_0)\ V_0^{-1} \cdot 100\%$ where V_{0c} and V_0 are the zero point energy corrected and uncorrected unit cell volumes at 0 K.

X=	H	D	T
LiX	6.4	5.1	4.5
NaX	4.7	3.6	3.1
TiX_2	3.2	2.3	1.9
ZrX_2	2.5	1.8	1.5
HfX_2	2.5	1.8	1.5

3.4 Isotope-Substituted Metal Hydride Relative Stability

For the NGNP application described in Chapter 1, metal hydrides can be considered as potential tritium sequestration materials at elevated temperatures. We have already shown for TiX_2 that heavier hydrogen isotopes destabilize metal hydrides above a critical temperature, but how much does this shift T_d at 1 bar hydrogen pressure? Table 3.2 presents the predicted stabilities in terms of T_d for each of the hydrogen isotope-substituted metal hydrides studied based on a simple harmonic calculation at V_0. The results of the simple harmonic calculation are very similar to those of the more computationally intensive quasiharmonic approximation with the largest differences for the lightest metals, and the order of the stabilities is unchanged using the lower level of theory. As expected, metal hydrides substituted with lighter hydrogen isotopes are more thermodynamically stable beyond low temperatures. However, since T_d of the protide is within 50 K of the deuteride and tritide for each of the materials studied, calculations simply based on protium are expected to yield an adequate description of the thermodynamic stability of metal hydrides for operation with tritium. This is useful because protiated metal hydrides have largely been the focus of both experimental and theoretical studies.

Table 3.2: T_d (K) for metal hydrides predicted via simple harmonic calculation at the uncorrected ground state volume.

X=	H	D	T	ΔT_d (H-D)	ΔT_d (H-T)
LiX	1053	1029	1020	24	33
NaX	620	591	579	29	41
TiX_2	930	920	915	10	15
ZrX_2	1108	1094	1089	14	19
HfX_2	986	974	969	12	17

3.5 Conclusions

Our aim was to determine if substitution of hydrogen isotopes affects the predicted stability of metal hydrides by a significant amount. We have confirmed previous experimental observations that the relative stabilities of metal hydrides substituted with hydrogen isotopes are temperature-dependent. At low temperatures, metal hydrides substituted with heavier hydrogen isotopes are more thermodynamically stable to decomposition, but this reverses at high temperature. In all cases, T_d for the protiated metal hydrides are within 50 K of the deuterides and tritides. Thus, for material screening purposes, hydrogen isotope effects can be neglected.

3.6 References

[1] H. L. Yakel Jr., *Acta Crystallogr.* **11**, 46 (1958).

[2] A. P. Zhernov and A. V. Inyushkin, *Phys. Usp.* **44**, 785 (2001).

[3] R. H. Wiswall Jr. and J. J. Reilly, *Inorg. Chem.* **11**, 1691 (1972).

[4] C. H. Hu, D. M. Chen, Y. M. Wang, and K. Yang, *J. Alloys Compd.* **450**, 369 (2008).

[5] H. F. Zhang, Y. Yu, Y. N. Zhao, W. H. Xue, and T. Gao, *J. Phys. Chem. Solids* **71**, 976 (2010).

CHAPTER 4

TERNARY INTERSTITAL HYDRIDE PHASE STABILITY IN THE Th-Zr-H SYSTEM*

4.1 Introduction

Computational methods that characterize the thermodynamic properties of metal hydrides that operate at high temperatures, i.e. $T > 800$ K, are desirable for a variety of applications, including nuclear fuels and energy storage systems. Binary hydrides MH_x of transition metals with high thermodynamic stability like thorium, titanium, and zirconium hydrides serve as neutron moderators in hydride nuclear fuels.[1] For example, in TRIGA reactors, U–Zr mixed fuel contains uranium particles embedded in a zirconium hydride matrix.[2] One motivation for using hydride fuels is that they allow core designs to be made more compact due to their high hydrogen densities relative to that of pressurized water reactor or boiling water reactor coolants.[1,3-5] The thermodynamic stabilities of binary hydrides are well characterized with both experimental data and theoretical predictions available.[6-8]

As discussed in Chapter 1, ternary hydrides MN_yH_x, in particular hydrides of transition metal alloys and intermetallics, are typically less thermodynamically stable than the associated binary hydrides, meaning that the compounds are either metastable or dissociate at lower T_d than the binary hydrides.[7] An apparent exception to this rule is the $ThZr_2$–H system, in which stable ternary interstitial metal hydrides $ThZr_2H_x$ have been

* The material in this chapter is in review as K. M. Nicholson and D. S. Sholl, "First Principles Prediction of Ternary Interstitial Hydride Phase Stability in the Th-Zr-H System" J. Chem. Eng. Data (2014). Reproduced with permission from J. Chem. Eng. Data, submitted for publication. Unpublished work copyright 2014 American Chemical Society.

isolated and characterized experimentally.[1,3,9] $ThZr_2H_6$ dissociates at $T_d \approx 1250$ K[5,9] compared with $T_d \approx 1154$ K (636 K) for ZrH_2[10,11] and ThH_2 (Th_4H_{15}).[12] This system is of interest because the U–Th–Zr hydride fuel absorbs more hydrogen at high temperature than U–Zr hydride fuels.[2] It has also been studied as a proxy for hydride systems of actinide materials such as the cubic Laves Pa_3H_x ($4 \leq x \leq 5$)[9] and ^{237}Np, ^{241}Am, and ^{243}Am hydride targets used in transmutation applications.[13] If computational tools can be used to accurately predict the thermodynamic properties of ternary hydrides that operate at high temperature, it may be possible to identify other systems with this enhanced thermodynamic stability relative to the binary hydrides or to predict operating parameters for these systems of interest without expensive experimental studies. In this chapter, we use DFT and grand potential minimization methods to predict the relative thermodynamic stabilities of Zr and Th binary hydrides, $ThZr_2H_6$, and $ThZr_2H_7$ as a function of hydrogen pressure and temperature to serve as a proof of principle calculation to judge whether or not the ternary hydride is a thermodynamically-preferred phase. To our knowledge, no other first principles study of the Th–Zr–H system has of yet been performed.

4.1.1 Phase diagram prediction via DFT and grand potential minimization

A challenge in hydrogen storage applications is to predict the temperature, hydrogen pressure, and composition-dependent stable phases and equilibrium reaction pathways for multicomponent systems. Phase diagrams detailing thermodynamic equilibria of components can provide valuable information regarding relevant reactions and processing conditions.[14] While equilibrium hydrogen release pathways can be determined manually by enumerating all possible reactions, this can be cumbersome and prone to error for multicomponent systems.[15] Akbarzadeh, Ozolins, and Wolverton

developed a grand canonical linear programming (GCLP) method to systematically and automatically compute all thermodynamically-favored reactions in a multicomponent system open to a hydrogen atmosphere based on a library of compound compositions and total energies determined through first principles and dynamical calculations.[16] The method identified all experimentally-observed reaction pathways in addition to previously unobserved high temperature decomposition pathways in the Li–Mg–N–H system. It has since been applied to other bulk hydride systems[15,17-20] and extended to incorporate nanoclusters[21] with general good agreement between theory and experiment in terms of computed thermodynamic properties.

Alapati et al. performed a large scale screening analysis of destabilized metal hydride systems using simplified calculations that assume changes in the free energy at finite temperatures are dominated by the hydrogen gas entropy.[17] Ong and colleagues have used similar simplified calculations based on grand potential minimization to predict phase diagrams for the Li–Fe–P–O element space as a function of oxygen chemical potential while ignoring the dynamical or vibrational contributions of the solids.[14] There are several reasons, however, to include vibrational corrections in phase diagram predictions. Wolverton et al. found that including vibrational corrections reduced the root mean square error in calculated vs. experimental reaction enthalpies for alkali, alkaline earth, and early transition metal binary hydrides from 19.4 to 14.7 kJ/mol H_2.[20] In cases where the agreement weakened, the effect was small. Beyond enthalpic effects, Akbarzadeh et al. also found that several of the preferred reaction pathways in the Li–Mg–N–H phase diagram computed using dynamically-corrected free energies had predicted entropy changes in the range of 109 – 137 J mol^{-1} K^{-1} at T = 500 K, deviating

significantly from the standard molar entropy of hydrogen, 130.6 J mol^{-1} K^{-1} at T = 300 K.[16] These entropic contributions may become more significant for metal hydride systems that operate at high temperature.

In Chapter 2 we benchmarked the performance of the DFT PAW method with GGA PW91 exchange-correlation functional for predicting T_d for very stable binary hydrides ZrH_2, HfH_2, TiH_2, LiH, and NaH at several levels of theory, including anharmonic contributions, quasiharmonic effects that incorporate thermal expansion, simple harmonic calculations that consider vibrational corrections to the free energy at a ground state volume, and constant entropy models.[22] We found that the simple harmonic level of theory predicts T_d to within 130 K for the alkali hydrides and to within 50 K for TiH_2 and ZrH_2 transition metal hydrides.

4.1.2 The Th-Zr-H system

Th and Zr have limited miscibility at low temperature, but form a metastable $ThZr_2$ bcc solid solution for T > 1150 K.[9] Bartscher, Rebizant, and Haschke studied the phase equilibria and thermodynamic properties of the $ThZr_2$–H system experimentally. Although incomplete, the general features of the Th–Zr–H phase diagram are that hydrogen dissolves in the bcc $ThZr_2$ lattice at high temperature up to a composition of $ThZr_2H_{0.6}$ (α-phase), a two phase (α+β) region exists in the range $ThZr_2H_{0.6–1.8}$, and the β-phase cubic Laves ternary hydride forms for $ThZr_2H_{1.8}$ to $ThZr_2H_{7–x}$.[1,9]

van Houten and Bartram were the first to isolate a cubic Laves $ThZr_2$ and hexagonal $ThTi_2$ ternary hydrides in 1971.[1] They determined the hydrogen capacity to be $ThZr_2H_7$ and, based on interstitial site availability, reasoned that hydrogen occupies 8b and 48f interstitial sites. Bartscher, Rebizant, and Haschke observed cubic Laves hydrides

for $ThZr_2H_x$ ($1.8 \leq x \leq 6.6$), but only materials with $x \geq 3.9$ were stable upon cooling to room temperature at P = 1 bar H_2; lower hydrides dissociated to mixtures of other hydride phases.[9] Bartscher et al. performed powder neutron diffraction studies at 290 K for $ThZr_2D_x$ (x = 3.6, 4.8, 6.0, and 6.3) to locate deuterium within the lattice and found that the deuterium atoms only occupy tetrahedrally-coordinated 96g and 32e sites for all compositions, not 8b or 48f sites as proposed by van Houten and Bartram.[1,3] The authors note that, based on comparison to their fitted lattice parameters, the compound isolated by van Houten and Bartram corresponds to $ThZr_2H_{5.63}$ not $ThZr_2H_7$, which calls into question the hydrogen site occupations reported for that structure. Terrani et al. used XRD and Rietveld refinement to obtain lattice parameters for $ThZr_2H_{7-x}$[4] and found good agreement with the lattice parameters obtained by Bartscher et al.[3] Further analysis via SEM indicated that the ternary hydride was the dominant phase in the system, strengthening the argument for enhanced stability relative to the binary hydrides.[4]

Binary hydrides of Zr and Th include fct ε-ZrH_2 and ThH_2. An fcc phase also exists in the hydrogen deficient δ-ZrH_x (x = 1.5–1.8), while ThH_{2-x} remains fct. Additionally, there is a higher hydride, Th_4H_{15}, that crystallizes with bcc symmetry.[1]

Konashi et al. calculated the enthalpy of formation for $ThZr_2H_x$ (x = 4 and 6) using the semi-empirical Miedema model based on geometric considerations and the Griessen-Driessen model based on electronic band structure.[5] They found that the Griessen model predicts van't Hoff plots in good agreement with the experimental result, predicting a T_d of 1210 K (1380 K) for $ThZr_2H_6$ ($ThZr_2H_4$). Pudjanto et al. then extended the Miedema and Griessen models to predict hydrogen partial pressures for theoretical

actinide Np–Zr–H, Am–Zr–H, and Pu–Zr–H systems for A_5B, A_2B, AB, AB_2, and AB_5 intermetallics.[23]

4.2 Theoretical Methods

4.2.1 Hydrogen grand potential

Details of the GCLP method for predicting the equilibrium mixture of metals, metal hydrides, and alloys from a library of compositions and energies at a given hydrogen chemical potential are described in Reference 16. A key constraint is that we cannot make predictions about the stability of compounds or phases that are not included in the library. Since we have used the pymatgen[24] software to perform the grand potential minimization and phase diagram predictions, we build upon the nomenclature of Ong, Ceder and colleagues.[14,25] The difference in our calculation and theirs is that we incorporate vibrational and configurational entropy corrections to the free energies of the condensed phases.

Phase equilibria for systems dominated by condensed phases and open to a hydrogen atmosphere are governed by minimization of the overall system free energy, specifically minimization of the hydrogen grand potential. In an isothermal and isobaric Th–Zr–H system, this hydrogen grand potential ϕ can be written as

$$\phi(T, P, N_{Th}, N_{Zr}, \mu_{H_2}) = G(T, P, N_{Th}, N_{Zr}, \mu_{H_2}) - \mu_{H_2} N_{H_2}(T, P, N_{Th}, N_{Zr}, \mu_{H_2}) \quad (4.1)$$

where *T*, *P*, *N*, and μ_{H_2} are temperature, pressure, number of atoms, and the chemical potential given by the total energy of a hydrogen molecule, respectively. Using the Gibbs free energy, defined in Eq. (2.4), and assuming that $\Delta(PV) \approx 0$ for reactions that primarily

involve condensed phases, we can write the free energy for a given solid *j* within the harmonic approximation as

$$G_j(T) \approx F_j(T) = E_{0,j} + F_j^{vib}(T) - TS_j^{conf} \tag{4.2}$$

where the free energy is the sum of the ground state electronic energy E_0, the vibrational contribution to the Helmholtz free energy F^{vib} including zero point and finite temperature effects, and configurational entropy corrections S^{conf}, if any. We determine E_0 using DFT geometry relaxations and F^{vib} using calculations of the material's VDOS. We refer to these below as phonon calculations for succinctness. S^{conf} is defined using the Boltzmann definition as

$$S^{conf} = k_B \ln(N_c) \tag{4.3}$$

where k_B is the Boltzmann constant, and N_c is the number of unique arrangements of the system in question. Below, S^{conf} is evaluated for $ThZr_2H_6$ in which N_c represents the number of ways to arrange hydrogen among the interstitial sites to meet the partial occupancy requirements of the ternary hydride.

If the atomic fraction of component *j* is written $x_j = N_j(N_{Th} + N_{Zr})^{-1}$, then the normalized grand potential becomes

$$\bar{\phi}(T, P, x_{Th}, x_{Zr}, \mu_{H_2}) \approx \frac{E_0 + F^{vib}(T) - TS^{conf} - \mu_{H_2}(T,P)N_{H_2}}{N_{Th} + N_{Zr}} \tag{4.4}$$

Specifying the chemical potential of H_2 for a *T* and *P* of interest as well as the relevant energies for a library of compounds that can form from a combination of Th, Zr, and H, one can determine the equilibrium mixture of compounds that minimizes the grand potential as a function of composition. Using the methodology of Ozolins and colleagues,[16] shifts in the mixture of stable phases for a given *P* can be tracked as a

function of *T* to identify relevant reactions and to construct a phase diagram. Finally van't Hoff plots can be computed via Eq. (2.3).

4.2.2 $ThZr_2H_6$ configurational entropy

$ThZr_2H_x$ crystallizes in the cubic Laves structure with compositions that range up to an experimentally-determined $x = 7$.[1,3,4,9] Each Th atom is surrounded by four Th and 12 Zr atoms.[3] The metal lattice forms three types of tetrahedrally-coordinated interstitial sites: 32e (coordinated to one Th and three Zr atoms), 96g (coordinated to two Th and two Zr atoms), and 8b (coordinated to four Zr atoms). Additionally, there are 48f triangularly-coordinated sites (coordinated to two Zr atoms and one Th atom). As previously mentioned, Bartscher et al. determined that hydrogen atoms occupy only 32e and 96g interstitial sites.[3] In the case of $ThZr_2D_6$, the hydrogen occupancy among the 32e and 96g sites was 0.598 ± 0.035 and 0.301 ± 0.012, respectively. In a unit cell with composition $Th_8Zr_{16}H_{48}$, the hydrogen loading is then approximately 19 and 29 H atoms to the 32e and 96g sites, respectively.

Random assignment of H atoms to 32e and 96g sites to fulfill the partial occupancy requirement for $ThZr_2H_6$ gives $N_c = \binom{32}{19}\binom{96}{29} = 1.1\times10^{33}$ unique ways to arrange H across the interstitial sites. This corresponds to a $S^{conf} \approx 79$ J mol^{-1} K^{-1} or a contribution to the free energy of $TS^{conf} \approx 26.3$ kJ mol^{-1} H_2 at 1000 K. This is a large overestimate of the configurational entropy that does not take into account H–H repulsive interactions.

The empirical Westlake criterion observes that H atoms prefer to not simultaneously occupy interstitial sites within a distance of 2.1 Å.[26] Given that each 32e site can be

uniquely mapped to three 96g sites within 1.42 ± 0.05 Å at the experimental lattice constant a_0 = 9.151 ± 0.008 Å,[3] we safely eliminate configurations with simultaneous occupation of a 32e site and the three associated 96g sites. This gives a more reasonable estimate $N_c = \binom{32}{19}\binom{96-3\cdot 19}{29} = 2.2\times 10^{17}$ configurations. This corresponds to a $S^{conf} \approx$ 41.5 J mol^{-1} K^{-1} or a contribution to the free energy of TS^{conf} = 13.8 kJ mol^{-1} H_2^{-1} at 1000 K. While this estimate takes into consideration the 96g sites blocked upon occupation of a nearby 32e site, it does not account for 96g sites blocked given occupancy of a neighboring 96g site associated with a different 32e site.

Considering both 32e-96g and 96g-96g site exclusions or the "exact" number of ways to arrange H atoms on the 32e and 96g sites to meet the occupancy requirement and Westlake criterion requires a numerical solution. One approach might fill the 32e sites with 19 H atoms (given that there are no 32e-32e sites within 2.1 Å of each other), block the three 96g sites associated with the chosen 32e sites, and then stochastically sample the 39 remaining 96g sites for ways to arrange 29 H atoms with no two atoms within 2.1 Å. For each of the 3.5×10^8 32e configurations, there are 6.4×10^8 possible ways to distribute 29 H atoms to the remaining 96g sites without taking into consideration the Westlake criterion. Our initial attempts to stochastically sample this space were unsuccessful due to the very low number of successful configurations observed.

As an alternative to inefficient stochastic sampling, we developed a method for computing the number of successful arrangements based on a cluster analysis. The cluster analysis quickly determines whether or not a given 32e configuration (i.e., random assignment of 19 H atoms to 32e sites) can support a single successful 96g configuration (i.e., 29 H atoms distributed to 96g sites without violating the Westlake criterion) rather

than randomly assigning atoms to 96g sites and testing for agreement. If the 32e configuration is not useful, it is discarded, but if it can support at least one 96g configuration, then the exact number of ways to arrange H on the available 96g sites for that 32e arrangement is computed. Using this approach we were able to sample many orders of magnitude more configurations than practical through a simplistic stochastic approach. Further details regarding the cluster analysis algorithm are discussed in Appendix B.

4.3 Computational Details

Plane-wave DFT calculations were carried out via VASP[27-31] using the projector augmented wave method with PW91 generalized gradient approximation exchange-correlation functional.[32-34] Experimental crystal structures of relevant compounds in the Th–Zr–H phase space were taken from the ICSD.[35,36] These include the low temperature hcp and high temperature bcc forms of Zr, fcc Th, cubic Th_4H_{15}, bct ThH_2, and bct ε-ZrH_2. The cubic Laves $ThZr_2H_7$ structure from van Houten and Bartram was studied with completely filled 48f and 8b sites.[1] The cubic Laves $ThZr_2H_6$ structure was taken from Bartscher et al., which includes site occupancy factors of approximately 0.598 (0.301) for the 32e (96g) sites or, in the unit cell, approximately 19 (29) H atoms in 32e (96g) sites.[3] Additionally, a hypothetical ordered cubic $ThZr_2$ phase was studied by removing H atoms from the $ThZr_2H_6$ structure. We make no attempt to account for unsaturated hydride phases or lower $ThZr_2H_x$ hydrides in this work. However, it has been observed that enthalpies of formation of $ThZr_2H_x$ tend to increase with decreasing hydrogen to metal ratios indicating that lower hydrides will be more thermodynamically stable than

$ThZr_2H_6$.[37] This observation is in agreement with the experimental van't Hoff plots for $ThZr_2H_x$ for $1.5 \leq x \leq 6.0$.[9]

$1 \times 1 \times 1$ supercells of the crystallographic unit cell for each compound were relaxed using the conjugate gradient method until forces on each atom were less than 10^{-4} eV $Å^{-1}$ and electronic steps were converged to within 10^{-7} eV. For $ThZr_2H_6$, we randomly assigned H atoms to 96g sites and 32e sites until 15 unique configurations were found that simultaneously met the partial occupancy and Westlake minimum separation requirements. We then fully relaxed each structure. The average predicted lattice parameter for the distorted cubic structures was $a = 9.124 \pm 0.005$ Å with $\alpha, \beta, \gamma = 89.9 \pm 0.3°$. E_0 was largely independent of the arrangement of H atoms across the 15 configurations with the largest difference in ground state energy of 0.043 eV $f.u.^{-1}$ (formula unit) or < 1.4 kJ mol^{-1} H_2. Therefore, only a representative $ThZr_2H_6$ configuration with the lowest ground state energy was utilized in the computationally-expensive phonon calculations.

Two Monkhorst-Pack *k*-point mesh densities, B_1 and B_2 with $B_2 \approx 2B_1$, and three cutoff energies, 350 eV, 425 eV, and 500 eV, were tested for each compound with the exception of $ThZr_2H_6$, which was studied with only one set of *k*-points. It is expected that the ground state energy convergence for $ThZr_2H_6$ is similar to that of $ThZr_2H_7$. Detailed results of the *k*-point and cutoff energy convergence testing are given Tables A1 and A2. in the Appendix. Initial tests indicate that a cutoff energy of 425 eV at the B_1 grid density is sufficient to converge ΔE_0 within 0.6 kJ mol^{-1} (0.6 kJ mol^{-1} H_2) for hydrogen-free (metal hydride decomposition) reactions with the exception of the hypothetical $ThZr_2$ dissociation reaction, which is converged to within 1.5 kJ mol^{-1}. Thus, the B_1 *k*-point

parameters in Table 4.1 were adopted for all free energy calculations. Table 4.1 also shows the computed reaction free energies at 0 K based on DFT electronic energies, ΔE_0.

Table 4.2 lists the DFT-predicted ground state lattice parameters and specific volumes, *V*, are in good agreement with the experimental crystal structures and previous theoretical calculations. The largest discrepancy in lattice parameter occurs for $ThZr_2H_7$, with the predicted lattice parameter (volume) approximately 0.2 Å (7%) larger than van Houten and Bartram's experimental value.[1] Based on a regression analysis of experimental cubic lattice parameters of protiated and deuterated $ThZr_2H_x$ compositions for $4 \leq x \leq 6.62$, which gives the relation $a = 8.81 + 0.0558x$ [Å] (std. dev. 0.0041Å),[9] $ThZr_2H_7$ should have a lattice constant of about 9.2 Å. This value is intermediate to our DFT results and the experimental 9.124 Å.

Table 4.1: Chosen *k*-point densities for studied compounds. B_i refers to total number of *k*-points per unit cell that are distributed as evenly as possible along reciprocal lattice vectors. M_i refers to the corresponding values for a $M_i \times M_i \times M_i$ Monkhorst-Pack mesh. Relevant predicted reaction free energies ΔE_0 at B_1 and 425 eV cutoff energy in units of kJ mol^{-1} reactant (kJ mol^{-1} H_2 released) for hydrogen-free (metal hydride decomposition) reactions.

	B_1	M_1	Reaction		ΔE_0
Zr_bcc	1024	8	1	$ThZr2H_7 \rightarrow Th+2Zr\_hcp+3.5H_2$	152.65
Zr_hcp	1458	9	2	$ThZr_2H_7 \rightarrow ThZr_2+3.5H_2$	161.31
Th	2048	8	3	$Th4H15 \rightarrow 4ThH_2+3.5H_2$	118.05
Th_4H_{15}	4864	4	4	$ThH_2 \rightarrow Th+H_2$	172.36
ThH_2	3072	8	5	$ZrH_2 \rightarrow Zr\_hcp+H_2$	192.57
ZrH_2	3072	8	6	$ThZr_2 \rightarrow Th+2Zr\_hcp$	-30.30
$ThZr_2$	1536	4	7	$Zr\_hcp \rightarrow Zr\_bcc$	7.25
$ThZr_2H_7$	5120	4	8	$ThZr_2H_6 \rightarrow Th+2Zr\_hcp+3H_2$	158.52
$ThZr_2H_6$	4608	4			

Table 4.2: Comparison of calculated and reference lattice parameters for studied compounds in the Th-Zr-H phase space. For $ThZr_2H_6$, the listed values are averaged values for 15 relaxed structures that simultaneously meet the partial hydrogen occupancy requirements and Westlake criterion such that no two hydrogen atoms are closer than 2.1 Å.[26]

		DFT relaxed			Experimental		
material	Space Group	$a = b$/Å	c/Å	V/Å^3 f.u.$^{-1}$	$a = b$/Å	c/Å	V/Å^3 f.u.$^{-1}$
Zr	Im3m	3.568	3.568	22.70	3.6162(20)[a]	3.6162(20)	23.65
Zr	P63 /mmc	3.229 3.215[l]	5.171 5.148	23.34 23.04	3.2332(4)[b] 3.2330[c]	5.1466(10) 5.1475	23.30
Th	Fm3m	5.050	5.050	32.20	5.08415[d]	5.08415	32.86
Th_4H_{15}	I43d	9.112 9.130[m]	9.112 9.130	189.17 190.30	9.11[e]	9.11	189.02
ThH_2	I4 /mmm	4.066 4.067[m]	4.906 4.9125	40.56 40.63	4.1(3)[f] 4.055(3)[g]	5.03(3) 4.9706(4)	42.275 40.865
ZrH_2	I4 /mmm	3.538	4.430	27.74	3.516[h] 3.522(10)[i]	4.48 4.451(10)	27.69 27.606
$ThZr_2$	Fd3m[n]	4.266	4.266	77.65			
$ThZr_2H_7$	Fd3mS	9.339	9.339	101.82	9.124[j]	9.124	94.94
$ThZr_2H_6$	Fd3m	9.124 ± 0.005	9.124 ± 0.005	94.94 ± 0.05	9.042(4)[k]	9.042(4)	92.41

[a] Skinner and Johnston (1953) at T = 1252 K[38]
[b] Kolesnikov et al. (1994) at T = 293 K[39]
[c] Skinner and Johnston (1953) at T = 298 K[38]
[d] James and Straumanis (1956) at T = 298 K[40]
[e] Mueller et al. (1977) at T = 92 K[41]
[f] Rundle, Shull, and Woolan (1952)[42]
[g] Korst (1962)[43]
[h] Pitt et al. (2011) at T = 293[44]
[i] Flotow and Osborne (1961)[45]
[j] van Houten and Bartram (1971)[1]
[k] Bartscher et al. (1986)[3]
[l] Srivastava, Chauhan, and Singh (2011) with PBE-GGA and 200 Ry cutoff energy[46]
[m] Wang et al. (2010) with PAW-GGA and 450 eV cutoff energy[47]
[n] theoretical

To determine $F^{vib}(T)$ we computed the VDOS for each compound using phonon calculations within the harmonic approximation based on the supercell approach.[48] 2 × 2 × 2 supercells were used with the exception of the Th–Zr structures, which were studied only in the 1 × 1 × 1 arrangement due to size constraints. The hcp Zr structure was transformed into a rhombohedral supercell for the phonon calculations. Supercells were relaxed using the same *k*-point density, cutoff energy, and tight force and electronic convergence criteria as before. Uniform *q*-point sampling meshes were used to sample the Fourier components of the dynamical matrix such that F^{vib} at T = 2000 K for each compound was converged to within 1 kJ mol^{-1}. Test calculations with displacement magnitudes of ±0.01 Å and ±0.03 Å for all compounds except $ThZr_2H_6$ show that $F^{vib}(T)$ is insensitive to the displacement magnitude with the largest difference occurring for $ThZr_2H_7$ with $|\Delta F^{vib}| < 0.8$ kJ mol^{-1} H_2 at 2000 K. Moreover the difference in reaction free energies based on vibrational contributions for those reactions listed in Table 4.1 are less than 0.2 kJ mol^{-1} H_2 at all T. Results from this convergence test are available in the Figures A.1 and A.2 in the Appendix. We use free energies obtained with a displacement magnitude of ± 0.03 Å in the following phase diagram prediction.

4.4 $ThZr_2H_6$ Configurational Entropy

Using the cluster analysis methodology, we sampled 4.5×10^7 out of 3.5×10^8 32e configurations or approximately 13% of the total configuration space to determine how many successful 96g arrangements could be formed such that both the partial H occupancy and Westlake criterion were met simultaneously. On average, only 1.74% of the tested 32e configurations were associated with a successful 96g configuration, or less

than 3×10^{-9} % of the total possible 2.2×10^{17} 32e-96g configurations. We determined $N_c \approx 6\times10^6$ and S^{conf} = 16.2 J mol^{-1} K^{-1} or TS^{conf} = 5.4 kJ mol^{-1} H_2 at 1000 K.

If we were to use the estimate of complete H disorder among the available 32e and 96g sites without applying the Westlake criterion, we would overestimate the configurational entropy five-fold. Applying this overestimate, the relative predicted T_d for $ThZr_2H_6$, ZrH_2, and ThH_2 would be 1392 K, 1113 K, and 1088 K, clearly stabilizing the ternary hydride relative to the binary hydrides. As we discuss below, our best estimate of S^{conf} gives a predicted T_d = 1168 K for $ThZr_2H_6$. This demonstrates that estimates based on complete disorder of H to interstitial sites without taking H-H site repulsion into consideration can significantly overestimate the influence of configurational entropy. However, based on the 32e-96g blocking effect described earlier, we can quickly cut the estimate for S^{conf} nearly in half to $S^{conf} \approx 41.5$ J mol^{-1} K^{-1}. Using this value yields a reduced T_d of 1248 K for $ThZr_2H_6$, within 80 K of the best estimate, but requiring no additional computational power.

4.5 Vibrational Free Energies

Figure 4.1 shows the computed vibrational Helmholtz free energies for the condensed phases in the Th–Zr–H element space. As expected, vibrational effects are more significant for the hydride phases due to the high frequencies associated with modes involving hydrogen. Zero point energies are 45.2 (36.1) kJ mol^{-1} H_2 for ZrH_2 (ThH_2) compared with just 2.1 (1.3) kJ mol^{-1} for hexagonal Zr (Th) phases. Other calculated zero point energies are 33.9, 40.2, 38.1 kJ mol^{-1} H_2 for Th_4H_{15} $ThZr_2H_6$, and $ThZr_2H_7$

compared with 1.5 and 1.5 kJ mol^{-1} $atom^{-1}$ for Zr(bcc) and $ThZr_2$, respectively. Of note, the vibrational contribution to $ThZr_2H_6$ is intermediate to the binary dihydrides.

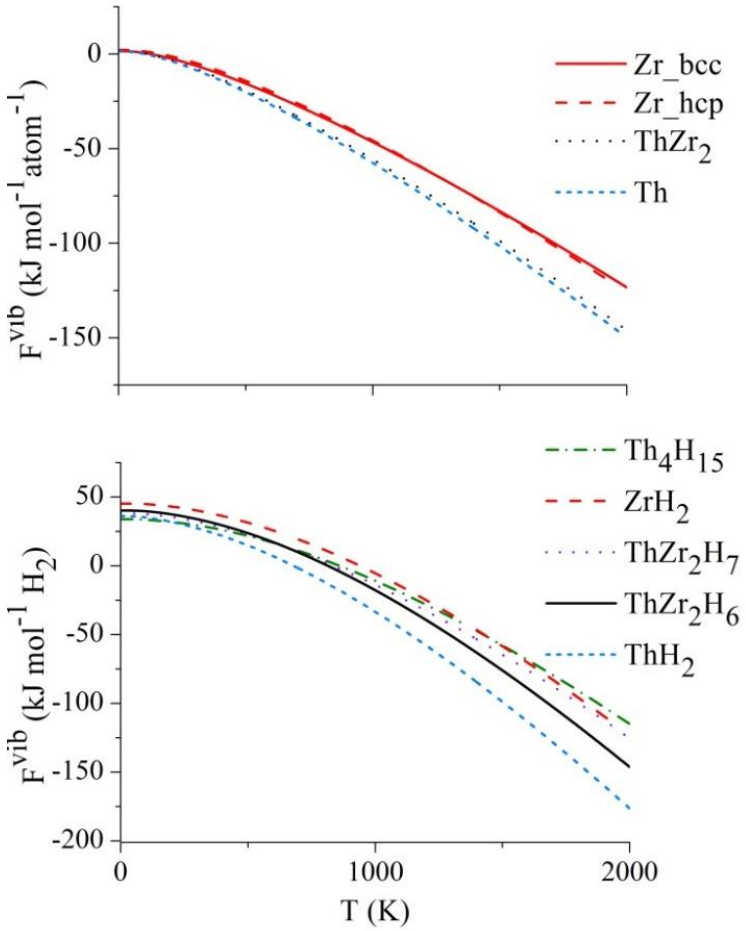

Figure 4.1: Helmholtz vibrational free energy contributions for solid phases in Th–Zr–H element space computed within the harmonic approximation.

Figure 4.2 shows the overall contributions of $F^{vib}(T)$ of the solid phases to the reaction free energy relative to the $T > 0$ H_2 contribution for key reactions listed in Table 4.1. For hydride dissociation reactions 1–5 and 8, the net vibrational contribution of the solids to the reaction free energy is nearly constant for $T < 800$ K. Over the entire temperature range, the net vibrational effect for all metal hydride dissociation reactions is

less than 50 kJ mol^{-1} H_2. At low temperatures, the net vibrational contribution tends to destabilize the metal hydride, and at temperatures greater than this, gaseous H_2 thermodynamics dominate.

$ThZr_2H_7$ decomposition reactions 1 and 2 are both highly endothermic with ΔE_0 = 152.7 and ΔE_0 = 161.3 kJ mol^{-1} H_2, respectively. However, the competing reaction $ThZr_2H_7 \rightarrow ThZr_2H_6 + 0.5H_2$ has ΔE_0 = -67.3 kJ mol^{-1} H_2 and remains exothermic for all *T*, indicating that it is more favorable to decompose the ordered higher hydride into a mixture of H_2 gas and the lower hydride $ThZr_2H_6$ with partial occupancy of interstitial sites. The hexagonal form of Zr is predicted to be the most stable form of the pure metal at all *T*. This disagrees with experimental evidence that cubic Zr becomes stable for $T >$ 1135 K at low pressures.[38] The difference in the overall free energies for these two phases is small, within 10 kJ mol^{-1} for all *T*, and, therefore, using the free energy of hcp Zr rather than bcc Zr for reactions at high temperature will not have a large effect on the results, in particular relative rankings of thermodynamic stability.

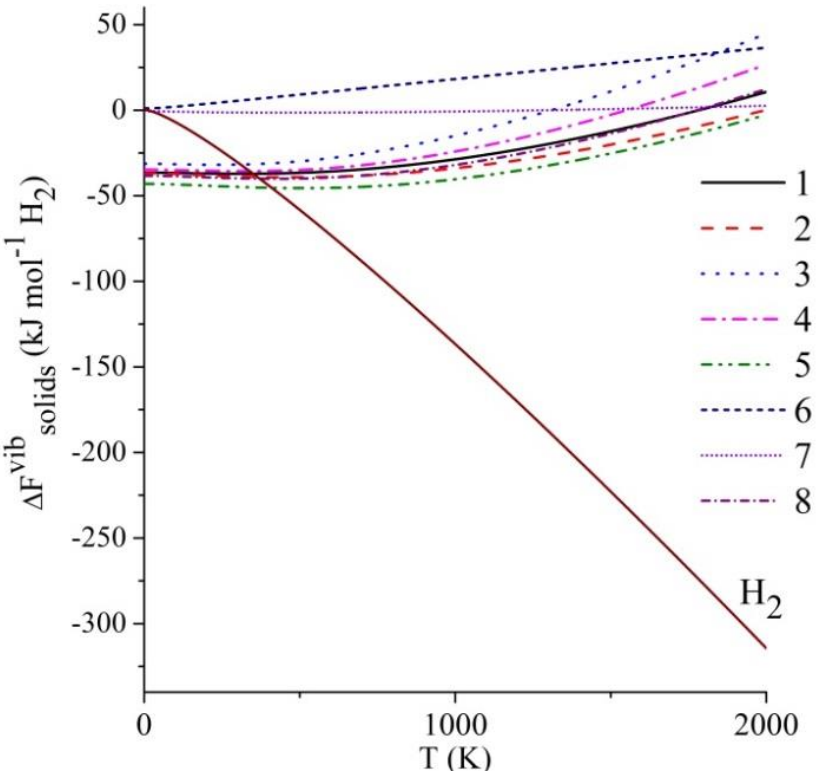

Figure 4.2: Reaction free energy due to Helmholtz vibrational free energies of solid phases. Reactions 1 - 8 are listed in Table 4.1. Metal hydride decomposition reaction free energies are given on a kJ mol^{-1} H_2 basis. Non-hydride reaction free energies are given as kJ mol^{-1} of reactant. For comparison of relative contributions to reaction free energies $F+PV$ for H_2 gas at $T > 0$ is also shown in units of kJ mol^{-1} H_2.

4.6 Phase Diagram

Figures 4.3a-c present three phase diagrams predicted using the GCLP method at P = 1 bar H_2 with values for the solid phase Helmholtz free energies that increase in computational complexity. Figure 4.3a displays the relative stabilities of the studied phases as a function of T and metal species composition based only on ground state DFT energies and the chemical potential of H_2, i.e., all phonon contributions are ignored. This simplified calculation correctly reproduces the basic decomposition pathways of the binary hydrides with the higher thorium hydride decomposing to the dihydride at moderate temperature and the thorium and zirconium dihydrides having comparable

thermodynamic stabilities. However, at this level of theory, ternary hydrides are not predicted to form. Rather, the reaction $ThZr_2H_6 + \frac{7}{8}H_2 \rightarrow \frac{1}{4}Th_4H_{15} + 2ZrH_2$ proceeds exothermically with ΔE_0 = -121.1 kJ mol^{-1} H_2 at low T and a similar reaction can be written at T > 887 K for decomposition to a mixture of the binary dihydrides.

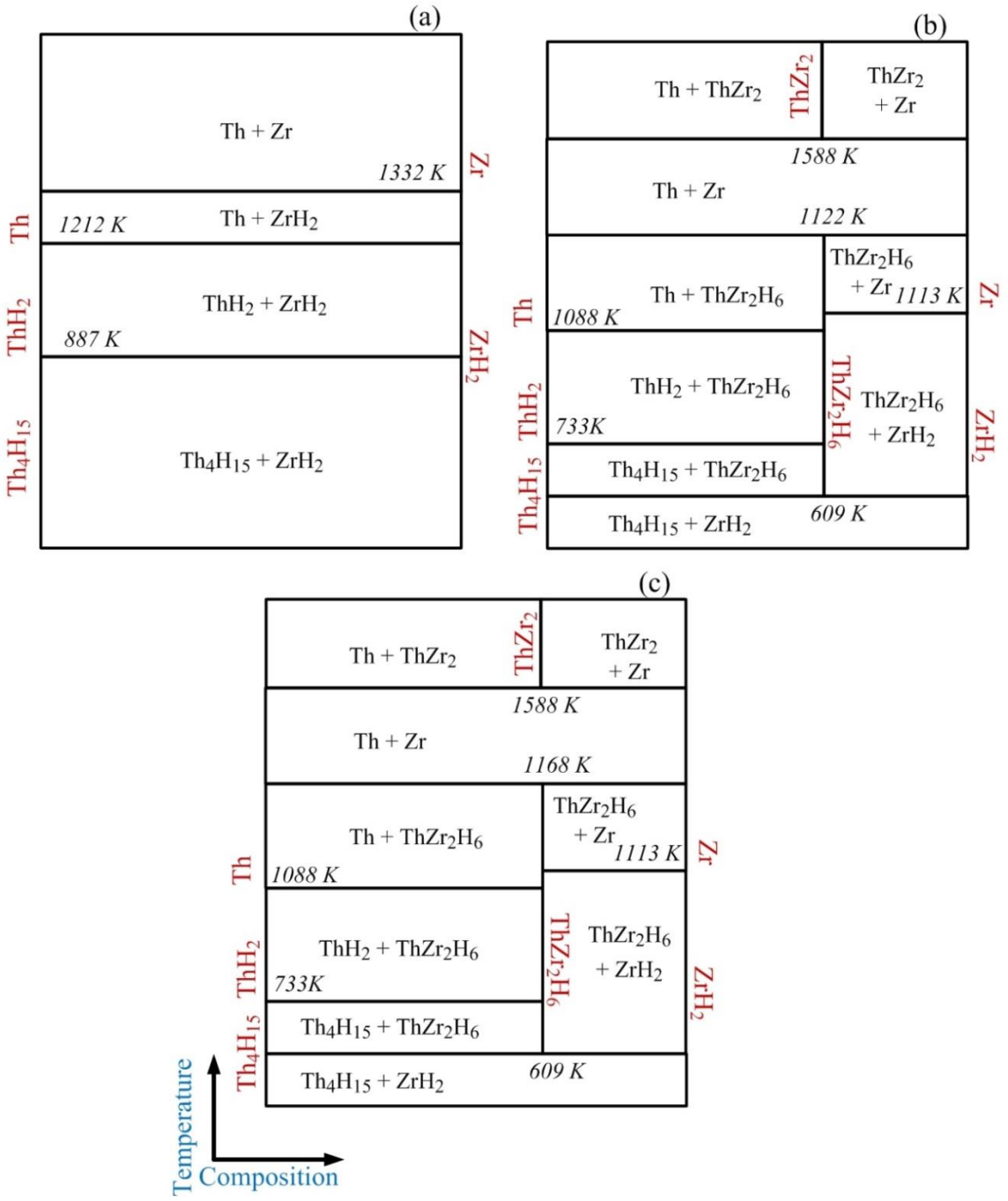

Figure 4.3: Predicted phase diagrams for Th–Zr–H element space for P = 1 bar H_2. (a) $F_{\text{solids}} = E_0$, (b) $F_{\text{solids}} = E_0 + F^{\text{vib}}(T)$, and (c) $F_{\text{solids}} = E_0 + F^{\text{vib}}(T) - TS^{\text{conf}}_{ThZr_2H_6}$. Experimental values for metal hydride decomposition temperatures, T_d, are 1250 K ($ThZr_2H_6$),[5] 1154 K (ZrH_2),[10,11] 1154 K (ThH_2),[12] and 636 K (Th_4H_{15}).[12]

Figure 4.3b includes vibrational effects computed using phonon calculations for the condensed phases but no configurational entropy correction for $ThZr_2H_6$. The ternary hydride $ThZr_2H_6$ is predicted to be thermodynamically stable for 609 K $\leq T \leq$ 1122 K, and $ThZr_2H_7$ does not form at any T. At 609 K, Th_4H_{15} and ZrH_{15} release hydrogen and form $ThZr_2H_6$. This is consistent with the general experimental behavior in which a mixture of Th_4H_{15} and ZrH_2 was isolated at $T <$ 1180 K with the ternary hydride forming at high T.[9] The ternary hydride and binary hydrides decompose to the elements at high T with the ternary hydride nominally more thermodynamically stable than ZrH_2. However, the difference in their predicted T_d's is only about 10 K or $\Delta\Delta H \approx 1.3$ kJ mol^{-1} H_2 assuming a constant $\Delta S = 0.130$ J mol^{-1} K^{-1}, given that at thermodynamic equilibrium $\Delta G = 0 = \Delta H - T\Delta S$. This value is on the order of the error expected from numerical convergence issues such as k-point sampling, finite cutoff energy, or q-point sampling. Therefore, a conservative statement is, rather, that the ternary and binary hydrides are of comparable thermodynamic stability. Additionally, at this level of theory, the theoretical binary alloy $ThZr_2$ is predicted to form from a mixture of the elements for $T \geq$ 1122 K. Again, this is generally in agreement with the experimental observation that a bcc solid solution of $ThZr_2$ is stable for $T \geq$ 1150 K. Here, we consider only an ordered $ThZr_2$ solid. Methods that further account for the thermodynamic mixing effects of the bcc solid solution of $ThZr_2$ may refine the details of the high temperature products.[49]

In Figure 4.3c we include our best estimate for configurational entropy effects due to partial hydrogen occupancy of the interstitial sites for the $ThZr_2H_6$ ternary hydride. Here, TS^{conf} is 5.4 kJ mol^{-1} H_2 at 1000 K. The effect of the configurational entropy on the stability of the ternary hydride is minor with only a slight rise in the predicted T_d when

accounting for vibrational effects. This phase diagram indicates that $ThZr_2H_6$ decomposes to a mixture of hydrogen and the pure metals at high temperature and that a high temperature bcc solid solution forms for $T \geq 1588$ K. This is our best estimate of the thermodynamic stability of $ThZr_2H_6$ relative to a simplified set of products that can form in the Th–Zr–H element space.

4.7 van't Hoff Plots

Figure 4.4 shows the computed van't Hoff plots for the metal hydride phases that are predicted to form. Fitting this data to lines, we obtained the enthalpies and entropies of formation for the three stable high temperature metal hydrides shown in Table 4.3. Experimentally-derived thermodynamic data are included for comparison. $ThZr_2H_6$ and ThH_2 have nearly identical entropies of formation at $\Delta S° = -133$ J K^{-1} mol^{-1} H_2, which is very close to the ideal entropy of H_2 gas, 130.6 J K^{-1} $mol^{-1}H_2$ at $T = 300$ K.[16]. The entropy of formation for ZrH_2 deviates significantly from this value, indicating a stronger influence of the vibrational free energies of the solid materials. This is confirmed in reactions 1, 4, and 5 in Figure 4.2. ΔF^{vib}_{solids} for the ZrH_2 decomposition reaction has a larger magnitude over the entire T range than either the ThH_2 or $ThZr_2H_6$ decomposition reactions. Bartscher et al. integrated P–C isotherms for 1183 K $\leq T \leq$ 1321 K to obtain the $\Delta H°$ and $\Delta S°$ for $ThZr_2H_6$ from $ThZr_2$.[9] Since continuous isotherms across the composition range were not available, they estimated equilibrium pressures via extrapolation for $ThZr_2H_x$ ($x > 3.9$) and $T > 1183$ K. Our predicted enthalpies and entropies overestimate the enthalpy and entropy of formation for $ThZr_2H_6$ compared with these experimental extrapolated values. The net effect is that $ThZr_2H_6$ decomposes to the elements and hydrogen gas at $T_d = 1168$ K compared with the experimental value of $T_d \approx$

1236 ± 150 K based on the equilibrium relation.[9] Thus, our calculations predict the overall thermodynamic stability of the ternary hydride with reasonable accuracy.

For P > 150 bar H_2, the GCLP method predicts $ThZr_2H_6$ decomposes via the reaction $ThZr_2H_6 \rightarrow ThZr_2 + H_2$ rather than $ThZr_2H_6 \rightarrow Th + 2Zr + 3H_2$. For P < 0.01 bar H_2, $ThZr_2H_6$ is predicted to dissociate via $ThZr_2H_6 \rightarrow Th + 2ZrH_2 + H_2$. Pathways are pressure-dependent, and more detailed methods are needed to differentiate amongst materials with these subtle differences in stability.[50] Further improvements to computed phase boundaries could be made with a more rigorous treatment of the high temperature $ThZr_2$ bcc solid solution free energy. While an unambiguous ranking of the relative thermodynamic stabilities of the $ThZr_2H_6$, ZrH_2, and ThH_2 is not reached at this level of theory, Figure 4.4 clearly shows that the ternary hydride is thermodynamically viable at high temperature and across a wide range of pressures.

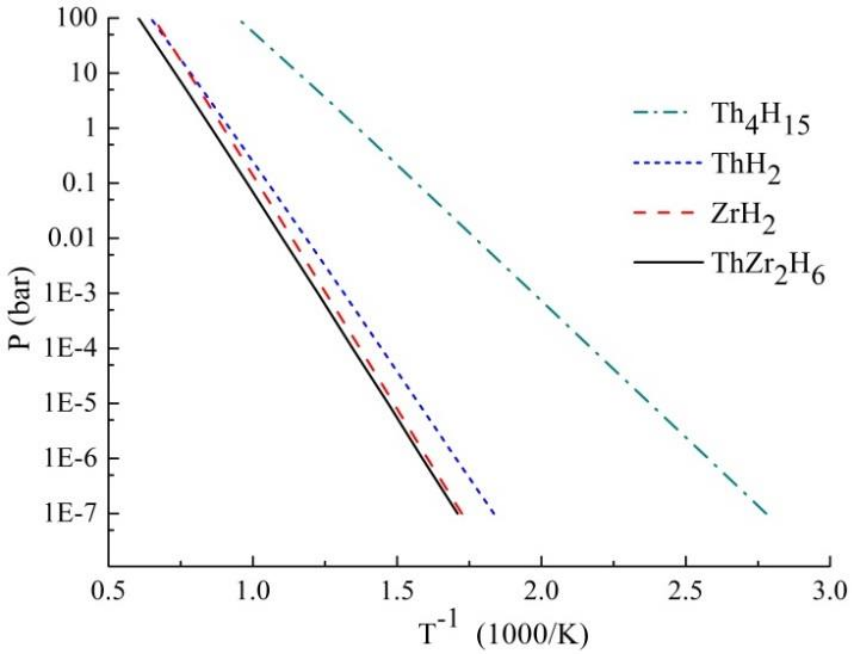

Figure 4.4: Computed van't Hoff plots for stable metal hydrides in the Th–Zr–H space.

Table 4.3: Comparison of predicted and experimental enthalpies and entropies of formation for high temperature metal hydrides. DFT values derived from Eq. (2.3).

	DFT Prediction		Experimental Reference	
metal hydride	$\Delta H°$ (kJ mol^{-1} H_2)	$\Delta S°$ (J K^{-1} mol^{-1} H_2)	$\Delta H°$ (kJ mol^{-1} H_2)	$\Delta S°$ (J K^{-1} mol^{-1} H_2)
$ThZr_2H_6$	-156.1	-133.3	-137.7 ± 8.3[a]	-111.3 ± 6.7
ZrH_2	-161.7	-145.1	-162.8 ± 1.3[b] -169.5[b]	-134.4 ± 0.2 -
ThH_2	-145.4	-133.3	-146 ± 8[c]	-129 ± 7

[a] at T = 1250 K[9]
[b] at T = 298.15 K Quoted in Zuzek, Abriata, and San-Martin[51]
[c] at T = 1000 K[52]

4.8 Conclusions

First principles methods capable of predicting the thermodynamic properties of metal hydrides that operate at high temperature will be useful in several applications such as informing the optimal operational conditions for hydride nuclear fuels. In this chapter, we considered the Th–Zr–H element space because it contains an experimentally-observed ternary interstitial metal hydride with lower H_2 overpressures than that of the competing binary hydrides, an anomaly for metallic hydrides. We predicted the phase diagram for a mixture of Th and Zr open to a hydrogen atmosphere using the GCLP method and DFT to compute free energies of relevant compounds, including saturated $ThZr_2H_7$ and $ThZr_2H_6$ with partial H occupancies. We developed a cluster analysis method that efficiently samples the $ThZr_2H_6$ 32e-96g interstitial site configuration space and computes the number of arrangements that simultaneously meet the hydrogen partial occupancy requirement as well as the Westlake minimum H-H separation distance. We drastically reduced the overestimate of the configurational entropy based on complete H

disorder for $ThZr_2H_6$ from 79 to 16 J mol^{-1} K^{-1} and conclude that the configurational entropy is not a major driver for the enhanced stability of $ThZr_2H_6$ relative to the binary hydrides. The $ThZr_2H_7$ ternary hydride of van Houten and Bartram[1] does not form for any temperature or pressure, and the relaxed lattice constants deviate significantly from the experimental structure. To our knowledge, $ThZr_2H_7$ has yet to be reproduced experimentally by another group and further work should be completed to verify the saturation hydrogen loading for the $ThZr_2H_x$ metal hydride.

We computed van't Hoff plots for the stable binary and ternary hydrides and estimated enthalpies and entropies of formation. Our predicted T_d of 1168 K for $ThZr_2H_6$ is in reasonable agreement with the experimental extrapolated $T_d \approx 1236 \pm 150$ K. The thermodynamic stabilities of the very stable metal hydrides, particularly $ThZr_2H_6$ and ZrH_2, are nearly degenerate at this level of theory. Nevertheless, this study shows that first principles methods can successfully reproduce general phase stability behavior of a simple ternary metal-hydrogen system that operates at high temperature. These methods may be useful in metal hydride applications where experiments are inconvenient or component materials are scarce.

4.9 References

[1] R. van Houten and S. Bartram, *Metall. Trans.*, **2**, 527 (1971).

[2] T. Yamamoto, H. Suwarno, F. Ono, H. Kayano, and M. Yamawaki, *J. Alloys Compd.* **271–273**, 702 (1998).

[3] W. Bartscher, J. Rebivant, A. Boeuf, R. Caciuffo, F. Rustichelli, J. M. Fournier, and W. F. Kuhs, *J. Less-Common Met* **121**, 455 (1986).

[4] K. A. Terrani, G. W. Chinthaka Silva, C. B. Yeamans, M. Balooch, and D. R. Olander, *J. Nucl. Mater.* **392**, 151 (2009).

[5] K. Konashi, B. A. Pudjanto, T. Terai, and M. Yamawaki, *J. Phys. Chem. Solids* **66**, 625 (2005).

[6] P. C. P. Bouten and A. R. Miedema, *J. Less-Common Met* **71**, 147 (1980).

[7] K. H. J. Buschow, P. C. P. Bouten, and A. R. Miedema, *Rep. Prog. Phys.* **45**, 937 (1982).

[8] W. Grochala and P. P. Edwards, *Chem. Rev.* **104**, 1283 (2004).

[9] W. Bartscher, J. Rebizant, and J. M. Haschke, *J. Less-Common Met* **136**, 385 (1988).

[10] G. Sandrock and G. Thomas, *Appl. Phys. A* **72**, 153 (2001).

[11] R. L. Beck and W. M. Mueller, in *Metal Hydrides* (Academic Press, New York, 1968), p. 241.

[12] P. F. Woerner and P. Chiotti, *Precipitation of Thorium as Thorium Hydride from Thorium-Magnesium Solutions*, United States Atomic Energy Commission Ames Laboratory, Iowa State College, Ames, 1957, p. 6.

[13] B. Tsuchiya, J. Huang, K. Konashi, W. Saiki, T. Onoue, and M. Yamawaki, *J. Alloys Compd.* **312**, 104 (2000).

[14] S. P. Ong, L. Wang, B. Kang, and G. Ceder, *Chem. Mater.* **20**, 1798 (2008).

[15] K. J. Michel, A. R. Akbarzadeh, and V. Ozolins, *J. Phys. Chem. C* **113**, 14551 (2009).

[16] A. R. Akbarzadeh, V. Ozoliņš, and C. Wolverton, *Adv. Mater.* **19**, 3233 (2007).

[17] S. V. Alapati, J. K. Johnson, and D. S. Sholl, *J. Phys. Chem. C* **112**, 5258 (2008).

[18] K. C. Kim, A. D. Kulkarni, J. K. Johnson, and D. S. Sholl, *Phys. Chem. Chem. Phys.* **13**, 7218 (2011).

[19] A. R. Akbarzadeh, C. Wolverton, and V. Ozolins, *Phys. Rev. B* **79**, 184102 (2009).

[20] C. Wolverton, J. S. Donald, A. R. Akbarzadeh, and V. Ozoliņš, *J. Phys. Condens. Matter* **20**, 064228 (2008).

[21] E. H. Majzoub, F. Zhou, and V. Ozoliņš, *J. Phys. Chem. C* **115**, 2636 (2011).

[22] K. M. Nicholson and D. S. Sholl, *Phys. Rev. B* **86**, 134113 (2012).

[23] B. A. Pudjanto, K. Konashi, T. Terai, and M. Yamawaki, *J. Phys. Chem. Solids* **66**, 665 (2005).

[24] S. P. Ong, et al., *Comput. Mater. Sci.* **68**, 314 (2013).

[25] S. P. Ong, A. Jain, G. Hautier, B. Kang, and G. Ceder, *Electrochem. Commun.* **12**, 427 (2010).

[26] D. G. Westlake, *J. Less-Common Met* **91**, 1 (1983).

[27] G. Kresse and J. Hafner, *Phys. Rev. B* **47**, 558 (1993).

[28] G. Kresse and J. Hafner, *Phys. Rev. B* **49**, 14251 (1994).

[29] G. Kresse and J. Furthmüller, *Phys. Rev. B* **54**, 11169 (1996).

[30] G. Kresse and J. Furthmüller, *Comput. Mater. Sci.* **6**, 15 (1996).

[31] D. S. Sholl and J. A. Steckel, *Density Functional Theory: A Practical Introduction* (John Wiley & Sons, Hoboken, 2009).

[32] P. E. Blöchl, *Phys. Rev. B* **50**, 17953 (1994).

[33] G. Kresse and D. Joubert, *Phys. Rev. B* **59**, 1758 (1999).

[34] J. P. Perdew, J. A. Chevary, S. H. Vosko, K. A. Jackson, M. R. Pederson, D. J. Singh, and C. Fiolhais, *Phys. Rev. B* **46**, 6671 (1992).

[35] FIZ Karlsruhe and NIST, *THE INORGANIC CRYSTAL STRUCTURE DATABASE (ICSD)*.

[36] G. Bergerhoff and I. D. Brown, in *Crystallographic Databases*, edited by F. H. Allen, G. Bergerhoff and R. Severs (International Union of Crystallography, Chester, 1987).

[37] K. A. Terrani, E. Mamontov, M. Balooch, and D. R. Olander, *J. Nucl. Mater.* **401**, 91 (2010).

[38] G. B. Skinner and H. L. Johnston, *J. Chem. Phys.* **21**, 1383 (1953).

[39] A. I. Kolesnikov, A. M. Balagurov, I. O. Bashkin, A. V. Belushkin, E. G. Ponyatovsky, and M. Prager, *J. Phys. Condens. Matter* **6**, 8977 (1994).

[40] W. J. James and M. E. Straumanis, *Acta Crystallogr.* **9**, 376 (1956).

[41] M. H. Mueller, R. A. Beyerlein, J. D. Jorgensen, T. O. Brun, C. B. Satter Thwaite, and R. Caton, *J. Appl. Cryst.* **10**, 79 (1977).

[42] R. E. Rundle, C. G. Shull, and E. O. Wollan, *Acta Crystallogr.* **5**, 22 (1952).

[43] W. L. Korst, *Acta Crystallogr.* **15**, 287 (1962).

[44] M. P. Pitt, L. K. W. Pitt, H. Fjellvåg, and B. C. Hauback, *J. Alloys Compd.* **509**, 5515 (2011).

[45] H. E. Flotow and D. W. Osborne, *J. Chem. Phys.* **34**, 1418 (1961).

[46] A. Srivastava, M. Chauhan, and R. K. Singh, *Phys. Status Solidi B* **248**, 2793 (2011).

[47] B.-T. Wang, P. Zhang, H. Song, H. Shi, D. Li, and W.-D. Li, *J. Nucl. Mater.* **401**, 124 (2010).

[48] A. Togo, F. Oba, and I. Tanaka, *Phys. Rev. B* **78**, 134106 (2008).

[49] C. Wolverton and V. Ozoliņš, *Phys. Rev. B* **73**, 144104 (2006).

[50] K. C. Kim, A. D. Kulkarni, J. K. Johnson, and D. S. Sholl, *Phys. Chem. Chem. Phys.* **13**, 21520 (2011).

[51] E. Zuzek, J. P. Abriata, A. San-Martin, and F. D. Manchester, *J. Phase Equilib.* **11**, 385 (1990).

[52] H. E. Flotow and D. W. Osborne, *J. Chem. Thermodyn.* **10**, 537 (1978).

CHAPTER 5

COMPLEX TRANSITION METAL HYDRIDE INTRODUCTION AND SCREENING METHODOLOGY*

5.1 CTMH Background

As discussed in Chapter 1, some complex transition metal hydrides are known to operate (release hydrogen) at higher temperatures than binary hydrides of the same metal species. Since the thermodynamic properties of CTMHs are not well established experimentally, computational methods based on DFT offer an opportunity to characterize a large library of such materials and potentially identify candidates that have similar enhanced stability, $T_d/T_{d,binary} \geq 1$, and that operate at high temperatures, taken here to be $T_d \geq 1000$ K for the NGNP application. In Chapters 6 and 7, we present the results from our screening of large libraries of known and proposed CTMH materials, respectively. Here, we review the background, theoretical approach, screening methodologies, and computational details for the screening.

5.1.1 CTMH characteristics

Yvon and Renaudin updated a comprehensive review of the known CTMHs in 2005.[1] In order to give an idea of the progress made in recent decades in reporting new CTMHs, consider that, in 1991, there were 13 CTMH structure types and in the latest 2005 update, there were 47 structure types or "prototypes" for over 127 unique compounds. CTMHs are stabilized via charge transfer from a cation, *M*, to an anionic

* Reproduced in part with permission from Inorg. Chem., submitted for publication. Unpublished work copyright 2014 American Chemical Society.

transition metal hydrido complex, [*Tr*H_n]. "Known" or "existing" CTMHs form from late 3d, 4d, and 5d transition metals of groups 7-10 with monovalent alkali, divalent alkaline earth, and/or trivalent lanthanide species. Currently, no known transition metal hydrido complexes have been identified for elements of groups 4, 5, or 6 or of Ag, Au, or Hg.[1,2] There are two broad classifications of CTMHs that describe the type(s) of hydrogen bonding in the material:[1]

1) Hydrogen covalently bound to a transition metal, *Tr*, to form anionic hydrido complexes, in which the charge on the complex is reduced and the structure is stabilized by surrounding cations:

$$M_m^{\delta+}\,[TrH_n]^{\delta-}\ (m, n, \delta = 1,2,3...) \qquad (5.1)$$

2) Composite hydrides that contain both hydrogen covalently bound to *Tr* to form complexes and anionic "intersitial" hydrogen that interact directly with the cations:

$$M_m^{\delta+}\,[TrH_n]^{\delta-}\,M_o^{\delta+}\,H^-_p\ (m, n, o, p, \delta = 1,2,3...) \qquad (5.2)$$

Again, [*Tr*H_n] tend to form for *Tr* to the right of Mn, Tc, and Re (metals that do not form stable binary hydrides) on the periodic table. To the left of this group, interestitial binary hydrides are stable.[2] Two examples of CTMH crystal structures with the common six-coordinated octahedral and four-coordinated tetrahedral homonuclear [*Tr*H_n] complexes are shown in Figure 5.1. The most common arrangement of *M* is the 8-fold cubic or nearly cubic structure. It has been argued that this arrangement allows cations to maximize interactions with hydrogen, stabilizing the overall structure.[1] For a given [*Tr*H_n] complex and different *M* species of the same valence, *Tr*−H bond lengths are largely fixed, and the *M*−H bond lengths scale with tabulated ionic radii.[1,3] Most CTMHs

have closed outer electron shells and are diagmetic. Some exceptions include materials with magnetic ions that order magneticallly at low *T* (e.g., K_3MnH_5).[1]

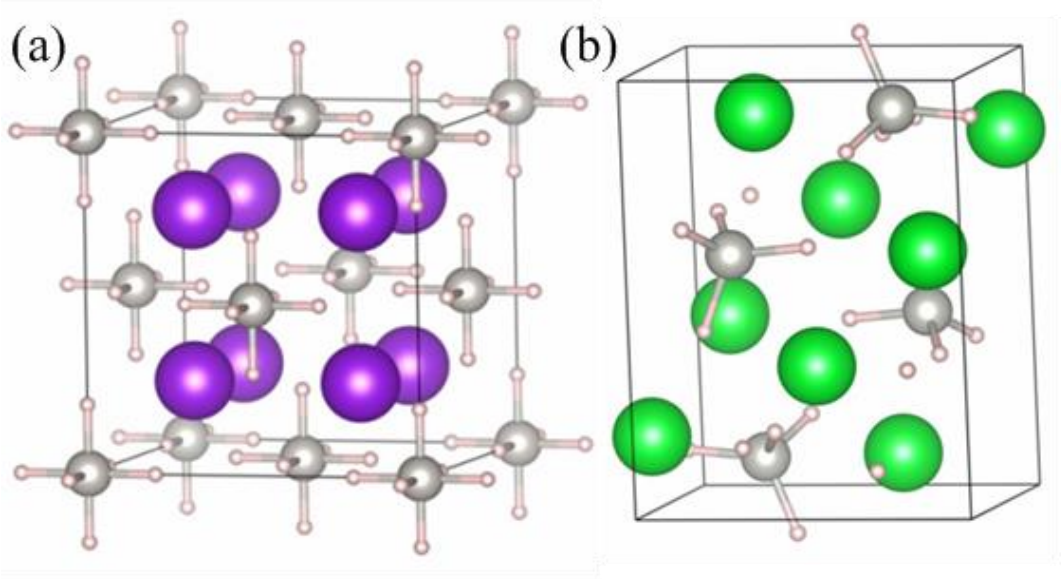

Figure 5.1: Representative crystal structures for (a) K_2PtH_6 (Sr_2PtH_6 prototype) with octahedral $[PtH_6]^{2-}$ complexes and (b) Sr_2PdH_4 (K_2ZnH_4 prototype) with tetrahedral $[PdH_4]^{4-}$ complexes. (largest sphere = K, Sr, medium sphere = Pt, Pd, smallest sphere = H)

5.1.2 Existing CTMH library

Figure 5.2 maps the known CTMHs with experimentally-reported crystal structures compiled from both the 2005 Yvon and Renaudin review[1] as well as a survey of the ICSD[4,5] for stoichiometric materials with CTMH-like compositions. The numeric classifications are consistent with the prototype numbering system of Yvon and Renaudin and describe the chronological order in which the prototype structure (chemical formula shown in figure) was reported. Prototypes without a numeric classifier were reported in the ICSD, but not in the review. Alkali, alkaline earth, and lanthanide *M* species are arranged vertically. Transition metal *Tr* species follow horizontally. Only "simulation

ready" ICSD entries that do not appear in the 2005 Yvon and Renaudin review are shown in Figure 5.2. "Simulation ready" implies that the entries have complete crystal structures with resolved atomic positions and no partial occupancies. $EuPdH_3$ and $CaNiH_3$ are listed in the Yvon and Renaudin review as crystallizing with the $CaPdH_2$ prototype PM3M structure, characterized by disorder and partial hydrogen occupancies. However, given that the ICSD entries for these two materials list the prototype structure as $CaTiO_3$ and there are no partial occupancies for that stoichiometry, we additionally report these materials with the $CaTiO_3$ prototype in Figure 5.2. Also, LiPdH and Na_3PdH_2 structures are shown as CTMHs in Figure 5.2 due to their structural similarities with the other materials. However, as Yvon and Renaudin note in the review, these materials have only a weak tendency toward complex formation.[1]

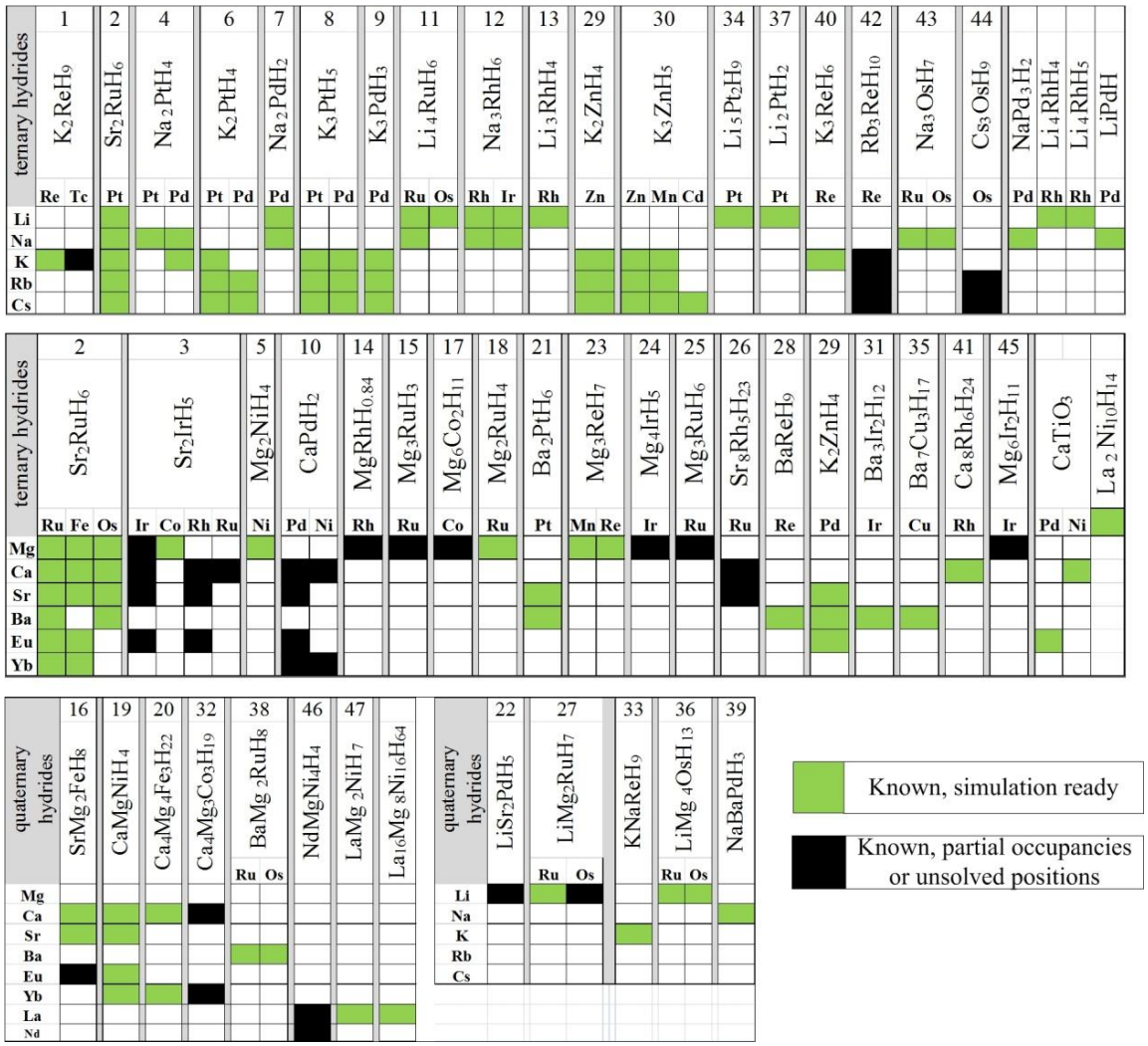

Figure 5.2: Experimentally-known ternary (*M*-Tr-*H*) and quaternary (M_1-M_2-*Tr*-H) Complex Transition Metal Hydrides from the ICSD[4,5] and the Yvon and Renaudin 2005 Review.[1] Numbers are consistent with Yvon and Renaudin[1] and describe the chronological discovery of the prototype ternary hydride M_x Tr_y H_z crystal structure shown vertically. Substitutional cations *M* of the same valence are grouped vertically. Substitutional transition metals *Tr* are listed horizontally. "Simulation ready" implies completely solved and ordered structure with no partial occupancies.

5.1.3 Other CTMH computational studies

Despite their potential high hydrogen volumetric storage capacities, the high thermal stabilities of CTMHs have currently made them unattractive for ambient condition fuel cell applications. Computational and experimental studies into the thermodynamics or kinetics of hydride systems have focused, instead, on the light complex hydrides such as the borohydrides and alanates.[6-27] The most well-studied CTMH system is Mg_2FeH_6 for which measurements of structural, vibrational, electronic, and thermodynamic properties have been made using both experimental measurements and first principles predictions.[3,28-30] Primarily, DFT calculations have been used to predict the bulk structural properties and vibrational densities of states of CTMHs.[2,31-34] To date, there has been no large scale computational screening of CTMHs for high temperature hydrogen storage applications. This work is the first to systematically study the relative thermodynamic stabilities of all "simulation ready" CTMHs using DFT.

As previously discussed, charge transfer from *M* to [*Tr*H_n] stabilizes CTMHs. Several studies have shown that the electronegativity of the cation is a good predictor of the standard heat of formation of complex hydrides.[3,6-8] However, this approach does not take into account the relative stabilities of competing compounds such as intermetallics or binary hydrides that could form in an element space. Our approach avoids this discrepancy since phase diagrams are generated for given element combinations, computing the the thermodynamically-preferred mix of compounds from a library of potential compounds at a given hydrogen chemical potential.

5.2 Theoretical Framework

Our method for predicting the thermodynamically stable mixture for a given set of compounds that could potentially form in an element space is similar to that described in Section 4.2.1 for the Th-Zr-H system. Given that we apply the GCLP method to quaternary as well as ternary element spaces, we develop the equations here to apply to a general element space. We have used the pymatgen[35] software to perform the grand potential minimization and phase diagram predictions, and so we build upon the nomenclature of Ong, Ceder and colleagues for consistency.[36,37]

For an isobaric, isothermal system that is open to a hydrogen atmosphere such as that described by the NGNP conditions, the thermodynamic phase equilibria can be described by the hydrogen grand potential

$$\phi(T, P, N_j, \mu_{H_2}) = G(T, P, N_j, \mu_{H_2}) - \mu_{H_2} N_{H_2}(T, P, N_j, \mu_{H_2}) \qquad (5.3)$$

where N_j refers to the number of atoms of non-H species j. Here, we limit our study to ternary N_1-N_2-H and quaternary N_1-N_2-N_3-H spaces. Primarily we are interested in probing the relative stabilities of condensed phases for which $(P\Delta V)_{\text{solids}} << P_{H2}$, and so we ignore the PV contributions for solid components. In this work, only ordered compounds without partial occupancies are considered, and the free energy for solid compounds is described by

$$G_j(T) \approx F_j(T) = E_{0,j} + F_j^{vib}(T) \qquad (5.4)$$

as in Eq. (4.2) without configurational or electronic entropy contributions. We normalize Eq. (5.3) with respect to the non-H species to give

$$\bar{\phi}(T,P,x_j,\mu_{H_2}) \approx \frac{E_0 + F^{vib}(T) - \mu_{H_2} N_{H_2}}{\sum_j^n N_j} \tag{5.5}$$

where the fractional component of *j* in the mixture is

$$x_j = \frac{N_j}{\sum_j N_j} \tag{5.6}$$

and $\sum_j x_j = 1$.

In these open metal-hydrogen systems, a simplifying assumption can be made that changes in the stable mixture of compounds are mainly due to the uptake or release of hydrogen gas such that the reaction entropy is dominated by the hydrogen gas entropy. Additionally, it is assumed that the zero point vibrational energy contribution of the solid phases is negligible compared with the change in ground state electronic energy. Under these approximations, temperature effects are controlled through the hydrogen chemical potential and Eq. (5.5) reduces to

$$\bar{\phi}(T,P,x_j,\mu_{H_2}) \approx \frac{E_0 - \mu_{H_2} N_{H_2}}{\sum_j^n N_j} \tag{5.7}$$

Eq. (5.7) is useful because it allows us to compute an approximate phase diagram using only DFT energies for a set of solid compounds. Interesting systems can then be studied with the more rigorous Eq. (5.5) using phonon calculations to determine F^{vib}(T) for each solid.

The hydrogen chemical potential is defined as

$$\mu_{H_2}(T,P_{H_2}) = \mu_{H_2}(T,P_0) + k_B T \ln \frac{P_{H_2}}{P_0} \tag{5.8}$$

which relates the temperature and partial pressure of hydrogen.[36] Here, $\mu_{H_2}(T, P_0)$ is the chemical potential at a reference pressure P_0 = 1 bar. The chemical potential of hydrogen at P_0 is taken to be the Gibbs free energy of the ideal diatomic gas

$$\mu_{H_2}(T, P_0) \approx G_{H_2}(T, P_0) = H_{H_2}(T, P_0) - TS_{H_2}(T, P_0) \tag{5.9}$$

where[10]

$$G_{\mathrm{H_2}} = U_{0,\mathrm{H_2}} + U_{\mathrm{trans+rot,H_2}}(T) + U_{\mathrm{vib,H_2}}(T) - TS_{\mathrm{H_2}}(T) + (PV)_{\mathrm{H_2}} \tag{5.10}$$

Here, G is computed using a combination of DFT-computed, statistical mechanical, and tabulated results. $U_{0,\mathrm{H2}}$ was computed using DFT as the total electronic energy of a hydrogen molecule in a 10 Å simulation box. The translational, rotational, and vibrational terms were determined via[38,39]

$$U_{\mathrm{trans+rot,H_2}} = \frac{5}{2}RT \tag{5.11}$$

and

$$U_{\mathrm{vib,H_2}}(T) = \frac{N_A h\nu}{2} + \frac{N_A h\nu e^{-\beta h\nu}}{1 - e^{-\beta h\nu}} \tag{5.12}$$

where N_A is Avogadro's number, h is Planck's constant, $\beta=(k_B T)^{-1}$, and ν is the H_2 vibrational frequency. [39, 40] We determined ν within the harmonic approximation using DFT to be 1.310×10^{14} s^{-1}, which corresponds to a zero point energy of ~26.1 kJ mol^{-1}, very close to the experimental value of 25.1 kJ mol^{-1} and the value obtained by Alapati et al. with similar DFT calculations.[10,40] Since we assume hydrogen behaves as an ideal gas, $(PV)_{\mathrm{H_2}} = RT$. We compute S_{H2} using

$$S(\mathrm{J\ mol^{-1}\ K^{-1}}) = 29.562647 \ln T - 37.482701 \tag{5.13}$$

which reflects a fitting of NIST-JANAF tabulated values for the entropy of diatomic hydrogen gas for $100 \leq T\,(\mathrm{K}) \leq 2000$ at 1 bar.[41] This fitting results in an error of less than 1 kJ mol^{-1} H_2 for *TS* contributions to the free energy for the temperature range of interest up to 2000 K. This approach to computing the chemical potential of hydrogen differs from that of Alapati et al.[12] who determined the temperature-dependent portion of the chemical potential using the partition function directly. However, our method results in less than a 0.5 kJ mol^{-1} difference in the chemical potential at $P = 1$ bar for the studied temperature range, and it allows us to clearly separate enthalpic and entropic effects for computing thermodynamic properties.

5.3 Screening Algorithms

5.3.1 Existing metal hydrides

Our aim in Chapter 6 is to identify known or "existing" CTMH candidate materials that are both more stable than the binary hydrides that form from the constituent metals and that release hydrogen only at high temperature. For computational efficiency, we use two rounds of screening at increasing levels of theory, down-selecting the interesting element spaces and, therefore, the CTMH candidates, with each step.

In Round 1, we compute phase diagrams at $P = 1$ bar H_2 and $0 \leq T\,(\mathrm{K}) \leq 2000$ using Eq. (5.7) for the 72 element spaces (57 *M*-*Tr*-H ternary and 15 M_1-M_2-*Tr*-H quaternary) shown in Figure 5.3 using a "simulation ready" DFT materials library (260+ materials) summarized in Table 5.1. This initial materials library is available in its entirety in Table C.1 in the Appendix. We exclude materials that are not simulation ready such as those with partial occupancies, e.g., materials that crystallize in the 10-Ca_2PdH_2 prototype with ⅔ occupancy of all H sites or 15-Mg_3RuH_3 with ½ occupancy of the 8i H

sites, etc. In Figure 5.3, cations are arranged according to valence and transition metals according to group number and molecular weight for the ternary hydrides. Each targeted element space contains at least one CTMH candidate material from Figure 5.2. Ternary alkaline earth (saline) hydrides (e.g., $Ba_2Mg_3H_{10}$ and $Mg_3Sr_2H_{10}$) are not strictly CTMHs but form in the phase spaces under consideration and are screened as a result. We include 96 binary intermetallics. It is notable that just over half of the element spaces with a CTMH under consideration do not contain binary intermetallics that are experimentally known and "simulation ready". This reflects the fact that most CTMHs are true ternary compounds that do not derive from the hydrogenation of stable intermetallics as previously discussed. Ten of the element spaces account for 54 of the 95 intermetallics indicating that the presence of intermetallics is highly concentrated among certain element combinations.

Critically, in this step, finite temperature contributions for the condensed phases are ignored. We retrieve an estimate of the relative and absolute stabilities of hydride phases that form in each element space, and retain those element spaces that contain a CTMH with enhanced stability with respect to the binary hydrides, $T_d/T_{d,binary} \geq 1$. At this step we do not require that all hydrides operate at high temperature $T_d \geq 1000$ K since T_d can change in either direction when including vibrational contributions. This might also affect the stability of the hydride with respect to the binary hydride, but we feel applying this screening criterion is more conservative while allowing us to down select to a reasonable number of materials to study at the higher level of theory.

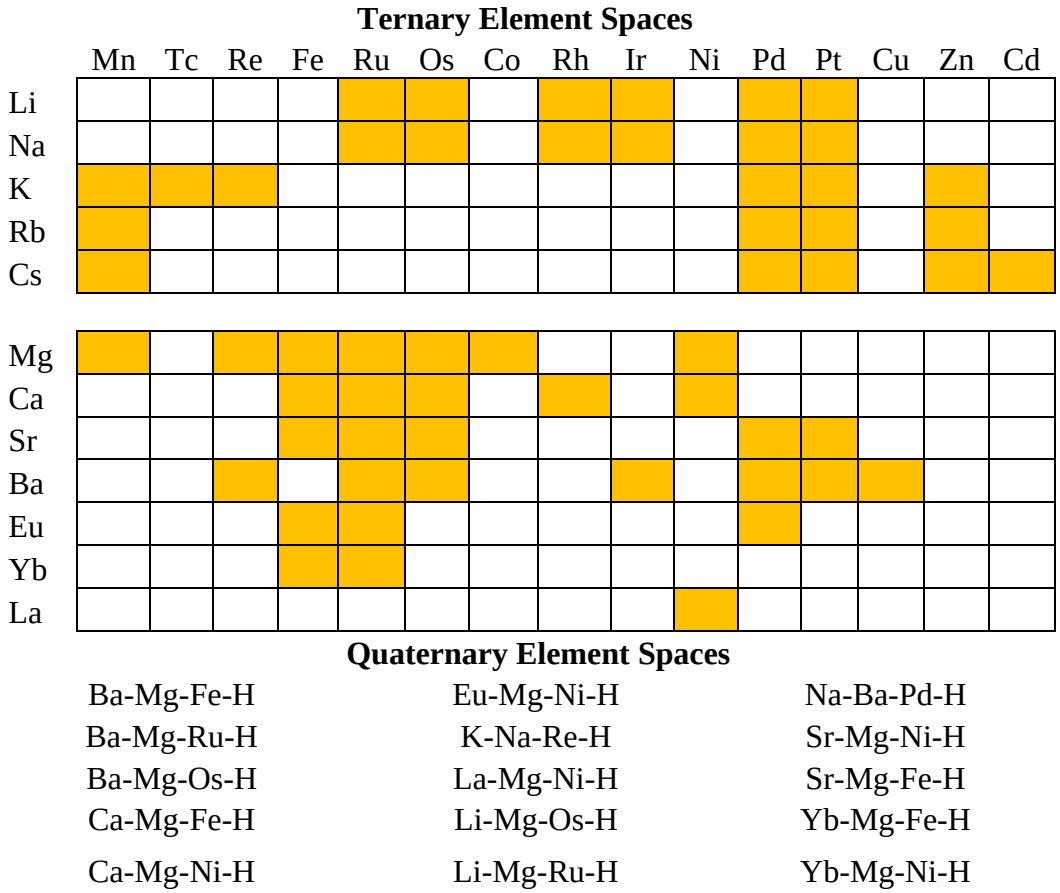

Figure 5.3: Mapping of existing (orange) ternary *M*-*Tr*-H and quaternary M_1-M_2-*Tr*-H element spaces studied with the Round 1 level of screening.

Table 5.1: Initial DFT materials library summary for screening of existing CTMH listed in Table C.1 in the Appendix.

Material Type	Number of Compounds
ternary CTMHs	84
quaternary CTMHs	18
binary hydrides	23
ternary alkaline earth (saline) hydrides	18
pure metals	28
binary intermetallics	95

In Round 2, we perform phonon calculations on the materials belonging to element spaces retained from Round 1. We compute phase diagrams using Eq. (5.5), taking into account finite temperature vibrational effects of the solid phases. This provides our best estimate of the relative stabilities of CTMH candidates with respect to the binary hydrides and other potential "simulation ready" materials. Additionally, compounds that are dynamically stabilized through vibrational contributions may be revealed in the set of stable compounds as a function of hydrogen chemical potential. Final candidates are chosen to be those with, again, enhanced stability relative to the binary hydrides, $T_d/T_{d,binary} \geq 1$, and $T_d \geq 1000$ K.

In this study, we consider only those compounds that have been observed experimentally with either a "simulation ready" crystal structure available in the ICSD or a template material with the same prototype crystal structure with all atomic positions resolved. Our calculations cannot make predictions about the stabilities of compounds not included in the DFT materials library. It is possible that either a stable ternary or higher hydride phase exists with higher T_d than our final candidates, but has not yet been experimentally observed, or that a high temperature intermetallic or alloy phase exists that is not included in our library that may destabilize our final candidates. Our calculations, however, are useful for rapidly characterizing thermodynamic properties, such as approximate heats of dehydrogenation and for identifying decomposition pathways for a large set of interesting materials at a moderate level of theory. Then more rigorous thermodynamic data regarding ΔH, ΔS, and equilibrium pressures as a function of temperature can be obtained that can be directly related to experimental measurements.

5.3.2 Proposed CTMH

From the mapping of known CTMHs in Figure 5.2, we see that stable compounds tend to form in a given prototype down a group with cations of the same valence, thus maintaining charge neutrality. For example, 2-$M_2[RuH_6]^{4-}$ (Sr_2RuH_6 prototype where 2 is the numeric identifier from Figure 5.2) forms compounds for M^{2+} = Mg, Ca, Ba, Sr, Eu, and Yb. Similarly, materials have been identified for 2-$M_2[FeH_6]^{4-}$ (M^{2+} = Mg, Ca, Sr, Eu, and Yb), but there is no known compound that forms with the composition Ba_2FeH_6 in this prototype. Additionally, there are no ICSD entries for Eu_2OsH_6 or Yb_2OsH_6 in the 2-Sr_2RuH_6 prototype structure. Currently, we have no indication as to whether or not synthesis of these compounds has ever been attempted, but as recently as 2010, Li_2PtH_6 was synthesized at high H_2 pressures in the 2-Sr_2RuH_6 prototype to complete the series of alkali metals.[42]

In Chapter 7, we perform DFT calculations to first predict if the 149 "missing" or "proposed" ternary compounds shown in Figure 5.4 are thermodynamically viable based on ground state energies with respect to our DFT materials library from Table 5.1. Then we subject the predicted stable materials to the same screening procedure used for known materials, described in Section 5.3.1, to identify candidates for the NGNP application. The proposed materials we test include only those materials for which there are available template materials that are "simulation ready". For example we exclude proposed materials such as $SrNiH_2$ that might form in the 10-$CaPdH_2$ or Ca_3RuH_3 in the 15-Mg_3RuH_3 structures due to the presence of partial occupancies on the H sites. These proposed materials require special and individualized treatment, outside of the scope of this large scale screening study. We exclude LiPdH and Li_4RhH_5 templates for this study since these were not found to be thermodynamically stable for any T based on our initial

screening of existing CTMH. We also do not consider quaternary hydrides at this time since we found that quaternary hydrides tend to decompose to mixtures of lower hydrides upon heating in our existing materials screening. Presented in Figure 5.5, our calculations greatly extend the range of element spaces probed to identify ternary hydrides for the NGNP application, covering 71 element spaces not previously examined in the screening of known materials.

Figure 5.4: Mapping of 149 proposed and known CTMH materials studied with DFT and screened for enhanced thermodynamic properties for the NGNP application. Experimentally-known ternary (*M*-*Tr*-H) Complex Transition Metal Hydrides are from the ICSD[4,5] and the Yvon and Renaudin 2005 Review.[1] Numbers are consistent with Yvon and Renaudin[1] and describe the chronological discovery of the prototype ternary hydride $M_x\ Tr_y\ H_z$ crystal structure shown vertically. Substitutional cations *M* of the same valence are grouped vertically. Substitutional transition metals *Tr* are listed horizontally. "Simulation ready" implies completely solved and ordered structure with no partial occupancies.

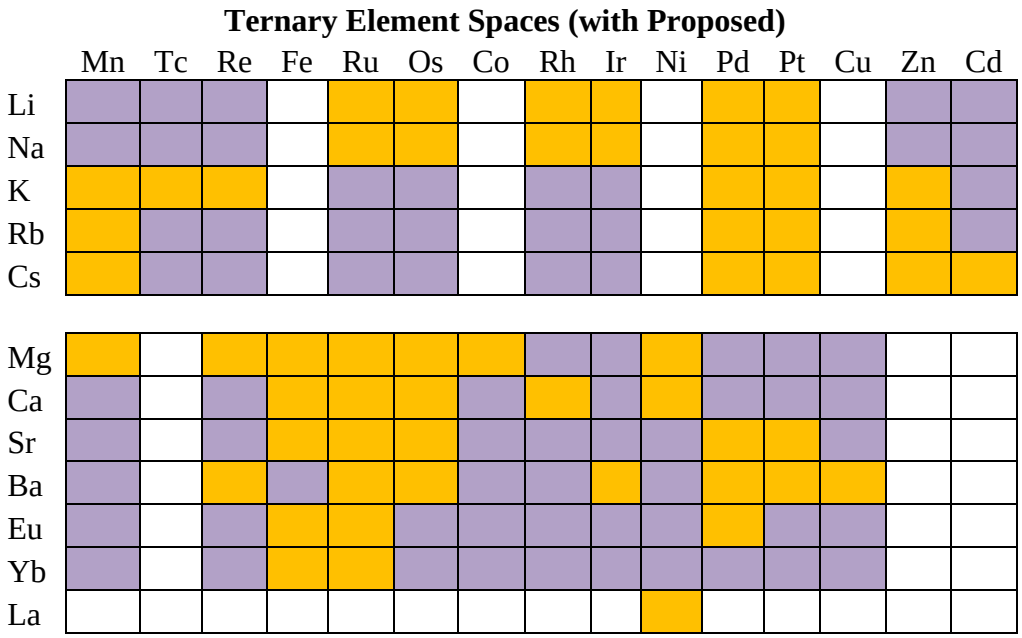

Figure 5.5 Mapping of existing (orange) and proposed (purple) ternary *M*-*Tr*-H element spaces studied with Round 1 level of screening.

The overall screening procedure for the proposed CTMH materials is described below. First, we relax 149 proposed materials using DFT to obtain E_0 and incorporate the composition and energy into the materials library from Table 5.1. The DFT calculations require an initial crystal structure. Since [*Tr*H_n] complexes behave largely as rigid units, as previously discussed, the volume of a CTMH unit cell scales roughly with the ionic radius of the cation. Figure 5.6 shows relaxed DFT volumes normalized by the ionic radius of the cation for a series of prototypes. The relationship is generally smooth, and so we estimate the initial unit cell volume of a given proposed material through simple scaling of the lattice constants of a reference material that crystallizes in the same prototype to account for the ionic radius of the target material. *M* = Ba is missing from the 2-M_2[FeH_6] series of existing materials in Figure 5.6 because there is no known Ba_2FeH_6 compound that crystallizes in the type 2-Sr_2RuH_6 prototype structure.

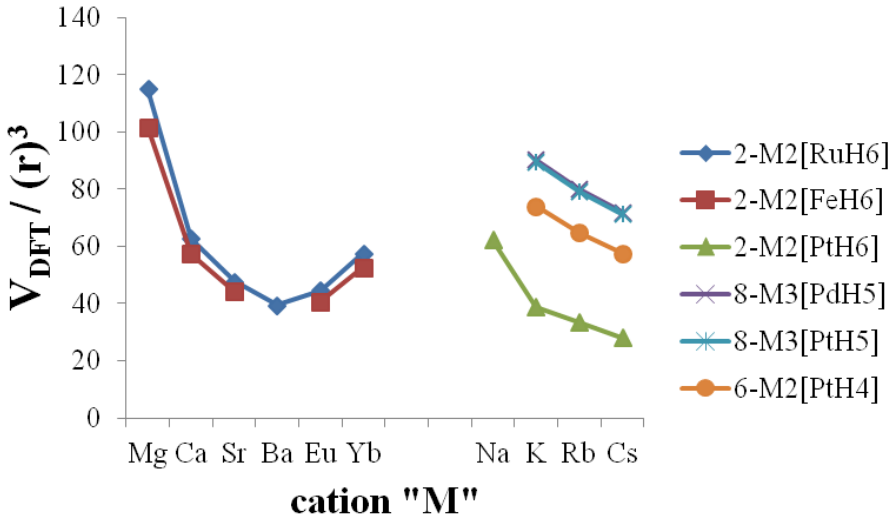

Figure 5.6: Relationship between cation, *M*, and unit cell volumes of existing CTMHs relaxed using DFT. Volumes are normalized by the ionic radius, *r*, of *M*.[43] Cations are arranged by valence. Numeric identifiers before compositions in legend refer to the prototype structure classification from Figure 5.2.

We predict phase diagrams at P = 1 bar H_2 for $0 \leq T$ (K) ≤ 2000 for the proposed element spaces in Figure 5.5 using Eq. (5.7), again initially ignoring vibrational effects. We retain element spaces for which there is a stable proposed CTMH. Next, we retrieve binary intermetallics from the ICSD that are "simulation ready" for retained element spaces not previously scrutinized with the initial existing materials screening. We again predict phase diagrams while including relaxed DFT energies for the additional intermetallics. This is to account for proposed CTMHs that are destabilized by binary intermetallic phase(s) not in the initial library from Table 5.1. For those element spaces that retain a stable proposed CTMH, we repeat the screening procedure described in Section 5.3.1 for the existing hydrides. We note that we continue to perform calculations for *all* proposed phases in a retained element space, regardless of whether or not the given materials were predicted to be stable initially. This is to ensure that proposed

phases that are dynamically stabilized through vibrational effects can be identified for element spaces with a candidate proposed material.

If a given proposed material is not predicted to be stable for any given round of screening, this suggests that a CTMH with that composition will not be observed experimentally. Our calculations cannot preclude, however, the possibility that a CTMH will form in a lower energy crystal structure not studied here. While DFT-based crystal structure prediction methods exist,[15,17,44-46] in this work we take advantage of the prior knowledge that known CTMHs tend to form in a given set of prototype structures and maintain charge neutrality.

5.4 Computational Details

Plane-wave DFT calculations were carried out using VASP[47-51] with the projector augmented wave method with PW91 GGA exchange-correlation functional.[52-54] Pseudopotentials for each element were taken to be the recommended PAW potentials listed in the VASP manual.[55] Experimental crystal structures for the low temperature, low pressure forms of target compositions were taken from the ICSD.[4,5] We utilized pymatgen automation tools to manage the DFT computation setup and Custodian for error handling.[35,56] These software allow us to efficiently perform calculations for the large set of materials considered in this work and to streamline the workflow.

Volume, shape, and ion position relaxations were performed on primitive cells for each compound using the conjugate gradient method until forces on each atom were less than 0.03 eV $Å^{-1}$ and electronic steps were converged to within 10^{-5} eV. We use Methfessel-Paxton smearing with width of 0.2. To determine a suitable *k*-point density, we performed initial convergence testing for a representative materials set: K_2ReH_9,

Sr_2RuH_6, Na_2PtH_4, Mg_2NiH_4, K_2PtH_4, K, Mg, Na, Ni, Re, and Ru. The test set was relaxed at a 400 eV cutoff energy without spin-polarization for three *k*-point meshes, representing low, medium, and high densities. Monkhorst-Pack meshes were used for all symmetries except hexagonal for which we adopted Γ-centered grids for faster convergence. The convergence of ground state energies with respect to the highest number of *k*-points for each material is shown in Figure 5.7. We find that a minimum density of 4000 *k*-points /(number of atoms per unit cell) distributed as evenly as possible across the reciprocal lattice vectors is sufficient to converge E_0 to within 0.3 kJ mol^{-1}(3 meV $atom^{-1}$) for the test set. We adopt this density for all materials in the study.

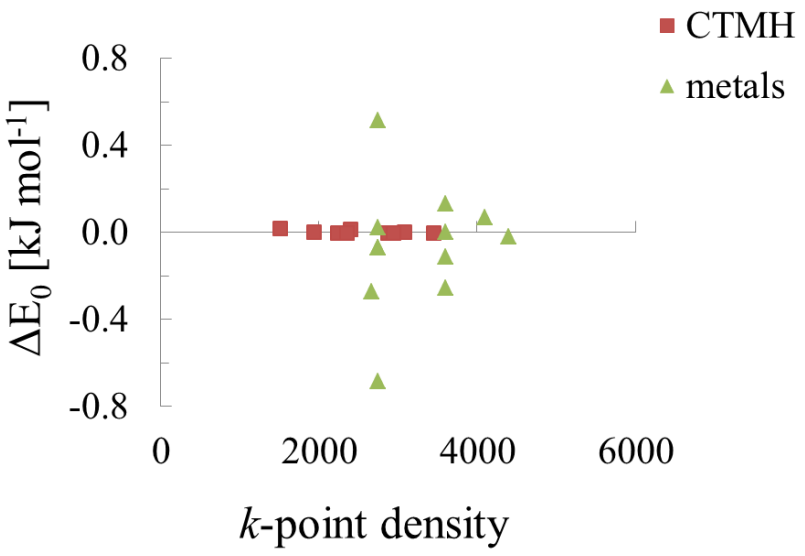

Figure 5.7: Convergence of test set with respect to the highest density, *k*-points/number of atoms in unit cell, tested.

To determine a suitable energy cutoff, we relaxed K_2ReH_9, Sr_2RuH_6, Na_2PtH_4, Mg_2NiH_4, K_2PtH_4, K, Mg, Na, and Cu at 300 eV, 400 eV, and 500 eV cutoff energies without spin polarization. The convergence of ground state energies with respect to a cutoff energy of

500 eV is shown in Figure 5.8. We find that a cutoff energy of 400 eV is sufficient to converge the absolute magnitudes of the test set to within 2.5 kJ mol^{-1} (3 meV $atom^{-1}$) for each material, and we expect that the relative energies of materials in confined element spaces will converge even more quickly. Thus we adopted a 400 eV cutoff energy for all calculations in this work.

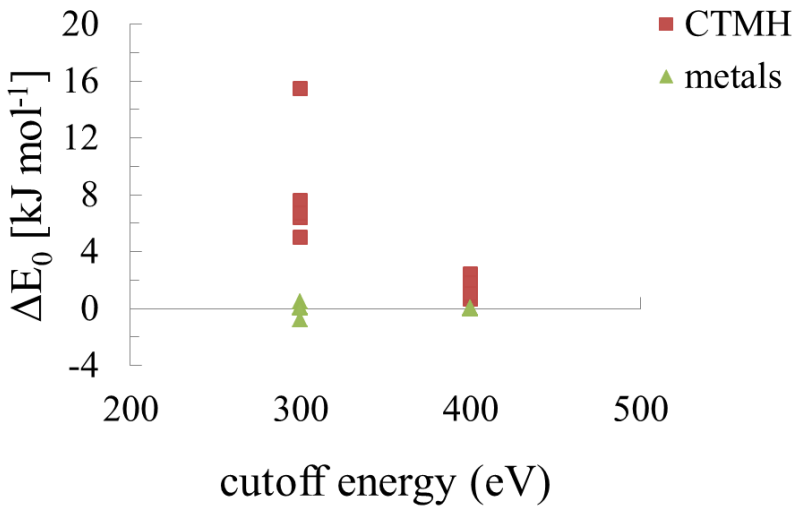

Figure 5.8: Convergence of test set relative to ground state energies obtained at a cutoff energy of 500 eV.

For each existing material, we performed spin-polarized DFT calculations for one step on the initial crystal structure, adopting high spin states for magnetic elements ferromagnetically.[56] In the style of Curtarolo et al., if after one step the magnetic moment was less than 0.025 μ_B/atom, indicating that the influence of spin polarity is negligible on the ground state energy, we turned spin off and relaxed the geometries as described above.[57] However, if the magnetic moment was greater than 0.025 μ_B/atom, we continued volume relaxations with spin-polarization activated. For computational speed, we make no attempt to search for antiferromagnetic ground states, particularly since most known

CTMHs are diagmagnetic. We did not perform DFT calculations with spin-polarization for proposed materials. However, interesting element spaces could be studied more rigorously if the magnetic properties were desired.

Phonon calculations were performed for materials in element spaces retained for Round 2 screening. Except where indicated, 2 × 2 × 2 supercells were adopted and *k*-points adjusted to maintain the same grid density. Hexagonal structures were studied in the rhombohedral settings following the guidelines of Parlinski.[58] We first relaxed volume, shape, and ion positions using the conjugate gradient method until forces on each atom were less than 10^{-4} eV $Å^{-1}$ and electronic steps were converged to within 10^{-7} eV. To determine $F^{vib}(T)$, we computed the VDOS for each compound within the harmonic approximation based on the supercell approach using a default atomic displacement of ± 0.01 Å.[59] Uniform *q*-point sampling meshes were used to sample the Fourier components of the dynamical matrix such that F^{vib} at 2000 K for each compound was converged to within 1 kJ mol^{-1}. Figure 5.9 shows the convergence of the vibrational free energy for Ca, Eu, CsH, NaH, and Yb_2RuH_6 with respect to supercell size. We find that 2 × 2 × 2 supercells are sufficient to converge $\Delta F^{vib}(T)$ for the pure metals and binary hydrides to within 1 kJ mol^{-1} 2000 K and 1 × 1 × 1 converges the CTMH to within 2 kJ mol^{-1} at 2000 K. We expect convergence is even better for the 2 × 2 × 2 supercell used in this work and expect that supercell size will not play a significant role in determining the relative stabilities of compounds in the studied element spaces.

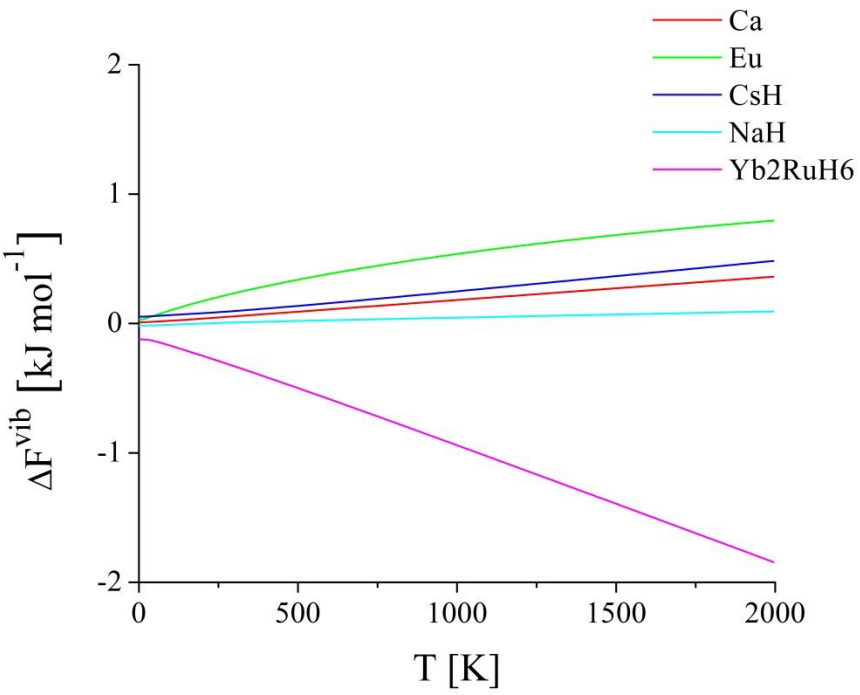

Figure 5.9: Convergence of vibrational Helmholtz free energy with respect to a $N \times N \times N$ supercell. $\Delta F^{vib} = (F^{vib}_{3 \times 3 \times 3} - F^{vib}_{2 \times 2 \times 2})$ for all materials except Yb_2RuH_6 for which $\Delta F^{vib} = (F^{vib}_{2 \times 2 \times 2} - F^{vib}_{1 \times 1 \times 1})$.

5.5 References

[1] K. Yvon and G. Renaudin, in *Encyclopedia of Inorganic Chemistry, Second Edition*, edited by B. R. King (John Wiley & Sons, Chichester, 2005), Vol. III, p. 1814.

[2] S. F. Parker, *Coord. Chem. Rev.* **254**, 215 (2010).

[3] K. Miwa, S. Takagi, M. Matsuo, and S. Orimo, *J. Phys. Chem. C* **117**, 8014 (2013).

[4] FIZ Karlsruhe and NIST, *THE INORGANIC CRYSTAL STRUCTURE DATABASE (ICSD)*.

[5] G. Bergerhoff and I. D. Brown, in *Crystallographic Databases*, edited by F. H. Allen, G. Bergerhoff and R. Severs (International Union of Crystallography, Chester, 1987).

[6] Y. Nakamori, K. Miwa, A. Ninomiya, H. Li, N. Ohba, S.-i. Towata, A. Züttel, and S.-i. Orimo, *Phys. Rev. B* **74**, 045126 (2006).

[7] K. Miwa, M. Aoki, T. Noritake, N. Ohba, Y. Nakamori, S. Towata, A. Züttel, and S. Orimo, *Phys. Rev. B* **74**, 155122 (2006).

[8] K. Miwa, N. Ohba, S. Towata, Y. Nakamori, A. Züttel, and S. Orimo, *J. Alloys Compd.* **446–447**, 310 (2007).

[9] S. V. Alapati, J. K. Johnson, and D. S. Sholl, *J. Phys. Chem. B* **110**, 8769 (2006).

[10] S. V. Alapati, J. K. Johnson, and D. S. Sholl, *Phys. Chem. Chem. Phys.* **9**, 1438 (2007).

[11] S. V. Alapati, J. K. Johnson, and D. S. Sholl, *J. Phys. Chem. C* **111**, 1584 (2007).

[12] S. V. Alapati, J. K. Johnson, and D. S. Sholl, *J. Phys. Chem. C* **112**, 5258 (2008).

[13] A. R. Akbarzadeh, V. Ozoliņš, and C. Wolverton, *Adv. Mater.* **19**, 3233 (2007).

[14] C. Wolverton and V. Ozoliņš, *Phys. Rev. B* **75**, 064101 (2007).

[15] C. Wolverton, J. S. Donald, A. R. Akbarzadeh, and V. Ozoliņš, *J. Phys. Condens. Matter* **20**, 064228 (2008).

[16] A. R. Akbarzadeh, C. Wolverton, and V. Ozolins, *Phys. Rev. B* **79**, 184102 (2009).

[17] V. Ozolins, A. R. Akbarzadeh, H. Gunaydin, K. Michel, C. Wolverton, and E. H. Majzoub, *J. Phys. Conf. Ser.* **180**, 012076 (2009).

[18] K. C. Kim and D. S. Sholl, *J. Phys. Chem. C* **114**, 678 (2009).

[19] K. C. Kim, A. D. Kulkarni, J. K. Johnson, and D. S. Sholl, *Phys. Chem. Chem. Phys.* **13**, 7218 (2011).

[20] K. C. Kim, A. D. Kulkarni, J. K. Johnson, and D. S. Sholl, *Phys. Chem. Chem. Phys.* **13**, 21520 (2011).

[21] E. H. Majzoub, F. Zhou, and V. Ozoliņš, *J. Phys. Chem. C* **115**, 2636 (2011).

[22] L. K. Wagner, E. H. Majzoub, M. D. Allendorf, and J. C. Grossman, *Phys. Chem. Chem. Phys.* **14**, 6611 (2012).

[23] K. J. Michel, A. R. Akbarzadeh, and V. Ozolins, *J. Phys. Chem. C* **113**, 14551 (2009).

[24] W. Yong-li, L. Shi, R. Li-jian, and W. Yuan-ming, *J. Phys. Condens. Matter* **22**, 175502 (2010).

[25] J. S. Hummelshøj, et al., *J. Chem. Phys.* **131** (2009).

[26] J. Chen, N. Kuriyama, Q. Xu, H. T. Takeshita, and T. Sakai, *J. Phys. Chem. B* **105**, 11214 (2001).

[27] D. Li, T. Zhang, S. Yang, Z. Tao, and J. Chen, *J. Alloys Compd.* **509**, 8228 (2011).

[28] B. Bogdanović, A. Reiser, K. Schlichte, B. Spliethoff, and B. Tesche, *J. Alloys Compd.* **345**, 77 (2002).

[29] L. George, V. Drozd, A. Durygin, J. Chen, and S. K. Saxena, *Int. J. Hydrogen Energy* **34**, 3410 (2009).

[30] J. A. Puszkiel, P. A. Larochette, and F. C. Gennari, *J. Alloys Compd.* **463**, 134 (2008).

[31] S. F. Parker, S. M. Bennington, A. J. Ramirez-Cuesta, G. Auffermann, W. Bronger, H. Herman, K. P. J. Williams, and T. Smith, *J. Am. Chem. Soc.* **125**, 11656 (2003).

[32] S. F. Parker, K. Refson, K. P. J. Williams, D. A. Braden, B. S. Hudson, and K. Yvon, *Inorg. Chem.* **45**, 10951 (2006).

[33] H. Kohlmann, R. O. Moyer Jr, T. Hansen, and K. Yvon, *J. Solid State Chem.* **174**, 35 (2003).

[34] R. O. Moyer Jr, S. M. Antao, B. H. Toby, F. G. Morin, and D. F. R. Gilson, *J. Alloys Compd.* **460**, 138 (2008).

[35] S. P. Ong, et al., *Comput. Mater. Sci.* **68**, 314 (2013).

[36] S. P. Ong, L. Wang, B. Kang, and G. Ceder, *Chem. Mater.* **20**, 1798 (2008).

[37] S. P. Ong, A. Jain, G. Hautier, B. Kang, and G. Ceder, *Electrochem. Commun.* **12**, 427 (2010).

[38] D. A. McQuarrie, *Statistical Mechanics* (University Science Books, Sausalito, California, 2000).

[39] D. A. McQuarrie and J. D. Simon, *Molecular Thermodynamics* (University Science Books, Sausalito, California, 1999).

[40] A. Gross and J. Scheffler, *J. Vac. Sci. Technol. A* **15**, 1624 (1997).

[41] M. W. Chase, Jr., ed., *NIST-JANAF Thermochemical Tables, Fourth Edition* (J. Phys. Chem. Ref. Data, Monograph 9, 1998).

[42] K. Puhakainen, E. Stoyanov, M. J. Evans, K. Leinenweber, and U. Haussermann, *J. Solid State Chem.* **183**, 1785 (2010).

[43] R. Shannon, *Acta Crystallogr.* **32**, 751 (1976).

[44] X. Ke, A. Kuwabara, and I. Tanaka, *Phys. Rev. B* **71**, 184107 (2005).

[45] V. Ozolins, E. H. Majzoub, and C. Wolverton, *Phys. Rev. Lett.* **100**, 135501 (2008).

[46] E. H. Majzoub and V. Ozoliņš, *Phys. Rev. B* **77**, 104115 (2008).

[47] G. Kresse and J. Hafner, *Phys. Rev. B* **47**, 558 (1993).

[48] G. Kresse and J. Hafner, *Phys. Rev. B* **49**, 14251 (1994).

[49] G. Kresse and J. Furthmüller, *Phys. Rev. B* **54**, 11169 (1996).

[50] G. Kresse and J. Furthmüller, *Comput. Mater. Sci.* **6**, 15 (1996).

[51] D. S. Sholl and J. A. Steckel, *Density Functional Theory: A Practical Introduction* (John Wiley & Sons, Hoboken, 2009).

[52] P. E. Blöchl, *Phys. Rev. B* **50**, 17953 (1994).

[53] G. Kresse and D. Joubert, *Phys. Rev. B* **59**, 1758 (1999).

[54] J. P. Perdew, J. A. Chevary, S. H. Vosko, K. A. Jackson, M. R. Pederson, D. J. Singh, and C. Fiolhais, *Phys. Rev. B* **46**, 6671 (1992).

[55] G. Kresse, M. Marsman, and J. Furthmüller, Vienna, 2014).

[56] A. Jain, G. Hautier, C. J. Moore, S. Ping Ong, C. C. Fischer, T. Mueller, K. A. Persson, and G. Ceder, *Comput. Mater. Sci.* **50**, 2295 (2011).

[57] S. Curtarolo, et al., *Comput. Mater. Sci.* **58**, 218 (2012).

[58] K. Parlinski, Software *PHONON*, 2005.

[59] A. Togo, F. Oba, and I. Tanaka, *Phys. Rev. B* **78**, 134106 (2008).

CHAPTER 6

SCREENING OF EXISTING CTMHs FOR NGNP APPLICATION - RESULTS*

Using computational tools, our aim in Chapter 6 is to identify known or "existing" CTMH candidate materials that have enhanced stability with respect to the binary hydrides that form from the constituent metals, $T_d/T_{d,binary} \geq 1$, and that release hydrogen at high temperature, $T_d \geq 1000$ K. The screening methods and computational details for these results were described in Chapter 5.

6.1 Round 1 Structure Relaxation

Crystal structures for >260 materials (breakdown summarized in Table 5.1) were relaxed with moderate force and electronic energy convergence thresholds to obtain ground state DFT energies. The DFT relaxed structural parameters as well as the experimental values for these materials are available in Table C.1 in the Appendix. Figures 6.1 and 6.2 present a comparison of the predicted and experimental unit cell volumes. In general, the overall agreement is good, as expected. For the metals, binary intermetallics, and ternary hydrides, more than 85% of DFT-predicted volumes are within 5% of the experimental reference. The agreement is somewhat deteriorated for the binary hydrides with 85% of 23 DFT-predicted volumes within 9% of the experimental reference. However, previous calculations have shown that DFT using Perdew-Wang GGA functionals like those utilized in this chapter tend to predict the enthalpies of

*Reproduced in part with permission from Inorg. Chem., submitted for publication. Unpublished work copyright 2014 American Chemical Society.

formation for binary hydrides to within a typical accuracy of 10-20 kJ mol^{-1} H_2, which we expect to be sufficient for our screening purposes.[1,2]

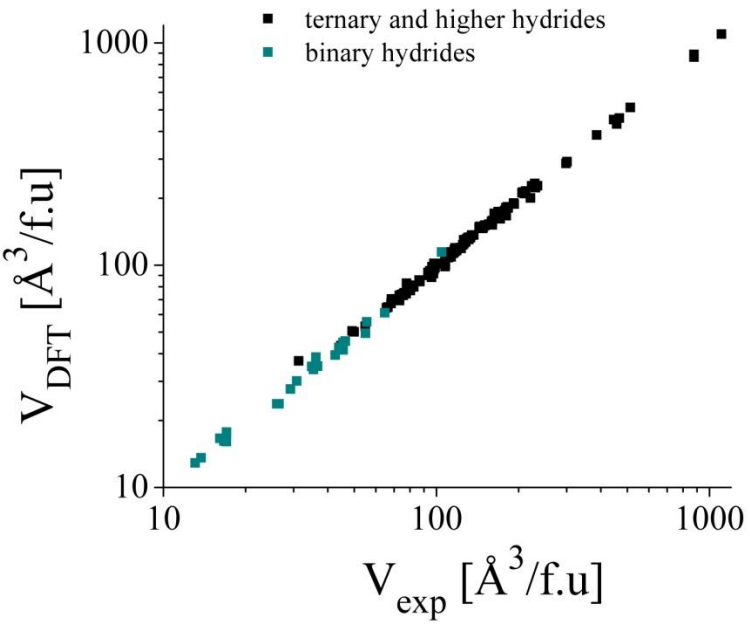

Figure 6.1: Comparison of the experimental and relaxed DFT volumes for the known complex transition metal hydrides, saline hydrides, and binary hydrides studied at the Round 1 level of screening.

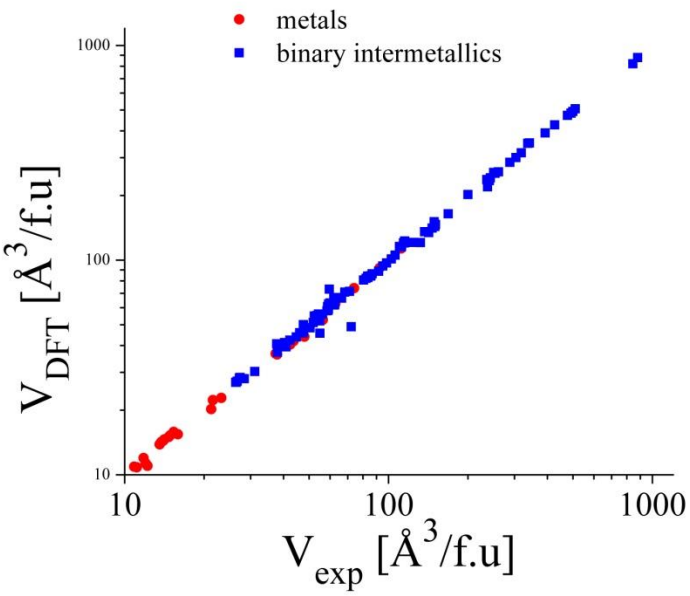

Figure 6.2: Comparison of the experimental and relaxed DFT volumes for the metals and binary intermetallics studied at the Round 1 level of screening.

There are several compounds for which the experimental and our DFT-predicted volumes differ by more than ~10%. For these, we compare our predicted structures with structures calculated by the Materials Project (MP),[3,4] an online database of over 80,000 materials with properties based on high-throughput DFT calculations. The DFT calculation details of this work and the current MP are not identical and not all of the compounds considered in this screening are included in the MP database. However, the MP provides a good check for consistency at least within DFT GGA methods. The materials for which predicted and experimental volumes vary by more than ~10% are listed in Table 6.1.

Table 6.1: Comparison of unit cell volumetric errors (with respect to the experimental reference) obtained using DFT with Round 1 [Round 2] convergence criteria for this work and the Materials Project DFT-based materials database.

material	this work (%)	Materials Project (%)
Mn	-9.8	7.4
Yb_3H_8	9.5 [8.8]	13.1
Ni_2H	-10.4 [-11.6]	-11
RbH	-10.2 [<2]	0.01
SrH_2	-8.8 [~3]	-1.5
MgSr	22.7	23.4
Cs_3MnH_5	-9.3	1.8
$EuFe_2$	-32.3	no entry
$EuNi_2$	-17.0	no entry
LiPdH	18.4	no entry

Continued relaxation of the unit cells for RbH and SrH_2 to the higher convergence criteria required for Round 2 phonon calculations brings the predicted DFT volumes into line with those predicted by the MP and experiment. However, continued relaxations do not improve agreement for Yb_3H_8 or Ni_2H, but errors relative to the experimental volumes are roughly the same for this work as in the MP. These binary hydrides are not critical to the screening of high temperature CTMHs since both materials decompose at low temperatures. While our calculations do obtain agreement with the MP for the ground state magnetic moments of pure Fe, Co, and Ni, the DFT methods used here do not rigorously search for the optimal spin state of magnetic materials in general, which could account for the disagreement in the case of $EuFe_2$ and $EuNi_2$.Our calculations fail to predict the same magnetic ground state for Mn and Cs_3MnH_5 as predicted with the MP, which likely accounts for underestimation of the predicted volumes. Therefore, heats of formation for reactions with Mn-based compounds may have larger errors than otherwise expected. If potentially interesting ternary hydrides of Eu-Fe, Eu-Ni, or Cs-Mn are

identified, more detailed DFT methods could be used to obtain global magnetic ground state of these materials to improve estimates of the CTMH relative stability.[5] Reasons for the discrepancy in the DFT-predicted and experimental LiPdH are not immediately apparent. As an additional check, we relaxed the experimental structure allowing only the atom positions to move while maintaining the unit cell volume and also relaxed the DFT-predicted structure allowing all degrees of freedom to change such that forces on each atom were less than 10^{-4} eV Å and the electronic energy steps were converged to 10^{-7} eV, two high accuracy conditions. The DFT-predicted structure is 0.84 eV lower in energy than the experimental structure indicating that the DFT structure is a more likely stable state.

6.2 Round 1 Thermodynamic Stability

We predicted phase diagrams at P = 1 bar H_2 for $0 \leq T$ (K) ≤ 2000 for the 72 element spaces in Figure 5.3 using Eq. (5.7), ignoring vibrational contributions to the free energies of solid phases. In lieu of presenting each individual diagram, Table 6.2 lists the decomposition (dehydrogenation) reactions for each metal hydride that is predicted to form within the conditions studied, the temperature of release, and the enthalpy of reaction approximated by ΔE_0, again ignoring zero point vibrational energies. For comparison, available experimental data for the binary hydrides is presented in Table 6.3. We see that the DFT, even based on ground state energies alone, separates the binary hydrides into high and low temperature materials, although the relative stabilities of some materials are not reproduced exactly. In a similar fashion, it is expected that the DFT calculations can separate the ternary and higher CTMH with reasonable fidelity.

In Table 6.2, 10 of the top 11 most thermodynamically stable CTMHs crystallize in the 2-Sr_2RuH_6 cubic crystal structure with metal cations that form very strong binary hydrides. Additionally, of the top 11 most thermodynamically stable CTMHs, only the Yb-Ru-H and Eu-Fe-H systems have a single binary intermetallic in the accompanying phase spaces. The presence of stable intermetallic phases tends to destabilize ternary hydrides.

Table 6.2: Round 1 metal hydride decomposition reactions, hydrogen release temperatures for 1 bar H_2, $T_{d,}$(K), and ground state reaction energies (kJ mol^{-1} H_2).

metal hydride	T_d	Decomposition Reaction	ΔE_0
		binary hydrides	
SrH_2	1545	$SrH_2 \leftrightarrow Sr + H_2$	203.3
EuH_2	1485	$EuH_2 \leftrightarrow Eu + H_2$	193.2
YbH_2	1440	$YbH_2 \leftrightarrow Yb + H_2$	169.1
CaH_2	1380	$CaH_2 \leftrightarrow Ca + H_2$	175.1
LiH	1350	$2\ LiH \leftrightarrow 2Li + H_2$	168.7
LaH_3	1260	$^2/_3\ LaH_3 \leftrightarrow {}^2/_3\ La + H_2$	154.2
BaH_2	1140	$BaH_2 \leftrightarrow Ba + H_2$	150.6
KH	855	$2\ KH \leftrightarrow 2K + H_2$	86.6
NaH	855	$2\ NaH \leftrightarrow 2Na + H_2$	85.5
MgH_2	720	$MgH_2 \leftrightarrow Mg + H_2$	64.5
RbH	600	$2\ RbH \leftrightarrow 2Rb + H_2$	45.8
CsH	585	$2\ CsH \leftrightarrow 2Cs + H_2$	43.0
PdH	465	$2\ PdH \leftrightarrow 2Pd + H_2$	25.2
NiH	420	$2\ NiH \leftrightarrow 2Ni + H_2$	19.6
RhH	120	$2\ RhH \leftrightarrow 2Rh + H_2$	-18.4
		complex transition metal hydrides	
Eu_2RuH_6	1530	$⅓\ Eu_2RuH_6 \leftrightarrow {}^2/_3\ Eu + ⅓\ Ru + H_2$	200.7
Yb_2RuH_6	1500	$⅓\ Yb_2RuH_6 \leftrightarrow ⅓\ Ru + {}^2/_3\ Yb + H_2$	196.8
Ca_2OsH_6	1425	$⅓\ Ca_2OsH_6 \leftrightarrow {}^2/_3\ Ca + ⅓\ Os + H_2$	183.8
Ca_2RuH_6	1425	$⅓\ Ca_2RuH_6 \leftrightarrow {}^2/_3\ Ca + ⅓\ Ru + H_2$	183.5
Sr_2RuH_6	1350	$Sr_2RuH_6 \leftrightarrow Ru + 2SrH_2 + H_2$	170.1
Sr_2OsH_6	1335	$Sr_2OsH_6 \leftrightarrow Os + 2SrH_2 + H_2$	165.8
Ba_2RuH_6	1305	$⅓\ Ba_2RuH_6 \leftrightarrow {}^2/_3\ Ba + ⅓\ Ru + H_2$	161.2
Eu_2FeH_6	1305	$Eu_2FeH_6 \leftrightarrow 2EuH_2 + Fe + H_2$	161.5
Ba_2OsH_6	1275	$⅓\ Ba_2OsH_6 \leftrightarrow ⅓Os + {}^2/_3\ Ba + H_2$	155.6
$Ba_3Ir_2H_{12}$	1275	$^1/_6\ Ba_3Ir_2H_{12} \leftrightarrow ⅓Ir + ½\ Ba + H_2$	157.1
Sr_2FeH_6	1245	$Sr_2FeH_6 \leftrightarrow Fe + 2SrH_2 + H_2$	151.2
K_2PtH_4	1215	$½\ K_2PtH_4 \leftrightarrow ½\ Pt + K + H_2$	145.9
$Ca_8Rh_6H_{24}$	1200	$^1/_7\ Ca_8Rh_6H_{24} \leftrightarrow {}^3/_7\ CaRh_2 + {}^5/_7\ CaH_2 + H_2$	143.3
Na_2PdH_2	1185	$Na_2PdH_2 \leftrightarrow Pd + 2Na + H_2$	140.6
Rb_2PtH_4	1185	$½\ Rb_2PtH_4 \leftrightarrow ½\ Pt + Rb + H_2$	141.0
Cs_2PtH_4	1170	$½\ Cs_2PtH_4 \leftrightarrow ½\ Cs_2Pt + H_2$	138.8
Li_3RhH_4	1110	$Li_3RhH_4 \leftrightarrow 2LiH + LiRh + H_2$	127.5
Na_3IrH_6	1110	$⅓\ Na_3IrH_6 \leftrightarrow Na + ⅓Ir + H_2$	128.5
Li_3IrH_6	1065	$½\ Li_3IrH_6 \leftrightarrow ½\ IrLi + LiH + H_2$	121.2
Li_4OsH_6	1065	$Li_4OsH_6 \leftrightarrow 4LiH + Os + H_2$	119.9

Table 6.2 (Continued).

$CaNiH_3$	1050	$^6/_5\ CaNiH_3 \leftrightarrow {}^4/_5\ CaH_2 + {}^2/_5\ CaNi_3 + H_2$	117.4
K_3PdH_3	1035	$^2/_3\ K_3PdH_3 \leftrightarrow {}^2/_3\ Pd + 2K + H_2$	114.8
Na_3RhH_6	1020	$⅓\ Na_3RhH_6 \leftrightarrow ⅓Rh + Na + H_2$	112.5
$SrMgNiH_4$	1020	$SrMgNiH_4 \leftrightarrow SrH_2 + ⅓Mg_2Ni + ⅓MgNi_2 + H_2$	112.4
$BaMg_2OsH_8$	1005	$^2/_5\ BaMg_2OsH_8 \leftrightarrow {}^4/_5\ Mg + {}^1/_5Ba_2OsH_6 + {}^1/_5Os + H_2$	111.2
Cs_3PdH_3	1005	$^2/_3\ Cs_3PdH_3 \leftrightarrow {}^2/_3\ Pd + 2Cs + H_2$	109.6
Sr_2PdH_4	1005	$Sr_2PdH_4 \leftrightarrow SrH_2 + PdSr + H_2$	111.3
$Yb_4Mg_4Fe_3H_{22}$	1005	$^1/_7Yb_4Mg_4Fe_3H_{22} \leftrightarrow {}^4/_7Mg + {}^3/_7\ Fe + {}^4/_7YbH_2 + H_2$	111.5
Ba_2PdH_4	975	$Ba_2PdH_4 \leftrightarrow BaPd + BaH_2 + H_2$	106.1
$BaMg_2FeH_8$	975	$^{17}/_{55}\ BaMg_2FeH_8 \leftrightarrow {}^{17}/_{55}\ Fe + {}^2/_{55}\ Ba_2Mg_{17} + {}^{13}/_{55}\ BaH_2 + H_2$	104.9
$Ca_4Mg_4Fe_3H_{22}$	975	$^1/_7\ Ca_4Mg_4Fe_3H_{22} \leftrightarrow {}^3/_7\ Fe + {}^4/_7\ Mg + {}^4/_7\ CaH_2 + H_2$	105.1
$EuMgNiH_4$	960	$EuMgNiH_4 \leftrightarrow ⅓Mg_2Ni + ⅓MgNi_2 + EuH_2 + H_2$	103.8
Mg_2OsH_6	960	$⅓\ Mg_2OsH_6 \leftrightarrow ⅓Os + {}^2/_3\ Mg + H_2$	103.9
Na_2PtH_4	960	$½\ \ Na_2PtH_4 \leftrightarrow 0.25NaPt_2 + 0.75Na + H_2$	102.8
Rb_3PdH_3	960	$^2/_3\ \ Rb_3PdH_3 \leftrightarrow 2Rb + {}^2/_3\ Pd + H_2$	102.8
$BaMg_2RuH_8$	945	$^2/_5\ BaMg_2RuH_8 \leftrightarrow {}^1/_{10}Mg_3Ru_2 + ½\ Mg + {}^1/_5\ Ba_2RuH_6 + H_2$	100.5
Mg_2RuH_4	945	$½\ \ Mg_2RuH_4 \leftrightarrow {}^1/_4\ Mg_3Ru_2 + {}^1/_4\ Mg + H_2$	101.2
Na_4RuH_6	945	$⅓\ Na_4RuH_6 \leftrightarrow ⅓Ru + {}^4/_3\ Na + H_2$	101.9
Cs_2PdH_4	930	$Cs_2PdH_4 \leftrightarrow {}^2/_3\ Cs_3PdH_3 + ⅓Pd + H_2$	97.5
K_2PdH_4	930	$K_2PdH_4 \leftrightarrow {}^2/_3\ K_3PdH_3 + ⅓Pd + H_2$	97.6
$LiMg_2OsH_7$	930	$2LiMg_2OsH_7 \leftrightarrow {}^3/_2Mg_2OsH_6 + Mg + ½Li_4OsH_6 + H_2$	97.9
$LiMg_4Os_2H_{13}$	930	$2\ LiMg_4Os_2H_{13} \leftrightarrow {}^7/_2\ Mg_2OsH_6 + Mg + ½\ Li_4OsH_6 + H_2$	98.5
Rb_2PdH_4	930	$Rb_2PdH_4 \leftrightarrow {}^2/_3\ Rb_3PdH_3 + ⅓Pd + H_2$	99.3
Sr_2PtH_6	930	$^4/_9\ Sr_2PtH_6 \leftrightarrow {}^1/_9\ Pt_4Sr_5 + ⅓SrH_2 + H_2$	98.2
$SrMg_2FeH_8$	930	$^2/_5\ SrMg_2FeH_8 \leftrightarrow {}^1/_5\ Sr_2FeH_6 + {}^1/_5\ Fe + {}^4/_5\ Mg + H_2$	98.4
Ba_2PtH_6	900	$½\ \ Ba_2PtH_6 \leftrightarrow ½\ BaPt + ½\ BaH_2 + H_2$	94.4
Mg_2FeH_6	900	$⅓\ Mg_2FeH_6 \leftrightarrow {}^2/_3\ Mg + ⅓Fe + H_2$	92.9
Cs_2ZnH_4	885	$½\ \ Cs_2ZnH_4 \leftrightarrow ½\ Zn + Cs + H_2$	90.7
Li_2PdH_2	885	$2\ Li_2PdH_2 \leftrightarrow 2LiH + 2LiPd + H_2$	98.1
Na_3OsH_7	885	$^2/_7\ Na_3OsH_7 \leftrightarrow {}^6/_7\ Na + {}^2/_7\ Os + H_2$	90.8
Yb_2FeH_6	885	$Yb_2FeH_6 \leftrightarrow Fe + 2YbH_2 + H_2$	90.1
$NaBaPdH_3$	870	$^6/_5NaBaPdH_3 \leftrightarrow {}^6/_5Na + {}^2/_5Ba_2PdH_4 + {}^2/_5BaPd_2 + H_2$	89.5
$EuPdH_3$	855	$EuPdH_3 \leftrightarrow ½\ EuPd_2 + ½\ EuH_2 + H_2$	84.9
Mg_2CoH_5	855	$^2/_5\ Mg_2CoH_5 \leftrightarrow {}^1/_5\ Co_2Mg + {}^3/_5\ Mg + H_2$	86.5
Mg_3ReH_7	855	$^2/_7\ Mg_3ReH_7 \leftrightarrow {}^6/_7\ Mg + {}^2/_7\ Re + H_2$	85.4
$NaPd_3H_2$	855	$2\ NaPd_3H_2 \leftrightarrow 5Pd + Na_2PdH_2 + H_2$	86.5
$YbMgNiH_4$	855	$YbMgNiH_4 \leftrightarrow ⅓MgNi_2 + ⅓Mg_2Ni + YbH_2 + H_2$	84.9
Li_2PtH_2	840	$Li_2PtH_2 \leftrightarrow Li_2Pt + H_2$	84.4
Li_4RuH_6	840	$Li_4RuH_6 \leftrightarrow Ru + 4LiH + H_2$	83.7

Table 6.2 (Continued).

Mg_3MnH_7	840	$^{2}/_{7}\ Mg_3MnH_7 \leftrightarrow {}^{2}/_{7}\ Mn + {}^{6}/_{7}\ Mg + H_2$	84.3
Rb_2ZnH_4	840	$½\ \ Rb_2ZnH_4 \leftrightarrow {}^{1}/_{26}\ RbZn_{13} + {}^{25}/_{26}\ \ Rb + H_2$	82.9
$CaMgNiH_4$	825	$CaMgNiH_4 \leftrightarrow ⅓Mg_2Ni + CaH_2 + ⅓MgNi_2 + H_2$	81.7
K_2ZnH_4	825	$^{26}/_{27}\ K_2ZnH_4 \leftrightarrow {}^{50}/_{27}\ KH + {}^{2}/_{27}\ KZn_{13} + H_2$	81.9
Li_3RhH_6	795	$Li_3RhH_6 \leftrightarrow Li_3RhH_4 + H_2$	76.2
Ca_2FeH_6	765	$Ca_2FeH_6 \leftrightarrow 2CaH_2 + Fe + H_2$	72.2
K_2PtH_6	765	$K_2PtH_6 \leftrightarrow K_2PtH4 + H_2$	70.6
Cs_2PtH_6	750	$Cs_2PtH_6 \leftrightarrow Cs_2PtH4 + H_2$	68.0
K_2ReH_9	750	$^{2}/_{7}\ K_2ReH_9 \leftrightarrow {}^{4}/_{7}\ KH + {}^{2}/_{7}\ Re + H_2$	69.8
Rb_2PtH_6	750	$Rb_2PtH_6 \leftrightarrow Rb_2PtH_4 + H_2$	70.1
Rb_3ZnH_5	750	$2\ Rb_3ZnH_5 \leftrightarrow 2Rb_2ZnH_4 + 2Rb + H_2$	69.7
Cs_3ZnH_5	735	$2\ Cs_3ZnH_5 \leftrightarrow 2Cs_2ZnH_4 + 2Cs + H_2$	67.8
$LiMg_2RuH_7$	735	$LiMg_2RuH_7 \leftrightarrow LiH + Mg_2RuH_4 + H_2$	67.3
Cs_3CdH_5	720	$^{2}/_{5}\ Cs_3CdH_5 \leftrightarrow {}^{76}/_{65}\ Cs + {}^{2}/_{65}\ Cd_{13}Cs + H_2$	64.7
Mg_2NiH_4	720	$½\ \ Mg_2NiH_4 \leftrightarrow ½\ Mg_2Ni + H_2$	64.5
Mg_2RuH_6	720	$Mg_2RuH_6 \leftrightarrow Mg_2RuH_4 + H_2$	64.0
$KNaReH_9$	705	$^{4}/_{7}KNaReH_9 \leftrightarrow {}^{4}/_{7}NaH + {}^{2}/_{7}K_2ReH_9 + {}^{2}/_{7}Re + H_2$	61.7
Na_2PtH_6	690	$Na_2PtH_6 \leftrightarrow Na_2PtH4 + H_2$	59.8
Rb_3PdH_5	690	$2\ Rb_3PdH_5 \leftrightarrow 2Rb + 2Rb_2PdH_4 + H_2$	59.9
Cs_3PdH_5	675	$2\ Cs_3PdH_5 \leftrightarrow 2Cs_2PdH_4 + 2Cs + H_2$	57.9
$La_{16}Mg_8Ni_{16}H_{64}$	675	$^{1}/_{8}\ La_{16}Mg_8Ni_{16}H_{64} \leftrightarrow 2LaH_3 + MgNi_2 + H_2$	57.5
K_2TcH_9	660	$^{2}/_{7}\ K_2TcH_9 \leftrightarrow {}^{4}/_{7}\ KH + {}^{2}/_{7}Tc + H_2$	55.6
Na_3RuH_7	630	$^{4}/_{5}\ Na_3RuH_7 \leftrightarrow {}^{3}/_{5}\ Na_4RuH_6 + {}^{1}/_{5}\ Ru + H_2$	51.5
$BaReH_9$	615	$^{2}/_{7}\ BaReH_9 \leftrightarrow {}^{2}/_{7}\ Re + {}^{2}/_{7}\ BaH_2 + H_2$	47.1
$Li_5Pt_2H_9$	615	$½\ Li_5Pt_2H_9 \leftrightarrow Li_2PtH_2 + ½\ LiH + H_2$	48.1
Na_2PdH_4	585	$Na_2PdH_4 \leftrightarrow Na_2PdH_2 + H_2$	43.7
$Ba_7Cu_3H_{17}$	570	$^{2}/_{3}\ Ba_7Cu_3H_{17} \leftrightarrow {}^{14}/_{3}\ BaH_2 + 2Cu + H_2$	41.2
$La_2Ni_10H_{14}$	570	$^{1}/_{7}\ La_2Ni_{10}H_{14} \leftrightarrow {}^{2}/_{7}\ LaNi_5 + H_2$	40.6
Li_2PtH_6	555	$½\ Li_2PtH_6\_p \leftrightarrow ½\ Li_2PtH_2 + H_2$	38.8
		ternary alkaline earth (saline) metal hydrides	
Ba_2MgH_6	960	$^{17}/_{19}\ Ba_2MgH_6 \leftrightarrow {}^{32}/_{19}\ BaH_2 + {}^{1}/_{19}\ Ba_2Mg_{17} + H_2$	104.2
$MgSr_2H_6$	930	$MgSr_2H_6 \leftrightarrow 2SrH_2 + Mg + H_2$	98.2
Eu_2MgH_6	870	$Eu_2MgH6 \leftrightarrow 2EuH_2 + Mg + H_2$	88.1
$Ba_6Mg_7H_{26}$	840	$^{1}/_{4}\ Ba_6Mg_7H_{26} \leftrightarrow Mg + {}^{3}/_{4}\ Ba_2MgH_6 + H_2$	82.5
$SrMgH_4$	840	$2\ SrMgH_4 \leftrightarrow Mg + MgSr_2H_6 + H_2$	84.5
$Ba_2Mg_3H_{10}$	795	$^{3}/_{2}\ Ba_2Mg_3H_{10} \leftrightarrow ½Ba_6Mg_7H_{26} + Mg + H_2$	75.3
$EuMg_2H_6$	795	$^{2}/_{3}\ EuMg_2H_6 \leftrightarrow {}^{1}/_{3}\ Eu_2MgH_6 + Mg + H_2$	76.4
$Mg_8Yb_{19}H_{54}$	750	$^{1}/_{8}\ Mg_8Yb_{19}H_{54} \leftrightarrow Mg + {}^{19}/_{8}\ YbH_2 + H_2$	69.3
$Ca_{19}Mg_8H_{54}$	735	$^{1}/_{8}\ Ca_{19}Mg_8H_{54} \leftrightarrow Mg + {}^{19}/_{8}\ CaH_2 + H_2$	66.9
$LaMg_2H_7$	735	$½\ LaMg_2H_7 \leftrightarrow ½LaH_3 + Mg + H_2$	66.8

Table 6.3: Decomposition reaction enthalpies and decomposition temperatures for binary hydrides studied in this work from experimental sources. Note: experimentally-reported values refer to heats of formation. Sign has been reversed in this table to reflect the hydrogen release reaction. melting point (m.p), liquid phase(ℓ).

Binary Hydride	T_d (K)	$\Delta H°$ [kJ mol^{-1} H_2]	$\Delta H(T)$ [kJ mol^{-1} H_2]	T(K)
YbH_2		182[b]		
LiH	993[a] ~1145[d,f]	180[b] 190[d]	194 (ℓ)[b,d] 144 (ℓ) [b,d]	< 967 > 967
BaH_2	948[a] m.p1473	177[a]		
LaH_2			208	600 ─ 1150
SrH_2	948[a] m.p1323[g]	180.3[a] 184[b]	200[b]	... ─1273
CaH_2	873[a] 1347[f] m.p1273	181.5[a] 188[b]	170[b]	1053 ─1173
NaH	~698[a,f]	113[a] 112[b]	106 (ℓ)[b]	380 ─ 670
KH	690[a]	115.4[a] 116[b]	112 [b]	561 ─688
CsH	662[c] 443[a]	113[c] 108.4[a]	112 (ℓ)[b]	518 ─651
RbH	636[e] 443[a]	108.8[e] 104.6[a]	108 (ℓ)[b]	519 ─ 623
MgH_2	603[b] 560[f]	75.3[a]	74[b]	713 ─ 833
$PdH_{0.6}$	298[a]	40[b]		
$NiH_{0.5}$		6[b]		
$RhH_{0.5}$		-20[b]		

[a] Grochala and Edwards 2004[6]
[b] Griessen and Riesterer 1988[7]
[c] Sangster and Pelton 1994[8]
[d] Veleckis 1979[9]
[e] Sangster and Pelton 1994[10]
[f] Orecchini and Naso 2012[11]
[g] CRC Handbook[12]

Figures 6.3 and 6.4 map each CTMH and ternary alkaline earth (saline) hydride based on the screening criterion. Along the vertical axis, decomposition temperatures are normalized by the most stable binary hydride that forms in a given element space, and materials normalized by the same binary hydride appear to form lines. Of the 102 CTMHs, 40 ternary hydrides have $T_d/T_{d,binary} \geq 1$ with 15 of these releasing H_2 at temperatures greater than 1000 K. No quaternary or ternary alkaline earth (saline) hydrides were predicted to have this enhanced stability relative to the binary hydrides. The most stable quaternary hydride of those studied is $SrMgNiH_4$, which decomposes to a mixture of the binary hydride SrH_2 and Mg-Ni intermetallics. Overall, we retain 31 of the original 72 element spaces for Round 2 screening, summarized in Figure 6.5. Although Mg_3MnH_7 is predicted to have a modest enhanced stability factor of ~1.17, we do not study this element space at the higher level of theory due to the computational expense of searching for appropriate ground state spin states.

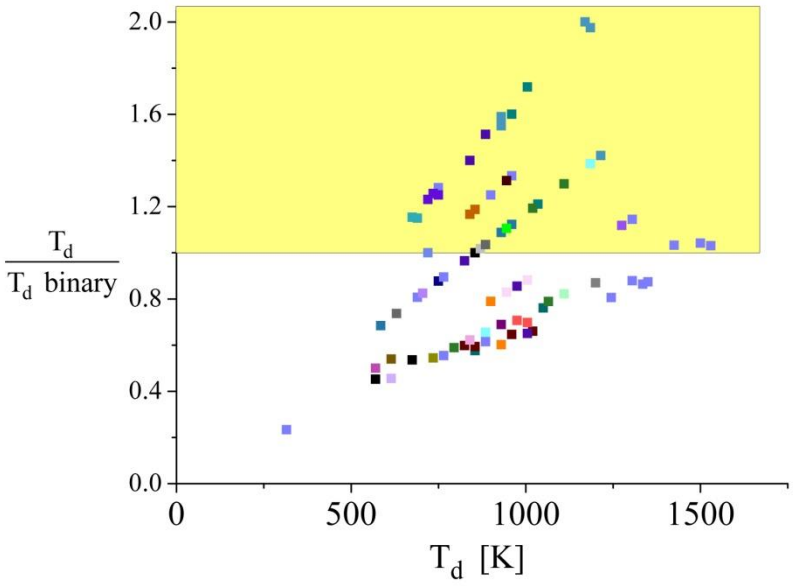

Figure 6.3: Relative and absolute thermal stabilities for existing ternary and quaternary CTMH predicted with Round 1 level of screening. Color indicates structure prototype.

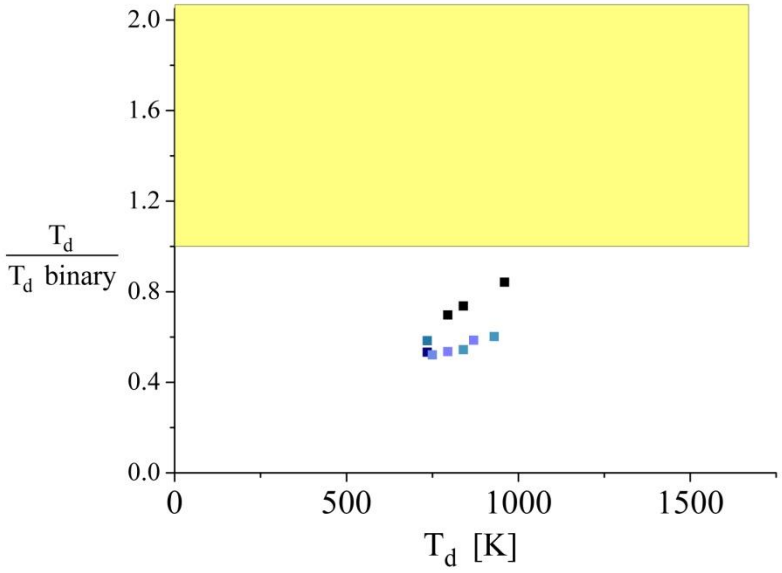

Figure 6.4: Relative and absolute thermal stabilities for existing M_i-Mg-H ternary alkaline earth (saline) hydrides predicted with Round1 level of screening. Color mapping indicates M_i cation.

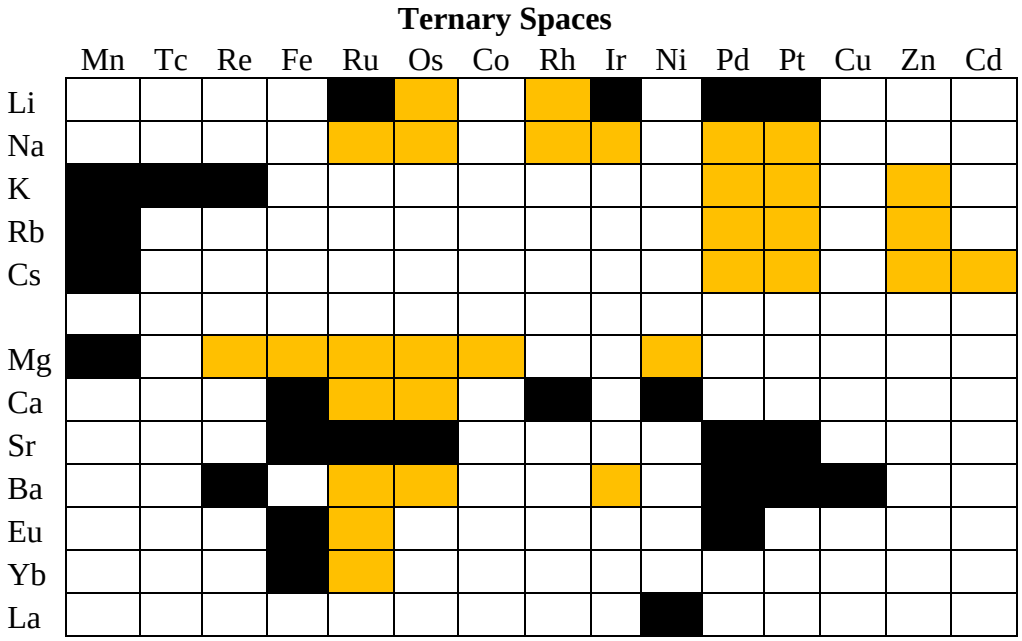

Figure 6.5: Mapping of ternary *M*-*Tr*-H element spaces retained (orange) and rejected (black) for Round 2 screening.

Table 6.4 lists the experimentally-observed compounds that were not predicted to be thermodynamically stable based on Round 1 GCLP minimizations along with the energy above the convex hull for each phase. A positive convex hull energy describes the decomposition energy of a given phase into the thermodynamically-preferred mixture of adjacent phases. A small value indicates that the phase is in close competition with another set of stable materials. Materials that appear in Table 6.4 may be dynamically stabilized through vibrational or kinetic effects. In general, pressure effects are small for condensed phases, but our calculations do not capture materials that are only thermodynamically stable at high pressures. However, the largest source of error in the calculation of energies results from the inability of the GGA pseudopotential to exactly describe exchange-correlation effects, which is an unavoidable consequence of DFT calculations. In Table 6.4, the binary hydrides CuH, Ni-H, and MnH form only very weak

hydrides experimentally and will not affect the screening of desirable materials. For the Yb-H and La-H spaces, more stable binary hydride phases than those listed in table 6.4 are predicted to be stable and are used in screening. 7 of the 12 ternary CTMHs not predicted to form in Round 1 screening will be subsequently studied at the Round 2 level of theory due to the presence of a stable candidate material that meets the screening criterion that forms in the element spaces: H and K−Zn, K−Pt, K−Pd, Cs−Pt, Rb−Pt, and Li−Rh. Of these 7 CTMHs, 5 are predicted to be dynamically stabilized through vibrational effects at the higher level of theory. While it is possible that our screening methodology may overlook some materials that are stabilized through vibrational or finite temperature contributions to the free energy, only the Eu-Pd and Li-Pd systems might contain ternary hydride that operates at the high temperatures of the NGNP and that is more stable than the corresponding binary hydride

Table 6.4: Existing compounds predicted not to be thermodynamically favored based on Round 1 ground state calculations and energies above the stable convex hull.

material	energy above convex hull (eV atom^{-1})	material	energy above convex hull (eV atom^{-1})
K_3ZnH_5	1.5E-04	YbH_2_	0.180
$LiMg_4Ru_2H_{13}$	3.4E-04	Eu_2PdH_4	0.201
$LaMg_2NiH_7$	8.5E-04	Cs_3PtH_5	0.233
$Mg_3Sr_2H_{10}$	9.1E-03	Rb_3PtH_5	0.240
$Ca_4Mg_3H_{14}$	5.6E-03	K_3PtH_5	0.273
$Mg_7Sr_6H_{26}$	0.012	Li_4RhH_5	0.333
$BaMgH_4$	0.013	Yb_3H_8	0.349
K_3PdH_5	0.016	LiPdH	0.375
$Yb_4Mg_3H_{14}$	0.017	Cs_3MnH_5	0.394
$EuMgH_4$	0.027	Li_4RhH_4	0.415
$Eu_6Mg_7H_{26}$	0.046	MnH	0.649
K_3MnH_5	0.050	K_3ReH_6	1.070
$Eu_2Mg_3H_{10}$	0.059	LaH_2	1.151
CuH	0.099	YbH_3	1.159
Ni_2H	0.15	Rb_3MnH_5	1.470
Ni_2H_	0.15		

6.3 Round 2 Final Candidates

Based on the results from Round 1, we computed vibrational densities of states for 106 solids including 24 metals, 16 binary hydrides, 12 intermetallics, and 53 ternary CTMHs listed with the relaxed structural parameters in Table C.2 in the Appendix. We include high temperature phases for Ca and Yb, subsequently listed as Ca_HT and Yb_. 1 × 1 × 1 supercells were used for Cs_3PdH_3 and Rb_3PdH_3 due to the prohibitive computational expense of computing vibrational properties for the 2 × 2 × 2 supercell. Similarly, spin polarization was turned off for magnetic Mg_2Co and MgCo. Based on Round 1 calculations, spin polarization was not required for the CTMHs studied at the Round 2 level of theory. Spin polarization was turned on for Co, Fe, Ni, Pd, Ni_2H and RhH.

We predicted phase diagrams using Eq. (5.5) for P = 1 bar H_2 and $0 \leq T$ (K) $\leq$ 2000, accounting for the vibrational Helmholtz free energy of the condensed phases. This constitutes our best estimate of the relative and absolute thermodynamic stabilities of candidate CTMHs. The stabilities of the 51 stable CTMHs are shown in Figure 6.6. Only Li_4RhH_5, Rb_3PdH_3, and Rb_3PtH_5 are not predicted to form at any temperature. In each of these element spaces, a stable CTMH of a different composition forms. As shown in Figure 6.6, 13 CTMHs meet both screening criterion, i.e., they have $T_d/T_{d,binary} \geq 1$ and $T_d \geq 1000$ K. The final candidates are listed in Table 6.5 in order of highest hydrogen release temperature. The top 5 materials crystallize in the 2-Sr_2RuH_6 cubic crystal structure, and 3 others crystallize with 6-K_2PtH_4 tetragonal prototype. In both of these examples, the cations adopt 8-fold cubic or nearly cubic arrangements, which Yvon and Renaudin argued may help maximize the M−H interactions, stabilizing the structures.[13] In the case of the 6-K_2PtH_4 prototype, there is evidence that the low temperature form studied in this work transforms to a disordered cubic structure similar to that of 2-Sr_2RuH_6 close to ambient conditions.[13]

It is notable that, of the 13 final candidates, 11 crystallize in either cubic or tetragonal symmetry, and most have high temperature disordered cubic phases. Since disordered phases are not studied in this work and the high temperature modifications, if thermodynamically stable, are expected to have lower free energies than the ordered materials, the T_d's reported here may be taken as lower bounds if one ignores the potential existence of other destabilizing intermetallic phases. Of the most stable element spaces from Table 6.5, only binary intermetallics RuYb, LiRh, and Cs_2Pt are listed in the ICSD as known compounds. Therefore, the most stable CTMHs decompose to the pure

metal phases and hydrogen, existing in element combinations in which the two constituent metals do not favor forming ordered intermetallics. This is a somewhat general feature of CTMHs as discussed earlier since most CTMHs are true ternary compounds, i.e., they do not form via hydrogen dissolution into an intermetallic lattice.[13]

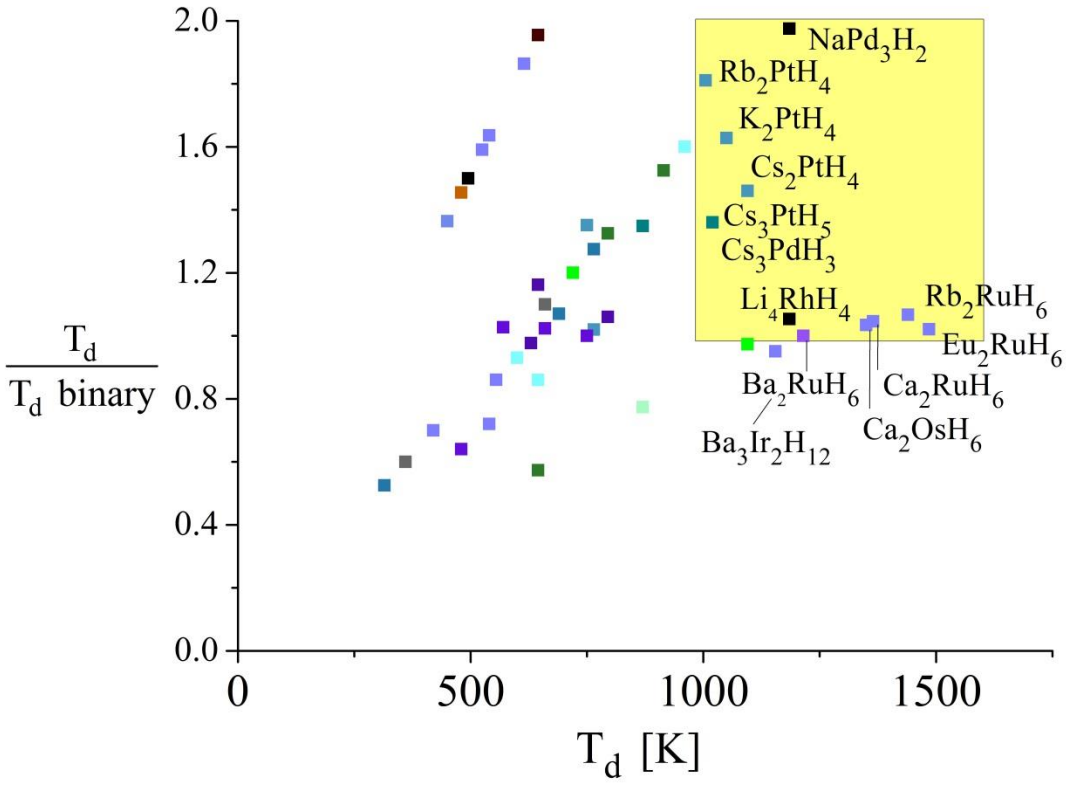

Figure 6.6: Relative and absolute thermal stabilities for the reduced set of existing ternary CTMHs predicted with Round 2 level of screening. Color indicates structure prototype.

Table 6.5: Final candidates from Round 2 screening with $T_d/T_{d,binary} \geq 1$ and $T_d \geq 1000$ K. Decomposition reactions, hydrogen release temperatures for 1 bar H_2, $T_{d,}$(K), and ground state reaction energies (kJ mol^{-1} H_2) are shown.

CTMH	T_d (K)	Decomposition Pathway	Structure Prototype
Eu_2RuH_6	1485	$\frac{1}{3}$ $Eu_2RuH_6 \leftrightarrow \frac{2}{3}$ Eu + $\frac{1}{3}$ Ru + H_2	2-Sr_2RuH_6
Yb_2RuH_6	1440	$\frac{1}{3}$ $Yb_2RuH_6 \leftrightarrow \frac{1}{3}$ Ru + $\frac{2}{3}$ Yb_ + H_2	2-Sr_2RuH_6
Ca_2RuH_6	1365	$\frac{1}{3}$ $Ca_2RuH_6 \leftrightarrow \frac{2}{3}$ Ca_HT + $\frac{1}{3}$ Ru + H_2	2-Sr_2RuH_6
Ca_2OsH_6	1350	$\frac{1}{3}$ $Ca_2OsH_6 \leftrightarrow \frac{2}{3}$ Ca_HT + $\frac{1}{3}$ Os + H_2	2-Sr_2RuH_6
Ba_2RuH_6	1215	$\frac{1}{3}$ $Ba_2RuH_6 \leftrightarrow \frac{2}{3}$ Ba + $\frac{1}{3}$ Ru + H_2	2-Sr_2RuH_6
$Ba_3Ir_2H_{12}$	1215	$\frac{1}{6}$ $Ba_3Ir_2H_{12} \leftrightarrow \frac{1}{2}$ Ba + $\frac{1}{3}$Ir + H_2	31-$Ba_3Ir_2H_{12}$
Li_4RhH_4	1185	$\frac{1}{2}$ $Li_4RhH_4 \leftrightarrow \frac{1}{2}$ LiRh + $\frac{3}{2}$ Li + H_2	Li_4RhH_4
$NaPd_3H_2$	1185	$NaPd_3H_2 \leftrightarrow$ 3 Pd + Na + H_2	$NaPd_3H_2$
Cs_2PtH_4	1095	$\frac{1}{2}$ $Cs_2PtH_4 \leftrightarrow \frac{1}{2}$ Cs_2Pt + H_2	6-K_2PtH_4
K_2PtH_4	1050	$\frac{1}{2}$ $K_2PtH_4 \leftrightarrow$ K + $\frac{1}{2}$ Pt + H_2	6-K_2PtH_4
Cs_3PtH_5	1020	2 $Cs_3PtH_5 \leftrightarrow$ 2 Cs_2PtH_4 + 2 Cs + H_2	8-K_3PtH_5
Cs_3PdH_3	1020	$\frac{2}{3}$ $Cs_3PdH_3 \leftrightarrow$ 2 Cs + $\frac{2}{3}$ Pd + H_2	9-K_3PdH_3
Rb_2PtH_4	1005	$\frac{1}{2}$ $Rb_2PtH_4 \leftrightarrow \frac{1}{2}$ Pt + Rb + H_2	6-K_2PtH_4

Table 6.6 presents key computed thermodynamic properties for the binary hydrides relevant for the Round 2 level of screening. Calculated values for enthalpy and entropy include temperature-dependent and zero point vibrational contributions from the condensed phases. These are directly computed values rather than linearly fit values and can be compared with the experimental reference data in Table 6.3. The experimental data are typically retrieved from van't Hoff plots generated from averages of measured pressures from pressure-composition isotherms and absolute agreement between experiment and DFT values should not be expected. In general, the calculations reproduce the increase in reaction enthalpy from 300 K to the high temperature reaction conditions due to inclusion of the temperature-dependent vibrational enthalpy. In most cases the DFT predicts T_d to within about 125 K of the experimental value where available. This is consistent with the previous thermodynamic stability calculations of

Chapter 2.[14] There are larger uncertainties for CaH_2 and BaH_2 for which the experimental data is ambiguous. LiH melts before releasing hydrogen, and so we also list the melting temperatures of the most stable binary hydrides for CaH_2 and BaH_2 as perhaps a better indicator of the thermodynamic stability compared to the values reported in Reference 6.

The average value of the ambient condition reaction entropy is 0.134 kJ K^{-1} mol H_2, very close to the entropy of the H_2 gas at 0.130 kJ K^{-1} mol H_2. However, $\Delta S°$ is calculated to fall between 0.098 and 0.185 kJ K^{-1} mol^{-1} H_2, a large spread. From the recommended values for $\Delta G°$ from Sangster and Pelton, the experimental value of $\Delta S°$ is 0.171 and 0.170 kJ K^{-1} mol^{-1} H_2 for RbH and CsH, respectively. This is, clearly, much larger than the standard entropy of the hydrogen gas. Our calculations predict smaller values for RbH and CsH at 0.153 and 0.116 kJ K^{-1} mol^{-1} H_2, respectively. In general, we note that the dihydride binary hydrides have computed values of $T\Delta S°$ at 300 K (40.6 ± 0.8 kJ mol^{-1} H_2) closer to the ideal entropic contribution of H_2 gas of 39.0 kJ mol^{-1}K, than the monohydrides (40.0 ± 6.3 kJ mol^{-1} H_2) for which the scatter is larger.

Table 6.6: Thermodynamic properties of binary hydride decomposition reactions from Round 2 calculations, including vibrational corrections to the Helmholtz free energy for condensed phases. Standard conditions (300 K,1 bar H_2). T_d (K), ΔH (kJ mol^{-1} H_2), $\Delta S°$ (kJ K^{-1} mol^{-1} H_2).

Binary Hydride	T_d	$\Delta H°$	$\Delta S°$	$\Delta H(T_d)$	Decomposition Pathway
BaH_2	1215	158.4	0.134	148.1	$BaH_2 \leftrightarrow Ba + H_2$
CaH_2	1305	179.2	0.138	171.0	$CaH_2 \leftrightarrow Ca\_HT + H_2$
CsH	750	80.9	0.116	69.5	$2\ CsH \leftrightarrow 2Cs + H_2$
EuH_2	1455	196.1	0.136	185.3	$EuH_2 \leftrightarrow Eu + H_2$
KH	645	97.7	0.152	94.8	$2\ KH \leftrightarrow 2K + H_2$
LiH	1125	169.1	0.149	164.4	$2\ LiH \leftrightarrow 2Li + H_2$
MgH_2	480	64.5	0.131	64.2	$MgH_2 \leftrightarrow Mg + H_2$
NaH	600	89.5	0.149	88.8	$2\ NaH \leftrightarrow 2Na + H_2$
NiH	255	29.1	0.116	28.8	$2\ NiH \leftrightarrow 2Ni + H_2$
PdH	510	49.0	0.098	49.1	$2\ PdH \leftrightarrow 2Pd + H_2$
RbH	555	83.6	0.153	81.5	$2\ RbH \leftrightarrow 2Rb + H_2$
YbH_2	1350	186.9	0.138	179.2	$YbH_2 \leftrightarrow Yb\_ + H_2$

Table 6.7 summarizes the thermodynamic properties for the hydrogen release reactions of final candidate materials from Table 6.5 as a result of the Round 2 screening. We note the very large thermodynamic driving force for hydrogen in the solid hydride for these materials, characterized by the reaction enthalpy. As with the binary hydride CsH, the $\Delta S°$ for the Cs-Pd and Cs-Pt hydrides are significantly reduced compared with the entropy of hydrogen gas and the other CTMHs. There are very few available experimental thermodynamic data available for the CTMHs, a point which highlights the utility of computational tools. However, we compare our results with experimental phase stability observations for a few examples below.

Table 6.7: Thermodynamic properties of final candidate decomposition reactions from Table 6.5 from Round 2 calculations, including vibrational corrections to the Helmholtz free energy for condensed phases. Standard conditions (300 K,1 bar H_2). T_d (K), ΔH (kJ mol^{-1} H_2), $\Delta S°$ (kJ K^{-1} mol^{-1} H_2).

CTMH	$\Delta H°$	$\Delta S°$	$\Delta H(T_d)$
Eu_2RuH_6	196.7	0.131	189.5
Yb_2RuH_6	192.1	0.132	185.9
Ca_2RuH_6	180.8	0.131	175.0
Ca_2OsH_6	179.0	0.130	173.8
Ba_2RuH_6	159.7	0.130	154.7
$Ba_3Ir_2H_{12}$	153.2	0.124	150.0
Li_4RhH_4	165.6	0.138	161.9
$NaPd_3H_2$	124.1	0.111	111.4
Cs_2PtH_4	133.6	0.123	128.5
K_2PtH_4	141.2	0.133	139.4
Cs_3PtH_5	63.9	0.075	44.5
Cs_3PdH_3	114.0	0.116	104.5
Rb_2PtH_4	136.8	0.134	135.3

6.4 Comparison of Example Experimental and Predicted Phase Diagrams

The most well-studied CTMH system is the Mg-Fe-H element space.[15-18] Puskiel et al. measured pressure-composition isotherms using a modified Sieverts type apparatus.[18] They found that the ternary hydride exhibits lower hydrogen equilibrium pressure than the binary hydride for the same temperature, indicating higher thermodynamic stability of the ternary hydride. Based on pressures determined through averages of experimental points and van't Hoff plot fitting, they determined characteristic thermodynamic properties for Mg_2FeH_6 of T_d = 673 K, ΔH(573−648 K) = 80 ± 7 kJ mol^{-1} H_2, ΔS = 0.137 ± 13 kJ K^{-1} mol^{-1} H_2 and for MgH_2 of ΔH(548−648 K) = 67 ± 2 kJ mol^{-1} H_2, ΔS = 0.123 ± 3 kJ K^{-1} mol^{-1} H_2. Similarly, Bogdanovic et al. found the ΔH (Mg_2FeH_6) = 77 kJ mol^{-1} H_2.[15] For comparison, our predictions from the Round 2 level screening calculations are shown in Table 6.8. We reproduce the enhanced stability of the CTMH,

both in terms of the relative stability with respect to the binary hydride and magnitude of the onset of hydrogen release temperatures. The predicted decomposition pathway and thermodynamic properties are in good agreement with the experimental values.

Table 6.8: Predicted thermodynamic properties for Mg−Fe−H system.

CTMH	Binary
$\frac{1}{3}Mg_2FeH_6 \leftrightarrow \frac{2}{3}Mg + \frac{1}{3}Fe + H_2$ T_d = 660 K $\Delta H(T_d)$ = 86.2 kJ mol^{-1} H_2 $\Delta S°$= 0.127 kJ K^{-1} mol^{-1} H_2	$MgH_2 \leftrightarrow Mg + H_2$ T_d = 480 K $\Delta H(T_d)$ = 62.4 kJ mol^{-1} H_2 $\Delta S°$= 0.131 kJ K^{-1} mol^{-1} H_2

Though not as well studied, the thermal stabilities of M_2ZnH_4 and M_3ZnH_5 ternary hydrides (M = K, Rb, and Cs) have been investigated via thermogravimetry methods.[19,20] Borst, Hewat, and Yvon found that all of the ternary compounds decomposed around 600 K at ambient pressures.[20] For M_2ZnH_4, the M = K and Rb compounds begin to decompose to a mixture of the binary intermetallic MZn_{13} and M_3ZnH_5 phases at 550 K and 580 K, respectively, and they attribute a second decomposition step to formation of the binary hydrides at 637 K and 680 K, respectively. Cs_2ZnH_4 releases hydrogen in one step.[19] For M_3ZnH_5 (M = K, Rb, and Cs), the hydrides release hydrogen at 620 K, 630 K, and 625 K, respectively. However, it is uncertain as to whether or not the hydride decomposes to the pure metals or to a mixture of the binary hydrides and/or intermetallic phases.[20]

Figure 6.7 shows our phase diagram predictions for these systems, including vibrational corrections to the Helmholtz free energies. We calculate that the ternary hydrides all decompose in the range 570 K−795 K and that each is at least as, if not

slightly more, thermodynamically stable than the binary hydride in each system. For the K−Zn−H system, the thermodynamically preferred decomposition path for K_2ZnH_4 is through a mixture of K_3ZnH_4 and KZn_{13}, in agreement with the experimental observation. However, the relative stabilities of the CTMH are reversed for the Rb−Zn−H. In both cases, the binary intermetallic phase is stable. Additionally, we find that Cs_2ZnH_4 releases hydrogen in one step, also in agreement with the experimental observation.

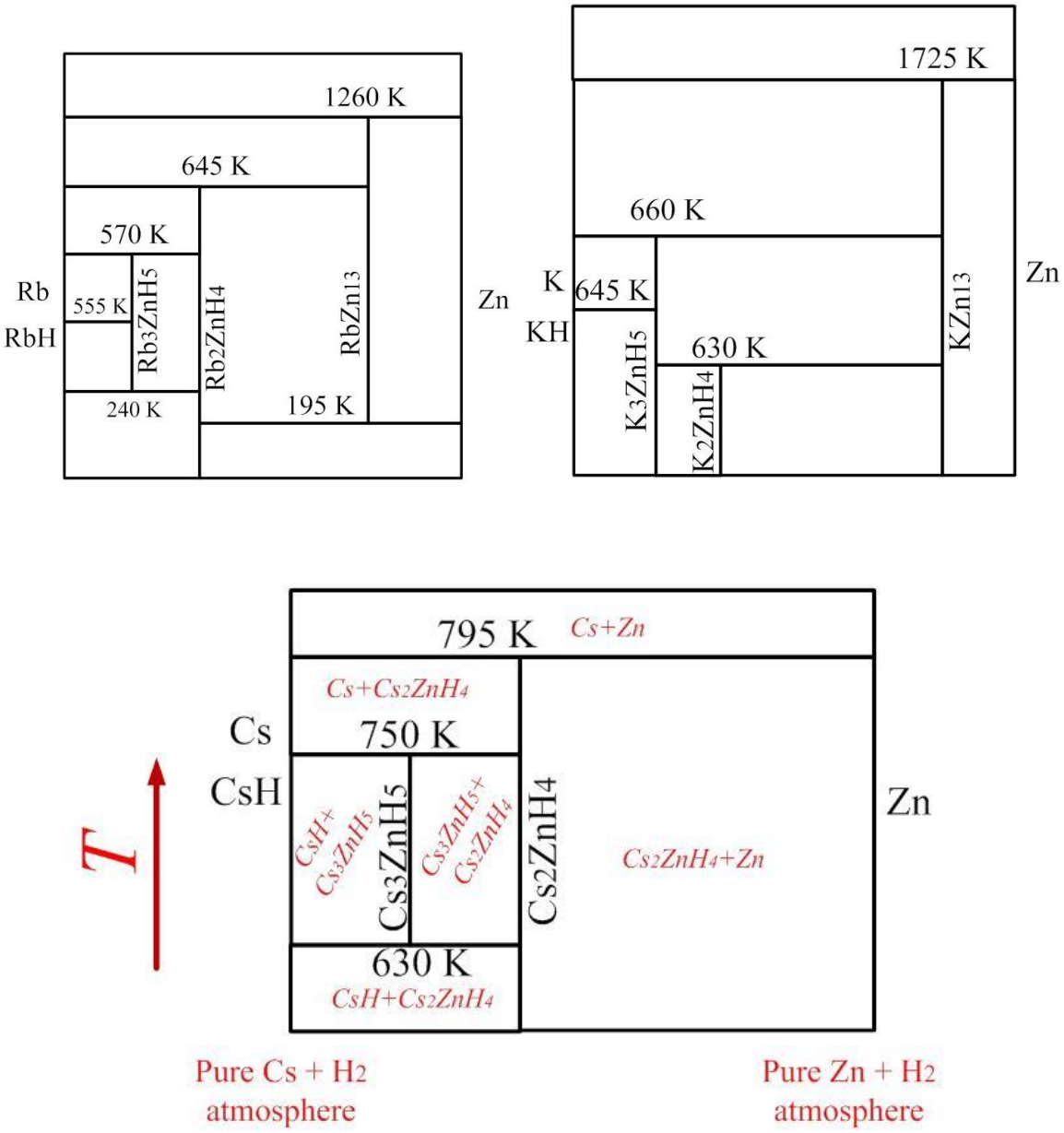

Figure 6.7: Predicted phase diagrams at 1 bar H_2 for the *M*−Zn−H (*M* = Rb, K, and Cs) systems with phonon corrections for the condensed phases (not drawn to scale). The horizontal axis represents the molar ratio of metals for a given composition with the pure cation species on the far left and the pure transition metal on the far right. Temperature is shown vertically. As demonstrated for the Cs−Zn−H element space, each box describes a unique mixture of stable compounds. The stable mix of compounds obtained from the GCLP method for a given *T* can be read from the intersection of a horizontal line drawn at that *T* with the vertical lines, which represent the stoichiometric compounds.

In computing the phase diagrams, we increment the hydrogen chemical potential by an amount equivalent to ΔT = 15 K, which sets one level of tolerance for the precision of the reported reaction temperatures. In this work, attempts have been made to control numerical convergence of compound free energies with respect to *k*-points, cutoff energy, supercell size, and q-point sampling to within approximately 5 kJ mol^{-1} (kJ mol^{-1} H_2 for hydride phases). One expects that there will be some cancellation of errors when considering relative phase stabilities, particularly with the cutoff energy. A larger issue is the accuracy of the DFT functionals themselves. While our predictions reproduce the experimental enthalpies for Mg_2FeH_6 and MgH_2 to within about 7 kJ $mol^{-1}H_2$, comparing the DFT computed and experimental heats of reaction for the binary hydrides in Tables 6.6 and 6.3 suggests that the PAW(GGA,PW91) pseudopotential used in this work can be expected to resolve reaction enthalpies either at ambient conditions or at the reaction temperature to within about 15 kJ mol^{-1} H_2 (on average) of the experimental reference value. However, deviations can be as large as 30 kJ mol^{-1} H_2 as is the case for CsH. This is consistent with the results of Wolverton et al. who found that the average root mean square error for computing dehydrogenation enthalpies at 298 K decreases from 19.4 to 14.7 kJ mol^{-1} H_2 when accounting for vibrational effects in Perdew-Wang GGA DFT calculations, similar to those used in this chapter.[1] Based on the average error (ΔH_{expt} - ΔH_{DFT}) = 15 kJ $mol^{-1}H_2$, and the average $\Delta S°$=0.125 kJ K^{-1} mol^{-1} H_2, we estimate that the absolute magnitudes of decomposition temperatures are typically accurate to within about 125 K. We expect that the relative magnitudes of binary and ternary hydrides are even better reproduced due to some cancellation of exchange-correlation effect errors. Therefore, the phase diagrams predicted in this work should be taken as guides rather

than as absolute answers. Phase diagrams for the element spaces of the final candidate materials listed in Table 6.5 are available in Figure E.1 in the Appendix. The calculations can clearly sort metal hydrides that have low, moderate, and high thermal stabilities and are useful for determining potential operating parameters of candidate systems for the NGNP application.

6.5 Round 2 Dynamically Stabilized Compounds

Some element spaces had significant changes in the predicted stable sets of compounds for given chemical potentials from Round 1 to Round 2, which incorporated the vibrational contributions to the free energy for the condensed phases. Notable differences include the stabilization of Li_4RhH_4 at 705 K via the reaction of LiH and Li_3RhH_4 as shown in Figure E.1g and, upon heating, Li_3RhH_4 phase separates into the intermetallic LiRh and Li_4RhH_4. This is a significant change from the phase diagram calculated based only on ground state energies for which Li_4RhH_4 was not predicted to form at any *T*. Other significant changes include the dynamic stabilization of K_3PtH_5, K_3PdH_5, K_3ZnH_5, Cs_3PdH_5, Cs_3PtH_5, and K_3ZnH_5 with corresponding change in the decomposition of K_2ZnH_4 ($^{76}/_{27}$ $K_2ZnH_4 \leftrightarrow {}^{50}/_{27}$ $K_3ZnH_5 + {}^{2}/_{27}$ $KZn_{13}+H_2$), the destabilization of Rb_3PdH_3 with corresponding change in decomposition of Rb_2PdH_4 ($½Rb_2PdH_4 \leftrightarrow Rb + ½Pd + H_2$) , and the flip-flop of relative stabilities of Na_2PdH_2 ($^{3}/_{2}$ $Na_2PdH_2 \leftrightarrow {}^{5}/_{2}$ $Na + {}^{1}/_{2}$ $NaPd_3H_2 + H_2$) and $NaPd_3H_2$ ($NaPd_3H_2 \leftrightarrow 3Pd + Na + H_2$).

6.6 Final Candidate van't Hoff Plots

Figures 6.7 and 6.8 show the computed van't Hoff plots for the final candidate CTMHs and the binary hydrides using Eq. (5.8) to correct the hydrogen chemical potential for pressure. The screening criteria were sufficient to ensure that the CTMHs in Figure 6.7 are at least as stable as the corresponding binary hydrides at the pressure conditions studied in this work from $P = 10^{-6}$ to 100 bar. At $T = 1000$ K, the most thermodynamically stable CTMHs are, in order from highest to lowest, Eu_2RuH_6, Yb_2RuH_6, Ca_2RuH_6, Ca_2OsH_6, and Ba_2RuH_6, which are all materials that crystallize in the 2-Sr_2RuH_6 cubic prototype.

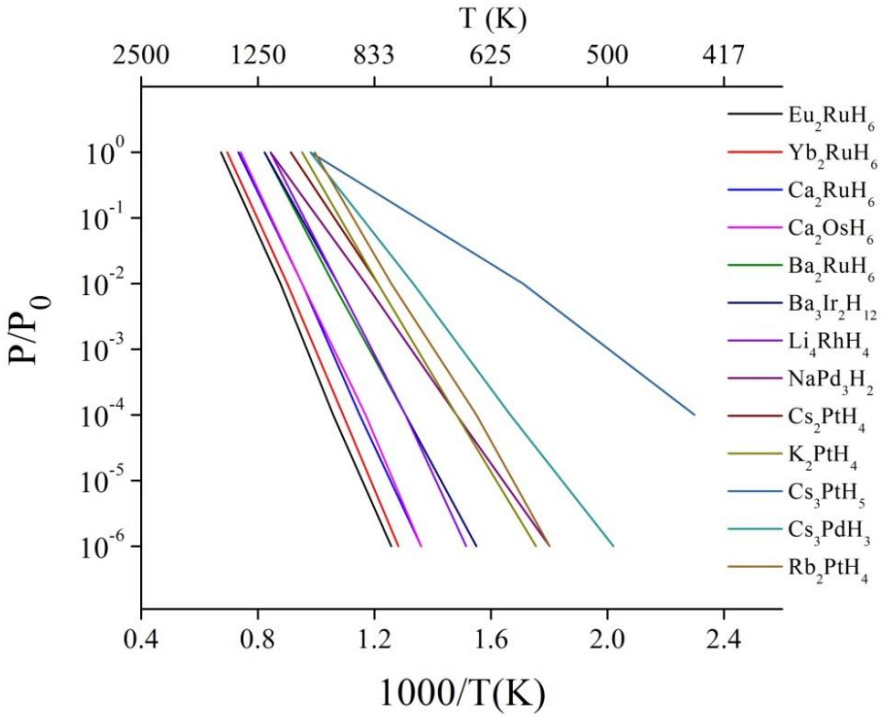

Figure 6.7: Calculated van't Hoff plots for final candidate CTMHs from Table 6.4 based on Round 2 level of screening.

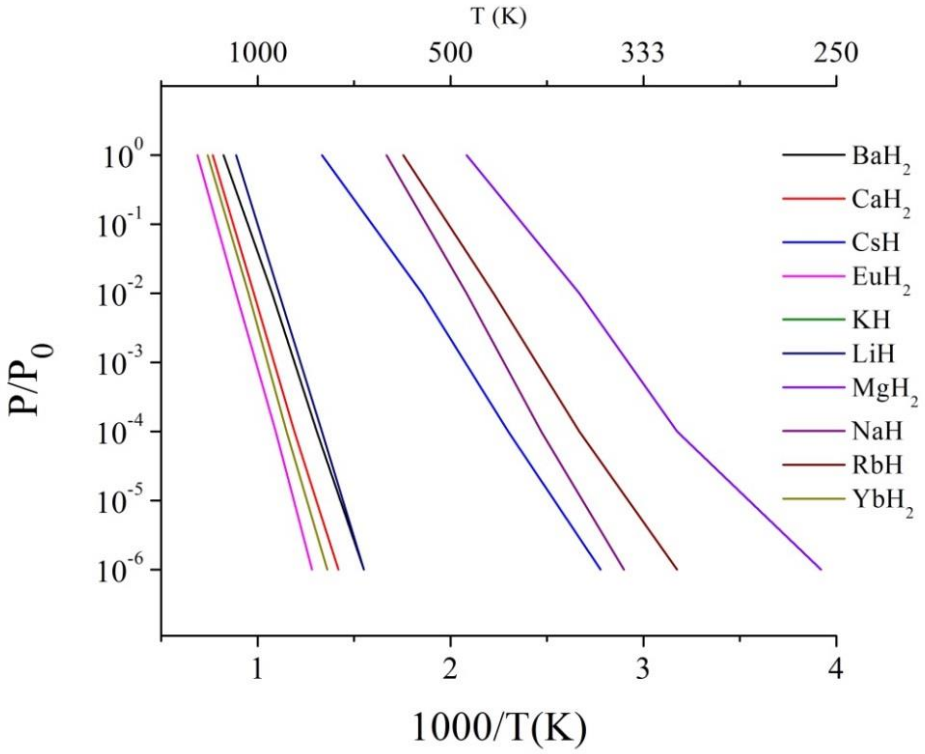

Figure 6.8: Calculated van't Hoff plots for binary hydrides corresponding to materials in Table 6.4 based on Round 2 level of screening.

The conditions of the NGNP may contain tritium contamination at levels of 10^{-10} bar H_2. The most stable predicted ternary hydride, Eu_2RuH_6, has an equilibrium pressure of ~10^{-4} bar at the NGNP condition T = 1000 K. A less expensive binary hydride, CaH_2, is calculated to have P_{eq} (1000 K) ~ 10^{-2} bar. Both of the most stable binary and ternary hydrides studied in this chapter have equilibrium pressures far above that of the target tritium contaminant. This implies that there will be a significant thermodynamic driving force for tritium to remain in the gas phase rather than form the solid hydride material at the temperature conditions of the NGNP.

One arrangement of the tritium gettering system could use a direct contact bed that exposes the metal hydriding material to a side stream of the helium coolant and

tritium contaminant at the reactor outlet temperatures. This has the advantage of greater thermal efficiency since the coolant may not be cooled and the gettering bed can be placed far upstream of other processing equipment to limit contamination of equipment such as heat exchangers. However, this arrangement will suffer from the thermodynamic drawback discuss above. Some processing options to enable the use of CTMHs for the gettering process could include raising the H_2 partial pressure. H_2 as protium will be present in the helium coolant in addition to tritium, but at levels that are currently unknown. However, since tritium and protium have very similar thermodynamic stabilities in metal hydrides at high temperature this may increase the amount of tritium taken up by the direct contact bed. Additionally, H_2 injection into the side stream could be considered. H_2 injection is being investigated for the NGNP as a method for raising the backpressure on heat exchangers to prevent tritium migration to downstream users.[21] Rainsing P_{H2} moves the equilibrium point for CTMH candidates in Figure 6.7 to the left, meaning that the material will absorb H_2 at higher temperatures. Based on the most thermodynamically stable CTMH candidate, Eu_2RuH_6, the P_{H2} would need to be raised to above ~10^{-3} bar to make the hydriding reaction energetically favorable. As the amount of hydrogen in the coolant increases the overall system will require more metal hydride material to accommodate the additional gas to be stored.

Other options could include cooling the side stream to move the equilibrium point for CTMHs to lower partial pressures on the van't Hoff plots. This would lower the thermodynamic driving force for hydrogen to remain in the gas phase, but would also cost energy and require tritium management materials in order to cool the stream, though some heat may be recoverable via the exothermic hydriding reaction.

6.7 Conclusion

Overall, the DFT calculations and GCLP phase diagram prediction methods can reproduce experimental trends in phase stability with reasonable fidelity and be considered as a guide for ranking metal hydrides based on hydrogen release temperatures at 1 bar H_2 to within ~125 K. Using two rounds of screening, we successfully identified 13 candidate CTMHs from an initial library of 102 ternary and quaternary CTMHs that have the desirable properties of enhanced thermodynamic stability relative to the associated binary hydrides that also release hydrogen at high temperature for 1 bar H_2 overpressures. We also observed the dynamic stabilization of some CTMH compositions (~10) with the inclusion of vibrational free energies in the GCLP phase diagram prediction. The most stable CTMHs tend to crystallize in the 2-Sr_2RuH_6 cubic prototype structure and decompose to the pure elements and hydrogen rather than to an intermetallic phase(s). As discussed, the most stable CTMHs and calculated binary hydrides are predicted to have equilibrium pressures orders of magnitude above the tritium contaminant levels of the NGNP application. Based on the ideal thermodynamic considerations of the very stable metal hydrides considered here, there are significant challenges to using binary hydrides or CTMHs in a direct contact gettering application at high temperature and low tritium overpressures. Process manipulations should be considered that either increase the hydrogen overpressure in the system or cool the feed drive the thermodynamic equilibrium toward the solid metal hydrides.

6.8 References

[1] C. Wolverton, J. S. Donald, A. R. Akbarzadeh, and V. Ozoliņš, *J. Phys. Condens. Matter* **20**, 064228 (2008).

[2] C. Wolverton, V. Ozoliņš, and M. Asta, *Phys. Rev. B* **69**, 144109 (2004).

[3] A. Jain, et al., *APL Materials* **1** (2013).

[4] S. P. Ong, et al., *Comput. Mater. Sci.* **68**, 314 (2013).

[5] A. Jain, G. Hautier, C. J. Moore, S. Ping Ong, C. C. Fischer, T. Mueller, K. A. Persson, and G. Ceder, *Comput. Mater. Sci.* **50**, 2295 (2011).

[6] W. Grochala and P. P. Edwards, *Chem. Rev.* **104**, 1283 (2004).

[7] R. Griessen and T. Riesterer, *Top. Appl. Phys.* **63**, 219 (1988).

[8] J. Sangster and A. D. Pélton, *J. Phase Equilib.* **1**, 84 (1994).

[9] E. Veleckis, *J. Nucl. Mater.* **79**, 20 (1979).

[10] J. Sangster and A. D. Pélton, *J. Phase Equilib.* **15**, 87 (1994).

[11] F. Orecchini and V. Naso, in *Energy Systems in the Era of Energy Vectors* (Springer, 2012), Vol. 8, p. 153.

[12] in *CRC Handbook of Chemistry and Physics, 88th Edition*.

[13] K. Yvon and G. Renaudin, in *Encyclopedia of Inorganic Chemistry, Second Edition*, edited by B. R. King (John Wiley & Sons, Chichester, 2005), Vol. III, p. 1814.

[14] K. M. Nicholson and D. S. Sholl, *Phys. Rev. B* **86**, 134113 (2012).

[15] B. Bogdanović, A. Reiser, K. Schlichte, B. Spliethoff, and B. Tesche, *J. Alloys Compd.* **345**, 77 (2002).

[16] J. J. Didisheim, P. Zolliker, K. Yvon, P. Fischer, J. Schefer, M. Gubelmann, and A. F. Williams, *Inorg. Chem.* **23**, 1953 (1984).

[17] L. George, V. Drozd, A. Durygin, J. Chen, and S. K. Saxena, *Int. J. Hydrogen Energy* **34**, 3410 (2009).

[18] J. A. Puszkiel, P. A. Larochette, and F. C. Gennari, *J. Alloys Compd.* **463**, 134 (2008).

[19] M. Bortz, A. Hewat, and K. Yvon, *J. Alloys Compd.* **248**, L1 (1997).

[20] M. Bortz, A. Hewat, and K. Yvon, *J. Alloys Compd.* **253–254**, 13 (1997).

[21] S. R. Sherman and T. M. Adams, *Tritium Barrier Materials and Separation Systems for the NGNP*, U. S. DOE Savannah River National Laboratory, Aiken, Nov. 2008.

CHAPTER 7

SCREENING OF PROPOSED CTMHs FOR NGNP APPLICATION - RESULTS*

Using computational tools, our aim in Chapter 7 is to identify proposed or hypothetical CTMH candidate materials based on known prototype structures that have enhanced stability with respect to the binary hydrides forming from the constituent metals, $T_d/T_{d,binary} \geq 1$, and that release hydrogen at high temperature, $T_d \geq 1000$ K. The screening methods and computational details for these results were described in Chapter 5.

7.1 Initial Calculation of Stability for Proposed Materials

We first relaxed crystal structures for the 149 proposed CTMHs displayed in Figure 5.4 using DFT at the moderate force and electronic energy convergence criteria. Relaxed geometrical parameters for these materials are listed in Table D.1 in the Appendix. We then computed initial GCLP phase diagrams (no phonon corrections) for 102 element spaces, including 71 element spaces not previously considered in Chapter 6, summarized in Figure 5.5 with >450 compound entries from the existing and proposed Round 1 materials libraries shown in Tables C.1 and D.1 in the Appendices, respectively. If a proposed material from a new element space was predicted to have $T_d/T_{d,binary} \geq 1$, we added any additional "simulation ready" binary intermetallic compounds to the GCLP input library that could form in the element space from the ICSD.[1,2] Overall, 29 new binary intermetallic compounds, listed in Table D.2 in the Appendix were incorporated

*Reproduced in part with permission from Inorg. Chem., submitted for publication. Unpublished work copyright 2014 American Chemical Society.

into the materials library from the 24 new element spaces with stable proposed phases. As previously observed, these intermetallics are concentrated among certain element combinations with 25 of the 29 intermetallics completing the Ca−Pd, Eu−Pt, Eu−Rh, Mg−Rh, and Pd−Yb element spaces.

Figure 7.1 shows the initial prediction of stable ternary CTMHs based on the Round 1 level of screening. If a proposed space was found to form at any *T, P* within the studied ranges, i.e., $0 \leq T$ (K) ≤ 2000 and 10^{-6}, 10^{-4}, 10^{-2}, 1, and 100 bar H_2, it is shown in solid yellow. If a compound was not observed in the set of stable mixtures over the tested chemical potential ranges, it is shown with an "X". 76 of the 149 hypothetical materials are calculated to be thermodynamically viable based on these initial calculations. Decomposition pathways and T_d for these are listed in Table D.1 in the Appendix. We re-iterate that additional intermetallics for new element spaces were only included if the stable CTMH met the initial enhanced stability screening criterion. For example, the Eu−Pt and Yb−Pt element spaces each have several intermetallic phases, but only the intermetallics for Eu−Pt were included since the initial stability calculation indicated Eu_2PtH_6 had $T_d/T_{d,binary} = 1.01$ whereas Yb_2PtH_6 had $T_d/T_{d,binary} = 0.98$. After including the Eu−Pt intermetallics, the T_d for Eu_2PtH_6 drops from 1500 K to 870 K since it is destabilized by Eu_5Pt_4. It is reasonable to assume that the Yb_2PtH_6 with the element space's close relationship with the Eu−Pt−H system would similarly be further destabilized by an intermetallic phase.

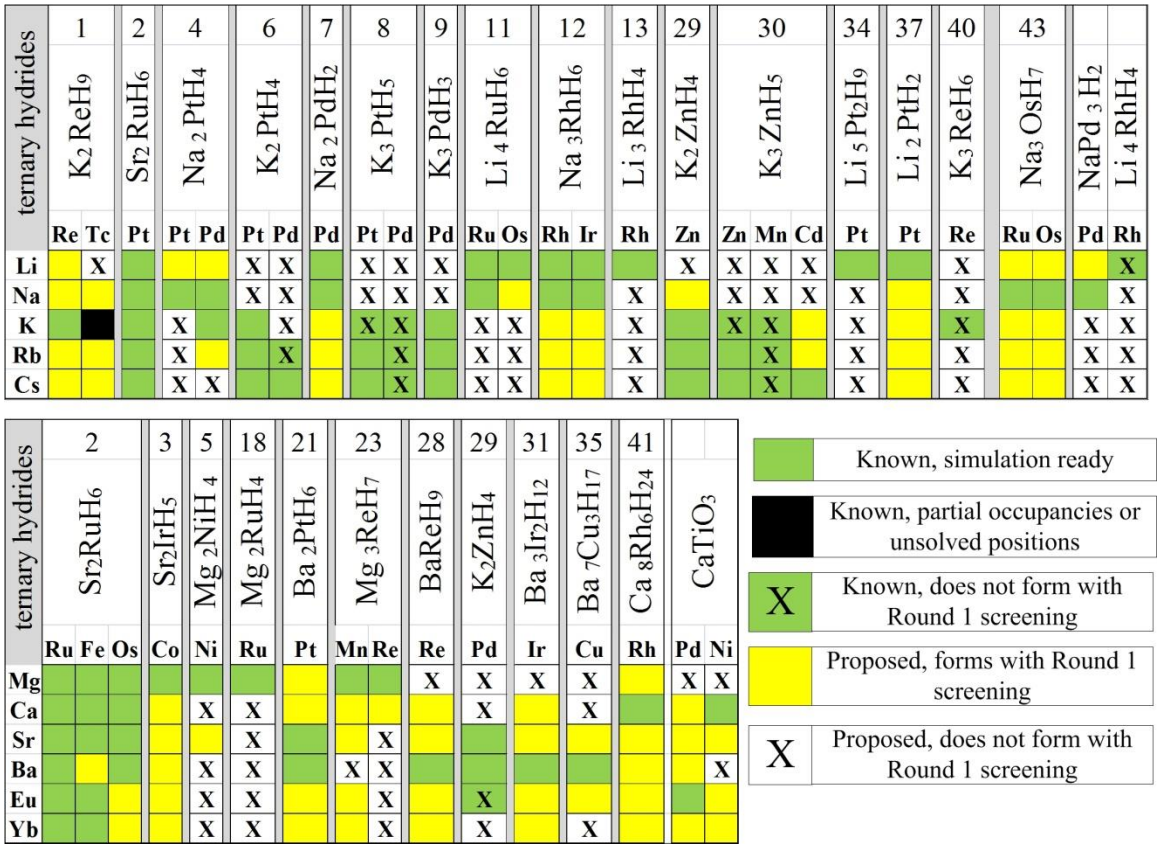

Figure 7.1: Mapping of initial stability prediction for 149 proposed and known CTMH materials based on Round 1 level of DFT calculations (no vibrational corrections to free energy) and GCLP minimization. Experimentally-known ternary (*M*-*Tr*-H) Complex Transition Metal Hydrides are from the ICSD[1,2] and the Yvon and Renaudin 2005 Review.[3] Calculations include additional intermetallic phases from the ICSD for new ternary element spaces that meet initial criterion $T_d/T_{d,binary} \geq 1$. Numbers are consistent with Yvon and Renaudin[3] and describe the chronological discovery of the prototype ternary hydride $M_x\ Tr_y\ H_z$ crystal structure shown vertically. Substitutional cations *M* of the same valence are grouped vertically. Substitutional transition metals *Tr* are listed horizontally. "Simulation ready" implies completely solved ordered structure with no partial occupancies.

It is immediately apparent from Figure 7.1 that several prototypes have stable compounds that form for the entire series of tested cations with the same valence. For example, Li_2PdH_2 and Na_2PdH_2 compounds were known to crystallize experimentally in the 7-Na_2PdH_2 prototype structure. Based on our initial calculations, K^+, Rb^+, and Cs^+ varieties may also be observed. With the exception of Li_2PdH_2, which decomposes to a mixture of LiPd, LiH, and H_2, the Na, K, Rb, and Cs compounds are predicted to be the most thermodynamically stable hydride phases in the respective element spaces, releasing H_2 to form the pure metals at high temperature based on Round 1 calculations. Similarly, our calculations indicate that 12-Na_3RhH_6, 37-Li_2PtH_2, 43-Na_3OsH_7, 2-Sr_2RuH_6, 21-Ba_2PtH_6, and 41-$Ca_8Rh_6H_{24}$ prototypes have stable compounds that span the entire series of tested cations of the same valence. This is impressive since the ionic radii vary widely from approximately 0.9 Å to 1.81Å for the alkali metals and 0.86 Å to 1.49 Å for the alkaline earth metals.[4]

As a reminder, these calculations include only ground state energies of the condensed phases with *T* and *P* effects controlled through μ_{H2} from Eq. (5.8). From our previous screening of existing materials from Chapter 6, we know that certain prototypes, in particular 8-K_3PtH_5 and 30-K_3ZnH_5, are dynamically stabilized through vibrational contributions. Materials that crystallize in these prototype structures might only be predicted to form if studied at the Round 2 level of screening to account for these vibrational contributions. In some cases, the experimental structure is not predicted to form at this level of theory. For example, Rb_2PdH_4_p ("_p" indicates a proposed material) is calculated to be thermodynamically stable in the tetragonal 4-Na_2PtH_4 structure, but only the tetragonal 6-K_2PtH_4 crystal has been observed experimentally. As

we discuss below, when this material is studied at the higher level of theory, the experimentally-observed 6-K_2PtH_4 phase is recovered. A similar situation occurs for Li_4RhH_4.

Figures 7.2 and 7.3 show the energies above the complex hull at 0 K for the unstable proposed CTMHs. Positive convex hull energies reflect endothermic formation energies for the given entry from the thermodynamically-preferred combination of compounds.[5] Compounds with convex hull energies close to zero are in close competition energetically with the most stable states.

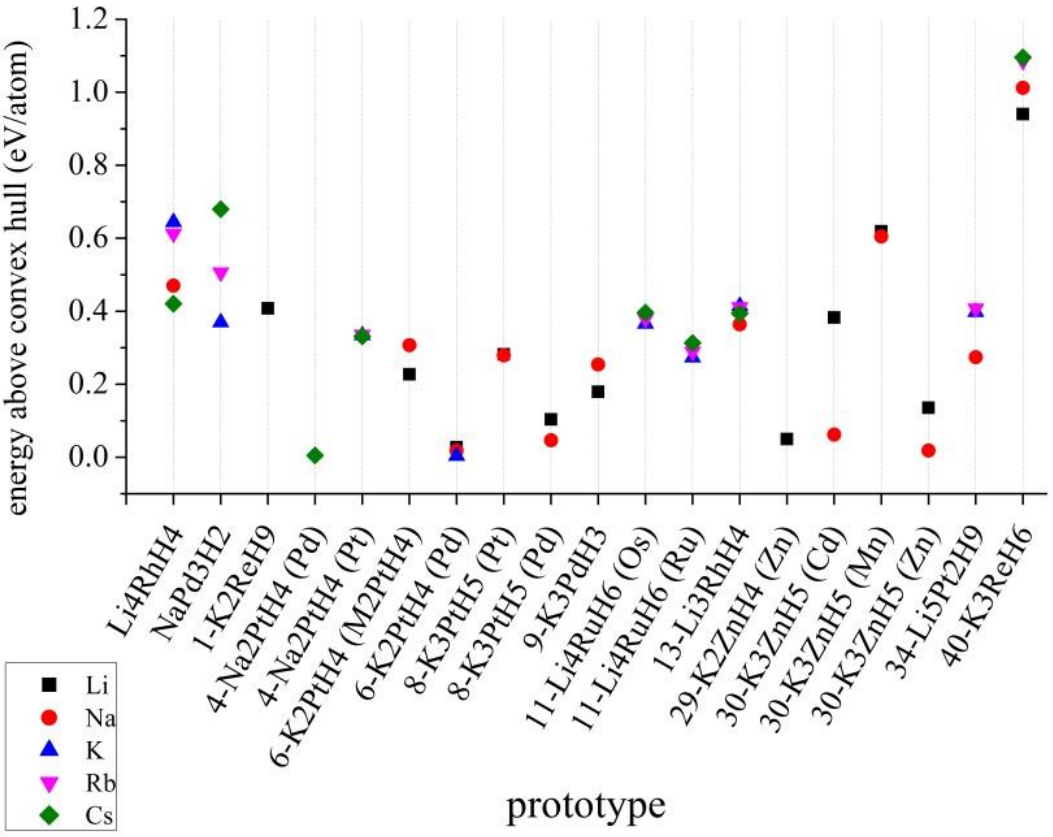

Figure 7.2: Energies above stable convex hull at 0 K for monovalent proposed *M*-*Tr*-H (*M* = alkali metal, *Tr* = transition metal) CTMHs not predicted to form at any *T*, *P* at the Round 1 level of screening. Reference prototype structure with substituted transition metal (*Tr*) from Figure 7.1 shown along horizontal axis.

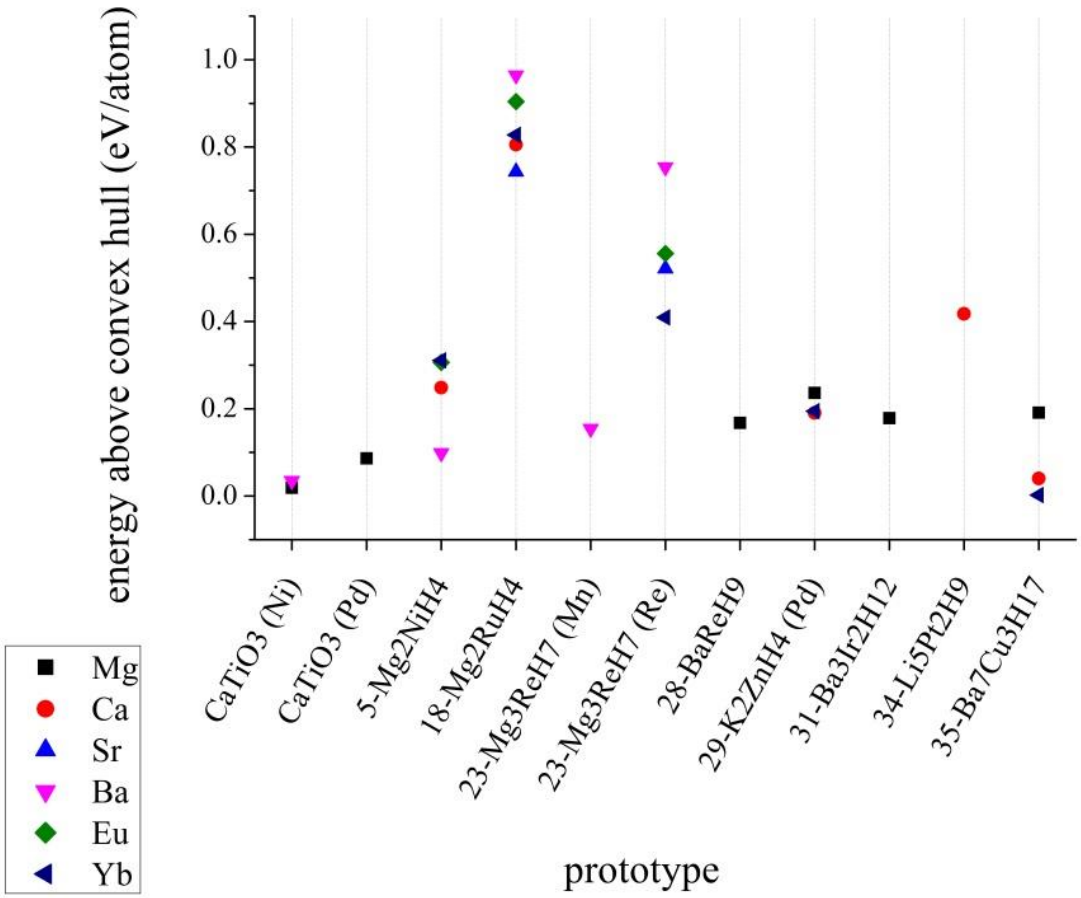

Figure 7.3: Energies above stable convex hull at 0 K for divalent proposed *M*-*Tr*-H (*M* = alkaline earth metal, *Tr* = transition metal) CTMHs not predicted to form at any *T*, *P* at the Round 1 level of screening. Reference prototype structure with substituted transition metal (*Tr*) from Figure 7.1 shown along horizontal axis.

7.2 Round 1 Thermodynamic Screening

Table D.1 in the Appendix lists the calculated decomposition pathways for all stable proposed CTMH materials at the Round 1 level of screening without phonon corrections. Figure 7.4 shows the thermodynamic stabilities of these compounds based on the ultimate screening criteria described at the beginning of the chapter. 28 have estimated $T_d/T_{d,binary} \geq 1$ and 12 operate at high temperature, $T_d \geq 1000$ K. Of the materials with enhanced stability relative to the binary hydrides, 8, 10, and 5 are Cs, Rb, and K-based materials, respectively. We add to these Sr_2NiH_4 with $T_d/T_{d,binary} = 0.85$ and T_d = 1320 K since the T_d (SrH_2) is significantly overestimated based on the ground state calculation by 360 K and Ni is a common metal, which may be interesting for the NGNP application. These candidate materials are listed in Table 7.1, and the thermodynamic stabilities of the referenced binary hydrides computed at the same level of theory are available in Table 6.2. This list comprises 28 element spaces, including 21 new element spaces for which a CTMH is not reported to form experimentally based on current entries in the ICSD.[1,2] In most cases the most stable ternary hydride in the element space releases hydrogen and forms a mixture of the pure metal species. Na_2PtH_2_p is the only example of a ternary hydride with enhanced stability that is destabilized by an intermetallic phase.

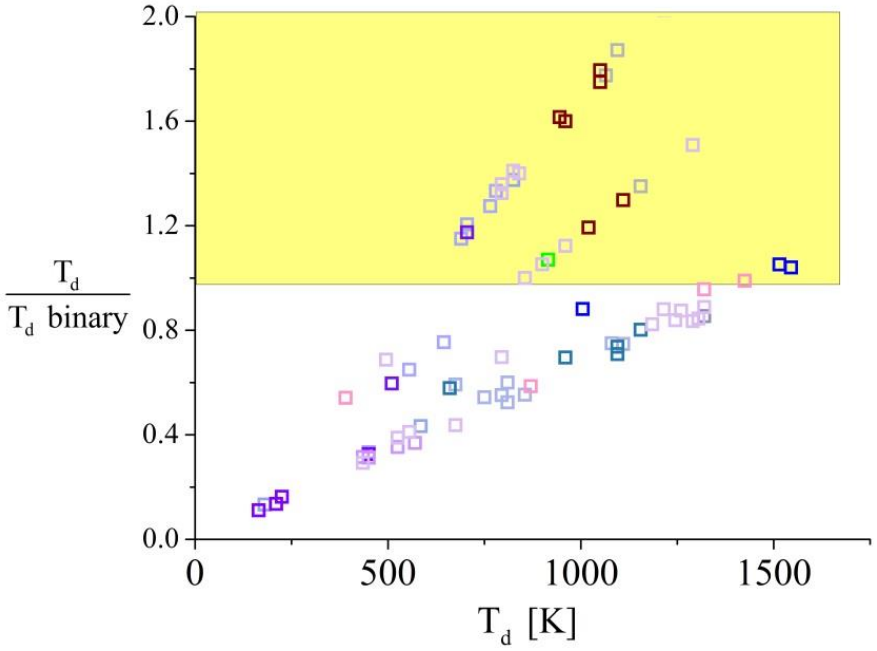

Figure 7.4: Relative and absolute thermal stabilities for stable proposed ternary CTMHs predicted with Round 1 level of screening. Color indicates structure prototype.

Table 7.1: Round 1 candidates with enhanced thermodynamic stability relative to binary hydrides and Sr_2NiH_4_p. "_p" indicates a proposed material.

CTMH	Structure Prototype	T_d (K)	Decomposition Pathway	ΔE_0 (kJ mol^{-1} H_2)
Eu_2OsH_6_p	2-Sr_2RuH_6	1545	$\frac{1}{3}$ Eu_2OsH_6_p ↔ $\frac{2}{3}$ Eu + $\frac{1}{3}$ Os + H_2	203.8
Yb_2OsH_6_p	2-Sr_2RuH_6	1515	$\frac{1}{3}$ Yb_2OsH_6_p ↔ $\frac{1}{3}$ Os + $\frac{2}{3}$ Yb + H_2	200.2
Sr_2NiH_4_p	5-Mg_2NiH_4	1320	$\frac{1}{2}$ Sr_2NiH_4_p ↔ $\frac{1}{2}$ Ni + Sr + H_2	165.3
K_2PtH_2_p	37-Li_2PtH_2	1290	K_2PtH_2_p ↔ Pt + 2K + H_2	160.4
Rb_2PtH_2_p	37-Li_2PtH_2	1215	Rb_2PtH_2_p ↔ Pt + 2Rb + H_2	147.5
Cs_2PtH_2_p	37-Li_2PtH_2	1215	Cs_2PtH_2_p ↔ Cs_2Pt + H_2	147.2
K_2PdH_2_p	7-Na_2PdH_2	1155	K_2PdH_2_p ↔ 2K + Pd + H_2	135.6
K_3IrH_6_p	12-Na_3RhH_6	1110	$\frac{1}{3}$ K_3IrH_6_p ↔ K + $\frac{1}{3}$ Ir + H_2	129.5
Cs_2PdH_2_p	7-Na_2PdH_2	1095	Cs_2PdH_2_p ↔ Pd + 2Cs + H_2	126.4
Rb_2PdH_2_p	7-Na_2PdH_2	1065	Rb_2PdH_2_p ↔ Pd + 2Rb + H_2	121.4
Rb_3IrH_6_p	12-Na_3RhH_6	1050	$\frac{1}{3}$ Rb_3IrH_6_p ↔ $\frac{1}{3}$ Ir + Rb + H_2	119.6
Cs_3IrH_6_p	12-Na_3RhH_6	1050	$\frac{1}{3}$ Cs_3IrH_6_p ↔ Cs + $\frac{1}{3}$ Ir + H_2	117.4
K_3RhH_6_p	12-Na_3RhH_6	1020	$\frac{1}{3}$ K_3RhH_6_p ↔ K + $\frac{1}{3}$ Rh + H_2	113.8
Rb_3RhH_6_p	12-Na_3RhH_6	960	$\frac{1}{3}$ Rb_3RhH_6_p ↔ Rb + $\frac{1}{3}$ Rh + H_2	103.9
Na_2PtH_2_p	37-Li_2PtH_2	960	Na_2PtH_2_p ↔ $\frac{3}{2}$ Na + $\frac{1}{2}$ $NaPt_2$ + H_2	103.6
Cs_3RhH_6_p	12-Na_3RhH_6	945	$\frac{1}{3}$ Cs_3RhH_6_p ↔ Cs + $\frac{1}{3}$ Rh + H_2	101.7
Na_4OsH_6_p	11-Li_4RuH_6	915	$\frac{1}{3}$ Na_4OsH_6_p ↔ $\frac{4}{3}$ Na + $\frac{1}{3}$ Os + H_2	95.5
K_3OsH_7_p	43-Na_3OsH_7	900	$\frac{2}{7}$ K_3OsH_7_p ↔ $\frac{2}{7}$ Os + $\frac{6}{7}$ K + H_2	92.7
K_3RuH_7_p	43-Na_3OsH_7	855	$\frac{2}{7}$ K_3RuH_7_p ↔ $\frac{6}{7}$ K + $\frac{2}{7}$ Ru + H_2	85.8
Rb_3OsH_7_p	43-Na_3OsH_7	840	$\frac{2}{7}$ Rb_3OsH_7_p ↔ $\frac{6}{7}$ Rb + $\frac{2}{7}$ Os + H_2	84.3
Cs_3OsH_7_p	43-Na_3OsH_7	825	$\frac{2}{7}$ Cs_3OsH_7_p ↔ $\frac{2}{7}$ Os + $\frac{6}{7}$ Cs + H_2	82.5
Rb_2PdH_4_p	4-Na_2PtH_4	825	Rb_2PdH_4_p ↔ Rb_2PdH_2_p + H_2	80.8
Rb_3RuH_7_p	43-Na_3OsH_7	795	$\frac{2}{7}$ Rb_3RuH_7_p ↔ $\frac{2}{7}$ Ru + $\frac{6}{7}$ Rb + H_2	77.5
Cs_3RuH_7_p	43-Na_3OsH_7	795	$\frac{2}{7}$ Cs_3RuH_7_p ↔ $\frac{6}{7}$ Cs + $\frac{2}{7}$ Ru + H_2	75.8
Cs_2ReH_9_p	1-K_2ReH_9	780	$\frac{2}{9}$ Cs_2ReH_9_p ↔ $\frac{4}{9}$ Cs + $\frac{2}{9}$ Re + H_2	73.3
Rb_2ReH_9_p	1-K_2ReH_9	765	$\frac{2}{9}$ Rb_2ReH_9_p ↔ $\frac{2}{9}$ Re + $\frac{4}{9}$ Rb + H_2	72.1
Cs_2TcH_9_p	1-K_2ReH_9	705	$\frac{2}{9}$ Cs_2TcH_9_p ↔ $\frac{2}{9}$ Tc + $\frac{4}{9}$ Cs + H_2	62.2
Rb_3CdH_5_p	30-K_3ZnH_5	705	$\frac{2}{5}$ Rb_3CdH_5_p ↔ $\frac{6}{5}$ Rb + $\frac{2}{5}$ Cd + H_2	61.9
Rb_2TcH_9_p	1-K_2ReH_9	690	$\frac{2}{9}$ Rb_2TcH_9_p ↔ $\frac{2}{9}$ Tc + $\frac{4}{9}$ Rb + H_2	61.0

7.3 Round 2 Thermodynamic Screening

We computed phase diagrams at the Round 2 level of theory for the 28 element spaces retained from Round 1 for $0 \leq T$ (K) ≤ 2000 at $P = 10^{-6}$, 10^{-4}, 10^{-2}, 1, and 100 bar H_2. In all, we computed the vibrational densities of states for 56 proposed CTMHs, including the 30 candidate materials listed in Table 7.1 and 27 other proposed CTMHs that complete the target element spaces. The updated structural parameters for these materials are available in Table D.3 in the Appendix. In general we used 2 × 2 × 2 supercells to compute phonon properties of the materials in this study. However, for computational expediency, we performed phonon calculations using 1 × 1 × 1 unit cells for Cs_3RhH_4, Cs_3RhH_6, Cs_3RuH_7, K_3OsH_7, K_3IrH_6, K_3RhH_6, Cs_3IrH_6, Cs_3OsH_7, Rb_3IrH_6, Rb_3OsH_7, Rb_3RhH_4, Rb_3RhH_6, and Cs_2TcH_9. We also neglected the proposed materials Rb_4OsH_6 or Cs_4OsH_6 in the 11-Li_4RuH_6 prototype, which are not predicted to form within the range of studied chemical potentials based on Round 1 screening, due to computational cost. K_4OsH_6 in the same prototype was not calculated to form at either Round 1 or Round 2 levels of theory. K_4RuH_6, Cs_4RuH_6, and Rb_4RuH_6 in the 11-Li_4RuH_6 prototype were studied with Round 2 level calculations, and none were predicted to be stable within the studied T, P range. For these reasons, neglecting Rb_4OsH_6 and Cs_4OsH_6 is not expected to affect the final phase stability results.

Figure 7.5 displays the mapping of the final stability predictions for both Round 1 calculations (stable = solid yellow and unstable = black "X") based on ground state energies for the condensed phases and Round 2 level calculations (stable = solid blue and unstable = blue "X") that include vibrational contributions to the free energies in the prediction of phase diagrams with the GCLP method. If a material was identified as a

stable component for the hydrogen chemical potentials associated with the *T* and *P* range studied, it is labeled as "forming". Based on our calculations, 34 and 46 proposed hydrides of the initial 149 hypothetical materials are predicted to be thermodynamically stable based on Round 2 and Round 1 levels of theory, respectively. All of the materials predicted to be stable based on Round 1 calculations that were subsequently studied at the higher level of theory were again indicated to be thermodynamically stable when accounting for vibrational effects.

Figure 7.5 indicates there are many hypothetical materials that should be thermodynamically preferred states in the given element spaces. These calculations assume that compound formation is thermodynamically controlled with no consideration of kinetics. Practically, there are kinetic limitations with the solid state reactions, and CTMH synthesis is performed at high hydrogen pressures and temperatures (~ 500-800 K), and it is difficult to obtain single crystals for high resolution materials characterization.[3,6] Bronger and Auffermann note that, for transition metals in multiple oxidation states across ternary hydrides, a higher reaction pressure is required to achieve the higher oxidation state.[6] Higher oxidation states have been particularly difficult to achieve experimentally when light cations like Li or Na are employed.[6] New synthesis techniques may be required to overcome kinetic barriers to reach the thermodynamically-preferred mixture of compounds. Since we are concerned, primarily, with identifying those proposed materials that operate at the conditions of the NGNP, we focused on thermodynamic screening rather than detailed characterization of new materials, including, for instance, magnetic and electronic properties. This area deserves future study.

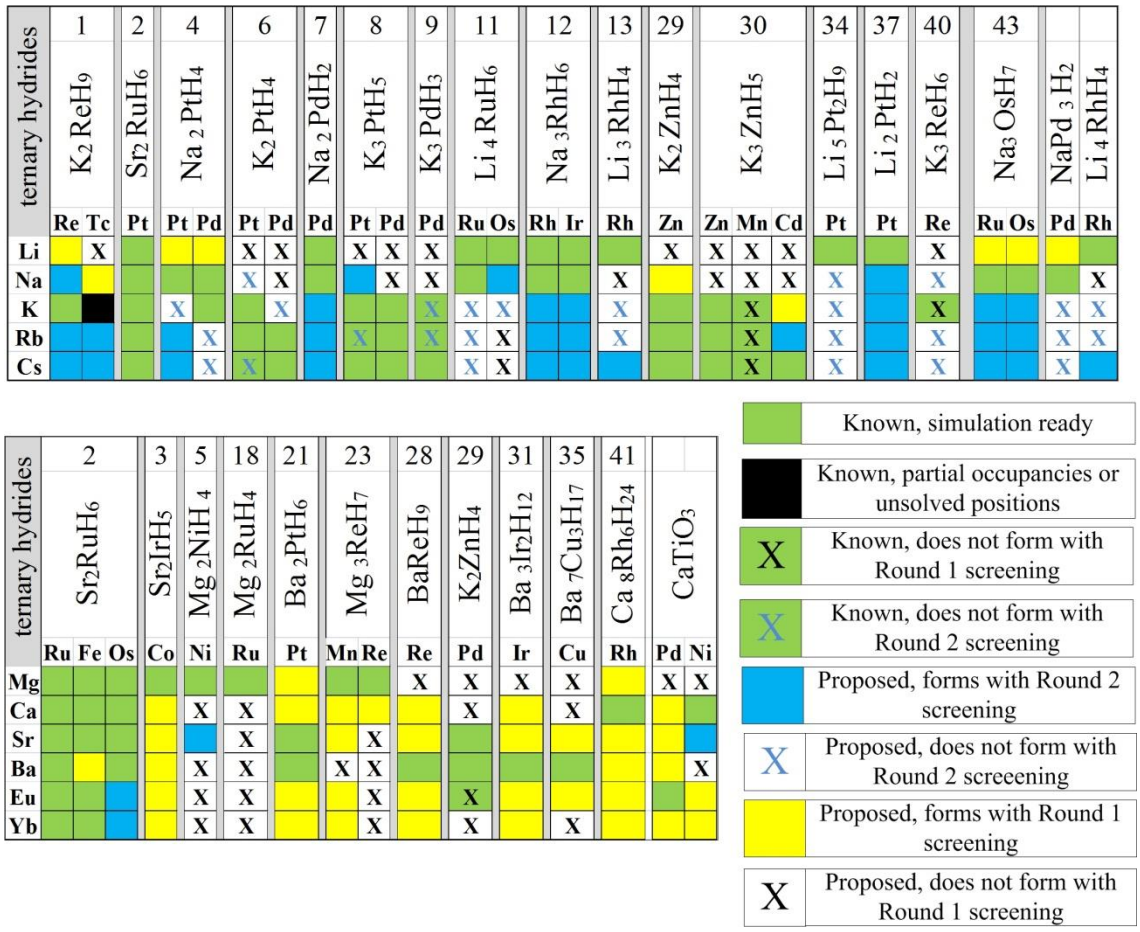

Figure 7.5: Mapping of final stability prediction for 149 proposed and known CTMH materials based on Round 1and Round 2 levels of DFT calculations and GCLP minimization. Experimentally-known ternary (*M*-*Tr*-H) Complex Transition Metal Hydrides are from the ICSD[1,2] and the Yvon and Renaudin 2005 Review.[3] Stable materials form between $0 \leq T$ (K) ≤ 2000 for $P = 10^{-6}$, 10^{-4}, 10^{-2}, 1, and 100 bar H_2. Calculations include additional intermetallic phases from the ICSD for new ternary element spaces that meet initial criterion $T_d/T_{d,binary} \geq 1$. Numbers are consistent with Yvon and Renaudin[3] and describe the chronological discovery of the prototype ternary hydride $M_x\ Tr_y\ H_z$ crystal structure shown vertically. Substitutional cations *M* of the same valence are grouped vertically. Substitutional transition metals *Tr* are listed horizontally. "Simulation ready" implies completely solved ordered structure with no partial occupancies.

Figure 7.6 shows the Round 2 absolute and relative decomposition temperatures for stable proposed CTMHs at 1 bar H_2. Relevant decomposition reactions and thermodynamic properties of all of the proposed materials that form for P = 1 bar H_2 are listed in Table 7.2. Seven of the proposed materials meet both screening criteria, i.e., $T_d/T_{d,binary} \geq 1$ and $T_d \geq 1000$ K. By comparison, 13 of the known or existing CTMHs that have been observed experimentally have enhanced stability relative to the binary hydrides and also release hydrogen at high temperature. As with the top candidates identified in Chapter 6 from the known materials, two of the top proposed materials are predicted to crystallize in the 2-Sr_2RuH_6 cubic prototype. Interestingly, where only its namesake was known to crystallize in the 37-Li_2PtH_2 prototype, our calculations predict that K_2PtH_2_p, Rb_2PtH_2_p, and Cs_2PtH_2_p are thermodynamically preferred at high temperature. Cs_2PdH_2 and Sr_2NiH_4, in the 7-Na_2PdH_2 and 5-Mg_2NiH_4 structures, respectively, are also the only materials studied, either existing or proposed, that meet the screening criteria and crystallize with those symmetries.

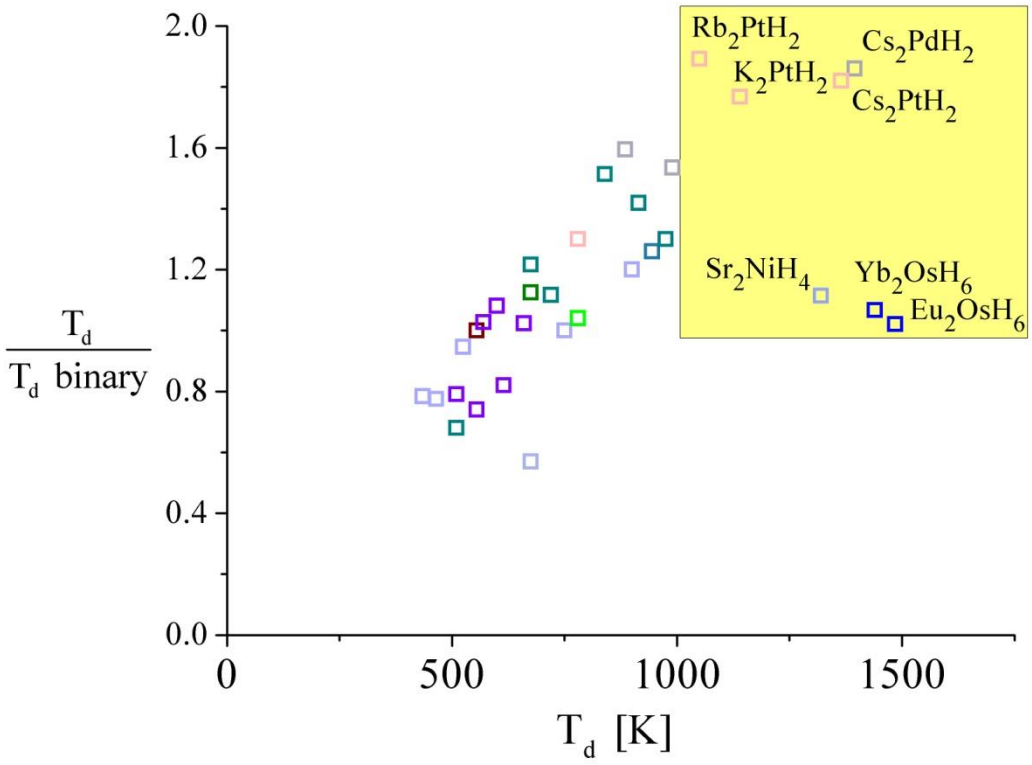

Figure 7.6: Relative and absolute thermal stabilities for stable proposed ternary CTMHs predicted with Round 2 level of screening. Color indicates structure prototype.

Table 7.2: Thermodynamic properties of stable proposed phases at P=1 bar H_2 from Round 2 calculations, including vibrational corrections to the Helmholtz free energy for condensed phases. Standard conditions (300 K, 1 bar H_2). T_d (K), ΔH (kJ mol^{-1} H_2), ΔS (kJ K^{-1} mol^{-1} H_2).

CTMH	T_d	Decomposition Pathway	$\Delta H°$	$\Delta S°$	$\Delta H(T_d)$
		final candidates			
Eu_2OsH_6_p	1485	⅓ Eu_2OsH_6_p ↔ ⅔ Eu + ⅓Os + H_2	197.6	0.131	191.0
Yb_2OsH_6_p	1440	⅓ Yb_2OsH_6_p ↔ ⅓ Os + ⅔ Yb_ + H_2	193.4	0.132	187.6
Cs_2PdH_2_p	1395	Cs_2PdH_2_p ↔ Pd + 2Cs + H_2	124.8	0.101	101.3
Cs_2PtH_2_p	1365	Cs_2PtH_2_p ↔ Cs_2Pt + H_2	144.3	0.111	130.3
Sr_2NiH_4_p	1320	½ Sr_2NiH4_p ↔ ½Ni + Sr + H_2	166.6	0.128	158.4
K_2PtH_2_p	1140	K_2PtH_2_p ↔ 2K + Pt + H_2	159.5	0.140	154.8
Rb_2PtH_2_p	1050	Rb_2PtH_2_p ↔ Pt + 2Rb + H_2	147.0	0.141	143.3
		screened candidates			
K_2PdH_2_p	990	K_2PdH_2_p ↔ 2K + Pd + H_2	137.2	0.140	133.2
Cs_3IrH_6_p	975	⅓ Cs_3IrH_6_p ↔ Cs + ⅓Ir + H_2	113.1	0.119	106.8
Cs_2PtH_4_p	945	Cs_2PtH_4_p ↔ Cs_2PtH_2_p + H_2	121.3	0.126	121.2
K_3IrH_6_p	915	⅓ K_3IrH_6_p ↔ K + ⅓Ir + H_2	125.9	0.137	125.1
Cs_2ReH_9_p	900	⅔ Cs_2ReH_9_p ↔ ⅔ Re + ⅘ Cs + H_2	81.9	0.085	91.9
Rb_2PdH_2_p	885	Rb_2PdH_2_p ↔ Pd + 2Rb + H_2	123.4	0.140	120.6
Rb_3IrH_6_p	840	⅓ Rb_3IrH_6_p ↔ ⅓Ir + Rb + H_2	116.5	0.138	116.1
Cs_3RhH_4_p	780	½ Cs_3RhH_4_p ↔ ⅗ Cs + ½Rh + H_2	88.1	0.116	101.5
Na_2PtH_2_p	780	Na_2PtH_2_p ↔ ⅗ Na + ½$NaPt_2$ + H_2	101.8	0.131	82.6
Cs_2TcH_9_p	750	⅖ Cs_2TcH_9_p ↔ ⅖Tc + ⅘ CsH + H_2	80.9	0.116	69.5
K_3RhH_6_p	720	⅓ K_3RhH_6_p ↔ ⅓Rh + K + H_2	114.1	0.156	118.4
Na_4OsH_6_p	675	⅓ Na_4OsH_6_p ↔ ⅓Os + ⅘ Na + H_2	92.5	0.137	106.9
Rb_3RhH_6_p	675	⅓ Rb_3RhH_6_p ↔ ⅓Rh + Rb + H_2	104.4	0.153	93.5
$SrNiH_3$_p	675	2 $SrNiH_3$_p ↔ Ni + Sr_2NiH4_p + H_2	94.6	0.141	94.5
K_3OsH_7_p	660	⅖ K_3OsH_7_p ↔ ⅖ Os + ⅖ K + H_2	87.7	0.133	88.9
Cs_3OsH_7_p	615	½ Cs_3OsH_7_p ↔ ⅗ CsH + ½Os + H_2	74.1	0.117	78.4
Rb_3OsH_7_p	600	⅖ Rb_3OsH_7_p ↔ ⅖ Rb + ⅖ Os + H_2	80.0	0.134	81.1
Rb_3RuH_7_p	570	⅖ Rb_3RuH_7_p ↔ ⅖ Ru + ⅖ Rb + H_2	75.7	0.134	76.7
Cs_3RuH_7_p	555	½ Cs_3RuH_7_p ↔ ½Ru + ⅗ CsH + H_2	66.5	0.119	46.5
Rb_3CdH_5_p	555	Rb_3CdH_5_p ↔ Cd + 3RbH + H_2	45.6	0.110	69.9
Rb_2ReH_9_p	525	⅖ Rb_2ReH_9_p ↔ ⅖ Re + ⅘ RbH + H_2	74.8	0.138	82.6
Cs_3RhH_6_p	510	Cs_3RhH_6_p ↔ Cs_3RhH_4_p + H_2	119.4	0.232	81.9
K_3RuH_7_p	510	½ K_3RuH_7_p ↔ ½Ru + ⅗ KH + H_2	76.0	0.146	130.4
Rb_2TcH_9_p	435	⅖ Rb_2TcH_9_p ↔ ⅖ Tc + ⅘ RbH + H_2	60.2	0.136	64.9

7.4 Phase Diagrams for Final Candidates

7.4.1 Eu_2OsH_6_p and Yb_2OsH_6_p (2-Sr_2RuH_6 prototype)

Eu_2RuH_6,[7] Eu_2FeH_6,[8] Yb_2RuH_6,[9,10] and Yb_2FeH_6[3] have been synthesized in the fcc 2-Sr_2RuH_6 prototype (Na_2PtCl_6-type structure). Previous Round 1 (ground state) calculations for Eu(Yb)−Fe−H and Round 2 (phonon-corrected) calculations for Eu(Yb)−Ru−H from Chapter 6 verify that these phases are thermodynamically-preferred. Our calculations in this chapter indicate that Eu_2OsH_6_p and Yb_2OsH_6_p in this prototype are also thermodynamically stable phases. The calculated phase diagrams for 1 bar H_2 are displayed in Figure 7.7. In both cases, the only known competing compounds are the pure metals and binary hydrides. While Huang et al. attempted syntheses for metal combinations (Ca−Fe, Sr−Fe, Eu−Fe, Mg−Ru, Mg−Os, and Ca−Os), resulting in the characterizations of known 2-Sr_2RuH_6 materials shown in Figure 7.5, they do not report attempting to form ternary hydrides from the combination of Eu−Os−H.[8] To our knowledge, no experimental investigations of these ternary series have been carried out.

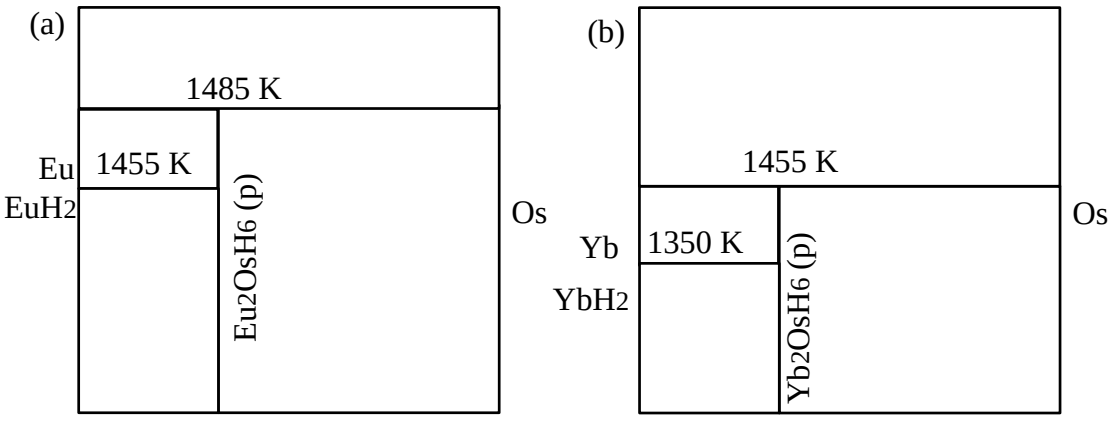

Figure 7.7: Predicted phase diagrams based on GCLP minimization including vibrational free energies for (a) Eu−Os−H and (b) Yb−Os−H at P = 1 bar H_2.

7.4.2 Cs_2PdH_2_p (7-Na_2PdH_2 prototype)

Stable compounds have been synthesized and characterized for Li_2PdH_2[11] and Na_2PdH_2[11-13] in the tetragonal I4/mmm 7-Na_2PdH_2 crystal structure with linear H−Pd−H complexes. However, no experimentally-identified CTMH has been reported for Cs_2PdH_2_p in this prototype structure. Synthesis of Cs_2PdH_4 has been carried out by Bronger and Auffermann, and they found that the high temperature form of the ternary hydride for the *M*:Pd ratio of 2:1 is a cubic K_2PtCl_6-type structure with a hydrogen partial occupancy factor of 2/3.[14] Materials with partial occupancies are not considered in the current work. However, comparing the ordered compounds without partial occupancies, we have computed the phase diagrams for the Cs−Pd−H system both based only on known compounds and with the proposed phases, shown in Figure 7.8. We predict a stable high temperature Cs_2PdH_2_p compound in the 7-Na_2PdH_2 prototype. The highest temperature achieved for a hydride phase based on known materials is T_d = 1020 K for Cs_3PdH_3. Including the proposed phase increases this predicted stability to T_d = 1395 K for Cs_2PdH_2_p. The Cs_3PdH_3 phase is destabilized by the proposed phase. If a Cs_2PdH_4 material with partial hydrogen occupancies is thermodynamically stable, but not included in these calculations, it would have a lower free energy than the Cs_2PdH_2_p phase and destabilize the Cs_3PdH_x hydrides to a greater degree. If a more stable ternary hydride exists in this elemental system, our calculations can be considered a lower limit to the hydrogen release temperature for Cs-Pd hydrides.

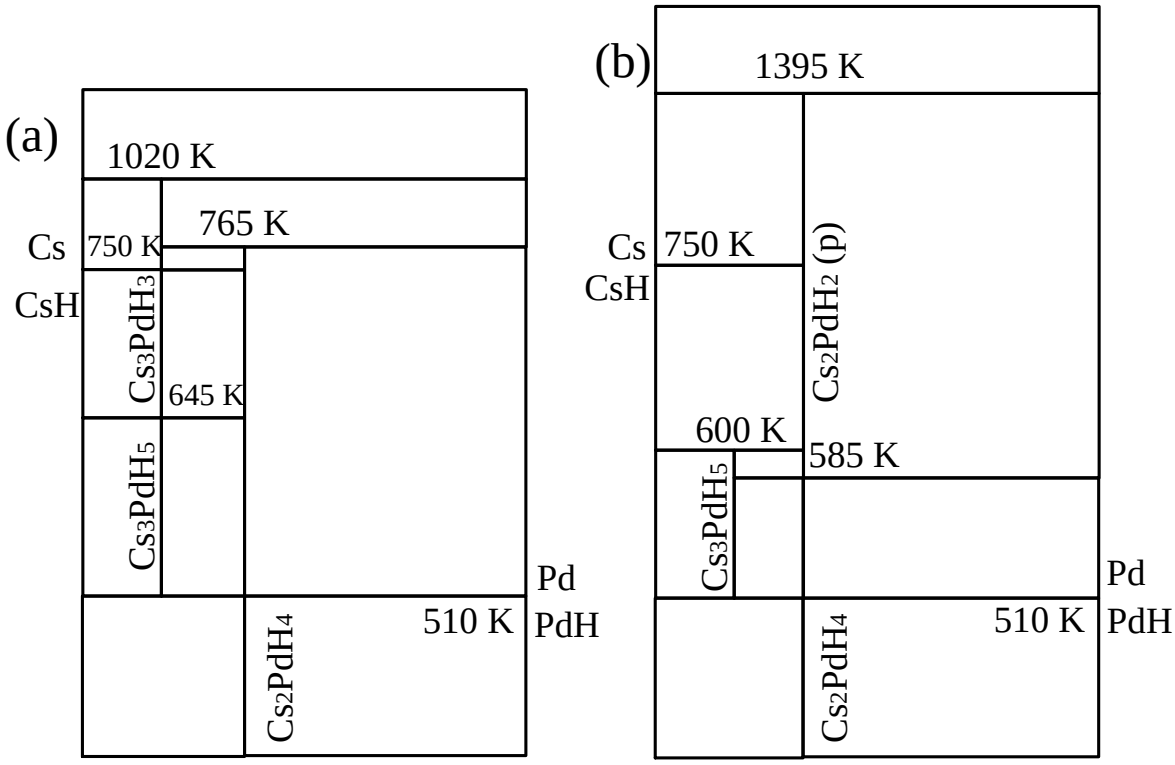

Figure 7.8: Predicted phase diagrams based on GCLP minimization including vibrational free energies for the Cs−Pd−H at P = 1 bar H_2 with (a) only known materials and (b) proposed phases.

7.4.3 K_2PtH_2_p, Rb_2PtH_2_p, Cs_2PtH_2_p (37-Li_2PtH_2 prototype)

The crystal structure for Li_2PtH_2, shown in Figure 7.9, is described as an orthorhombic distortion of tetragonal Li_2PdH_2 (7-Na_2PdH_2 prototype) with linear $[PtH_2]^{2-}$ complexes.[3]

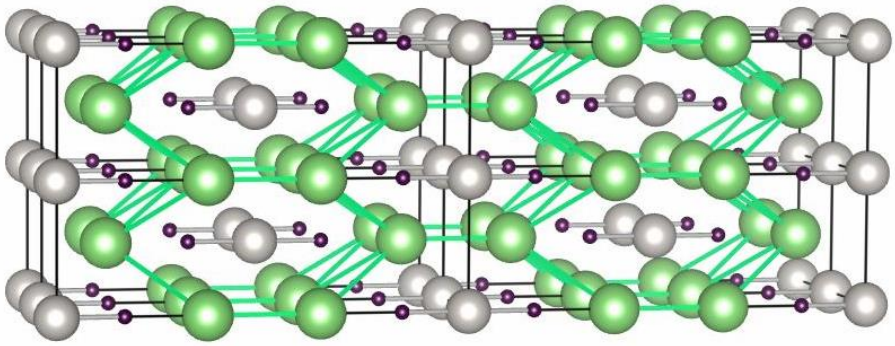

Figure 7.9: Crystal structure for 37-Li_2PtH_2 with Immm symmetry. Li, Pt, and H atoms are represented by green (large), grey (medium), and black (small) spheres, respectively. Li-Li bonds shown for effect.

37-Li_2PtH_2 has been synthesized experimentally by decomposing $Li_5Pt_2H_9$ at 493 K in an argon atmosphere into $2Li_2PtH_2 + LiH + 2H_2$.[15,16] Our calculations for the Li−Pt−H system based on Round 1 level ground state energies for condensed phases, including all known binary intermetallic phases, are consistent with the experiment. We predict $Li_5Pt_2H_9$ decomposes at 615 K with P = 1 bar H_2 via

$$\tfrac{1}{2}Li_5Pt_2H_9 \leftrightarrow Li_2PtH_2 + \tfrac{1}{2}LiH + H_2 \quad (7.1)$$

and that Li_2PtH_2 releases hydrogen at 840 K via

$$Li_2PtH_2 \leftrightarrow Li_2Pt + H_2 \quad (7.2)$$

It appears that no attempt has been made to synthesize K_2PtH_2_p, Rb_2PtH_2_p, or Cs_2PtH_2_p experimentally, but our calculations indicate that these compositions are

stable at high temperature in the 37-Li_2PtH_2 prototype crystal structure. Unlike the Li−Pt—H element space, no other alkali metal-substituted hydride is stable in the 34-$Li_5Pt_2H_9$ prototype, and hydrides that form from a 2 *M* : 1 Pt ratio in the K−Pt—H and -Rb−Pt−H systems are predicted to decompose via (Eqs. (7.3-7.5)) with T_d (*M* = K, *M* = Rb) shown in parentheses:

$$M_2PtH_6 \leftrightarrow M_2PtH_4 + H_2 \text{ (555 K, 570 K)} \quad (7.3)$$

$$M_2PtH_4 \leftrightarrow M_2PtH_2\_p + H_2 \text{ (660 K, 975 K)} \quad (7.4)$$

$$M_2PtH_2\_p \leftrightarrow 2M + Pt + H_2 \text{ (1140 K, 1050 K)} \quad (7.5)$$

The binary intermetallic Cs_2Pt, the analog of which is not known for the K−Pt or Rb−Pt systems, destabilizes Cs_2PtH_2_p, and the hydrides at a 2 Cs : 1 Pt ratio in the Cs−Pt−H system decompose via:

$$Cs_2PtH_6 \leftrightarrow Cs_2PtH_4\_p + H_2 \ (T_d = 510 \text{ K}) \quad (7.6)$$

$$Cs_2PtH_4\_p \leftrightarrow Cs_2PtH_2\_p + H_2 \ (T_d = 945 \text{ K}) \quad (7.7)$$

$$Cs_2PtH_2\_p \leftrightarrow Cs_2Pt + H_2 \ (T_d = 1365 \text{ K}) \quad (7.8)$$

Besides the binary intermetallic that forms in the Cs−Pt space, the ternary CTMH Cs_2PtH_4_p is also predicted to form. Based on the calculated phase diagram at 100 bar H_2, we also note that Rb_2PtH_4_p (4-Na_2PtH_4) with I4/mmm is stabilized over the known Rb_2PtH_4 (6-K_2PtH_4) with P42/mmm symmetry. The main difference between these crystal structures is the rotation of the $[PtH_4]^{2-}$ square planar complex perpendicular to the tetragonal base for the P42/mmm structure. Both materials have cubic or nearly cubic cation submatrices.[3] Our calculations do not account for disordered structures or structures with partial hydrogen occupancies. Experimentally, it has been observed that K_2PtH_4, Rb_2PtH_4, and Cs_2PtH_4 transition to disordered cubic structures similar to 2-

Sr_2RuH_6 with 2/3 partial hydrogen occupancies close to room temperature.[3,6] As previously discussed, if this disordered modification is a thermodynamically stable state, it is expected to have a lower free energy than the materials considered here, and hydrogen would be further stabilized in the structure. Our calculations can then be taken as a lower bound on the thermodynamic stability of CTMHs in the element spaces, again assuming that no high temperature binary intermetallic phase exists but is unknown at this time.

Calculated phase diagrams at P = 1 bar H_2 with and without proposed phases are shown in Figures (7.10-7.12) for K−Pt−H, Rb−Pt−H, and Cs−Pt−H, respectively. We highlight the increase in hydrogen release temperature when including the proposed phases for these element spaces. Experimentally, K_3PtH_5 decomposes at 673 K into KH and K_2PtH_4.[3] Our calculations predict a slightly less thermodynamically stable binary hydride, but cannot resolve the energy difference associated with 15 K or ~ 2 kJ mol^{-1} H_2 (assuming $\Delta T_d \sim \Delta H/\Delta S$ and ΔS = 0.131 kJ K^{-1} mol^{-1} H_2). We can expect that the DFT resolves the relative stabilities of K_3PtH_5 and K_2PtH_4 with higher fidelity due to the broad difference in the predicted T_d of nearly 300 K. Our calculations do not capture the experimentally-observed Rb_3PtH_5 phase for any of the studied hydrogen pressures. Since this composition is predicted to form in the similar Cs−Pt−H element space, this suggests that the DFT calculations are in error for this composition. For the Rb−Pt−H and Cs−Pt−H element spaces, the M_3PtH_5 composition is known to transition to a high temperature disordered cubic phase at 465 K and 615 K, respectively. Again, our calculations do not consider disordered phases.

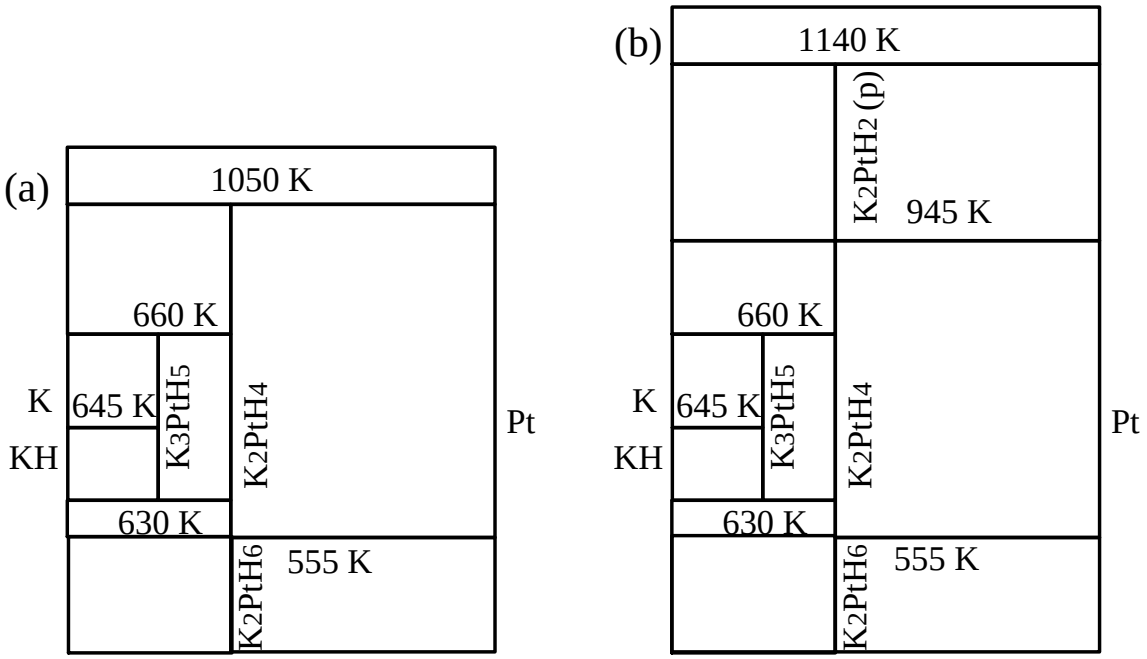

Figure 7.10: Predicted phase diagrams based on GCLP minimization including vibrational free energies for the K−Pt−H at P = 1 bar H_2 with (a) only known materials and (b) proposed phases.

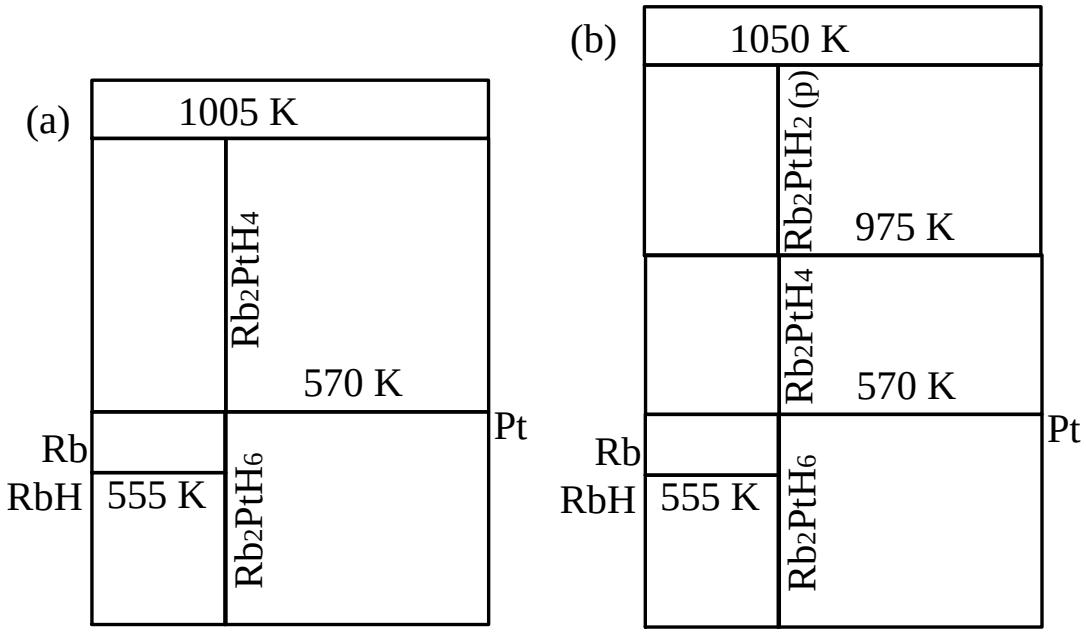

Figure 7.11: Predicted phase diagrams based on GCLP minimization including vibrational free energies for the Rb−Pt−H at P = 1 bar H_2 with (a) only known materials and (b) proposed phases.

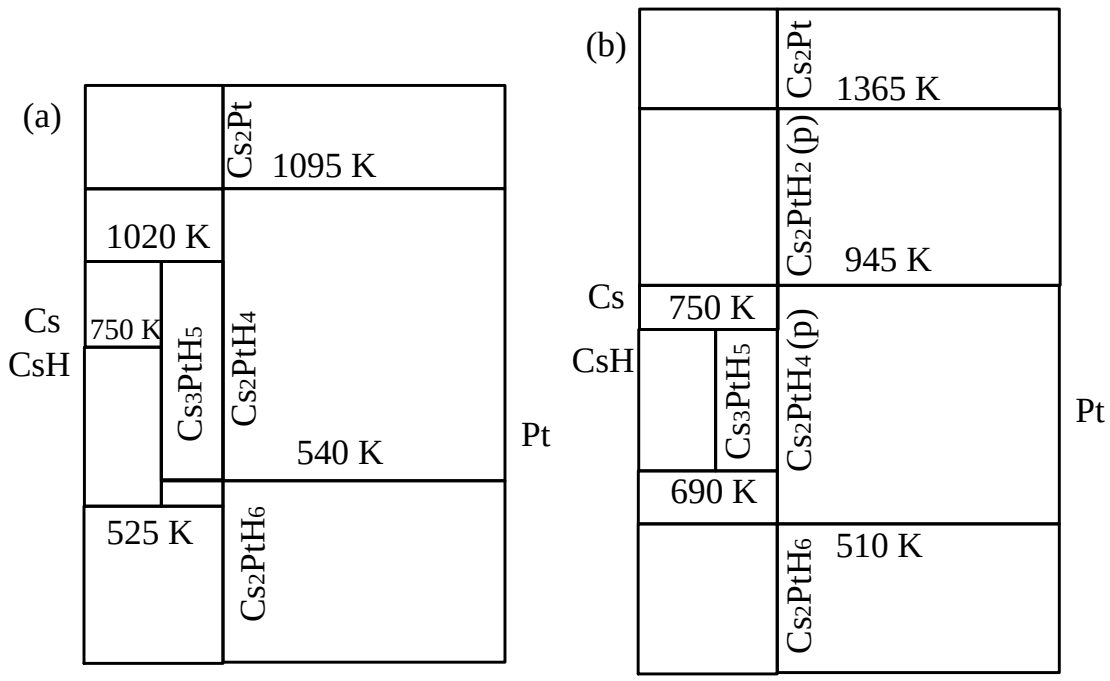

Figure 7.12: Predicted phase diagrams based on GCLP minimization including vibrational free energies for the Cs−Pt−H at P = 1 bar H_2 with (a) only known materials and (b) proposed phases.

7.4.4 Sr_2NiH_4_p (5-Mg_2NiH_4 prototype)

Based on Round 2 level calculations, Sr_2NiH_4_p is thermodynamically stable in the 5-Mg_2NiH_4 prototype structure. There are currently no known CTMHs that form in the Sr−Ni−H element space, which makes this and the other predicted stable proposed compound, $SrNiH_3$_p, unique among the materials studied in this chapter. Figure 7.13 shows the predicted phase diagrams for the known Mg−Ni−H and proposed Sr−Ni−H element spaces, including vibrational corrections, at P = 1 bar H_2. Literature reports for T_d of Mg_2NiH_4, which forms the intermetallic Mg_2Ni and hydrogen upon heating experimentally, are about 520 K.[17,18] However, other authors have reported values up to 673 K depending on the measurement method used. [17,19] Our calculations give T_d = 495 K for Mg_2NiH_4 in reasonable agreement with the experimental value. We neglected the

high temperature disordered phase of Mg_2NiH_4, similar to 2-Sr_2RuH_6 with partial occupancies, and so our calculations may be taken as a lower limit on the thermal stability of this composition.[3]

To our knowledge, no attempt has been made to synthesize either Sr_2NiH_4_p or $SrNiH_3$_p. While there is a Sr_2Ni_3 intermetallic compound with partial occupancies, there is no known Sr_2Ni intermetallic compound that is analogous to the Mg_2Ni phase, and our calculations show that the hypothetical Sr_2NiH_4 decomposes to the elements and hydrogen at T_d = 1320 K. This represents the only compound from either Chapter 6, based on existing CTMHs, or Chapter 7, including hypothetical materials that are similar to the known compounds, that meets both screening criteria and that contains the relatively common Ni metal.

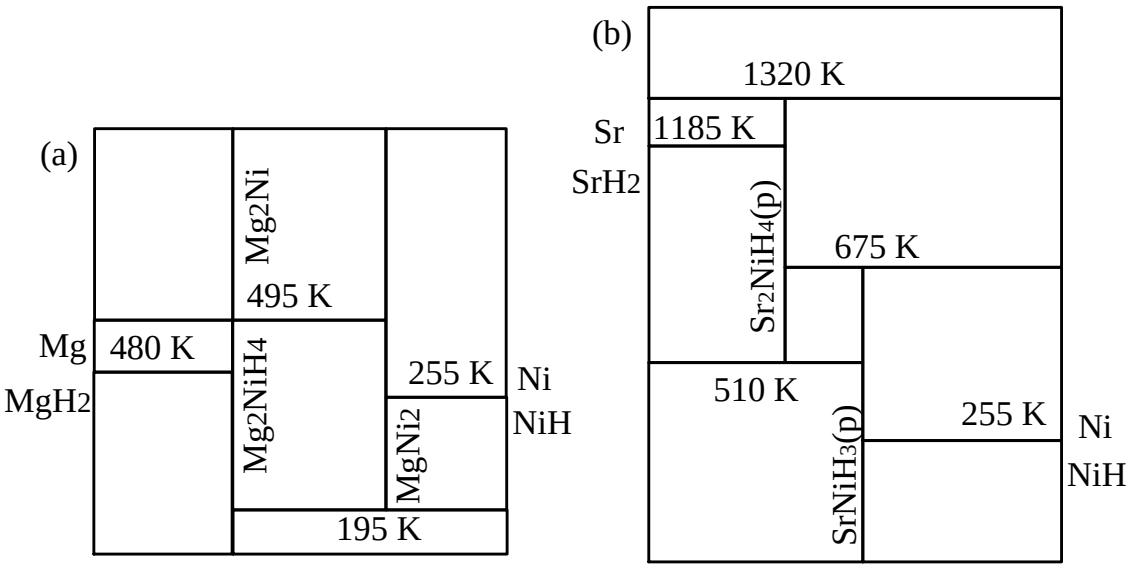

Figure 7.13: Predicted phase diagram based on GCLP minimization including vibrational free energies for (a) the known Mg−Ni−H and (b) proposed Sr−Ni−H element spaces at P = 1 bar H_2.

7.5 van't Hoff Plots

Figure 7.14 shows the van't Hoff plots for the final candidate proposed materials from Table 7.2. Eu_2OsH_6_p and Yb_2OsH_6_p are the most stable of the hypothetical hydrides over the studied temperature range. The calculations predict that, at the highest temperatures, Cs_2PdH_2_p and Cs_2PtH_2_p are nearly as thermodynamically stable as the rare earth osmium hydrides. This is primarily attributed to the low calculated entropy of reaction for the Cs-based materials.

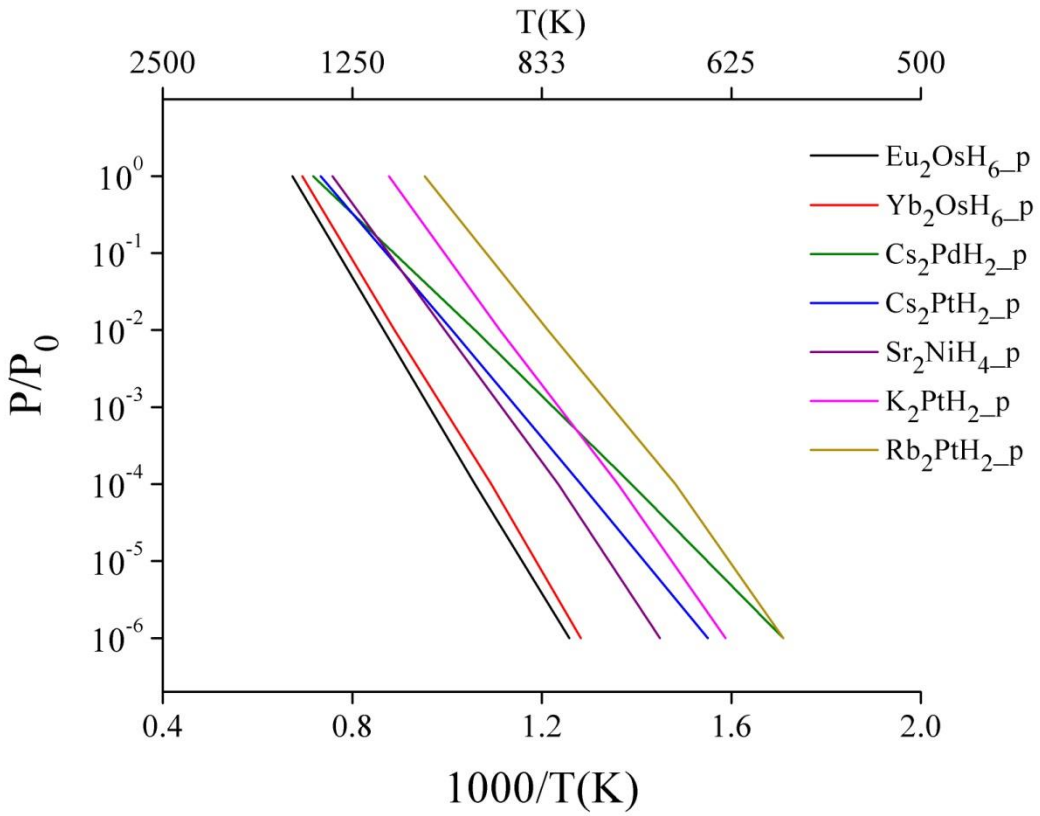

Figure 7.14: van't Hoff plots for final proposed candidate CTMHs from Table 7.2 based on Round 2 level of screening.

Figure 7.15 shows the van't Hoff plots for the most thermodynamically stable proposed and known CTMHs along with the associated binary hydrides. Several of the curves are nearly degenerate: (1,3) Eu_2RuH_6 and Eu_2OsH_6_p, (2,7) Yb_2OsH_6_p, EuH_2, and Yb_2RuH_6, (8,5) YbH_2 and Ca_2RuH_6, and (6) CaH_2. In each case, the CTMH exhibits lower H_2 overpressures than the associated binary hydride, as expected. This work also shows that hypothetical hydrides of Eu and Yb are at least as thermodynamically stable as the most stable known material. These curves represent the CTMHs with lowest overall hydrogen equilibrium pressures for the NGNP application and should be useful for determining whether or not this class can meet systems design parameters once the target overall uptake of hydrogen and tritium are determined.

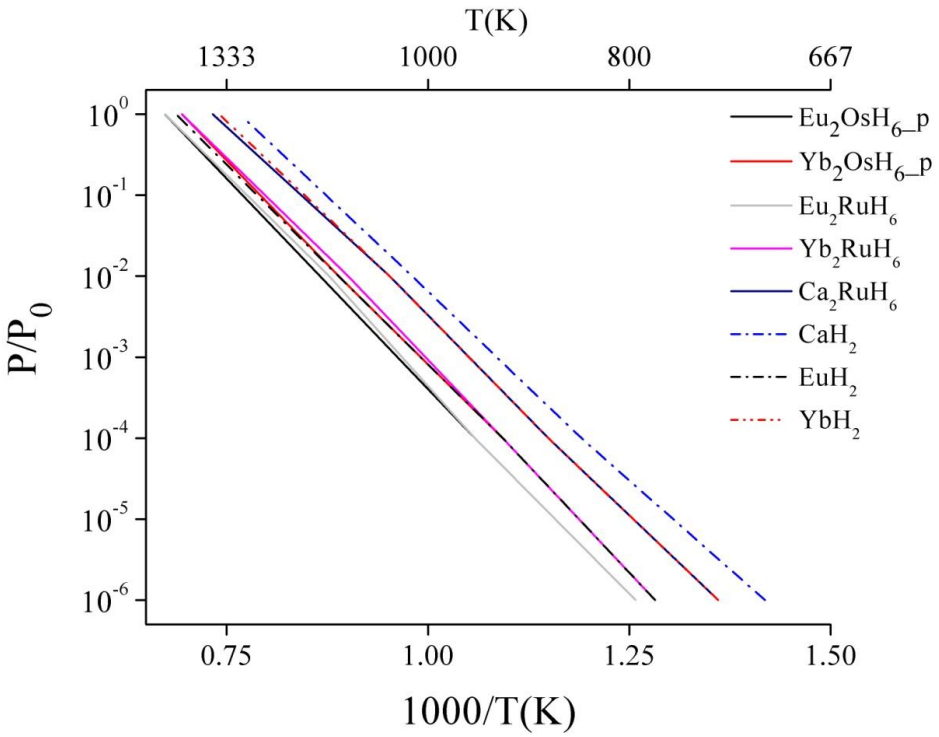

Figure 7.15: van't Hoff plots for top known and proposed CTMH candidates that meet screening criteria from Tables 6.5 and Table 7.2 based on Round 2 level calculations including vibrational corrections to free energy.

7.6 Conclusions

We have successfully used DFT and GCLP minimization calculations to screen a set of 149 proposed or hypothetical CTMH materials based on the existing prototypes studied in Chapter 6. Using a tiered approach for computational efficiency that computes the stable mixture of compounds pulled from a materials library for a given chemical potential, we predict that 81 of the 149 materials are thermodynamically preferred in the studied *T*, *P* range. Thirty four were stable at the Round 2 level of theory that accounts for vibrational effects, and 46 stable materials were indicated at only the Round 1 levels of theory based on ground state energies alone for condensed phases. Of these stable materials, seven meet the screening criteria of enhanced stability relative to the binary hydrides and high hydrogen release temperature for the NGNP application. Two of the proposed materials have hydrogen equilibrium pressures nearly identical to the most thermodynamically stable known materials. The calculated phase diagrams should be useful for setting operating limits for the hydrides. Future computational work could focus on further characterizing the properties of the stable proposed materials, in particular electronic and magnetic properties that may be unique for the hypothetical materials.

7.7 References

[1] FIZ Karlsruhe and NIST, *THE INORGANIC CRYSTAL STRUCTURE DATABASE (ICSD)*.

[2] G. Bergerhoff and I. D. Brown, in *Crystallographic Databases*, edited by F. H. Allen, G. Bergerhoff and R. Severs (International Union of Crystallography, Chester, 1987).

[3] K. Yvon and G. Renaudin, in *Encyclopedia of Inorganic Chemistry, Second Edition*, edited by B. R. King (John Wiley & Sons, Chichester, 2005), Vol. III, p. 1814.

[4] R. Shannon, *Acta Crystallogr.* **32**, 751 (1976).

[5] C. Wolverton and V. Ozoliņš, *Phys. Rev. B* **75**, 064101 (2007).

[6] W. Bronger and G. Auffermann, *Chem. Mater.* **10**, 2723 (1998).

[7] J. S. Thompson, R. O. Moyer, and R. Lindsay, *Inorg. Chem.* **14**, 1866 (1975).

[8] B. Huang, F. Bonhomme, P. Selvam, K. Yvon, and P. Fischer, *J. Less-Common Met* **171**, 301 (1991).

[9] R. Lindsay, R. O. Moyer, J. S. Thompson, and D. Kuhn, *Inorg. Chem.* **15**, 3050 (1976).

[10] R. O. Moyer Jr, D. F. R. Gilson, and B. H. Toby, *J. Solid State Chem.* **184**, 1895 (2011).

[11] R. V. Kasowski, D. Noreus, L. Wang, and M. H. Whangbo, *Inorg. Chem.* **31**, 4737 (1992).

[12] D. Noréus and J. Tomkinson, *Chem. Phys. Lett.* **154**, 439 (1989).

[13] D. Noréus, K. W. Törnroos, A. Börje, T. Szabò, W. Bronger, H. Spittank, G. Auffermann, and P. Müller, *J. Less-Common Met* **139**, 233 (1988).

[14] W. Bronger and G. Auffermann, *J. Alloys Compd.* **187**, 87 (1992).

[15] W. Bronger and L. à. Brassard, *Z. Anorg. Allg. Chem.* **622**, 462 (1996).

[16] M.-S. Liao, Q.-E. Zhang, and W. H. E. Schwarz, *Z. Anorg. Allg. Chem.* **624**, 1419 (1998).

[17] R. Martínez-Coronado, M. Retuerto, B. Torres, M. J. Martínez-Lope, M. T. Fernández-Díaz, and J. A. Alonso, *Int. J. Hydrogen Energy* **38**, 5738 (2013).

[18] J. Jiang, S. Zhang, S. Huang, P. Wang, and H. Tian, *Comput. Mater. Sci.* **74**, 55 (2013).

[19] M. Polanski, T. K. Nielsen, I. Kunce, M. Norek, T. Płociński, L. R. Jaroszewicz, C. Gundlach, T. R. Jensen, and J. Bystrzycki, *Int. J. Hydrogen Energy* **38**, 4003 (2013).

CHAPTER 8

ELPASOLITE HALIDES*

8.1 Introduction

Scintillators with improved performance that can be produced cost effectively at industrial scales are needed in fields such as national defense, nuclear activity monitoring, and particle physics research. [1-3] Cerium-doped lanthanum halides exhibit excellent room temperature radiation detection properties, but efforts to replace the size-limited Bridgman single crystal growth process with methods that produce high quality polycrystalline ceramics have been unsuccessful.[1,3] Anisotropic crystal structures, mechanical instability, and temperature sensitivity of these materials present manufacturing difficulties. Elpasolite-type scintillator materials such as Cs_2LiYCl_6, conversely, are attractive for large scale production because some of these compounds crystallize in the fcc double perovskite structure associated with desirable isotropic optical and mechanical properties.[4] The cubic structure minimizes lattice strain during single crystal growth and reduces light scattering at grain boundaries.[1,2]

Elpasolite halides possess the chemical formula $A_2^+B^+B'^{3+}X_6^-$ where A^+ and B^+ are typically alkali metal cations, B'^{3+} is a trivalent cation such as a rare-earth or transition metal, and X^- is a halogen anion. While the majority of known elpasolite halides crystallize in the Fm-3m cubic structure, lower symmetry variations occur with changes in composition, temperature, and pressure.[5] Commonly, elpasolites transition reversibly

* Reprinted from J. Alloys Compd, 577, K. M. Nicholson, S. G. Kang, and D. S. Sholl, "First principles methods for elpasolite halide crystal structure prediction at finite temperatures", 463-468, Copyright (2013), with permission from Elsevier.

from a low temperature tetragonal phase to a high temperature cubic symmetry. For instance, $Cs_2NaPrCl_6$ and $Rb_2NaTmCl_6$ undergo tetragonal to cubic phase transitions at 158 K and 441 K, respectively.[5] Elpasolites have also been observed in trigonal and orthorhombic symmetries.[5]

In this chapter, we extend methods developed in Chapter 2 in order to determine the minimum level of theory needed to identify the temperature-dependent stable crystal structure of four elpasolite halides using DFT. Such modeling capabilities will be useful for identifying cubic elpasolite halide scintillators and for providing phase stability information to guide experiments. Specifically, we use DFT to study the relative thermodynamic stabilities of common cubic, tetragonal, and trigonal phases for $Cs_2NaGdBr_6$, $Cs_2NaLaBr_6$, Cs_2LiLaI_6, and Cs_2LiScI_6. The bromo-elpasolites are known experimentally to undergo phase transitions from tetragonal to cubic structures at 173 K and 316 K for $Cs_2NaGdBr_6$ and $Cs_2NaLaBr_6$, respectively.[6] Cs_2LiScI_6 crystallizes in the trigonal P-3ml crystal structure, presumably at low temperature,[5] and no experimental data on the crystal structure of Cs_2LiLaI_6 is available. Useful thermodynamic models should be able to reproduce the known phase behavior and make an informed prediction for the stable structure of Cs_2LiLaI_6 at finite temperatures. We compare phase predictions based on three levels of theory. In order of increasing computational complexity, these levels include DFT total energies at 0 K that ignore vibrational contributions, a simple harmonic model at uncorrected ground state volumes, and a quasiharmonic model that accounts for thermal expansion.

Methods that have been previously applied to predict phase stability of scintillator materials include both semi-empirical and atomistic approaches. The semi-empirical

Goldschmidt tolerance factor has been successful in predicting low temperature crystal structures of perovskite materials.[5] This quantity is based on ideal fcc packing of hard-core spheres with volumes referenced from the ionic radii of constituent atoms. Tolerance factors much greater or less than one indicate distortions of the ideal cubic structure are likely. Babel et al. adapted the tolerance factor for double perovskite elpasolites as

$$t' = \frac{r(A) + r(X)}{\sqrt{2}\left(\frac{r(B) + r(B')}{2} + r(X)\right)} \tag{8.1}$$

where *r* indicates the ionic radius.[7] Use of this criterion, however, does not take into account environmental considerations such as charge transfer and polarizability of ions, and it breaks down for materials such as the chloro-elpasolites.[5] Moving beyond the Goldschmidt criterion, a molecular dynamics approach based on an embedded ion method that accounts for charge transfer has recently been developed that accepts various properties such as bond lengths, electronegativities, and bond energies. It has been used to predict the crystal structures of alkali halides through simulated annealing and to probe mechanical properties of $LaBr_3$.[4]

While simulated annealing methods are useful for predicting crystal structures for materials with no information available regarding phase stability, DFT-based methods that probe relative stabilities of phases directly may be more computationally efficient for elpasolite halides since the observed crystal structures tend to fall within a small set of likely structures. DFT-based methods are routinely used for geometry optimization, electronic property determination, and ground state crystal structure prediction.[8-14] Several large scale efforts have been made to determine the stable phases of alloys based on DFT total energies at 0 K.[15-19] Higher level methods that evaluate the thermodynamic

properties of solids at finite temperature are also commonplace. For example, calculations of the free energy within the simple harmonic level of theory have been used to construct phase diagrams and compute free energies of reaction.[20,21] Quasiharmonic and even explicit anharmonic correction methods have been applied to compute thermodynamic properties of solids, particularly of minerals at elevated pressure.[22-27]

8.2 Levels of Theory

At a given temperature, the thermodynamically-preferred phase is that with the lowest Gibbs free energy as given by Eq. (2.4). In our calculations the external pressure P was zero so the quantity calculated was $G = F$, referred to below as the free energy. Three approximations to F with varying computational complexities were utilized:

(1) The simplest ground state model is described by Eq. (2.6). This model ignores vibrational contributions to the free energy and cannot explicitly predict temperature-dependent phase transitions.

(2) The next level of theory, the simple harmonic model given by Eq. (2.9), introduces temperature-dependencies through the vibrational free energy evaluated at the uncorrected ground state volume. $F^{vib}(T) = F^{qh}(T)$ for a given volume was calculated via an integral over the VDOS.[21] The direct method as implemented by Parlinski based on small displacements of non-equivalent atoms in the computational supercell was used to determine and integrate the VDOS, hereafter referred to as a phonon calculation.[28] The computational cost of a simple harmonic model depends greatly on the degree of symmetry of the crystal structure, in particular the number of ion displacements required to compute the VDOS. The cubic, tetragonal, and trigonal symmetries studied in this

work required 5, 11, and 21 displacements, respectively.

(3) The third and highest level of theory applied is based on a quasiharmonic model given by Eq. (2.11) in which the volume dependence of vibrational frequencies is taken into account. In contrast to the simple harmonic model, which requires a single phonon calculation at V_0, the quasiharmonic model requires phonon calculations at multiple volumes to determine the free energy surface. At a given temperature, the volume that minimizes $F(V)$ is taken to be the equilibrium volume. Thus, thermal expansion of the solid is implicitly included. In this study, quasiharmonic calculations required an order of magnitude more computational effort than simple harmonic models.

8.3 Computational Details

Plane wave DFT calculations were performed using VASP[29-33] with the projector augmented wave PW91 GGA exchange-correlation functional.[29,34,35] A cutoff energy of 500 eV was used for the plane wave basis set. Monkhorst-Pack *k*-point meshes were chosen to give approximately 0.028 $Å^{-1}$ spacing along the reciprocal lattice vectors. First, geometry optimizations were performed on 1 × 1 × 1 unit cells of $Cs_2NaGdBr_6$, $Cs_2NaLaBr_6$, Cs_2LiLaI_6, and Cs_2LiScI_6 in the cubic (Fm-3m), tetragonal (I4-m), and trigonal (R-3m) orientations depicted in Figure 8.1. Volumes and ion positions were simultaneously relaxed until the Hellman-Feynman forces on each atom were less than 10^{-3} eV $Å^{-1}$. Crystal structure stabilities based on computed DFT 0 K energies were then compared to remove high energy structures from further consideration for computational efficiency.

For each structure maintained for higher level consideration, volume-only stress

minimization (static) quasiharmonic computations were completed, and final values for the ground state and simple harmonic models, ground state Eq. (2.6) and simple harmonic Eq. (2.9), were derived from the quasiharmonic parameterization in Eq. (2.11). Static quasiharmonic methods described in Chapter 2 involve performing phonon calculations at each volume in a range of volumes for which the cell shape and ion positions have been simultaneously relaxed, i.e., the potential energy has been minimized. Between 8 and 15 volumes were used to parameterize $F(V,T)$ for $T \leq 500$ K for all materials with the exception of Cs_2LiScI_6, which was studied for $T \leq 1000$ K. Volumetric spacing ranged between 10 and 20 $Å^3$ with the exception of Cs_2LiScI_6, which employed a grid spacing of 5 $Å^3$ close to the ground state volume and 20 $Å^3$ at higher volumes to account for volume expansion at high temperatures. For each volume, cell shape and ion positions were relaxed until residual forces on each atom were less than 10^{-3} eV $Å^{-1}$. Displacement magnitudes were chosen to yield significant maximum forces per atom in the range 0.5-0.8 eV$Å^{-1}$.[28] For the direct method ion displacement force calculations, trigonal structures were transformed from the hexagonal setting used for initial geometry optimization to a rhombohedral orientation to better approximate a spherical supercell shape. Where soft modes were observed, manifested as negative frequencies in the VDOS, the VDOS was assumed to be zero, and no further adjustment to the free energy was made.[28]

At each temperature, $F(V)$ in Eq. (2.11) was fit to a 4th order polynomial using MATLAB. The corresponding quasiharmonic equilibrium volume was taken to be that for which $dF(V)/dV=0$ and $d^2F(V)/dV^2 >0$ with value greater than the smallest tested volume. This ensured that the predicted equilibrium volume corresponded to a minimum of the free energy curve in close proximity to the range of tested volumes. A similar

method was used to locate V_0 at the minimum of $E_0(V)$. This method neglects zero point energy shifts in the predicted ground state volume. For a given temperature, the values of the fitted $F(V)$ polynomial at the computed quasiharmonic equilibrium volume and at the fixed V_0 were taken to be the quasiharmonic and simple harmonic free energies, respectively.

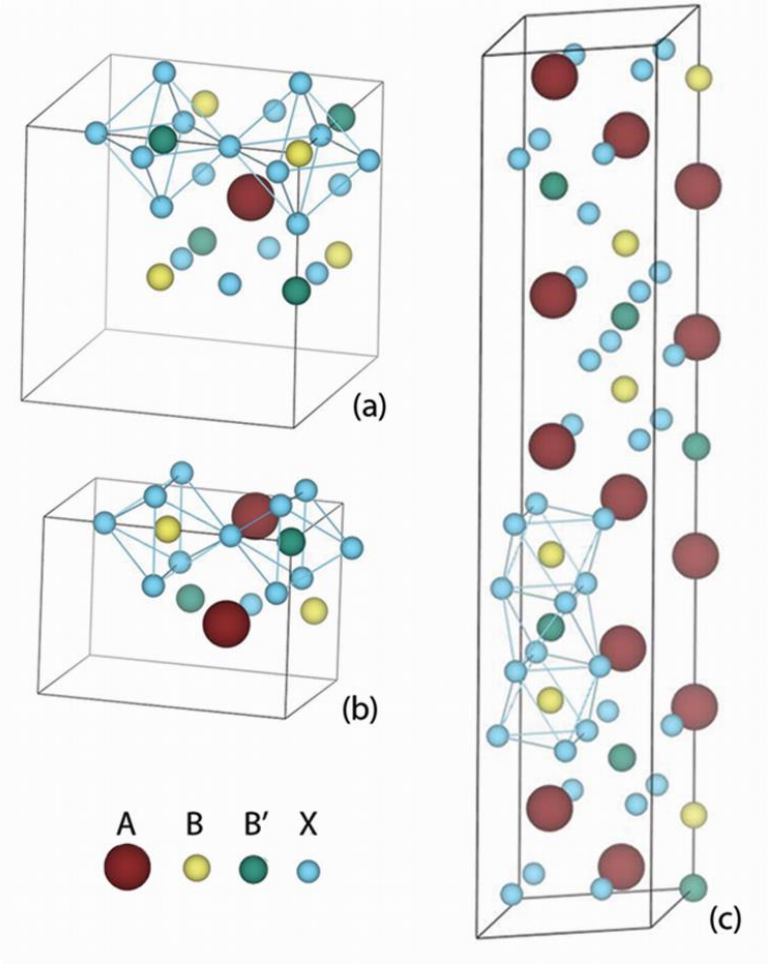

Figure 8.1: Unit cells of elpasolite halide crystal structures with $A_2^+B^+B'^{3+}X_6^-$ stoichiometry: (a) cubic, (b) tetragonal, and (c) trigonal phases. Cages indicate BX_6 and $B'X_6$ octahedra.

8.4 Cs_2LiScI_6

The cubic, tetragonal, and trigonal crystal structures for Cs_2LiScI_6 were optimized using DFT to obtain ground state lattice properties and relative electronic energies. Table 8.1 presents the ground state energies from Eq. (2.6) in terms of relative energy per formula unit (f.u.). At this lowest level of theory based on DFT electronic energies alone, the trigonal phase is 0.162 eV $f.u.^{-1}$ (0.160 eV $f.u.^{-1}$) more stable than the tetragonal (cubic) phase. Including zero point energies at the predicted ground state volumes does not change the predicted lowest energy structure at 0 K since the differences in zero point energy among the phases are less than 0.01 eV $f.u.^{-1}$. Including the zero point energy reverses the predicted relative stabilities of the metastable cubic and tetragonal phases due to the slightly larger zero point energy of the cubic phase.

Experimentally, Cs_2LiScI_6 adopts a 2L Cs_2LiGaF_6 prototype ($P\bar{3}m1$ space group) trigonal structure at low temperature with a different stacking sequence than the 12L Cs_2NaCrF_6 prototype ($R\bar{3}m$ space group) trigonal structure applied in this work.[5] DFT optimization of Cs_2LiScI_6 in the 2L trigonal geometry indicates that the 2L arrangement is 0.128 eV $f.u.^{-1}$ lower in energy than the 12L structure at 0 K, not including zero point energy corrections. Thus, DFT correctly predicts the low temperature trigonal geometry for this material. As previously discussed, DFT methods exist for crystal structure prediction, including database search methods that compare relative energies of all known crystal structures consistent with a given stoichiometry.[36] However, since the aim of this chapter is to compare the relative performance of different levels of theory and for consistency, we present results for the 12L trigonal structure considered for each elpasolite halide studied.

Table 8.1: Lattice properties of Cs_2LiScI_6 at 0 K predicted using Eq. (2.6) and Eq. (2.9). ΔE_0 is the DFT electronic energy of the indicated phase relative to that of the most stable phase.

	cubic	tetragonal	trigonal
V_0 (Å^3 f.u.$^{-1}$)	415.2	415.3	425.0
a_0 (Å)	11.843	8.362	8.388
c_0 (Å)		11.878	41.843
ΔE_0 (eV f.u.$^{-1}$)	0.160	0.162	0.0
F^{vib} (eV f.u.$^{-1}$)	0.137	0.127	0.136

Figure 8.2a displays the temperature-dependent free energies for the three crystal structures based on the simple harmonic level of theory, which takes into account harmonic vibrational effects at the ground state volume but does not capture thermal expansion. For clarity, Figure 8.2b shows the free energies relative to that of the ground state trigonal phase. Free energies computed at this level of theory predict that Cs_2LiScI_6 undergoes a phase transition from trigonal to cubic at T = 685 K. Above this temperature, inclusion of $F^{vib}(T)$ is sufficient to overcome the 0.16 eV f.u.$^{-1}$ energy difference between the two phases at 0 K. Although, to our knowledge, there are no experimental data available regarding phase transitions in Cs_2LiScI_6, elpasolite halides are known to undergo similar transitions to the high symmetry cubic phase, as previously mentioned.

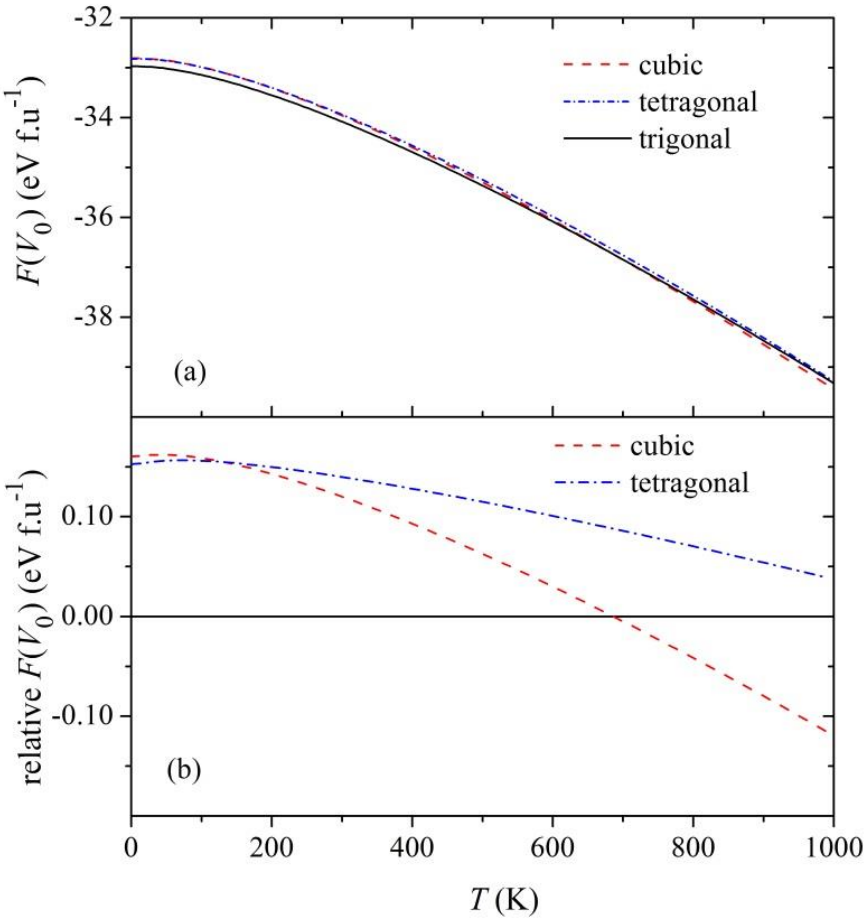

Figure 8.2: Simple harmonic free energies for Cs_2LiScI_6 crystal structures: (a) absolute free energies and (b) free energies relative to $F(V_0,T)$ of ground state trigonal phase.

Figure 8.3 presents the free energies of the tetragonal and cubic structures relative to the ground state trigonal phase based on the full quasiharmonic calculation from Eq. (2.11), the highest level of theory, which allows for volume expansion. The shaded regions depict uncertainties in the relative free energies due to polynomial fitting errors. The fitting error in the free energy of a crystal structure at a given temperature was taken to be

$$\left|F_{\text{fit}} - \min(F_{\text{data}})\right| \tag{8.2}$$

where F_{fit} and F_{data} indicate the free energy from the interpolated polynomial fit as

previously discussed and the lowest energy computed directly from the tested volumes. The quasiharmonic level of theory lowers the predicted trigonal to cubic phase transition to T = 391 ± 43 K. While the free energy difference between the trigonal and cubic structure over the studied temperatures spanned a range of approximately 0.15 eV f.u.$^{-1}$ for the simple harmonic case, the quasiharmonic level of theory expanded this relative energy range to 0.15-0.5 eV f.u.$^{-1}$. In comparison, ΔE_0 was 0.160 eV f.u.$^{-1}$. Thus, for this material, the effect of the simple harmonic level theory on the free energy is just able to overcome the ground state energy difference whereas the quasiharmonic free energy change is considerably larger. The quasiharmonic model is valid only at temperatures not approaching the melting point.[22,37] While specific information on the melting point of Cs_2LiScI_6 is unavailable, melting temperatures of Cs_2NaLaI_6, $Cs_2NaLaBr_6$, Cs_2LiLaI_6, and $Cs_2LiLaBr_6$ fall between 749 K and 868 K.[1] Assuming that this range is a reasonable proxy for Cs_2LiScI_6, the use of the quasiharmonic approximation in this case is justified since the predicted phase transition occurs well below the melting range.

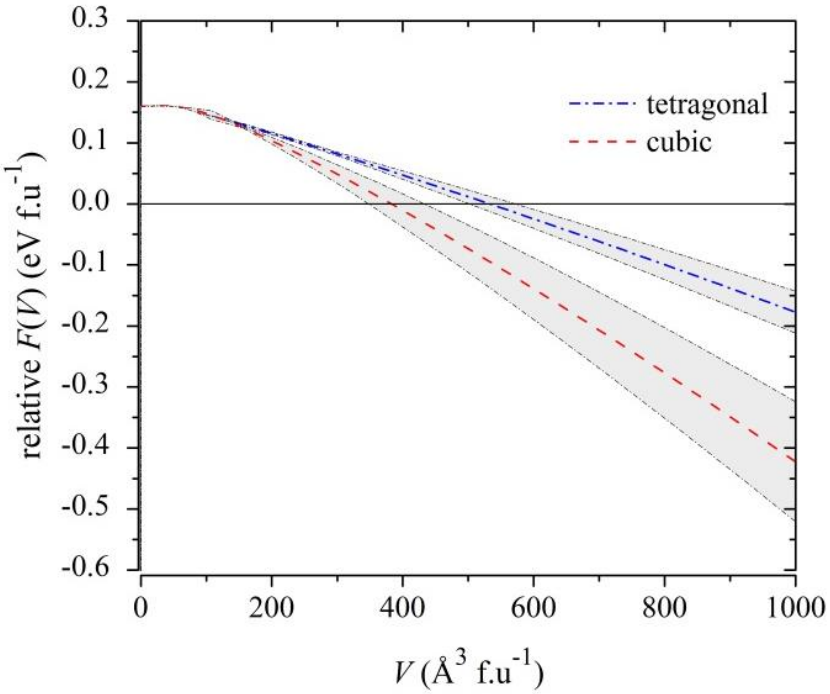

Figure 8.3: Cs2LiScI6 quasiharmonic free energies relative to F(V,T) of ground state trigonal crystal structure. Bounds indicate predicted uncertainties due to fitting.

8.5 Ground State Structure Prediction

Ground state DFT energies provide the most computationally inexpensive way to rank the relative stabilities of crystal structures based on the *ab initio* methods studied in this work. Table 8.2 shows the predicted ground state structures and the relative energies of the metastable phases based only on DFT electronic energies. The DFT energies for all structures except the trigonal phases of $Cs_2NaGdBr_6$ and $Cs_2NaLaBr_6$ were obtained by curve fitting and minimizing Eq. (2.6). For computational efficiency, the DFT energies for the two exceptions were found via simultaneous relaxation of the unit cell and ion positions rather than curve fitting. Examination of the relative stabilities based on ground state energies predicted using both methods for all other phases except trigonal $Cs_2NaGdBr_6$ and $Cs_2NaLaBr_6$ shows that the discrepancies in the two methods are less

than 0.01 eV f.u.$^{-1}$ in all cases, changing neither the predicted stable structures nor the relative energy rankings. For $Cs_2NaGdBr_6$ and $Cs_2NaLaBr_6$, the tetragonal crystal structure is most favored at 0 K followed closely by the cubic phase. This is consistent with experimental observations that these two materials undergo phase transitions from tetragonal to cubic structures at low temperature.[5] Cs_2LiLaI_6 is also predicted to adopt a tetragonal structure at 0 K with trigonal and cubic structures of comparable relative energies. However, to our knowledge, experimental data regarding the phase stability of Cs_2LiLaI_6 is unavailable. The trigonal structure is predicted to be most stable at 0 K for Cs_2LiScI_6 followed by the cubic and tetragonal structures with comparable higher DFT energies. Since the DFT energies of the elpasolite-bromide trigonal structures were greater than 0.4 eV f.u.$^{-1}$ higher in energy than both cubic and tetragonal structures, these were excluded from further study at higher levels of theory.

Though not shown, the differences in zero point energy between the lowest energy phase and the next most stable structure were less than 0.01 eV f.u.$^{-1}$ in all cases, smaller than ΔE_0 for the competing phases. Thus, we find that DFT electronic energies alone, uncorrected for zero point energies, are sufficient to determine the stable crystal structures at 0 K for these materials.

Table 8.2: Relative stabilities of crystal structures based on E_0.

	Free energy relative to predicted stable structure (eV f.u.$^{-1}$)		
material	cubic	tetragonal	trigonal
$Cs_2NaGdBr_6$	0.017	0.0	0.469[a]
$Cs_2NaLaBr_6$	0.054	0.0	0.435[a]
Cs_2LiLaI_6	0.044	0.0	0.026
Cs_2LiScI_6	0.160	0.162	0.0

[a] Ground state energies for trigonal structures obtained using simultaneous volume and ion relaxation rather than curve fitting.

8.6 Phase Prediction Comparison based on Levels of Theory

While the DFT ground state energy model is the least expensive computationally, no material was predicted to crystallize in the cubic symmetry. This was not unexpected since elpasolite halides commonly undergo low temperature phase transitions. For comparison, Table 8.3 presents the phase stability predictions at the simple harmonic and quasiharmonic levels of theory, including temperature and volume-dependent vibrational effects, respectively. The experimental phase transitions, if known, are shown for comparison.

For $Cs_2NaGdBr_6$ both levels of theory predict that the material transitions from tetragonal to cubic at low temperature, in good agreement with the experimental transition temperature. Of the materials studied, the tetragonal and cubic phases for $Cs_2NaGdBr_6$ have the closest DFT electronic energies with only a 0.017 eV f.u.$^{-1}$ difference, easily overcome with inclusion of $F^{vib}(T)$ at low temperatures. As previously mentioned, the simple harmonic and quasiharmonic models also predict trigonal to cubic phase transitions for Cs_2LiScI_6. However, the two levels of theory produce different results for $Cs_2NaLaBr_6$ and Cs_2LiLaI_6. The simple harmonic level of theory indicates that

the ground state structure remains most stable through the tested temperature range. For $Cs_2NaLaBr_6$, the quasiharmonic level of theory correctly predicts the experimentally-observed tetragonal to cubic phase transition. For Cs_2LiLaI_6, the quasiharmonic free energies of the tetragonal and cubic phases are very close above 280 K, within the estimated curve fitting error. Based on knowledge of similar systems, this suggests that a tetragonal to cubic transition is possible at higher temperatures, but the quasiharmonic calculation does not resolve the question clearly.

Table 8.3: Comparison of crystal structure prediction based on two levels of theory. Phase transition temperatures, if applicable, are shown in parentheses.

	Phase transition prediction		
material	Simple Harmonic Model	Quasiharmonic Model	Experimental
$Cs_2NaGdBr_6$	tet. → cubic (195 K)	tet. → cubic (190 ± 8 K)	tet. → cubic (173 K) [6]
$Cs_2NaLaBr_6$	tet. (no transition)	tet. → cubic (237 ± 49 K)	tet. → cubic (316 K) [6]
Cs_2LiLaI_6	tet. (no transition)	tet. → cubic (above 280 K)	unknown
Cs_2LiScI_6	trig. → cubic (685 K)	trig. → cubic (391 ± 43 K)	trigonal [5]

Our results show that the simple harmonic level of theory is insufficient for determining phase stability of elpasolite halides at finite temperature. All simple harmonic calculations were performed at the DFT ground state volume, corresponding to the minimum of the $E_0(V)$ curves. A small shift in the ground state volume occurs when the zero point energy is taken into account.[24,38] Free energies obtained through simple harmonic calculations at this ZPE-corrected ground state volume are slightly closer to the full quasiharmonic free energies. However, for these materials, this effect does not

change the simple harmonic model predictions in Table 8.3. With the exception of Cs_2LiLaI_6, the quasiharmonic level of theory is able to predict stable crystal structures in agreement with experimental phase information. Therefore, if interested in phase transition temperatures of elpasolite halides, quasiharmonic free energies or other higher order methods are needed.

Compared with the two higher levels of theory, the predictive power of the inexpensive ground state model is limited. One might consider assessing the 0 K energy of the cubic phase relative to the predicted ground state structure as a method for screening elpasolite halides likely to transition to the high symmetry cubic lattice at finite temperatures. Ideally, the material would be a candidate if the cubic phase ground state energy was within a threshold ΔE_0 of the ground state structure. Unfortunately, our results based on four materials provide little support for setting such a threshold value. The highest level of theory predicts a phase transition from tetragonal to cubic for $Cs_2NaLaBr_6$ where $\Delta E_0 = 0.054$ eV f.u.$^{-1}$, but does not clearly indicate a phase transition in the case of Cs_2LiLaI_6 with a smaller $\Delta E_0 = 0.044$ eV f.u.$^{-1}$. Also, the material with the largest ground state energy barrier, Cs_2LiScI_6, is clearly predicted to transition from trigonal to cubic with $\Delta E_0 = 0.162$ eV f.u.$^{-1}$ and so is unhelpful in setting an upper limit on ΔE_0. Based on the materials studied, there is not a clear way to use ground state energies alone to predict the existence of elpasolite halides that crystallize with cubic symmetry or to use relative ground state energy magnitudes to anticipate the behavior of higher level thermodynamic models.

8.7 Quasiharmonic Vibrational Free Energy Fitting

Figure 8.4 shows the vibrational contribution to the free energy as a function of volume for Cs_2LiScI_6 at 0 K and 300 K. For this system, the ground state volume is 415.2 $Å^3$ f.u.$^{-1}$ based on minimization of $E_0(V)$. The zero point energies display smooth and linear behavior over the tested volume range. However, $F^{vib}(V)$ increasingly deviates from linearity for larger volumes with temperature. The vibrational entropy component of F^{vib} of the extended volumes is responsible for the anomalous behavior. Conversely, $E_0(V)$ is largely smooth and parabolic. This behavior was observed with varying severity for all materials examined in this work with the exception of the tetragonal and trigonal phases of $Cs_2NaGdBr_6$ and $Cs_2NaLaBr_6$. These trigonal structures were not studied within the quasiharmonic approximation as previously discussed, and we cannot rule out the presence of linear deviations in the tetragonal phases at volumes greater than those studied.

Initially, only the composite free energies $F(V) = E_0(V) + F^{vib}(V)$ were curve-fit to find $F(T)$. To ensure that the instabilities in $F^{vib}(V)$ at larger volumes did not affect the predicted phase stabilities, we also computed quasiharmonic phase transitions using a linear fit of $F^{vib}(V)$ at each temperature for volumes in the small volume linear regime, i.e, volumes less than the onset of non-linear behavior, followed by extrapolation to the excluded volumes. For $Cs_2NaLaBr_6$, $Cs_2NaGdBr_6$, and Cs_2LiScI_6, the linear fit method predicts the same phase transitions as shown in Table 8.3 though at slightly shifted temperatures. The linear fit does not stabilize an otherwise high energy phase. For Cs_2LiLaI_6, the linear fit of $F^{vib}(V)$ stabilizes the cubic phase relative to the trigonal phase at room temperature while the direct-use of $F^{vib}(V)$ without linear fitting predicts a phase

transition within the curve-fitting error bar as previously discussed. This comparison indicates that while the relative stabilities of the phases are largely unaffected by the non-linear characteristics of $F^{vib}(V)$ for large volumes, more accurate methods may be needed to precisely resolve finite temperature free energies of close competing phases. Phase transition predictions based on the simple harmonic level of theory are, of course, not affected by vibrational properties of extended volumes.

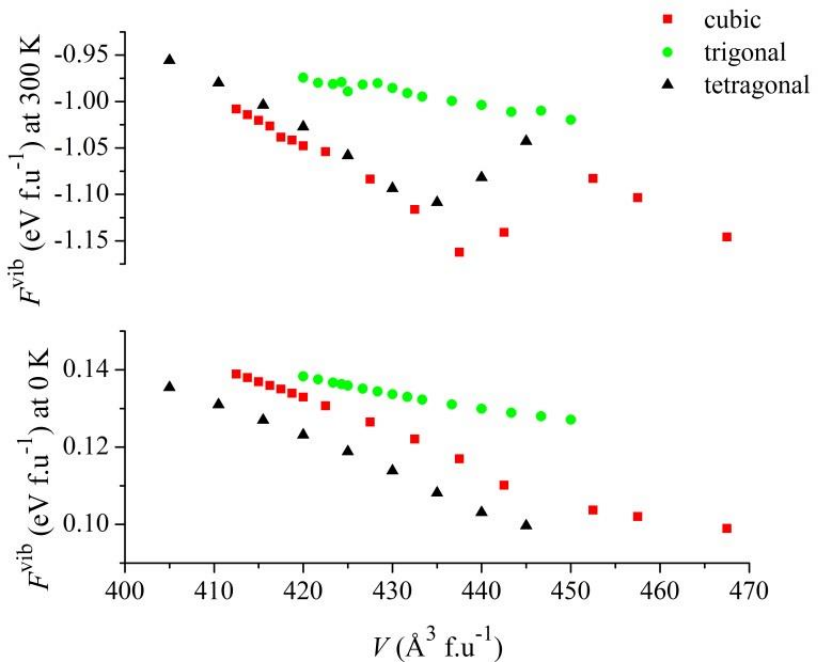

Figure 8.4: Comparison of volume-dependent vibrational contribution to free energy for Cs_2LiScI_6 at 0 K and 300 K.

8.8 Conclusions

Computational methods that can screen large materials libraries to identify cubic elpasolite halides or provide finite temperature stability information to experimentalists are desirable for scintillator materials discovery. We studied four elpasolite halides with three levels of theory based on DFT ground state, simple harmonic, and quasiharmonic

free energies in common cubic, tetragonal, and trigonal symmetries to determine the minimum level of theory required to predict the finite temperature equilibrium phase. Candidate screening based on ground state energies alone did not successfully identify materials that crystallize with cubic symmetry since the cubic structure was predicted to be metastable in all cases. The results also do not indicate a clear or consistent method for using ground state energies alone for materials screening.

The calculations do show, however, that *ab initio* methods that include finite temperature vibrational effects are capable of reproducing the low temperature phase transitions of elpasolite halides. The relatively computationally-expensive quasiharmonic model, which accounts for thermal expansion, outperformed the simple harmonic model. It produced results consistent with available experimental information while the simple harmonic model failed to predict a known low temperature tetragonal to cubic phase transition for $Cs_2NaLaBr_6$. However, the quasiharmonic calculation was unable to clearly differentiate between the phases in all cases. More accurate quasiharmonic calculations may be able to resolve these relative energies with higher fidelity.

8.9 References

[1] P. Yang, F. P. Doty, M. A. Rodriguez, M. R. Sanchez, X. Zhou, and K. S. Shah, *MRS Online Proc. Libr.* **1164** (2009).

[2] C. W. E. van Eijk, *IEEE Trans. Nucl. Sci.* **59**, 2242 (2012).

[3] P. Yang, T. J. Boyle, N. S. Bell, M. R. Sanchez, L. A. M. Ottley, and C. Chen, *Fabrication of Large-Volume, Low-Cost Ceramic Lanthanum Halide Scintillators for Gamma Ray Detection*, U.S. DOE Sandia National Laboratories, 2008.

[4] X. W. Zhou, F. P. Doty, and P. Yang, in *Proc. of SPIE 7806, Penetrating Radiation Systems and Applications XI*, edited by F. P. Doty, H. B. Barber, H. Roehrig and R. C. Schirato, (San Diego, California, 2010), p. 1.

[5] G. Meyer, *Prog. Solid State Chem.* **14**, 141 (1982).

[6] A. Furrer and H.-U. Güdel, *Phys. Rev. B* **56**, 15062 (1997).

[7] D. Babel, R. Haegele, G. Pausewang, and F. Wall, *Mat. Res. Bull.* **8**, 1371 (1973).

[8] D. S. Aidhy and C. Wolverton, *Phys. Rev. B* **83**, 144111 (2011).

[9] M. A. Ghebouli, H. Choutri, N. Bouarissa, B. Ghebouli, A. Bouhemadou, F. Soyalp, E. Ucgun, and H. Y. Ocak, *J. Solid State Chem.* **196**, 498 (2012).

[10] H. Smithson, C. A. Marianetti, D. Morgan, A. Van der Ven, A. Predith, and G. Ceder, *Phys. Rev. B* **66**, 144107 (2002).

[11] B. Meredig and C. Wolverton, *Nat Mater* **12**, 123 (2013).

[12] V. Milman, B. Winkler, J. A. White, C. J. Pickard, M. C. Payne, E. V. Akhmatskaya, and R. H. Nobes, *Int. J. Quantum Chem.* **77**, 895 (2000).

[13] C. J. Pickard and R. J. Needs, *J. Phys. Condens. Matter* **23** (2011).

[14] R. Caputo and A. Tekin, *J. Solid State Chem.* **184**, 1622 (2011).

[15] C. Fischer, K. Tibbetts, D. Morgan, and G. Ceder, *Nat Mater* **5**, 641 (2008).

[16] C. Wolverton, *Acta Mater.* **49**, 3129 (2001).

[17] S. Curtarolo, D. Morgan, and G. Ceder, *Calphad* **29**, 163 (2005).

[18] C. Wolverton, X. Y. Yan, R. Vijayaraghavan, and V. Ozoliņš, *Acta Mater.* **50**, 2187 (2002).

[19] C. Wolverton and V. Ozoliņš, *Phys. Rev. B* **75**, 064101 (2007).

[20] S. V. Alapati, J. K. Johnson, and D. S. Sholl, *Phys. Chem. Chem. Phys.* **9**, 1438 (2007).

[21] G. J. Ackland, *J. Phys. Condens. Matter* **14**, 2975 (2002).

[22] P. Carrier, R. Wentzcovitch, and J. Tsuchiya, *Phys. Rev. B* **76**, 064116 (2007).

[23] A. M. Teweldeberhan and S. A. Bonev, *Phys. Rev. B* **78**, 140101 (2008).

[24] K. M. Nicholson and D. S. Sholl, *Phys. Rev. B* **86**, 134113 (2012).

[25] B. Grabowski, P. Söderlind, T. Hickel, and J. Neugebauer, *Phys. Rev. B* **84**, 214107 (2011).

[26] Y.-J. Hao, L. Zhang, X.-R. Chen, L.-C. Cai, Q. Wu, and D. Alfè, *Phys. Rev. B* **78** (2008).

[27] T. J. Frankcombe and G. Kroes, *Phys. Rev. B* **73**, 174302 (2006).

[28] K. Parlinski, Software *PHONON*, 2005.

[29] G. Kresse and D. Joubert, *Phys. Rev. B* **59**, 1758 (1999).

[30] G. Kresse and J. Furthmüller, *Phys. Rev. B* **54**, 11169 (1996).

[31] G. Kresse and J. Hafner, *Phys. Rev. B* **49**, 14251 (1994).

[32] D. S. Sholl and J. A. Steckel, *Density Functional Theory: A Practical Introduction* (John Wiley & Sons, Hoboken, 2009).

[33] G. Kresse and J. Hafner, *Phys. Rev. B* **47**, 558 (1993).

[34] J. P. Perdew, J. A. Chevary, S. H. Vosko, K. A. Jackson, M. R. Pederson, D. J. Singh, and C. Fiolhais, *Phys. Rev. B* **46**, 6671 (1992).

[35] P. E. Blöchl, *Phys. Rev. B* **50**, 17953 (1994).

[36] V. Ozolins, A. R. Akbarzadeh, H. Gunaydin, K. Michel, C. Wolverton, and E. H. Majzoub, *J. Phys. Conf. Ser.* **180**, 012076 (2009).

[37] B. Grabowski, L. Ismer, T. Hickel, and J. Neugebauer, *Phys. Rev. B* **79**, 134106 (2009).

[38] C. H. Hu, D. M. Chen, Y. M. Wang, and K. Yang, *J. Alloys Compd.* **450**, 369 (2008).

CHAPTER 9

CONCLUSIONS

The U.S. DOE Next Generation Nuclear Plant is the U.S. priority in implementing its Generation IV nuclear strategy.[1,2] The NGNP seeks to improve the overall efficiency of conventional nuclear plants by using a VHTR with a helium coolant to generate low cost electricity and to provide high temperature process heat to industrial users such as a hydrogen production plant. However, the radioactive and extremely mobile tritium contaminant in the helium coolant must be removed without cooling the bulk helium stream in order to maximize these gains in overall efficiency. In addition to their potential use at low to moderate temperatures in hydrogen-powered fuel cell vehicles[3-11] and as long term storage materials for tritium,[12] metal hydrides may also find application as high temperature tritium gettering materials for the NGNP application.[1,13] Since *ab initio* methods have proven successful in describing the thermodynamics of metal hydrides, we used DFT in this thesis to characterize very stable metal hydride thermodynamics and to identify metal hydrides capable of sequestering tritium at temperatures in excess of 1000 K.

First, in Chapter 2, we investigated the minimum level of theory required to reliably predict the free energy of reaction, $\Delta G(T)$, and the hydrogen release temperature, T_d, of five highly stable binary hydrides with both ionic and interstitial (metallic) type metal-hydrogen bonding.[14] The levels of theory considered included PAW(PW91, GGA) predictions based solely on ground state energies, simple harmonic models of the vibrational free energy, quasiharmonic calculations, and the inclusion of an explicit

anharmonic correction term. We found that the latter two methods, which include estimates of thermal expansion and are much more computationally expensive, produce only minor corrections to ΔG(T). The simplest model based on ground state energies reproduced the experimental T_d value to within 200 K, and the simple harmonic model that includes temperature-dependent vibrational effects improved this agreement to 130 K for the alkali hydrides and 50 K for the hydrides of transition metals. These results suggest that an efficient screening algorithm of high temperature metal hydrides would first use predictions of hydriding thermodynamics based on ΔE_0 and then study interesting materials more thoroughly with a simple harmonic calculation at the uncorrected ground state volume.

In Chapter 8, we extended methods developed in Chapter 2 to establish the minimum level of theory to identify cubic elpasolite halide materials from a set of likely symmetries for a scintillator application.[15] Candidate screening based on ground state energies alone did not successfully identify materials that crystallize with cubic symmetry since the cubic structure was predicted to be metastable at $T = 0$ K in all cases. The calculations indicate that *ab initio* methods that include finite temperature vibrational effects are capable of reproducing the low temperature phase transitions of elpasolite halides. The relatively computationally-expensive quasiharmonic model better produced results consistent with available experimental information while the simple harmonic model failed to predict a known low temperature tetragonal to cubic phase transition for $Cs_2NaLaBr_6$. While the quasiharmonic calculation was unable to clearly differentiate between the phases in all cases, more accurate quasiharmonic calculations may be able to resolve these relative energies with higher fidelity.

In Chapter 3, we used different levels of theory to determine if hydrogen isotope effects have a significant effect on the thermodynamics of very stable binary metal hydrides and should be accounted for in material screening for the NGNP application.[16] We confirmed previous experimental observations that the relative stabilities of hydrogen isotope-substituted metal hydrides are temperature-dependent with the stability increasing as metal tritides > metal deuterides > metal protides at T = 0 K and reversing beyond the low temperature regime, e.g., 360 K and 390 K for TiT_2 and TiD_2 relative to TiH_2. The differences in T_d for the metal tritides and protides were within 50 K for the five binary hydrides studied, and, thus, hydrogen isotope effects were neglected for material screening purposes.

Since higher hydrides, in particular of transition metals and intermetallics, are typically either metastable or decompose at lower temperatures than the corresponding binary hydrides,[17] we focused primarily on exploring high temperature ternary and higher materials classes that have proven experimentally to exhibit exceptions to this rule. Of the interstitial hydrides, the $ThZr_2$–H system provides at least one example of a ternary interstitial hydride that has been experimentally observed to have lower hydrogen overpressures than the Zr and Th binary hydrides.[18-20] In Chapter 4, we used DFT and grand potential minimization methods to predict the relative thermodynamic stabilities of Zr and Th binary hydrides, $ThZr_2H_6$, and $ThZr_2H_7$ as a function of hydrogen pressure and temperature to serve as a proof of principle calculation to judge whether or not the ternary hydride is a thermodynamically-preferred phase. A primitive, analytical estimate of the $ThZr_2H_6$ configurational entropy (79 J mol^{-1} K^{-1}) based on a random distribution of hydrogen erroneously suggests that the configurational entropy is the major driver of the

enhanced thermodynamic stability of the ternary hydride at high temperatures. However, we used a cluster analysis method to obtain a better estimate (16 J mol^{-1} K^{-1}) that takes interstitial site blocking into account, indicating that the configurational entropy is not primarily responsible for the ternary hydride overall stability. Similar cluster analysis methods could be applied to compute the configurational entropies of other hydride interstitial systems with known geometries. Our predicted T_d of 1168 K for $ThZr_2H_6$ is in reasonable agreement with the extrapolated experimental $T_d \approx 1236 \pm 150$ K. The thermodynamic stabilities of the very stable metal hydrides, particularly $ThZr_2H_6$ and ZrH_2, are nearly degenerate at this level of theory. The ability of DFT-based methods to accurately reproduce phase behavior of high temperature ternary hydride systems indicate these methods will be useful in applications such as hydride nuclear fuels where, for example, experiments are inconvenient or component materials are scarce.

In Chapters 6 and 7, we used a high throughput screening methodology described in Chapter 5 to predict the thermodynamic stabilities of all known, simulation ready ternary and quaternary CTMHs (102 materials) and 149 hypothetical ternary materials based on existing prototypes. First principles characterizations of these materials are particularly useful since experimental thermodynamic data is scarce for most CTMHs. Our calculations indicate that 34 of the proposed materials are thermodynamically preferred states at the Round 2 level of theory that accounts for vibrational effects, and 46 proposed materials are thermodynamically stable based on ground state energies alone for condensed phases. This is a significant expansion of the potential composition space for CTMHs. Overall, the DFT calculations and GCLP phase diagram prediction methods can reproduce experimental trends in phase stability with reasonable fidelity and be

considered as a guide for ranking metal hydrides based on hydrogen release temperatures at 1 bar H_2 to within ~125 K. Using two rounds of screening, we successfully identified 13 existing ternary CTMHs and seven proposed materials with higher T_d than the associated binary hydrides and high operating temperature greater than 1000 K at 1 bar H_2. The most stable CTMHs tend to crystallize in the 2-Sr_2RuH_6 cubic prototype structure and decompose to the pure elements and hydrogen rather than to an intermetallic phase(s).

Our calculations characterize many of the most thermodynamically stable metal hydride materials, either hypothetical or experimentally known and serve as a reasonable upper boundary on the potential performance of CTMHs for the NGNP application. Figure 9.1 shows the calculated van't Hoff plots of the six most stable CTMHs and the associated binary hydrides. The most stable CTMHs and binary hydrides are predicted to have equilibrium pressures orders of magnitude above the tritium contaminant levels of the NGNP application. This poses a challenge for direct contact gettering systems as discussed in Section 6.6. A redeeming quality of metal hydride systems is that unsaturated hydrides, at least of interstitial systems, have H_2 vapor pressures below the equilibrium pressure of the saturated hydride. For example, $YH_{0.1}$ has a characteristic vapor pressure of ~10^{-6} bar at 1000 K, below that of YH_2 at ~10^{-4} bar.[1] This indicates that metal hydrides may take up tritium even at the dilute levels of the NGNP.

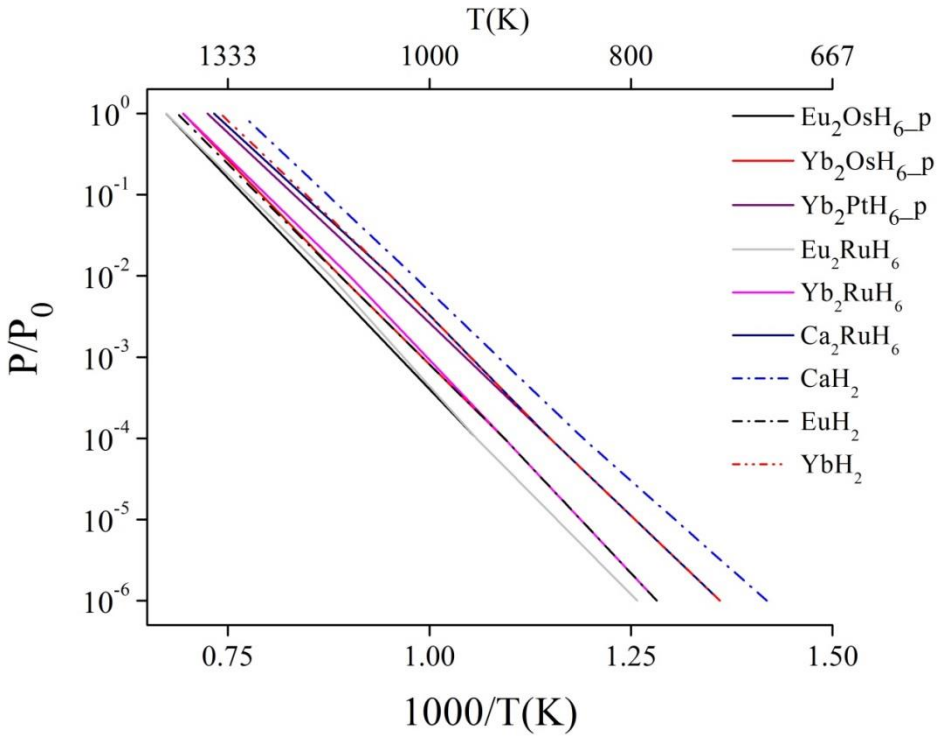

Figure 9.1: Calculated van't Hoff plots for six most stable existing CTMHs, proposed CTMHs, and binary hydrides from Chapters 6 and 7.

Based on the ideal thermodynamic considerations of the very stable metal hydrides considered here, there are significant challenges to using binary hydrides or CTMHs in a direct contact gettering application at high temperature and low tritium overpressures. Process manipulations should be considered that either increase the hydrogen overpressure in the system or cool the feed in order to drive the thermodynamic equilibrium toward the solid metal hydrides. Substantial quantities of protium (e.g., H(g)/T(g) > 20,000 from Appendix F) will likely be present in the real system in addition to the radioactive tritium contaminant that is present on the order of 10^{-10} bar.[1,13] While this raises the partial pressure of hydrogen species and increases the driving force for hydride formation, the amount of base metal for the hydriding bed increases dramatically

with the amount of hydrogen to be removed from the feed stream, as discussed below. A cost estimate based on the bulk price of the pure metal constituents of the most stable CTMHs and binary hydrides is available in Appendix F. Table 9.1 lists the cost of the metal constituents for each hydride as well as the mass of metal needed to absorb pure protium and tritium on a gravimetric basis.

Table 9.1: Estimated costs of pure metal components of metal hydrides from Tables F.2 and F.3 in the Appendix.

metal hydride	T_d (K)	\$/(100 g metal)[b]	$W_{protide}$ g metal/g H	$W_{tritide}$ g metal/g T
EuH_2	1455	20000	44.1	14.7
$Cs_2PtH_2\_p$	1365	6137	67.0	22.4
$Rb_2PtH_2\_p$	1050	7489	81.7	27.3
$K_2PtH_2\_p$	1140	9309	75.4	25.2
$Eu_2OsH_6\_p$	1485	15265	73.9	24.7
Eu_2RuH_6	1485	15358	88.7	29.6
$Cs_2PdH_2\_p$	1395	2453	184.6	61.7
$Yb_2OsH_6\_p$	1440	3635	30.0	10.0
Ca_2OsH_6	1350	5423	228.6	76.4
Yb_2RuH_6	1440	1400	44.7	14.9
$Ba_3Ir_2H_{12}$	1215	2771	58.0	19.4
Ba_2RuH_6	1215	417	19.9	6.6
Ca_2RuH_6	1365	790	62.1	20.8
YH_2	> 1400	430	12.0	4.0
TiH_2	916	661	45.3	15.1
ZrH_2	1154	157	135.6	45.3
$Sr_2NiH_4\_p$	1320	77	181.6	60.7
CaH_2[a]	1305	20	23.7	7.9

[a] melts at 1273 K[21]
[b] \$USD from Reference 22

As described in Appendix F, one estimate of the amount of tritium to be removed from the feed stream is less than a gram of tritium per year based on exhausting the cleaned product gas to the atmosphere. The metals cost for absorbing this small amount of pure tritium is relatively small. However, the metals cost increases by orders of magnitude as the concentration of protium in the feed increases. One estimate for the rate of hydrogen release to the primary helium coolant for Japan's 600 MW_{th} future very high temperature gas-cooled reactor, the GTHTR300C, gives $2.0 \times 10^{-2}\ m^3\ hr^{-1}$(STP) based on scale up of a high temperature test reactor.[23] If all of this hydrogen is taken up by the hydride bed, the mass of protium to be removed on an annual basis is 7.9 kg. This quickly escalates the cost and weight of the metal hydride base metals as shown in Table F.3 in the Appendix, e.g., $1,865,448/yr for a 236 kg bed of Ca_2RuH_6 metal assuming uptake of protium and tritium compared with a bed with less than a kilogram of metal with no uptake of protium. These values seem extreme, but could be mitigated if multiple circulating beds are utilized that alternately hydride and dehydride. The final tritiated waste could be stored long term in less expensive metal hydrides as currently practiced in nuclear applications.[12] Additional low temperature H/T separation could reduce the overall quantity of tritiated material to be stored. Clearly, from these basic cost estimates, the overall economic viability of the hydride gettering bed will depend largely on the rate of hydrogen release as protium for the NGNP system in contact with the metal hydride.

Metal hydrides with high thermodynamic stability may be desirable in other high temperature applications such as concentrated solar energy storage services.[24-26] In general terms, heat generated by solar energy is stored as hydrogen gas or in solid form as a low temperature metal hydride during the day. At night, the hydrogen is released to

form a very stable metal hydride, generating high temperature heat due to the strongly exothermic hydriding reaction. This heat is used to generate high temperature steam that drives a turbine to produce electricity from the sun at night. In this system, it is desirable to use metal hydrides with very high stability (T_d > 1000 K) so that systems can operate at high temperature and utilize high efficiency Stirling or Brayton thermodynamic cycles.[16,27,28] The hydrogen operating pressure is a design parameter unlike in the NGNP case where the hydride beds are envisioned to remove a trace contaminant. As a consequence of our research, a database of CTMH and binary hydride thermodynamic data has been generated that could be mined to rank and match candidate materials for this application.

Finally, our database of metal hydride materials includes 80 proposed CTMHs that were predicted to be thermodynamically stable based on DFT calculations and GCLP minimization at different levels of theory. Some known CTMHs such as Mg_2NiH_4 and $Mg_6Ir_2H_{11}$ that derive from hydrogenation of intermetallics show induced metal to nonmetal transitions, which make them useful for such technological applications such as switchable mirrors or tuneable optic windows.[29] Further computational study of the electronic and magnetic properties of these materials could yield interesting results.

9.1 References

[1] S. R. Sherman and T. M. Adams, *Tritium Barrier Materials and Separation Systems for the NGNP*, U. S. DOE Savannah River National Laboratory, Aiken, Nov. 2008.

[2] U.S. DOE, *The U.S. Generation-IV Implementation Strategy*, DOE Office of Nuclear Energy, 2003.

[3] L. Zhou, *Renewable Sustainable Energy Rev.* **9**, 395 (2005).

[4] L. Schlapbach and A. Zuttel, *Nature* **414**, 353 (2001).

[5] A. Züttel, *Mater. Today* **6**, 24 (2003).

[6] W. Grochala and P. P. Edwards, *Chem. Rev.* **104**, 1283 (2004).

[7] B. Sakintuna, F. Lamari-Darkrim, and M. Hirscher, *Int. J. Hydrogen Energy* **32**, 1121 (2007).

[8] S. V. Alapati, J. K. Johnson, and D. S. Sholl, *J. Phys. Chem. C* **112**, 5258 (2008).

[9] S. V. Alapati, J. K. Johnson, and D. S. Sholl, *Phys. Chem. Chem. Phys.* **9**, 1438 (2007).

[10] K. C. Kim and D. S. Sholl, *J. Phys. Chem. C* **114**, 678 (2009).

[11] C. Wolverton, J. S. Donald, A. R. Akbarzadeh, and V. Ozoliņš, *J. Phys. Condens. Matter* **20**, 064228 (2008).

[12] *DOE Handbook: Tritium Handling and Safe Storage*, U. S. D. o. Energy, Washington, D.C., March 1999.

[13] S. R. Sherman, *A Tritium Research and Collaboration Plan for the NGNP Project*, U. S. DOE Savannah River National Laboratory, Aiken, Aug. 2008.

[14] K. M. Nicholson and D. S. Sholl, *Phys. Rev. B* **86**, 134113 (2012).

[15] K. M. Nicholson, S. G. Kang, and D. S. Sholl, *J. Alloys Compd.* **577**, 463 (2013).

[16] K. M. Nicholson and D. S. Sholl, *J. Chem. Eng. Data* (2014).

[17] K. H. J. Buschow, P. C. P. Bouten, and A. R. Miedema, *Rep. Prog. Phys.* **45**, 937 (1982).

[18] W. Bartscher, J. Rebivant, A. Boeuf, R. Caciuffo, F. Rustichelli, J. M. Fournier, and W. F. Kuhs, *J. Less-Common Met* **121**, 455 (1986).

[19] R. van Houten and S. Bartram, *Metall. Trans.*, **2**, 527 (1971).

[20] W. Bartscher, J. Rebizant, and J. M. Haschke, *J. Less-Common Met* **136**, 385 (1988).

[21] in *CRC Handbook of Chemistry and Physics, 88th Edition*.

[22] D. Steward, (Chemicool.com, 2012), Vol. 5/19/2014.

[23] H. Ohashi, N. Sakaba, T. Nishihara, Y. Tachibana, and K. Kunitomi, *J. Nucl. Sci. Technol.* **45**, 1215 (2008).

[24] B. Bogdanović, H. Hofmann, A. Neuy, A. Reiser, K. Schlichte, B. Spliethoff, and S. Wessel, *Journal of Alloys and Compounds* **292**, 57 (1999).

[25] B. Bogdanović, A. Reiser, K. Schlichte, B. Spliethoff, and B. Tesche, *J. Alloys Compd.* **345**, 77 (2002).

[26] M. Felderhoff and B. Bogdanović, *Int. J. Mol. Sci.* **10**, 325 (2009).

[27] D. N. Harries, M. Paskevicius, D. A. Sheppard, T. E. C. Price, and C. E. Buckley, *Proc. IEEE* **100**, 539 (2012).

[28] W. E. Wentworth and E. Chen, *Sol. Energy* **18**, 205 (1976).

[29] K. Yvon and G. Renaudin, in *Encyclopedia of Inorganic Chemistry, Second Edition*, edited by B. R. King (John Wiley & Sons, Chichester, 2005), Vol. III, p. 1814.

APPENDIX A

CONVERGENCE TESTING FOR Th-Zr-H SYSTEM DFT AND PHONON CALCULATIONS[*]

Table A.1: *k*-point densities for studied compounds. B_i refers to total number of *k*-points per unit cell that are distributed as evenly as possible along reciprocal lattice vectors. M_i refers to the corresponding values for a $M_i \times M_i \times M_i$ Monkhorst-Pack mesh.

	B_1	B_2	M_1	M_2
Zr_bcc	1024	2000	8	10
Zr_hcp	1458	2662	9	11
Th	2048	4000	8	10
Th_4H_{15}	4864	16416	4	6
ThH_2	3072	6000	8	10
ZrH_2	3072	6000	8	10
$ThZr_2$	1536	5184	4	6
$ThZr_2H_7$	5120	17280	4	6
$ThZr_2H_6$	4608	-	4	-

[*] The material in this chapter is in review as K. M. Nicholson and D. S. Sholl, "First Principles Prediction of Ternary Interstitial Hydride Phase Stability in the Th-Zr-H System: Supporting Information" J. Chem. Eng. Data (2014).

Table A.2: Reaction energy convergence with respect to cutoff energy and *k*-point parameters. Reaction energies, ΔE_0, are written in units of either kJ $mol^{-1}H_2$ released for metal hydride decomposition reactions or kJ mol^{-1} reactant for non-hydride dissociation reactions. B_1 and B_2 *k*-point densities correspond to values shown in Table A.1.

		ΔE_0	$\Delta\Delta E_0$ relative to 500 eV cutoff energy		$\Delta\Delta E_0$ relative to B_2 *k*-points
	Reaction	425 eV and B_1 *k*-points	350 eV	425 eV	B_1
1	$ThZr2H_7 \rightarrow Th+2Zr\_hcp+3.5H_2$	152.65	-1.51	-0.39	-0.56
2	$ThZr_2H_7 \rightarrow ThZr_2+3.5H_2$	161.31	-1.51	-0.39	-0.18
3	$Th_4H_{15} \rightarrow 4ThH_2+3.5H_2$	118.05	-1.57	-0.37	-0.01
4	$ThH_2 \rightarrow Th+H_2$	172.36	-1.37	-0.36	0.29
5	$ZrH_2 \rightarrow Zr\_hcp+H_2$	192.57	-1.54	-0.42	-0.58
6	$ThZr_2 \rightarrow Th+2Zr\_hcp$	-30.30	0.01	0.01	-1.31
7	$Zr\_hcp \rightarrow Zr\_bcc$	7.25	0.00	0.00	-0.03
8	$ThZr_2H_6 \rightarrow Th+2Zr\_hcp+3H_2$	158.52			

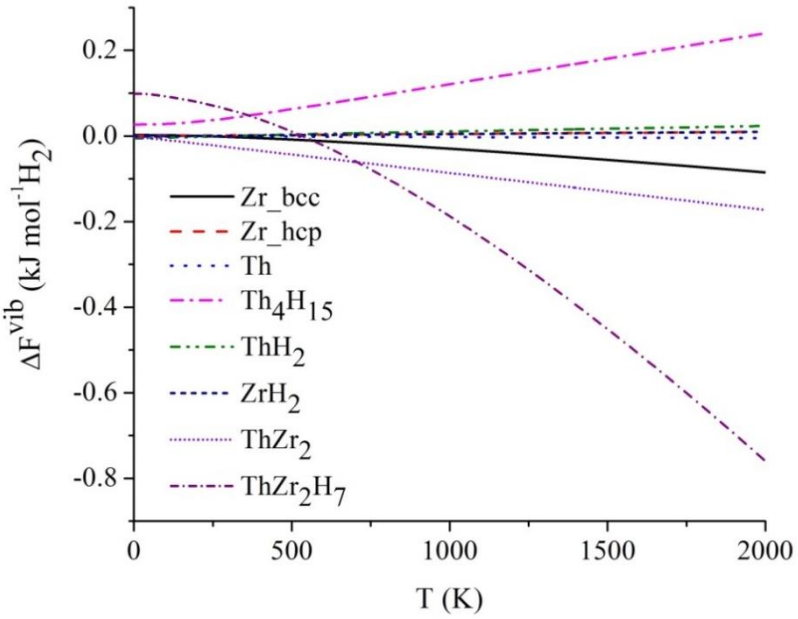

Figure A.1: Convergence of vibrational free energies with respect to the displacement magnitude for phonon calculations. $\Delta F^{vib} = F^{vib}$ (0.01 Å) - F^{vib} (0.03 Å).

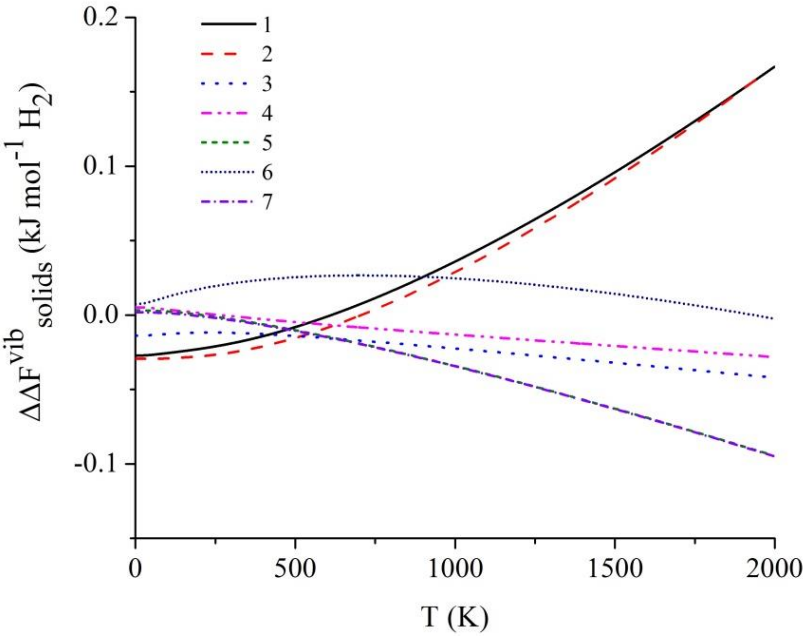

Figure A.2: Convergence of vibrational reaction free energies with respect to the displacement magnitude for phonon calculations. $\Delta\Delta F^{vib}_{solids} = \Delta F^{vib}_{solids}$ (0.01Å) - ΔF^{vib}_{solids} (0.03 Å), ignoring free energy of H_2 and solids ground state energy contributions. Reactions numbers refer to those listed in Table A.2.

APPENDIX B

CLUSTER ANALYSIS ALGORITHM TO COMPUTE SUCCESSFUL H CONFIGURATIONS IN $ThZr_2H_6$ TERNARY HYDRIDE [*]

Objective: Find number of ways to arrange 19 H atoms to 32e sites and 29 H atoms to 96g sites such that no two H atoms are closer than 2.1 Å in accordance with the Westlake criterion.[1]

Figure B.1a shows the $ThZr_2H_6$ cubic Laves structure with all available 32e and 96g sites. Figure B.1b is the same as Figure B.1a with metal atoms removed, with all interstitial sites located at a distance of less than 2.1 Å shown as connected. Figure B.1c shows that each 32e site is associated with three unique 96g sites, i.e., each 96g site is within 2.1 Å of only one 32e site. Therefore, when a 32e site is occupied, those three associated 96g sites are blocked from additional H loading. 32e-32e distances are on the order of 2.5 Å, so occupation of one 32e site does not block occupation of a neighboring 32e site from the perspective of the Westlake criterion. 19 32e sites can be chosen at random and the $19 \times 3 = 57$ associated 96g sites removed from consideration. The remaining 39 available 96g sites are shown for one example in Figure B.1d. 29 H atoms must be distributed to these 39 sites such that no two are connected in order to meet the partial occupancy requirements of $ThZr_2H_6$.[2] Care is taken to account for periodic boundary conditions.

[*] The material in this chapter is in review as K. M. Nicholson and D. S. Sholl, "First Principles Prediction of Ternary Interstitial Hydride Phase Stability in the Th-Zr-H System: Supporting Information" J. Chem. Eng. Data (2014).

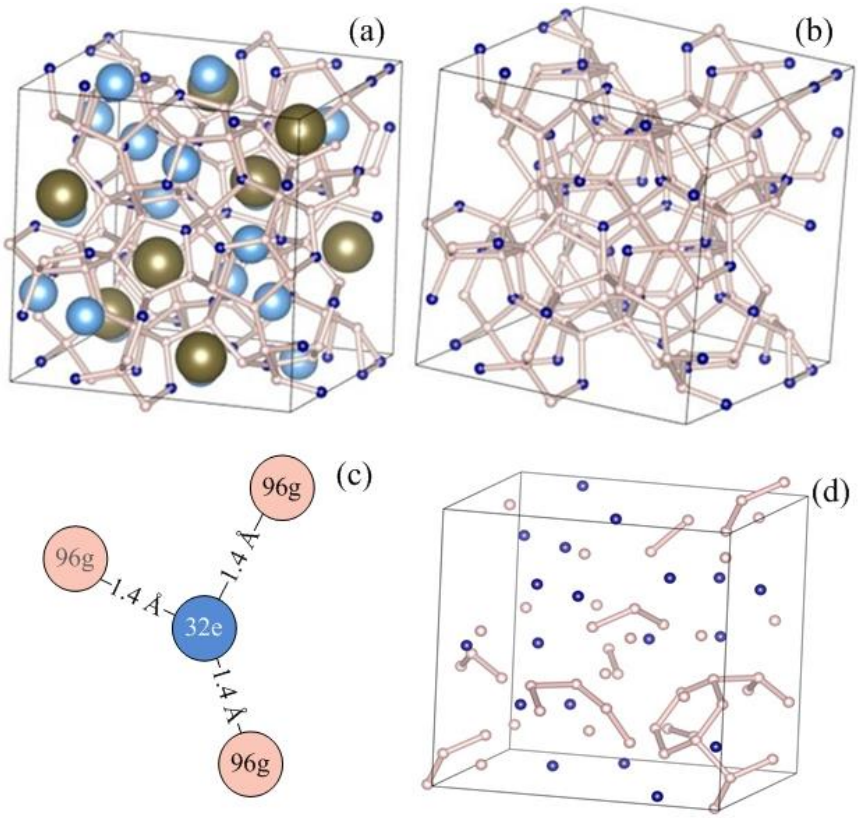

Figure B.1: ThZr2H6 structure featuring Zr (light blue), Th (brown), H 32e interstitial sites (peach), and H 96g interstitial sites (blue), (a) $ThZr_2H_6$ cubic Laves unit cell with metal atoms and all 32e and 96g sites. H-H distances less than 2.1 Å are highlighted. (b) Network of all 32e sites and 96g sites with H-H distances less than 2.1 Å. (c) 32e-96g interstitial site connectivity. (d) Remaining 96g sites after 19 32e sites are chosen at random and the blocked 96g sites removed.

The available 39 96g sites can be broken down as follows: "free" sites in which the 96g site is not located within 2.1 Å of another 96g site and can be chosen with no blocking penalty, "linear" clusters in which the 96g sites form linear chains and each site is connected to at most two other sites, and "branched" clusters in which 96g sites can be connected to three or more 96g sites. Figure B.2 illustrates this site breakdown from the example 32e configuration shown in Figure B.1d.

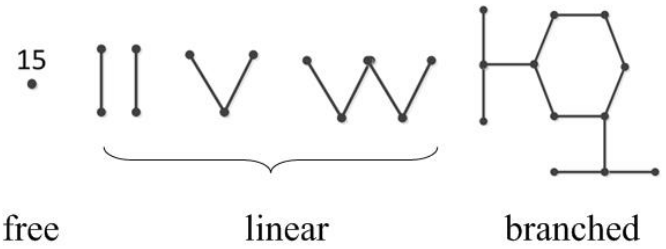

Figure B.2: Breakdown of remaining 39 available 96g sites from Figure B.1d into sets of free sites, linear clusters, and branched clusters. Lines between sites indicate distances less than 2.1 Å.

We can quickly determine whether or not a given 32e configuration (19 H atoms distributed randomly to 32e sites) can possibly support 29 H atoms placed into the remaining 96g sites without violating the Westlake criterion by determining the maximum loading on the remaining 96g site clusters. This is the maximum number of H atoms that can be distributed to the cluster breakdown such that no two sites are connected. If this maximum loading, L_{max}, is greater than or equal to 29 then the 32e configuration will have at least one successful arrangement of 29 H atoms to the 96g sites. The maximum loading is calculated via

$$L_{\text{max}} = L_{\text{free}} + L_{\text{linear}} + L_{\text{branched}} \tag{B.1}$$

where L_{free} is equal to the number of free sites, and L_{linear} and L_{branched} are the maximum number of H atoms the linear and branched clusters can each support. The maximum loading on a linear cluster of size N_{linear} is

$$L_{\text{linear}} = \text{floor}\left(\frac{N_{\text{linear}}}{2} + \text{modulus}(N_{\text{linear}}, 2)\right) \tag{B.2}$$

This equation gives one success for each pair of atoms in the chain and adds another success if N_{linear} is an odd number. In the example from Figure B.2, the free sites and

linear clusters can support 15 and 7 H atoms, respectively, such that no two H atoms are connected.

Given that the maximum loading on any cluster is 2/3 for a three atom chain, we can apply a heuristic to determine an estimate of the maximum number of H atoms a branched cluster of size N_{branch} can support. This is given by

$$L_{branch,H} = \text{floor}\left(0.667 N_{branch}\right) \tag{B.3}$$

In the example from Figure B.2, the maximum number of H atoms the given 32e configuration can support when the heuristic is applied is $L_{max,H} = 15 + 7 + 8 = 30$, which is greater than the needed 29 H sites. If $L_{max,H} < 29$, the 32e configuration is discarded since there is no way to arrange 19 H atoms on the available 96g such that no two H atoms are closer than 2.1 Å.

If $L_{max,H} \geq 29$, then we determine the maximum number of H atoms that can be loaded onto the branched clusters. Then, using this number for L_{branch}, if $L_{max} \geq 29$, we determine the exact number of ways to arrange H onto the 96g cluster breakdown for that 32e configuration. First, we compute $L_{branch,max}$ exactly. We use a numerical lock and key approach to do this in which the branched cluster connectivity is coded into a "lock" and "keys" that describe H loading arrangements are generated and tested. If a key fits a lock then that indicates that the key arrangement of H atoms has no two sites of the branched cluster connected. We are interested in first finding the largest key (or number of H atoms) that can fit the lock. For computational efficiency, we start with keys that are the same size as the maximum loading indicated by the heuristic from Eq. (B.3) and reduce the key size by 1 H atom successively. If at any time the key size falls below that which is needed to make the 32e configuration successful, L_{min}, the 32e configuration is

discarded. For example, the branched cluster from the example Figure B.2 must be able to support 29 - 15 - 7 = 7 H atoms. The lock-key algorithm for a simple three atom linear chain is described in Figure B.3. The maximum loading to the three atom chain is two. Two H atoms can be loaded to chain ends without connecting sites

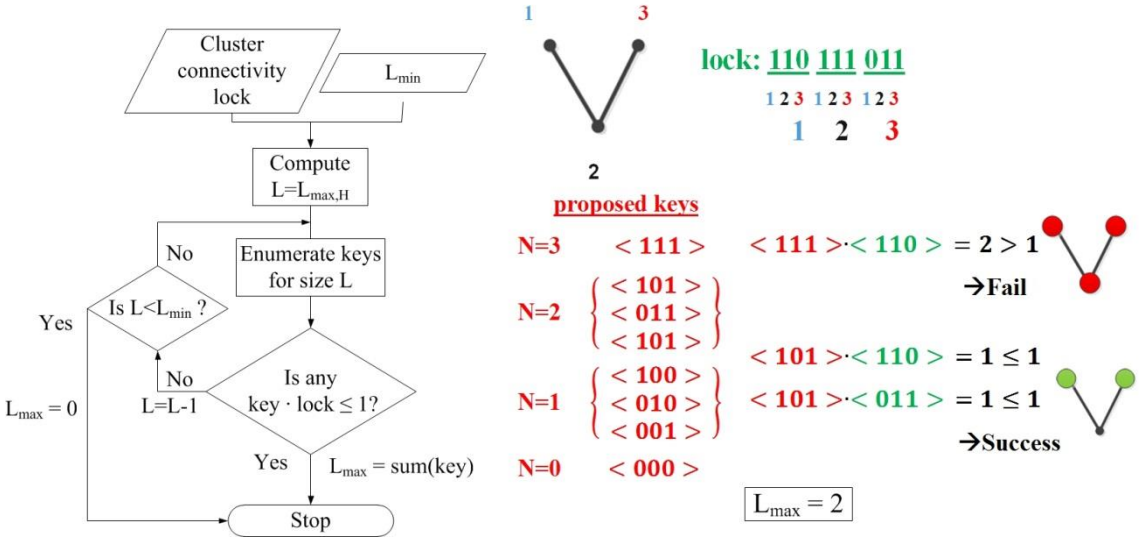

Figure B.3: Algorithm for computing maximum loading L_{branch} of hydrogen atoms onto a given cluster of 96g interstitial sites in $ThZr_2H_6$ such that no two atoms are closer than 2.1Å per the Westlake criterion.[1] L_{min} is the minimum loading required to satisfy total hydrogen occupancy requirements for the 32e-96g overall configuration.

If the branched cluster can support at least L_{min} number of H atoms, the exact number of ways to arrange H atoms to the cluster breakdown is computed. In the example from Figure B.2, there are 2 ways to load 7 atoms to the branched cluster shown in Figure B.4.

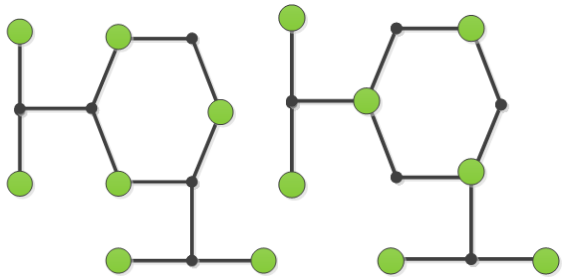

Figure B.4: Two arrangements of H atoms in a connected set of 96g sites that satisfy L_{min} = 7.

We then compute the exact number of unique arrangements of H, L_{unique}, that successfully populate the 96g sites for a given 32e site as illustrated in Figure B.5 for the example calculation. Here, each base number represents the number of ways to arrange H atoms on each cluster such that the total number of loaded H atoms is 29. In this example, there are 8 successful arrangements of 19 H atoms to the 29 remaining 96g sites for the given 32e configuration.

Figure B.5: Calculation of the number of unique arrangements of H atoms to the cluster breakdown for the 32e configuration shown in Figure B.1d.

The total number of successful configurations for $ThZr_2H_6$, N_c, is given by

$$N_c = \sum_{i=1}^{n} L_{unique} \tag{B.4}$$

where n is the number of 32e configurations that can support at least one successful 96g configuration. The overall algorithm we implemented via MATLAB[3] to determine N_c is shown in Figure B.6. Over nine parallel runs of $i=5\times10^6$ iterations, we sampled 4.5×10^7 32e configurations, averaged the total number of successful configurations for each run, and extrapolated the averaged value to the full 3.5×10^8 32e configurations. We set a branched cluster size cutoff $N_{cutoff} = 19$ to limit the computational time spent computing the maximum loading on large clusters. We found that using $N_{cutoff} = 20$ increased the TS^{conf} at 1000 K negligibly by < 0.02 kJ mol^{-1} H_2.

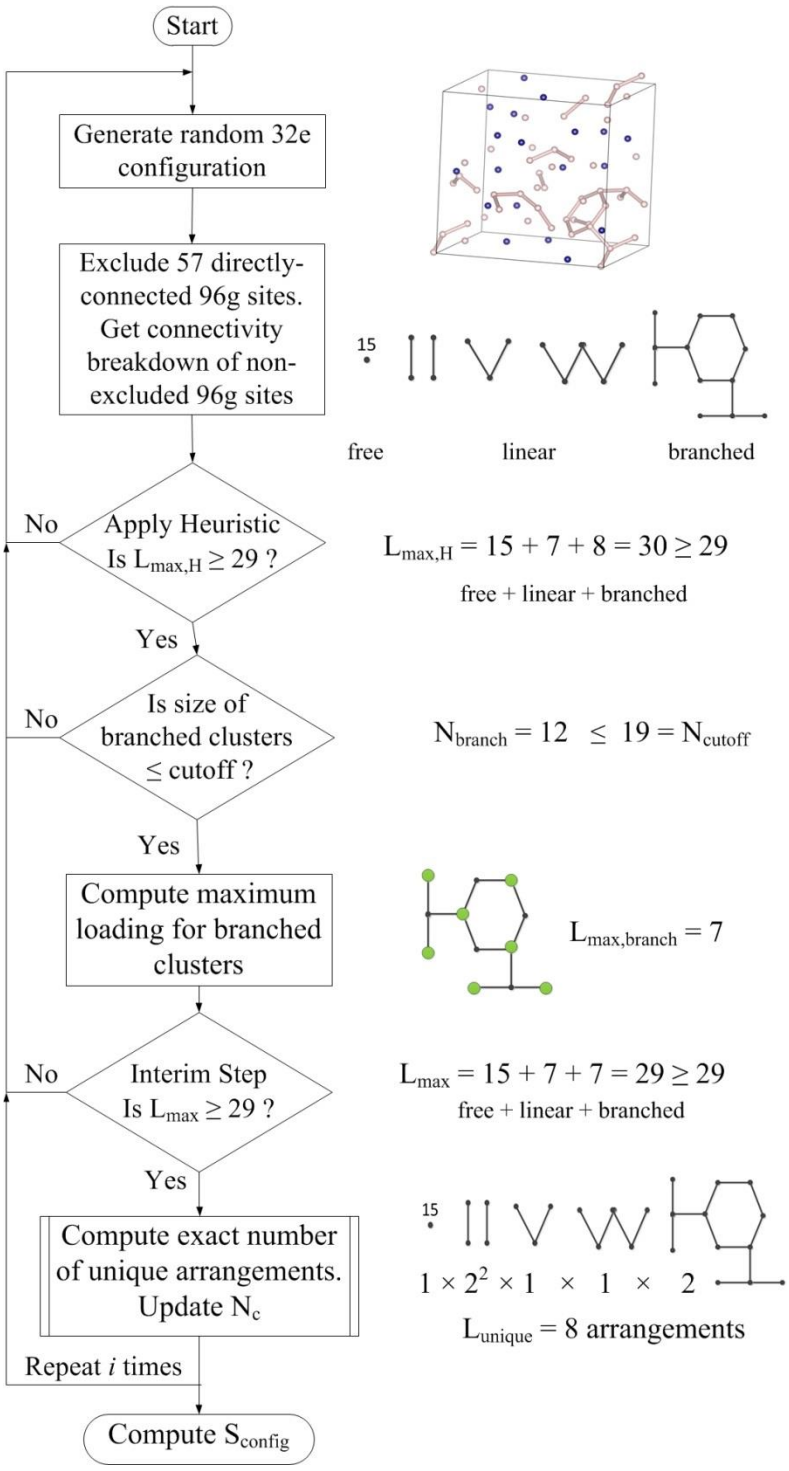

Figure B.6: Algorithm and example for computing configurational entropy contribution S to free energy for ThZr2H6 based on 19 hydrogen atoms onto 32e sites and 29 hydrogen atoms onto 96g sites such that no two hydrogen atoms are closer than 2.1 Å per the Westlake criterion. $L_{max,H}$ is the maximum loading for the 96g clusters calculated using a heuristic 0.667N scaling factor, and N is the size of the cluster. N_{cutoff} is the largest size cluster considered in the calculation. $N_{success}$ is the total number of successful configurations.

B. References

[1] D. G. Westlake, *J. Less-Common Met* **91**, 1 (1983).

[2] W. Bartscher, J. Rebivant, A. Boeuf, R. Caciuffo, F. Rustichelli, J. M. Fournier, and W. F. Kuhs, *J. Less-Common Met* **121**, 455 (1986).

[3] *MATLAB* MathWorks, Inc., 2010.

APPENDIX C

STRUCTURAL PARAMETERS FOR EXISTING MATERIALS LIBRARY*

Table C.1: Metals, binary hydrides, intermetallics, and higher hydrides from the ICSD included in Round 1 Complex Transition Metal Hydride Screening. *a*,*b*,*c* in Å

		DFT		EXPERIMENT	
material	space group		*V* (Å^3 f.u.$^{-1}$)		*V* (Å^3 f.u.$^{-1}$)
		metals			
Ba	IM3M	*a* = 5.004	62.7	*a* = 5.01	62.9
Ca	FM3M	*a* = 5.517	42.0	*a* = 5.5884(2)	43.6
Cd	P63/MMC	*a* = 3.032, *c* = 5.598	22.3	*a* = 2.97912(14) *c* = 5.61827(45)	21.6
Co	P63/MMC	*a* = 2.492, *c* = 4.028	10.8	*a* = 2.5054, *c* = 4.0893	11.1
Cs	IM3M	*a* = 6.096	113.3	*a* = 6.067(2)	111.7
Cu	FM3M	*a* = 3.632	12.0	*a* = 3.613	11.8
Eu	IM3M	*a* = 4.447	44.0	*a* = 4.578	48.0
Fe	IM3M	*a* = 2.826	11.3	*a* = 2.886	12.0
Ir	FM3M	*a* = 3.881	14.6	*a* = 3.8394	14.2
K	IM3M	*a* = 5.291	74.1	*a* = 5.291(1)	74.1
La	P63/MMC	*a* = 3.751, *c* = 12.034	36.7	*a* = 3.77, *c* = 12.13	37.3
Li	IM3M	*a* = 3.433	20.2	*a* = 3.491(2)	21.3
Mg	P63/MMC	*a* = 3.196, *c* = 5.159	22.8	*a* = 3.20944, *c* = 5.21076	23.2
Mn	I43M	*a* = 8.609	11.0	*a* = 8.911(2)	12.2
Na	P63/MMC	*a* = 3.72, *c* = 6.06	36.3	*a* = 3.767(1), *c* = 6.154(1)	37.8
Ni	FM3M	*a* = 3.521	10.9	*a* = 3.5157	10.9
Os	P63/MMC	*a* = 2.76, *c* = 4.363	14.4	*a* = 2.7341, *c* = 4.3197	14.0
Pd	FM3M	*a* = 3.953	15.4	*a* = 3.991(2)	15.9
Pt	FM3M	*a* = 3.986	15.8	*a* = 3.944(4)	15.3
Rb	IM3M	*a* = 5.682	91.7	*a* = 5.697	92.5
Re	P63/MMC	*a* = 2.778, *c* = 4.487	15.0	*a* = 2.76, *c* = 4.458	14.7
Rh	FM3M	*a* = 3.844	14.2	*a* = 3.8043(3)	13.8
Ru	P63/MMC	*a* = 2.726, *c* = 4.309	13.9	*a* = 2.7059, *c* = 4.2815	13.6
Sr	FM3M	*a* = 5.952	52.7	*a* = 6.0849(5)	56.3
Tc	P63 MMC	*a*=2.759 *c* =4.405	14.5	*a* = 2.7407(1) *c* = 4.3980(1)	14.3
Yb	FM3M	*a* = 5.429	40.0	*a* = 5.4847	41.2
Yb_	P63/MMC	*a* = 3.849, *c* = 6.305	40.5	*a* = 3.911(3), *c* = 6.403(3)	42.4
Zn	P63 MMC	*a* = 2.631, *c* = 5.093	15.3	*a* = 2.6590(1) *c* = 4.8632(2)	14.9

* Reproduced in part with permission from Inorg. Chem., submitted for publication. Unpublished work copyright 2014 American Chemical Society.

Table C.1. (Continued)

binary hydrides					
BaH_2	PNMA	*a* = 6.816 *b* = 4.152 *c* = 7.851	55.5	*a* = 6.792(1) *b* = 4.168(1) *c* = 7.858(2)	55.6
CaH_2	PNMA	*a* = 5.877 *b* = 3.542 *c* = 6.744	35.1	*a* = 5.9696(12) *b* = 3.6022(8) *c* = 6.8336(14)	36.7
CsH	FM3M	*a* = 6.25	61.1	*a* = 6.3741(3)	64.7
CuH	P63MC	*a* = 2.856, *c* = 4.578	16.2	*a* = 2.89, *c* = 4.61	16.7
EuH_2	PNMA	*a* = 6.044 *b* = 3.704 *c* = 7.038	39.4	*a* = 6.239(2) *b* = 3.796(1) *c* = 7.196(2)	42.6
KH	FM3M	*a* = 5.668	45.5	*a* = 5.704	46.4
LaH_3	FM3M	*a* = 5.64	42.7	*a* = 5.667	44.0
LaH_2	FM3M	*a* = 5.546	44.9	*a* = 5.603	45.5
LiH	FM3M	*a* = 4.006	16.1	*a* = 4.0834(5)	17.0
MgH_2	P42/MNM	*a* = 4.483, *c* = 2.997	30.1	*a* = 4.5168, *c* = 3.0205	30.8
MnH	P63/MMC	*a* = 2.626, *c* = 4.552	13.6	*a* = 2.695, *c* = 4.373	13.8
NaH	FM3M	*a* = 4.803	27.7	*a* = 4.89	29.2
NiH	FM3M	*a* = 3.722	12.9	*a* = 3.74	13.1
Ni_2H	P3M1	*a* = 2.552, *c* = 4.214	23.8	*a* = 2.643, *c* = 4.308	26.5
$Ni_2H\_$	P3M1	*a* = 2.551, *c* = 4.215	23.8	*a* = 2.66, *c* = 4.33	26.1
PdH	FM3M	*a* = 4.138	17.7	*a* = 4.085(5)	17.0
RbH	FM3M	*a* = 5.824	49.4	*a* = 6.037	55.0
RhH	FM3M	*a* = 4.052	16.6	*a* = 4.01	16.1
SrH_2	PNMA	*a* = 5.724 *b* = 7.104 *c* = 4.086	41.5	*a* = 6.377(5) *b* = 7.358(5) *c* = 3.883(3)	45.6
YbH_2	PNMA	*a* = 5.785 *b* = 3.513 *c* = 6.673, α = 89.9°	33.9	*a* = 5.875(2) *b* = 3.565(2) *c* = 6.781(2)	35.5
$YbH_{2\_}$	FM3M	*a* = 5.364	38.6	*a* = 5.253(15)	36.2
YbH_3	FM3M	*a* = 5.192	35.0	*a* = 5.192(4)	35.0
Yb_3H_8	P31M	*a* = 6.557, *c* = 9.223	114.5	*a* = 6.3428(1) *c* = 9.0018(2)	104.5
intermetallics					
Ba_2Mg_{17}	R3MH	*a* = 10.619, *c* = 15.566	506.7	*a* = 10.65, *c* = 15.587	510.4
Ba_6Mg_{23}	FM3M	*a* = 15.199	877.7	*a* = 15.21	879.7
BaCu	P63/MMC	*a* = 4.483, *c* = 16.415	71.4	*a* = 4.499(3), *c* = 16.25(1)	71.2
$BaCu_{13}$	FM3C	*a* = 11.732	201.9	*a* = 11.697(8)	200.0
$BaMg_2$	P63/MMC	*a* = 6.65, *c* = 10.576	101.2	*a* = 6.6786(4) *c* = 10.6133(7)	102.5
$BaNa_2$	P63/MMC	*a* = 7.254, *c* = 11.782	134.2	*a* = 7.393(4), *c* = 11.999(9)	142.0
BaPd	CMCM	*a* = 4.471, *b* = 11.973 *c* = 4.706	62.8	*a* = 4.35, *b* = 11.79 *c* = 4.68	60.0
$BaPd_2$	FD3MS	*a* = 8.118	66.9	*a* = 7.967	63.2

Table C.1. (Continued)

$BaPd_5$	P6MMM	a = 5.61, c = 4.405	120.1	a = 5.54(1), c = 4.33(2)	115.1
BaPt	P63/MMC	a = 5.136, c = 5.524	63.1	a = 5.057(2), c = 5.420(3)	60.0
$BaPt_2$	FD3MS	a = 8.091	66.2	a = 7.918	62.1
$BaPt_5$	P6/ MMM	a = 5.633, c = 4.373	120.2	a = 5.505, c = 4.342	114.0
Ca_2Ni_7	R3MH	a = 4.977, c = 36.019	257.6	a = 5.009, c = 36.06	261.2
$CaMg_2$	P63/MMC	a = 6.222, c = 10.079	84.5	a = 6.2528(6) c = 10.1435(9)	85.9
$CaNi_2$	FD3MS	a = 7.184	46.3	a = 7.251	47.7
$CaNi_3$	R3MH	a = 4.999, c = 8.589	58.4	a = 5.03, c = 8.595	59.1
$CaNi_5$	P6/ MMM	a = 4.935, c = 3.93	82.9	a = 4.952, c = 3.937	83.6
$CaRh_2$	FD3MZ	a = 7.574	54.3	a = 7.525	53.3
$Cd_{13}Cs$	FM3C	a = 14.093	349.9	a = 13.920(3)	337.2
Co_2Mg	P63/MMC	a = 4.812, c = 7.855	39.4	a = 4.867, c = 7.973	40.9
CoMg	Fd3MS	a = 11.325	30.3	a = 11.434(2)	31.1
Cs_2Pt	P63/MMC	a = 5.825, c = 8.216	120.7	a = 5.676(1), c = 9.471(3)	132.1
Eu_2Mg_{17}	P63/MMC	a = 10.436, c = 10.242	483.0	a = 10.498(7), c = 10.30(1)	491.5
Eu_2Ni_{17}	P63/MMC	a = 8.33, c = 8.044	241.7	a = 8.35, c = 8.06	243.3
Eu_3Pd_2	R3H	a = 9.001, c = 17.38	135.5	a = 9.204, c = 17.384	141.7
Eu_5Pd_2	C12C1	a = 16.762, b = 6.787 c = 7.768, β = 97.07°	219.3	a = 17.299, b = 6.985 c = 7.919, β = 97.25°	237.3
$EuFe_2$	P63/MMC	a = 5.167, c = 8.463	48.9	a = 5.889, c = 9.624	72.3
EuMg	PM3M	a = 4.049	66.4	a = 4.0493	66.4
$EuMg_2$	P63/MMC	a = 6.327, c = 10.23	88.7	a = 6.4, c = 10.35	91.8
$EuMg_4$	P63/MMC	a = 10.3, c = 27.595	140.8	a = 10.416, c = 28.051	146.4
$EuMg_5$	P63/MMC	a = 10.365, c = 10.595	164.3	a = 10.412(6) c = 10.762(6)	168.4
$EuNi_2$	P63/MMC	a = 5.041, c = 16.596	45.7	a = 5.39, c = 17.49	55.0
$EuNi_5$	P6/MMM	a = 4.92, c = 3.951	82.2	a = 4.905, c = 3.948	82.3
EuPd	CMCM	a = 3.985, b = 10.922 c = 4.443	48.3	a = 4.092, b = 11.075 c = 4.45	50.4
$EuPd_2$	FD3MS	a = 7.744	58.1	a = 7.763	58.5
$EuPd_3$	PM3M	a = 4.138	70.9	a = 4.088	68.3
$Fe_{17}Yb_2$	P63/MMC	a = 8.441, c = 8.219	253.5	a = 8.406, c = 8.288	253.6
$Fe_{23}Yb_6$	FM3M	a = 11.945	426.1	a = 11.95	426.6
Fe_2Yb	FD3MS	a = 7.149	45.7	a = 7.239(5)	47.4
Ir_3Li	IMM2	a = 2.705, b = 8.788 c = 4.712	56.0	a = 2.6726, b = 8.6946 c = 4.6703	54.3
IrLi	P6M2	a = 2.673, c = 4.405	27.3	a = 2.649, c = 4.3968	26.7
KNa_2	P63/MMC	a = 7.382, c = 12.143	143.3	a = 7.5, c = 12.31	149.9
KZn_{13}	FM3C	a = 12.353	235.6	a = 12.379(3)	237.1
La_2Mg_{17}	P63/MMC	a = 10.362, c = 10.15	471.9	a = 10.35, c = 10.28	476.8
La_2Ni_3	CMCM	a = 5.059, b = 9.514 c = 8.053	96.9	a = 5.1138, b = 9.7316 c = 7.9075	98.4
La_2Ni_7	P63/MMC	a = 5.036, c = 24.686	135.6	a = 5.0577(4) c = 24.7336(22)	137.0

Table C.1. (Continued)

La_3Ni	PNMA	a = 7.157, b = 10.214 c = 6.606	120.7	a = 7.22, b = 10.275 c = 6.718	124.6
La_7Ni_{16}	I4-2M	a = 7.34, c = 14.507	390.8	a = 7.355(1), c = 14.51(1)	392.5
La_7Ni_3	P63MC	a = 10.059, c = 6.507	285.1	a = 10.140(5), c = 6.475(3)	288.3
LaMg	PM3M	a = 3.961	62.2	a = 3.970(3)	62.6
$LaMg_{12}$	I4MMM	a = 10.305, c = 5.951	316.0	a = 10.34, c = 5.96	318.6
$LaMg_2$	FD3MS	a = 8.765	84.2	a = 8.806	85.4
$LaMg_3$	FM3M	a = 7.499	105.4	a = 7.51	105.9
LaNi	CMCM	a = 5.736, b = 10.816 c = 4.433	45.8	a = 3.9, b = 10.79 c = 4.38	46.1
$LaNi_2$	FD3MS	a = 7.368	50.0	a = 7.247	47.6
$LaNi_3$	R3MH	a = 5.054, c = 25.114	61.7	a = 5.083, c = 25.09	62.4
$LaNi_5$	P6/ MMM	a = 5.003, c = 3.978	86.2	a = 5.016, c = 3.982	86.8
$Li_{15}Pd_4$	I4-3D	a = 10.628, c = 10.628	300.1	a = 10.676, c = 10.676	304.2
Li_2Pd	P6/ MMM	a = 4.233, c = 2.73	42.4	a = 4.2267, c = 2.7319	42.3
Li_2Pt	P6/MMM	a = 4.197, c = 2.703	41.3	a = 4.186, c = 2.661	40.4
Li_3Pd	FM3M	a = 6.187	59.2	a = 6.187	59.2
LiPd	P6M2	a = 2.805, c = 4.165	28.4	a = 2.7673, c = 4.1306	27.4
LiPd_	PM3M	a = 2.998	26.9	a = 2.977	26.4
$LiPd_7$	FM3M	a = 7.846	120.7	a = 7.713(4)	114.7
LiPt	P6M2	a = 2.77, c = 4.249	28.2	a = 2.728, c = 4.226	27.2
$LiPt_2$	FD3-Ms	a = 7.467	52.0	a = 7.6	54.9
$LiPt_7$	FM3M	a = 7.889	122.7	a = 7.725	115.2
LiRh	P6	a = 2.671, c = 4.367	27.0	a = 2.649(3), c = 4.359(2)	26.5
$Mg_{17}Sr_2$	P63/MMC	a = 10.508, c = 10.291	492.0	a = 10.53, c = 10.408	499.7
$Mg_{23}Sr_6$	FM3M	a = 14.864	820.9	a = 15	843.8
Mg_2Ni	P6222	a = 5.188, c = 13.152	51.1	a = 5.216(6), c = 13.20(6)	51.8
Mg_2Sr	P63/MMC	a = 6.454, c = 10.405	93.8	a = 6.4845(8) c = 10.4558(14)	95.2
Mg_2Yb	P63/MMC	a = 6.212, c = 10.072	84.2	a = 6.2015(2) c = 10.0614(2)	83.8
$Mg_{38}Sr9$	P63/MMC	a = 10.5, c = 28.251	1334.1	a = 10.500(2) c = 28.251(3)	1348.7
Mg_3Ru_2	P4132	a = 6.952	84.0	a = 6.9352(6)	83.4
Mg_4Sr	P63/MMC	a = 10.438, c = 27.925	146.4	a = 10.511(8) c = 28.362(11)	150.8
$MgNi_2$	P63/MMC	a = 4.805, c = 15.837	39.6	a = 4.824(2) c = 15.826(10)	39.9
MgSr	PM3M	a = 4.189	73.2	a = 3.908	59.7
MnRb	PM3M	a = 3.037	28.0	a = 3.051	28.4
$NaPt_2$	FD3MZ	a = 7.601	54.9	a = 7.482(2)	52.4
$Ni_{17}Yb_2$	P63/MMC	a = 8.271, c = 8.007	237.2	a = 8.25, c = 8.005	235.9
Ni_2Yb	FD3MS	a = 7.05	43.8	a = 7.099	44.7
Ni_3Yb	R3MH	a = 4.918, c = 24.076	56.0	a = 4.92, c = 24.16	56.3
Ni_5Yb	P6/ MMM	a = 4.862, c = 3.943	80.7	a = 4.845, c = 3.958	80.5

Table C.1. (Continued)

NiYb	PNMA	a = 7.455, b = 4.048 c = 5.394	40.7	a = 6.9, b = 4.06, c = 5.38	37.7
Pd_2Sr	FD3MS	a = 7.933	62.4	a = 7.800(2)	59.3
Pd_5Sr	P6/ MMM	a = 5.457, c = 4.459	115.0	a = 5.411, c = 4.416	112.0
PdSr	CMCM	a = 4.233, b = 11.405 c = 4.57	55.2	a = 4.19, b = 11.31 c = 4.52	53.6
Pt_2Sr	FD3MZ	a = 7.859	60.7	a = 7.777	58.8
Pt_2Sr_3	R3H	a = 9.334, c = 17.989	150.8	a = 9.337, c = 17.762	149.0
Pt_3Sr_7	PNMA	a = 7.996, b = 24.491 c = 7.178	351.4	a = 7.929(1), b = 24.326(6) c = 7.100(4)	342.4
Pt_4Sr_5	PNMA	a = 7.968, b = 15.726 c = 8.168	255.9	a = 7.879, b = 15.606 c = 8.147	250.4
Pt_5Sr_1	P6/ MMM	a = 5.5, c = 4.417	115.7	a = 5.397, c = 4.364	110.1
$RbZn_{13}$	FM3C	a = 12.409	234.5	a = 12.45191(16)	241.3
RuYb	PM3M	a = 3.337	37.2	a = 3.36	37.9
Complex Transition Metal Hydrides					
Ba_2OsH_6	FM3M	a = 8.08	131.9	a = 8.0357(4)	129.7
Ba_2PdH_4	PNMA	a = 8.053, b = 5.789 c = 10.257	119.6	a = 7.999(1), b = 5.7620(9) c = 10.157(2)	117.0
Ba_2PtH_6	CMCA	a = 5.996, c = 7.888	131.2	a = 6.001,c = 7.831	130.3
Ba_2RuH_6	FM3M	a = 8.054	130.6	a = 8.0166(7)	128.8
$Ba_3Ir_2H_{12}$	P3M1	a = 5.507, c = 8.874	233.1	a = 5.4761(4) c = 8.8318(8)	229.4
$Ba_7Cu_3H_{17}$	P31C	a = 11.814 c = 7.476	451.8	a = 11.7633(1) c = 7.4495(1)	446.4
$BaMg_2FeH_8$	P3M1	a = 4.535 c = 6.924	123.3	a = 4.5683(4) c = 6.9163(3)	125.0
$BaMg_2OsH_8$	P42 MMC	a = 4.971 c = 10.828	133.8	a = 4.9672(1) c = 10.8210(3)	133.5
$BaMg_2RuH_8$	P42 MMC	a = 4.957 c = 10.805	132.7	a = 4.9623(1) c = 10.7957(3)	132.9
$BaReH_9$	P63/ MMC	a = 5.236, c = 9.653	114.6	a = 5.287(1), c = 9.323(2)	112.8
Ca_2FeH_6	FM3M	a = 6.978	84.9	a = 7.036(1)	87.1
Ca_2OsH_6	FM3M	a = 7.223	94.2	a = 7.2361(6)	94.7
Ca_2RuH_6	FM3M	a = 7.189	92.9	a = 7.2214(1)	94.1
$Ca_4Mg_4Fe_3H_{22}$	P43M	a = 6.637	292.3	a = 6.7016(4)	301.0
$Ca_8Rh_6H_{24}$	IM3M	a = 7.276	385.2	a = 7.283(1)	386.3
$CaMgNiH_4$	P213	a = 6.697	75.1	a = 6.7301(4)	76.2
$CaNidH_3$	PM3M	a = 3.516	43.5	a = 3.551(4)	44.8
Cs_2PdH_4	P42/ MNM	a = 6.247, c = 8.917	174.0	a = 6.17(1), c = 8.85(1)	168.5
Cs_2PtH_4	P42/ MNM	a = 6.188, c = 8.926	170.9	a = 6.114(9), c = 8.72(2)	163.0
Cs_2PtH_6	FM3M	a = 8.742	167.0	a = 8.9681(1)	180.3
Cs_2ZnH_4	PNMA	a = 8.563 b = 6.335 c = 11.097	150.5	a = 8.5536(3), b = 6.3296(3) c = 11.0954(6)	150.2

Table C.1. (Continued)

Cs_3CdH_5	I4MCM	*a* = 8.464 *c* = 8.721	227.2	*a* = 8.423 *c* = 8.667	223.4
Cs_3MnH_5	I43M	*a* = 8.255 *c* = 11.599	197.6	*a* = 8.339(1) *c* = 12.538(2)	221.1
Cs_3PdH_3	P42/ MNM	*a* = 11.885 *c* = 11.462	202.4	—	
Cs_3PdH_5	P4MBM	*a* = 8.223 *c* = 6.308	213.3	*a* = 8.301(7), *c* = 6.024(5)	207.5
Cs_3PtH_5	P4MBM	*a* = 8.244, *c* = 6.22	211.4	*a* = 8.347(7) *c* = 5.914(6)	206.0
Cs_3ZnH_5	I4MCM	*a* = 8.279 *c* = 8.472	209.9	*a* = 8.3052(3) *c* = 12.1875(5)	210.2
Eu_2FeH_6	FM3M	*a* = 7.154	91.5	*a* = 7.23(2)	94.5
Eu_2PdH_4	PNMA	*a* = 7.372 *b* = 5.297 *c* = 9.375	91.5	*a* = 7.4947(1) *b* = 5.4334(1) *c* = 9.5791(1)	97.5
Eu_2RuH_6	FM3M	*a* = 7.38	100.4	*a* = 7.557	107.9
$EuMgNiH_4$	P213	*a* = 6.753	76.9	*a* = 6.8486(7)	80.3
$EuPdH_3$	PM3M	*a* = 3.759	53.1	*a* = 3.8001(2)	54.9
K_2PdH_4	I4MMM	*a* = 5.888, *c* = 7.688	133.3	*a* = 5.831(1) *c* = 7.692(1)	130.8
K_2PtH_4	P42/ MNM	*a* = 5.626, *c* = 8.221	130.1	*a* = 5.582(1), *c* = 8.085(2)	126.0
K_2PtH_6	FM3M	*a* = 8.173	136.5	*a* = 8.1399(6)	134.8
K_2ReH_9	P62M	*a* = 9.541 *c* = 5.568	146.3	*a* = 9.599(1) *c* = 5.549(1)	147.6
K_2ZnH_4	PNMA	*a* = 7.742 *b* = 5.812 *c* = 10.219	145.2	*a* = 7.7579(4) *b* = 5.8631(3) *c* = 10.2813(5)	116.9
K_3MnH_5	I4MCM	*a* = 7.544 *c* = 7.877	115.0	*a* = 7.519(1) *c* = 7.894	165.0
K_3PdH_3	P42/ MNM	*a* = 10.819 *c* = 10.348	164.9	*a* = 10.700(8) *c* = 10.535(9)	150.8
K_3PdH_5	P4MBM	*a* = 7.387 *c* = 5.811	151.4	*a* = 7.432(3) *c* = 5.811(2)	160.5
K_3PtH_5	P4MBM	*a* = 7.397 *c* = 5.747	158.5	*a* = 7.472(1) *c* = 5.706(1)	159.3
K_3ReH_6	FM3M	*a* = 8.467	157.2	*a* = 8.623(1)	160.3
K_2TcH_9	P62M	*a* = 9.506 *c* = 5.567	151.7	—	149.2
K_3ZnH_5	I4MCM	*a* = 7.523 *c* = 11.125	157.4	*a* = 7.5819(4) *c* = 11.1671(5)	160.5
$KNaReH_9$	PNMA	*a* = 9.132 *b* = 5.429 *c* = 10.083	125.0	*a* = 9.2045(9) *b* = 5.4218(5) *c* = 10.1195(10)	126.3
$La_{16}Mg_8Ni_{16}H_{64}$	P121/ C1	*a* = 11.77, *b* = 7.758 *c* = 12.013 β = 92.67°	1095.8	*a* = 11.84482, *b* = 7.8211 *c* = 11.9631 β = 92.78°	1106.9
$La_2Ni_{10}H_{14}$	P63MC	*a* = 5.349 *c* = 8.698	215.5	*a* = 5.332 *c* = 8.626	212.4

Table C.1. (Continued)

$LaMg_2NiH_7$	P121/ C1	a = 13.93, b = 4.662 c = 15.964 β = 125.16°	106.0	a = 13.9789(7) b = 4.7026(2) c = 16.0251(8), β = 125.24°	107.5
Li_2PdH_2	I4MMM	a = 3.118 c = 10.305	50.1	a = 3.1108(4) c = 10.331(3)	50.0
Li_2PtH_2	IMMM	a = 5.515, b = 3.078 c = 10.078	50.6	a = 3.268(1), b = 2.992(1) c = 10.049(1)	49.1
Li_2PtH_6	FM3M	a = 6.685	74.7	a = 6.7681(3)	77.5
Li_3IrH_6	PNMA	a = 8.482, b = 4.741 c = 8.524	85.7	a = 8.480(3), b = 4.788(2) c = 8.521(3)	86.5
Li_3RhH_4	CMCM	a = 3.784, b = 8.926 c = 8.795	74.3	a = 3.865(2), b = 8.968(6) c = 8.968(6)	76.6
Li_3RhH_6	PNMA	a = 8.434, b = 4.701 c = 8.511	84.4	a = 8.516(3), b = 4.799(3) c = 8.507(3)	86.9
Li_4OsH_6	R3CH	a = 5.831	99.1	a = 5.822	98.7
Li_4RhH_4	I4/M	a = 6.235, c = 4.106	79.8	a = 6.338(5), c = 4.113(8)	82.6
Li_4RhH_5	CMCM	a = 3.893, b = 9.201 c = 9.255	82.9	a = 3.88, b = 9.02 c = 8.895	77.8
Li_4RuH_6	R3CH	a = 7.906, c = 9.775	88.2	a = 8.1163, c = 9.9761	96.0
$Li_5Pt_2H_9$	I4/MCM	a = 7.259, c = 7.259 α = 108.54° β = γ = 109.93°	147.2	a = 7.28, c = 7.28 α = 108.33°, β = γ = 110.04°	148.5
$LiMg_2OsH_7$	P63/ MMC	a = 4.695, c = 10.729	102.4	—	
$LiMg_2RuH_7$	P63/ MMC	a = 4.682 c = 10.676	101.3	a = 4.6998(1) c = 10.6674(3)	102.0
$LiMg_4Os_2H_{13}$	P63/ MMC	a = 4.703 c = 18.406	176.3	a = 4.7214(2) c = 18.4437(2)	178.0
$LiMg_4Ru_2H_{13}$	P63/ MMC	a = 4.679, c = 18.31	173.6	—	
LiPdH	P4 MMM	a = 2.759, c = 4.868	37.1	a = 2.7960(2) c = 4.0042(4)	31.3
Mg_2CoH_5	P4N MMZ	a = 4.435, c = 6.529	64.2	a = 4.463(4), c = 6.593(6)	65.7
Mg_2FeH_6	FM3M	a = 6.373	64.7	a = 6.430(1)	66.5
Mg_2NiH_4	C12/C1	a = 7.815, b = 6.365 c = 6.445,α=111.2° β=114.03°, γ=90°	67.2	a = 6.403, b = 6.483 c = 7.853 α=111.4°, β=114.1°, γ=90°	68.2
Mg_2OsH_6	FM3M	a = 6.658	73.8	a = 6.6828(6)	74.6
Mg_2RuH_4	CMCM	a = 6.978, b = 8.411 c = 4.801	70.5	a = 6.9696(3), b=8.3886(3) c = 4.8039(2)	70.2
Mg_2RuH_6	FM3M	a = 6.641	73.2	a = 6.6409(9)	73.2
Mg_3MnH_7	P63/ MMC	a = 4.652, c = 10.24	96.0	a = 4.6998(1) c = 10.2590(2)	98.1
Mg_3ReH_7	P63/ MMC	a = 4.834, c = 10.574	107.0	a = 4.8539(2) c = 10.5699(7)	107.8
Na_2PdH_2	I4MMM	a = 3.564, c = 11.346	72.1	a = 3.599(1) c = 11.327(3)	73.4
Na_2PdH_4	I4MMM	a = 5.323, c = 6.513	92.3	a = 5.338(1) c = 6.614(2)	94.2
Na_2PtH_4	I4MMM	a = 5.26, c = 6.692	92.6	a = 5.2548(9) c = 6.7509(14)	93.2

Table C.1. (Continued)

Na_2PtH_6	FM3M	a = 7.305	97.5	a = 7.3410(5)	98.9
Na_3IrH_6	PNMA	a = 9.349, b =5.238 c = 9.555	117.0	a = 9.303(2), b = 5.236(1) c = 9.551(2)	116.3
Na_3OsH_7	P42/ MNM	a = 9.541 c = 5.268	119.9	a = 9.5836(1) c = 5.3541(1)	122.9
Na_3RhH_6	PNMA	a = 9.326, b = 5.222 c = 9.561	116.4	a = 9.369(2), b = 5.279(1) c = 9.600(2)	118.7
Na_3RuH_7	P42/ MNM	a = 9.528, c = 5.24	118.9	a = 9.589(1), c = 5.365(2)	123.3
Na_4RuH_6	R3CH	a = 6.489, c = 6.489	136.6	a = 6.496, c = 6.496	137.1
$NaBaPdH_3$	P63/ MMC	a = 6.082, c = 6.14	98.4	a = 6.0513(4) c = 6.0813(19)	96.4
$NaPd_3H_2$	CMMM	a = 5.705, b =8.673 c = 2.845	70.4	a = 5.6532(7), b = 8.590(3) c = 2.8197(4)	68.5
Rb_2PdH_4	P42/ MNM	a = 5.904, c = 8.569	149.3	a = 5.827(1), c = 8.495(2)	144.2
Rb_2PtH_4	P42/ MNM	a = 5.923, c = 8.44	148.1	a = 5.853(1), c = 8.380(2)	143.5
Rb_2PtH_6	FM3M	a = 8.311	152.9	a = 8.5369(1)	155.5
Rb_2ZnH_4	PNMA	a = 8.128, b =6.048 c = 10.624	130.6	a = 8.1371(4), b= 6.0702(3) c = 10.6461(5)	131.5
Rb_3MnH_5	I4MCM	a = 7.919, c = 8.21	188.3	a = 8.0079(7), c= 12.033(1)	192.9
Rb_3PdH_3	I4MMM	a = 11.328 c = 10.859	174.2	a = 11.215, c = 11.083	174.2
Rb_3PdH_5	P4MBM	a = 7.769, c= 6.064	183.0	a = 7.800(3), c = 5.987(2)	182.1
Rb_3PtH_5	P4MBM	a = 7.777, c = 5.993	181.2	a = 7.828(4), c = 5.868(3)	179.8
Rb_3ZnH_5	I4MCM	a = 7.885, c = 11.629	180.8	a = 7.9404(2) c = 11.6293(7)	183.3
Sr_2FeH_6	FM3M	a = 7.411	101.8	a = 7.317(9)	97.9
Sr_2OsH_6	FM3M	a = 7.612	110.3	a = 7.626(1)	110.9
Sr_2PdH_4	PNMA	a = 5.502 b = 7.616 c = 9.722	101.8	a = 5.4975(3) b = 7.5841(3) c = 9.6933(5)	101.0
Sr_2PtH_6	CMCA	a = 7.446 c = 5.628	109.2	—	
Sr_2RuH_6	FM3M	a = 7.6	109.8	a = 7.6	109.7
$SrMg_2FeH_8$	P3M1	a = 4.472 c = 6.538	113.2	a = 4.5072(2) c = 6.5663(4)	115.5
$SrMgNiH_4$	P213	a = 6.873	81.2	a = 6.8953(4)	82.0
Yb_2FeH_6	FM3M	a = 6.897	82.0	—	
Yb_2RuH_6	FM3M	a = 7.11	89.9	a = 7.2157(18)	93.9
$Yb_4Mg_4Fe_3H_{22}$	P43M	a = 6.595	286.9	a = 6.6839(5)	298.6
$YbMgNiH_4$	P213	a = 6.638	73.1	a = 6.7114(6)	75.6
ternary saline metal hydrides					
$Ba_2Mg_3H_{10}$	C12M1	a = 5.838, b = 7.851 c = 9.413 α = 110.80° β = 108.06° γ = 90°	190.2	a = 5.856, b = 7.869 c = 9.44 α = 110.75° β = 108.07° γ = 90°	191.9
Ba_2MgH_6	P3M1	a = 5.7, c = 4.523	127.3	a = 5.7257, c = 4.5148	128.2

Table C.1. (Continued)

$Ba_6Mg_7H_{26}$	IMMM	*a* = 5.78 *b* = 11.903 *c* = 14.895	512.4	*a* = 5.8005(6) *b* = 11.925(1) *c* = 14.836(2)	513.1
$BaMgH_4$	CMCM	*a* = 4.172 *b* = 13.68 *c* = 5.688	81.2	*a* = 4.1992(1) *b* = 13.7374(5) *c* = 5.6852(2)	82.0
$Ca_{19}Mg_8H_{54}$	IM3	*a* = 12.105	887.0	*a* = 12.0642(8)	877.9
$Ca_4Mg_3H_{14}$	P62M	*a* = 6.202 *c* = 6.832	227.6	*a* = 6.2902(2) *c* = 6.8540(3)	234.9
$Eu_2Mg_3H_{10}$	C12/M1	*a* = 17.189 *b* = 5.585, *c* = 7.213 β = 111.05°	161.6	*a* = 17.4841(5) *b* = 5.7231(2) *c* = 7.3647(2), β = 114.48°	171.4
Eu_2MgH_6	P3-M1	*a* = 5.301 *c* = 4.051	98.6	*a* = 5.50644(6) *c* = 4.10054(6)	107.7
$Eu_6Mg_7H_{26}$	I12/M1	*a* = 14.258 *b* = 5.689 *c* = 11.599 β = 91.80°	431.3	*a* = 14.0939(4) *b* = 5.6455(2) *c* = 11.5090(3) β = 90.68°	457.9
$EuMg_2H_6$	P4/ MMM	*a* = 3.702, *c* = 7.947	108.9	*a* = 3.7657(5), *c* = 7.992(2)	113.3
$EuMgH_4$	CMC21	*a* = 3.871 *b* = 13.041 *c* = 5.489	69.3	*a* = 3.9297(5) *b* = 13.468(2) *c* = 5.5386(7)	73.3
$LaMg_2H_7$	P41212	*a* = 6.329, *c* = 9.484	95.0	*a* = 6.3900(2) *c* = 9.5782(4)	97.8
$Mg_3Sr_2H_{10}$	C12M1	*a* = 17.449 *b* = 5.674, *c* = 7.425 β = 111.26°	171.3	*a* = 17.539(4), *b* = 5.730(1), *c* = 7.480(2) β = 111.48°	174.9
$Mg_7Sr_6H_{26}$	I12M1	*a* = 18.125 *b* = 5.617 *c* = 14.204 β = 39.41°	459.1	*a* = 14.254(2) *b* = 5.6711(4) *c* = 11.575(1)	467.8
$Mg_8Yb_{19}H_{54}$	IM-3	*a* = 10.391 α = 109.45°	863.4	*a* = 10.484, α = 109.471°	887.2
$MgSr_2H_6$	P3M1	*a* = 5.463 *c* = 4.183	108.1	*a* = 5.5458(2) *c* = 4.1630(2)	110.9
$SrMgH_4$	CMC21	*a* = 3.941 *b* = 13.459 *c* = 5.593	74.2	*a* = 3.9661(3) *b* = 13.685(1) *c* = 5.5755(6)	75.7
$Yb_4Mg_3H_{14}$	P-62M	*a* = 6.168 *c* = 6.773	223.2	*a* = 6.2479(5) *c* = 6.8173(9)	230.5

Table C.2: Calculated and experimental lattice properties for metals, binary hydrides, intermetallics, and higher hydrides included in Round 2 CTMH Hydride Screening. *a,b,c* in Å

		DFT		EXPERIMENT	
material	space group		*V* (Å^3 f.u.$^{-1}$)		*V* (Å^3 f.u.$^{-1}$)
		metals			
Ba	IM3M	*a* = 4.998	62.4	*a* = 5.01	62.9
Ca	FM3M	*a* = 5.507	41.7	*a* = 5.5884(2)	43.6
Ca_HT	IM3M	*a* = 4.368	41.7	*a* = 4.480	45.0
Cd	P63/MMC	*a* = 3.036, *c* = 5.595	22.3	*a* = 2.97912(14) *c* = 5.61827(45)	21.6
Co	P63/MMC	*a* = 2.492, *c* = 4.024	10.8	*a* = 2.5054, *c* = 4.0893	11.1
Cs	IM3M	*a* = 6.139	115.7	*a* = 6.067(2)	111.7
Eu	IM3M	*a* = 4.441	43.8	*a* = 4.578	48.0
Fe	IM3M	*a* = 2.829	11.3	*a* = 2.886	12.0
Ir	FM3M	*a* = 3.882	14.6	*a* = 3.8394	14.2
K	IM3M	*a* = 5.276	73.4	*a* = 5.291(1)	74.1
Li	IM3M	*a* = 3.436	20.3	*a* = 3.491(2)	21.3
Mg	P63/MMC	*a* = 3.192, *c* = 5.187	22.9	*a* = 3.20944, *c* = 5.21076	23.2
Na	P63/MMC	*a* = 3.717, *c* = 6.076	36.3	*a* = 3.767(1), *c* = 6.154(1)	37.8
Ni	FM3M	*a* = 3.518	10.9	*a* = 3.5157	10.9
Os	P63/MMC	*a* = 2.762, *c* = 4.350	14.4	*a* = 2.7341, *c* = 4.3197	14.0
Pd	FM3M	*a* = 3.954	15.5	*a* = 3.991(2)	15.9
Pt	FM3M	*a* = 3.985	15.8	*a* = 3.944(4)	15.3
Rb	IM3M	*a* = 5.656	90.5	*a* = 5.697	92.5
Re	P63/MMC	*a* = 2.779, *c* = 4.485	15.0	*a* = 2.76, *c* = 4.458	14.7
Rh	FM3M	*a* = 3.845	14.2	*a* = 3.8043(3)	13.8
Ru	P63/MMC	*a* = 2.730, *c* = 4.303	13.9	*a* = 2.7059, *c* = 4.2815	13.6
Yb	FM3M	*a* = 5.421	39.8	*a* = 5.4847	41.2
Yb_	P63/MMC	*a* = 3.849, *c* = 6.297	40.4	*a* = 3.911(3), *c* = 6.403(3)	42.4
Zn	P63 MMC	*a* = 2.657, *c* = 4.927	15.1	*a* = 2.6590(1) *c* = 4.8632(2)	14.9
		binary hydrides			
BaH_2	PNMA	*a* = 6.812 *b* = 4.151 *c* = 7.852	55.5	*a* = 6.792(1) *b* = 4.168(1) *c* = 7.858(2)	55.6
CaH_2	PNMA	*a* = 5.862 *b* = 3.549 *c* = 6.736	35.0	*a* = 5.9696(12) *b* = 3.6022(8) *c* = 6.8336(14)	36.7
CsH	FM3M	*a* = 6.394	65.3	*a* = 6.3741(3)	64.7
EuH_2	PNMA	*a* = 6.038 *b* = 3.707 *c* = 7.024	39.3	*a* = 6.239(2) *b* = 3.796(1) *c* = 7.196(2)	42.6
KH	FM3M	*a* = 5.660	45.3	*a* = 5.704	46.4
LiH	FM3M	*a* = 3.999	16.0	*a* = 4.0834(5)	17.0
MgH_2	P42/MNM	*a* = 4.480, *c* = 3.000	30.1	*a* = 4.5168, *c* = 3.0205	30.8

Table C.2. (Continued)

NaH	FM3M	a = 4.798	27.6	a = 4.89	29.2
NiH	FM3M	a = 3.720	12.9	a = 3.74	13.1
Ni_2H	P3M1	a = 2.550, c = 4.222	23.8	a = 2.66, c = 4.33	26.1
PdH	FM3M	a = 4.139	17.7	a = 4.085(5)	17.0
RbH	FM3M	a = 6.006	54.1	a = 6.037	55.0
RhH	FM3M	a = 4.054	16.7	a = 4.01	16.1
YbH_2	PNMA	a = 5.763 b = 3.522 c = 6.666	33.8	a = 5.875(2) b = 3.565(2) c = 6.781(2)	35.5
YbH_3	FM3M	a = 5.189	34.9	a = 5.192(4)	35.0
Yb_3H_8	P31M	a = 6.559, c = 9.232	114.7	a = 6.3428(1) c = 9.0018(2)	104.5
		intermetallics			
$Cd_{13}Cs$	FM3C	a = 14.093	349.9	a = 13.920(3)	337.2
Co_2Mg	P63/MMC	a = 4.743, c = 7.787	58.3	a = 4.867, c = 7.973	40.9
CoMg	Fd3MS	a = 11.27	29.8	a = 11.434(2)	31.1
Cs_2Pt	P63/MMC	a = 5.825, c = 8.153	119.8	a = 5.676(1), c = 9.471(3)	132.1
KZn_{13}	FM3C	a = 12.334	234.5	a = 12.379(3)	237.1
LiRh	P6	a = 2.673, c = 4.365	27.0	a = 2.649(3), c = 4.359(2)	26.5
Mg_2Ni	P6222	a = 5.196, c = 13.151	51.2	a = 5.216(6), c = 13.20(6)	51.8
Mg_3Ru_2	P4132	a = 6.952	84.0	a = 6.9352(6)	83.4
$MgNi_2$	P63/MMC	a = 4.802, c = 15.817	39.5	a = 4.824(2) c = 15.826(10)	39.9
$NaPt_2$	FD3MZ	a = 7.601	54.9	a = 7.482(2)	52.4
$RbZn_{13}$	FM3C	a = 12.396	238.1	a = 12.45191(16)	241.3
RuYb	PM3M	a = 3.337	37.1	a = 3.36	37.9
		Complex Transition Metal Hydrides			
Ba_2OsH_6	FM3M	a = 8.084	132.1	a = 8.0357(4)	129.7
Ba_2RuH_6	FM3M	a = 8.062	131.0	a = 8.0166(7)	128.8
$Ba_3Ir_2H_{12}$	P3M1	a = 5.501, c = 8.873	232.6	a = 5.4761(4) c = 8.8318(8)	229.4
Ca_2OsH_6	FM3M	a = 7.216	93.9	a = 7.2361(6)	94.7
Ca_2RuH_6	FM3M	a = 7.189	92.9	a = 7.2214(1)	94.1
Cs_2PdH_4	P42/MNM	a = 6.247, c = 8.917	173.5	a = 6.17(1), c = 8.85(1)	168.5
Cs_2PtH_4	P42/MNM	a = 6.188, c = 8.926	171.2	a = 6.114(9), c = 8.72(2)	163.0
Cs_2PtH_6	FM3M	a = 8.742	182.2	a = 8.9681(1)	180.3
Cs_2ZnH_4	PNMA	a = 8.563 b = 6.335 c = 11.097	150.8	a = 8.5536(3) b = 6.3296(3) c = 11.0954(6)	150.2
Cs_3CdH_5	I4MCM	a = 8.404, c = 8.701	224.4	a = 8.423 c = 8.667	223.4
Cs_3PdH_3	P42/MNM	a = 11.908, c = 11.524	204.2	—	
Cs_3PdH_5	P4MBM	a = 8.218, c = 6.320	213.4	a = 8.301(7), c = 6.024(5)	207.5

Table C.2. (Continued)

Cs_3PtH_5	P4MBM	a = 8.229, c = 6.257	211.8	a = 8.347(7), c = 5.914(6)	206.0
Cs_3ZnH_5	I4MCM	a = 8.288, c = 8.477	210.3	a = 8.3052(3) c = 12.1875(5)	210.2
Eu_2RuH_6	FM3M	a = 7.365	99.9	a = 7.557	107.9
K_2PdH_4	I4MMM	a = 5.872, c = 7.657	132.0	a = 5.831(1), c = 7.692(1)	130.8
K_2PtH_4	P42/ MNM	a = 5.627, c = 8.186	129.6	a = 5.582(1), c = 8.085(2)	126.0
K_2PtH_6	FM3M	a = 8.166	136.1	a = 8.1399(6)	134.8
K_2ZnH_4	PNMA	a = 7.757 b = 5.798 c = 10.232	115.0	a = 7.7579(4) b = 5.8631(3) c = 10.2813(5)	116.9
K_3PdH_3	P42/ MNM	a = 10.827 c = 10.332	151.4	a = 10.700(8) c = 10.535(9)	150.8
K_3PdH_5	P4MBM	a = 7.395, c = 5.802	158.6	a = 7.432(3) c = 5.811(2)	160.5
K_3PtH_5	P4MBM	a = 7.417, c = 5.737	157.8	a = 7.472(1) c = 5.706(1)	159.3
K_3ZnH_5	I4MCM	a = 7.498, c = 11.167	156.9	a = 7.5819(4) c = 11.1671(5)	160.5
Li_3RhH_4	CMCM	a = 3.777, b = 8.922 c = 8.798	74.1	a = 3.865(2), b = 8.968(6) c = 8.968(6)	76.6
Li_3RhH_6	PNMA	a = 8.435, b = 4.700 c = 8.516	84.4	a = 8.516(3), b = 4.799(3) c = 8.507(3)	86.9
Li_4OsH_6	R3CH	a = 5.771	96.1	a = 5.822, c = 5.822	98.7
Li_4RhH_4	I4/M	a = 6.277, c = 4.064	80.1	a = 6.338(5), c = 4.113(8)	82.6
Li_4RhH_5	CMCM	a = 3.909, b = 9.230 c = 9.230	83.3	a = 3.88, b = 9.02 c = 8.895	77.8
Mg_2CoH_5	P4N MMZ	a = 4.428, c = 6.545	64.2	a = 4.463(4), c = 6.593(6)	65.7
Mg_2FeH_6	FM3M	a = 6.370	64.6	a = 6.430(1)	66.5
Mg_2NiH_4	C12/C1	a = 6.363, b = 6.445 c = 7.822, α=111.17° β=114.00°, γ=90°	67.3	a = 6.403, b = 6.483 c = 7.853, α=111.4° β = 114.1°, γ=90°	68.2
Mg_2OsH_6	FM3M	a = 6.654	73.6	a = 6.6828(6)	74.6
Mg_2RuH_4	CMCM	a = 6.988 b = 8.402 c = 4.804	70.5	a = 6.9696(3) b = 8.3886(3) c = 4.8039(2)	70.2
Mg_2RuH_6	FM3M	a = 6.618	72.5	a = 6.6409(9)	73.2
Mg_3ReH_7	P63/ MMC	a = 4.829, c = 10.592	107.0	a = 4.8539(2) c = 10.5699(7)	107.8
Na_2PdH_2	I4MMM	a = 3.570, c = 11.314	72.1	a = 3.599(1), c = 11.327(3)	73.4
Na_2PdH_4	I4MMM	a = 5.301, c = 6.551	92.0	a = 5.338(1) c = 6.614(2)	94.2
Na_2PtH_4	I4MMM	a = 5.245, c = 6.685	91.9	a = 5.2548(9) c = 6.7509(14)	93.2
Na_2PtH_6	FM3M	a = 7.299	97.2	a = 7.3410(5)	98.9
Na_3IrH_6	PNMA	a = 9.328, b = 5.230 c = 9.586	116.9	a = 9.303(2), b = 5.236(1) c = 9.551(2)	116.3
Na_3OsH_7	P42/ MNM	a = 9.542, c = 5.263	119.8	a = 9.5836(1) c = 5.3541(1)	122.9

Table C.2. (Continued)

Na_3RhH_6	PNMA	*a* = 9.301 *b* = 5.220 *c* = 9.581	116.3	*a* = 9.369(2) *b* = 5.279(1) *c* = 9.600(2)	118.7
Na_3RuH_7	P42/ MNM	*a* = 9.518, *c* = 5.256	119.0	*a* = 9.589(1), *c* = 5.365(2)	123.3
Na_4RuH_6	R3CH	*a* = 6.463	134.9	*a* = 6.496	137.1
$NaPd_3H_2$	CMMM	*a* = 5.709 *b* = 8.707 *c* = 2.838	70.5	*a* = 5.6532(7) *b* = 8.590(3) *c* = 2.8197(4)	68.5
Rb_2PdH_4	P42/ MNM	*a* = 5.892, *c* = 8.622	149.7	*a* = 5.827(1), *c* = 8.495(2)	144.2
Rb_2PtH_4	P42/ MNM	*a* = 5.900, *c* = 8.501	148.0	*a* = 5.853(1), *c* = 8.380(2)	143.5
Rb_2PtH_6	FM3M	*a* = 8.545	156.0	*a* = 8.5369(1)	155.5
Rb_2ZnH_4	PNMA	*a* = 8.149 *b* = 6.037 *c* = 10.619	130.6	*a* = 8.1371(4) *b* = 6.0702(3) *c* = 10.6461(5)	131.5
Rb_3PdH_3	I4MMM	*a* = 11.357 *c* = 10.867	175.2	*a* = 11.215, *c* = 11.083	174.2
Rb_3PdH_5	P4MBM	*a* = 7.790, *c* = 6.041	183.3	*a* = 7.800(3), *c* = 5.987(2)	182.1
Rb_3PtH_5	P4MBM	*a* = 7.806, *c* = 5.979	182.2	*a* = 7.828(4), *c* = 5.868(3)	179.8
Rb_3ZnH_5	I4MCM	*a* = 7.871 *c* = 11.658	180.6	*a* = 7.9404(2) *c* = 11.6293(7)	183.3
Yb_2RuH_6	FM3M	*a* = 7.108	89.8	*a* = 7.2157(18)	93.9

APPENDIX D

STRUCTURAL PARAMETERS FOR PROPOSED MATERIALS LIBRARY*

Table D.1: Structural parameters for proposed or hypothetical CTMHs. lattice constants *a,b,c* (Å), volume *V* (Å^3 f.u.$^{-1}$), decomposition temperature T_d (K), reaction energy ΔE_0 (kJ mol^{-1} H_2).

CTMH	prototype	lattice parameters	*V*	T_d	Decomposition Pathway	ΔE_0
Eu_2OsH_6_p	2-Sr_2RuH_6	*a* = 7.372	100.2	1545	⅓ Eu_2OsH_6_p ↔ ⅔ Eu + ⅓ Os + H_2	203.8
Yb_2OsH_6_p	2-Sr_2RuH_6	*a* = 7.124	90.4	1515	⅓ Yb_2OsH_6_p ↔ ⅓ Os + ⅔ Yb + H_2	200.2
Yb_2PtH_6_p	21-Ba_2PtH_6	*a* = 12.809, *c* = 5.250	88.3	1425	Yb_2PtH_6_p ↔ 2YbH_2 + Pt + H_2	217.2
$Eu_3Ir_2H_{12}$_p	31-$Ba_3Ir_2H_{12}$	*a* = 5.026, *c* = 8.245	180.4	1320	⅓ $Eu_3Ir_2H_{12}$_p ↔ ⅔ Ir + EuH_2 + H_2	164.2
Ca_2PtH_6_p	21-Ba_2PtH_6	*a* = 13.097, *c* = 5.296	91.8	1320	Ca_2PtH_6_p ↔ 2CaH_2 + Pt + H_2	163.0
Sr_2NiH_4_p	5-Mg_2NiH_4	*a* = 16.075, *b* = 7.457, *c* = 7.560 β =110.42°	106.2	1320	½ Sr_2NiH_4_p ↔ ½ Ni + Sr + H_2	165.3
$Sr_3Ir_2H_{12}$_p	31-$Ba_3Ir_2H_{12}$	*a* = 5.203, *c* = 8.463	198.4	1305	⅙ $Sr_3Ir_2H_{12}$_p ↔ ½ Sr + ⅓ Ir + H_2	162.9
$Sr_8Rh_6H_{24}$_p	41-$Ca_8Rh_6H_{24}$	*a* = 7.596	438.2	1290	1/12 $Sr_8Rh_6H_{24}$_p ↔ ¼ $SrRh_2$ + 5/12 Sr + H_2	159.2
K_2PtH_2_p	37-Li_2PtH_2	*a* = 4.163, *b* = 4.166, *c* = 12.219	106.0	1290	K_2PtH_2_p ↔ Pt + 2K + H_2	160.4
$Yb_3Ir_2H_{12}$_p	31-$Ba_3Ir_2H_{12}$	*a* = 4.868, *c* = 8.056	165.4	1260	⅓ $Yb_3Ir_2H_{12}$_p ↔ YbH_2 + ⅔ Ir + H_2	172.2
$Eu_8Rh_6H_{24}$_p	41-$Ca_8Rh_6H_{24}$	*a* = 7.411	407.0	1245	1/12 $Eu_8Rh_6H_{24}$_p ↔ 7/48 $EuRh_2$ + 5/48 Eu_5Rh_2 + H_2	151.3
Cs_2PtH_2_p	37-Li_2PtH_2	*a* = 4.492, *b* = 4.503, *c* = 13.401	135.5	1215	Cs_2PtH_2_p ↔ Cs_2Pt + H_2	147.2
Rb_2PtH_2_p	37-Li_2PtH_2	*a* = 4.330, *b* = 4.339, *c* = 12.639	118.7	1215	Rb_2PtH_2_p ↔ Pt + 2Rb + H_2	147.5
$Ca_3Ir_2H_{12}$_p	31-$Ba_3Ir_2H_{12}$	*a* = 4.927, *c* = 8.132	171.0	1215	⅓ $Ca_3Ir_2H_{12}$_p ↔ ⅔ Ir + CaH_2 + H_2	145.3
$Yb_8Rh_6H_{24}$_p	41-$Ca_8Rh_6H_{24}$	*a* = 7.219	376.2	1185	1/10 $Yb_8Rh_6H_{24}$_p ↔ ⅗ YbRh + ⅕ YbH_2 + H_2	145.1
K_2PdH_2_p	7-Na_2PdH_2	*a* = 4.144, *c* = 12.415	106.6	1155	K_2PdH_2_p ↔ 2K + Pd + H_2	135.6
Yb_2CoH_5_p	Mg_2CoH_5_ P_{42}/mm	*a* = 4.847, *c* = 6.999	82.2	1155	2 Yb_2CoH_5_p ↔ 4YbH_2 + 2Co + H_2	205.7

* Reproduced in part with permission from Inorg. Chem., submitted for publication. Unpublished work copyright 2014 American Chemical Society.

Table D.1. (Continued)

K_3IrH_6_p	12-Na_3RhH_6	a = 10.420, b = 5.854, c = 10.744	163.8	1110	⅓ K_3IrH_6_p ↔ K + ⅓ Ir + H_2	129.5
$EuNiH_3$_p	$CaTiO_3$	a = 3.567	45.4	1110	$EuNiH_3$_p ↔ ½ $EuNi_2$ + ½ EuH_2 + H_2	127.7
Cs_2PdH_2_p	7-Na_2PdH_2	a = 4.546, c = 13.624	140.4	1095	Cs_2PdH_2_p ↔ Pd + 2Cs + H_2	126.4
Eu_2CoH_5_p	Mg_2CoH_5_P_{42}/mm	a = 5.030, c = 7.265	91.9	1095	2 Eu_2CoH_5_p ↔ 4EuH_2 + 2Co + H_2	126.1
Sr_2CoH_5_p	Mg_2CoH_5_P_{42}/mm	a = 5.234, c = 7.543	103.3	1095	2 Sr2CoH_5_p ↔ 4SrH_2 + 2Co + H_2	125.9
$YbNiH_3$_p	$CaTiO_3$	a = 3.475	42.0	1080	$YbNiH_3$_p ↔ ½YbH_2 + ½ Ni_2Yb + H_2	133.1
Rb_2PdH_2_p	7-Na_2PdH_2	a = 4.354, c = 12.947	122.7	1065	Rb_2PdH_2_p ↔ Pd + 2Rb + H_2	121.4
Cs_3IrH_6_p	12-Na_3RhH_6	a = 11.378, b = 6.405, c = 11.800	215.0	1050	⅓ Cs_3IrH_6_p ↔ Cs + ⅓ Ir + H_2	117.4
Rb_3IrH_6_p	12-Na_3RhH_6	a = 10.899, b = 6.140, c = 11.276	188.6	1050	⅓ Rb_3IrH_6_p ↔ ⅓ Ir + Rb + H_2	119.6
K_3RhH_6_p	12-Na_3RhH_6	a = 10.412, b = 5.846, c = 10.777	164.0	1020	⅓ K_3RhH_6_p ↔ K + ⅓ Rh + H_2	113.8
Ba_2FeH_6_p	2-Sr_2RuH_6	a = 7.886	122.6	1005	Ba_2FeH_6_p ↔ Fe + 2BaH_2 + H_2	111.3
Na_2PtH_2_p	37-Li_2PtH_2	a = 3.596, b = 3.684, c = 11.062	73.4	960	Na_2PtH_2_p ↔ ³⁄₂ Na + ½ $NaPt_2$ + H_2	103.6
Rb_3RhH_6_p	12-Na_3RhH_6	a = 10.868, b = 6.112, c = 11.270	187.2	960	⅓ Rb_3RhH_6_p ↔ Rb + ⅓ Rh + H_2	103.9
Ca_2CoH_5_p	Mg_2CoH_5_P_{42}/mm	a = 4.926, c = 7.114	86.3	960	2 Ca_2CoH_5_p ↔ 4CaH_2 + 2Co + H_2	103.1
Cs_3RhH_6_p	12-Na_3RhH_6	a = 11.409, b = 6.440, c = 11.870	218.0	945	⅓ Cs_3RhH_6_p ↔ Cs + ⅓ Rh + H_2	101.7
Na_4OsH_6_p	11-Li_4RuH_6	a = 9.087, c = 11.377	135.6	915	⅓ Na_4OsH_6_p ↔ ⁴⁄₃ Na + ⅓ Os + H_2	95.5
K_3OsH_7_p	43-Na_3OsH_7	a = 10.768, c = 5.792	167.9	900	²⁄₇ K_3OsH_7_p ↔ ²⁄₇ Os + ⁶⁄₇ K + H_2	92.7
Eu_2PtH_6_p	21-Ba_2PtH_6	a = 13.249, c = 5.433	97.8	870	⁴⁄₉ Eu_2PtH_6_p ↔ ⅑ Eu_5Pt4 + ⅓ EuH_2 + H_2	88.4
K_3RuH_7_p	43-Na_3OsH_7	a = 10.745, c = 5.784	167.0	855	²⁄₇ K_3RuH_7_p ↔ ⁶⁄₇ K + ²⁄₇ Ru + H_2	85.8
$SrNiH_3$_p	$CaTiO_3$	a = 3.670	49.4	855	2 $SrNiH_3$_p ↔ Ni + Sr_2NiH_4_p + H_2	86.4
Rb_3OsH_7_p	43-Na_3OsH_7	a = 11.261, c = 6.047	191.7	840	²⁄₇ Rb_3OsH_7_p ↔ ⁶⁄₇ Rb + ²⁄₇ Os + H_2	84.3
Cs_3OsH_7_p	43-Na_3OsH_7	a = 11.830, c = 6.305	220.6	825	²⁄₇ Cs_3OsH_7_p ↔ ²⁄₇ Os + ⁶⁄₇ Cs + H_2	82.5
Rb_2PdH_4_p	4-Na_2PtH_4	a = 6.123, c = 8.118	152.2	825	Rb_2PdH_4_p ↔ Rb_2PdH_2_p + H_2	80.8
$LiPd_3H_2$_p	$NaPd_3H_2$	a = 5.594, b = 8.254, c = 2.844	65.7	810	$LiPd_3H_2$_p ↔ LiPd + 2Pd + H_2	78.9
$SrPdH_3$_p	$CaTiO_3$	a = 3.839	56.6	810	⁶⁄₅ $SrPdH_3$_p ↔ ²⁄₅ Sr_2PdH_4 + ²⁄₅ Pd_2Sr + H_2	78.2

Table D.1. (Continued)

$YbPdH_3$_p	$CaTiO_3$	a = 3.683	50.0	795	$^{4}/_{5}\ YbPdH_3$_p ↔ $^{1}/_{5}\ Pd_4Yb_3$ + $^{1}/_{5}\ YbH_2$ + H_2	79.0
Cs_3RuH_7_p	43-Na_3OsH_7	a = 11.836, c = 6.308	220.9	795	$^{2}/_{7}\ Cs_3RuH_7$_p ↔ $^{6}/_{7}$ Cs + $^{2}/_{7}$ Ru + H_2	75.8
Rb_3RuH_7_p	43-Na_3OsH_7	a = 11.257, c = 6.05	191.7	795	$^{2}/_{7}\ Rb_3RuH_7$_p ↔ $^{2}/_{7}$ Ru + $^{6}/_{7}$ Rb + H_2	77.5
$Ba_8Rh_6H_{25}$_p	41-$Ca_8Rh_6H_{24}$	a = 7.971	506.5	795	$^{2}/_{9}\ Ba_8Rh_6H_{25}$_p ↔ $^{4}/_{3}$ Rh + $^{16}/_{9}\ BaH_2$ + H_2	76.5
Cs_2ReH_9_p	1-K_2ReH_9	a = 10.429, c = 6.082	191.0	780	$^{2}/_{9}\ Cs_2ReH_9$_p ↔ $^{4}/_{9}$ Cs + $^{2}/_{9}$ Re + H_2	73.3
Rb_2ReH_9_p	1-K_2ReH_9	a = 9.945, c = 5.817	166.1	765	$^{2}/_{9}\ Rb_2ReH_9$_p ↔ $^{2}/_{9}$ Re + $^{4}/_{9}$ Rb + H_2	72.1
$CaPdH_3$_p	$CaTiO_3$	a = 3.713	51.2	750	$CaPdH_3$_p ↔ ½ CaH_2 + ½ $CaPd_2$ + H_2	68.5
Rb_3CdH_5_p	30-K_3ZnH_5	a = 8.004, c = 8.27	193.1	705	$^{2}/_{5}\ Rb_3CdH_5$_p ↔ $^{6}/_{5}$ Rb + $^{2}/_{5}$ Cd + H_2	61.9
Cs_2TcH_9_p	1-K_2ReH_9	a = 10.478, c = 6.113	193.7	705	$^{2}/_{9}\ Cs_2TcH_9$_p ↔ $^{2}/_{9}$ Tc + $^{4}/_{9}$ Cs + H_2	62.2
Rb_2TcH_9_p	1-K_2ReH_9	a = 9.938, c = 5.814	165.8	690	$^{2}/_{9}\ Rb_2TcH_9$_p ↔ $^{2}/_{9}$ Tc + $^{4}/_{9}$ Rb + H_2	61.0
$Sr_7Cu_3H_{17}$_p	35-$Ba_7Cu_3H_{17}$	a = 11.130, c = 6.963	373.5	675	$^{2}/_{3}\ Sr_7Cu_3H_{17}$_p ↔ 2Cu + $^{14}/_{3}\ SrH_2$ + H_2	58.5
$BaPdH_3$_p	$CaTiO_3$	a = 3.993	63.6	675	$^{6}/_{5}\ BaPdH_3$_p ↔ $^{2}/_{5}\ BaPd_2$ + $^{2}/_{5}\ Ba_2PdH_4$ + H_2	58.3
Ba_2CoH_5_p	Mg_2CoH_5_P_{42}/mm	a = 5.551, c = 8.000	123.3	660	2 Ba_2CoH_5_p ↔ 2Co + 4BaH_2 + H_2	56.0
Na_2ReH_9_p	1-K_2ReH_9	a = 8.661, c = 5.058	109.5	645	$^{2}/_{7}\ Na_2ReH_9$_p ↔ $^{2}/_{7}$ Re + $^{4}/_{7}$ NaH + H_2	53.3
$SrReH_9$_p	28-$BaReH_9$	a = 4.995, c = 9.204	99.5	570	$^{2}/_{7}\ SrReH_9$_p ↔ $^{2}/_{7}$ Re + $^{2}/_{7}\ SrH_2$ + H_2	40.6
Li_3RuH_7_p	43-Na_3OsH_7	a = 8.437, c = 4.865	86.6	555	$^{2}/_{5}\ Li_3RuH_7$_p ↔ $^{3}/_{5}\ Li_4RuH_6$ + $^{1}/_{5}$ Ru + H_2	39.4
Na_2TcH_9_p	1-K_2ReH_9	a = 8.626, c = 5.044	108.3	555	$^{2}/_{7}\ Na_2TcH_9$_p ↔ $^{2}/_{7}$ Tc + $^{4}/_{7}$ NaH + H_2	39.6
Li_3OsH_7_p	43-Na_3OsH_7	a = 8.477, c = 4.900	88.0	525	$^{4}/_{5}\ Li_3OsH_7$_p ↔ $^{3}/_{5}\ Li_4OsH_6$ + $^{1}/_{5}$ Os + H_2	35.7
$EuReH_9$_p	28-$BaReH_9$	a = 4.887, c = 8.98	92.8	525	$^{2}/_{7}\ EuReH_9$_p ↔ $^{2}/_{7}$ Re + $^{2}/_{7}\ EuH_2$ + H_2	35.3
K_3CdH_5_p	30-K_3ZnH_5	a = 7.624, c = 7.940	169.8	510	K_3CdH_5_p ↔ 3KH + Cd + H_2	31.9
Na_2ZnH_4_p	29-K_2ZnH_4	a = 6.835, b = 5.318, c = 9.367	85.1	510	Na_2ZnH_4_p ↔ 2NaH + Zn + H_2	32.7
$Mg_8Rh_6H_{24}$_p	41-$Ca_8Rh_6H_{24}$	a = 6.886	326.5	495	$^{1}/_{12}\ Mg_8Rh_6H_{24}$_p ↔ $^{1}/_{6}\ Mg_2Rh$ + ⅓ MgRh + H_2	30.7
$YbReH_9$_p	28-$BaReH_9$	a = 4.790, c = 8.755	87.0	450	$^{2}/_{7}\ YbReH_9$_p ↔ $^{2}/_{7}$Re + $^{2}/_{7}YbH_2$ + H_2	29.0
Ca_3ReH_7_p	23-Mg_3ReH_7	a = 5.220, c = 12.098	142.8	450	2 Ca_3ReH_7_p ↔ 2Re + 6CaH_2 + H_2	23.6
Yb_3MnH_7_p	23-Mg_3ReH_7	a = 4.946, c = 11.844	125.5	450	2 Yb_3MnH_7_p ↔ 2Mn + 6YbH_2 + H_2	128.2
Li_2ReH_9_p	1-K_2ReH_9	a = 8.055, c = 4.788	89.7	450	$^{2}/_{7}\ Li_2ReH_9$_p ↔ $^{4}/_{7}$ LiH + $^{2}/_{7}$ Re + H_2	25.1
$Eu_7Cu_3H_{17}$_p	35-$Ba_7Cu_3H_{17}$	a = 10.702, c = 6.784	336.4	435	$^{2}/_{3}\ Eu_7Cu_3H_{17}$_p ↔ 2Cu + $^{14}/_{3}\ EuH_2$ + H_2	21.8

Table D.1. (Continued)

$CaReH_9$_p	28-$BaReH_9$	a = 4.835, c = 8.840	89.5	435	$^{3}/_{10}$ $CaReH_9$_p ↔ $^{1}/_{10}$ Ca_3ReH_7_p + $^{1}/_{5}$ Re + H_2	21.1
Mg_2PtH_6_p	21-Ba_2PtH_6	a = 12.322, c = 4.996	75.2	390	Mg_2PtH_6_p ↔ Pt + 2MgH_2 + H_2	15.4
Ca_3MnH_7_p	23-Mg_3ReH_7	a = 5.053, c = 11.845	131.0	225	2 Ca_3MnH_7_p ↔ 2Mn + 6CaH_2 + H_2	-5.7
Sr_3MnH_7_p	23-Mg_3ReH_7	a = 5.361, c = 12.76	158.8	210	2 Sr_3MnH_7_p ↔ 6SrH_2 + 2Mn + H_2	-9.6
Li_2PdH_4_p	4-Na_2PtH_4	a = 4.819, c = 5.670	65.8	180	Li_2PdH_4_p ↔ Li_2PdH_2 + H_2	-11.5
Eu_3MnH_7_p	23-Mg_3ReH_7	a = 5.134, c = 12.385	141.4	165	2 Eu_3MnH_7_p ↔ 2Mn + 6EuH_2 + H_2	-14.0

Table D.2: Structural parameters of additional intermetallics added to complete libraries of new element spaces for proposed CTMHs *a*,*b*,*c* (Å), volume *V* (Å^3 f.u.$^{-1}$).

		DFT		EXPERIMENT	
material	space group	structural parameters	*V*	structural parameters	*V*
Ca_3Pd	P n m a	a = 7.759, b = 9.731, c = 6.615	124.9	a = 7.699, b = 9.937, c = 6.691	128.0
Ca_3Pd_2	R -3 H	a = 7.662, b = 7.662, c = 7.662 α = β = γ = 71.37°	130.7	a = 7.64, b = 7.64, c = 7.64 α = β = γ = 71.61°	129.9
Ca_5Pd_2	C 1 2/c 1	a = 16.492, b = 6.667, c = 7.722, β = 97.4°	210.5	a = 16.492, b = 6.667, c = 7.722, β = 97.3°	213.9
CaPd	P m -3 m	a = 3.529	43.9	a = 3.516	43.5
$CaPd_2$	F d -3 m S	a = 7.741	58.0	a = 7.652	56.0
$CaPd_5$	P 6/ m m m	a = 5.349, c = 4.486	111.2	a = 5.147, c = 4.224	96.9
Eu_2Pt_7	P 63/ m m c	a = 5.445, c = 26.694	171.3	a = 5.304, c = 26.87	163.7
Eu_3Pt_2	R -3 H	a = 7.753, b = 7.753, c = 7.753 α = β = γ = 69.62°	131.9	a = 7.779, b = 7.779, c = 7.779 α = β = γ = 71.25°	136.5
Eu_3Rh	P n m a	a = 7.679, b = 9.709, c = 6.571	122.5	a = 7.818, b = 9.967, c = 6.759	131.7
Eu_5Pt_2	C 1 2/c 1	a = 16.477, b = 6.764, c = 7.751, β = 97.30°	214.2	a = 16.776, b = 6.877, c = 7.843, β = 97.24°	224.4
Eu_5Pt_4	P n m a	a = 7.615, b = 14.910, c = 7.809	221.7	a = 7.703, b = 15.217, c = 7.982	233.9
Eu_5Rh_2	C 1 2/c 1	a = 16.174, b = 6.638, c = 7.639, β = 96.56°	210.5	a = 16.649, b = 6.76, c = 7.796, β = 96.82°	217.8

Table D.2. (Continued)

$EuPt_2$	F d -3 m S	a = 7.749	58.2	a = 7.731	57.8
$EuRh_2$	F d -3 m S	a = 7.599	54.8	a = 7.522	53.2
Mg_2Rh	I 4/m m m	a = 3.208, c = 10.087	51.9	a = 3.188, c = 10.067	51.2
Mg_3Rh	P 63 c m	a = 7.920, c = 8.300	75.2	a = 7.905, c = 8.256	74.5
$Mg_{44}Rh_7$	F -4 3 m	a = 20.142	1021.4	a = 20.148	1022.4
Mg_5Rh_2	P 63/ m m c	a = 8.624, c = 8.034	129.3	a = 8.536, c = 8.025	126.6
MgRh	P m -3 m	a = 3.121	30.4	a = 3.099	29.8
Pd_4Yb_3	R -3 H	a = 5.773, b = 7.661, c = 7.661 α = 113.91° β = 104.55° γ = 104.55°	137.5	a = 5.664, b = 7.693, c = 7.693 α = 114.18° β = 104.21° γ = 104.21°	136.4
$RbCd_{13}$	F m -3 c	a = 14.043	346.1	a = 13.844	332.0
$SrRh_2$	F d -3 m S	a = 7.766	58.6	a = 7.706	57.2
Yb_3Pd	P n m a	a = 7.616, b = 9.568, c = 6.487	118.2	a = 7.664, b = 9.678, c = 6.5	120.5
Yb_5Pd_2	C 1 2/c 1	a = 16.166, b = 6.532, c = 7.589, β = 97.47°	198.6	a = 16.321, b = 6.55, c = 7.68	203.5
YbPd	P n m a	a = 3.453	44.1	a = 3.44	41.5
YbPd	P m -3 m	a = 7.099, b = 4.402, c = 5.641	41.2	a = 7.22, b = 4.123, c = 5.578	40.7
$YbPd_3$	P m -3 m	a = 4.080	67.9	a = 4.036	65.8
YbRh	P m -3 m	a = 3.347	37.5	a = 3.347	37.5
$YbRh_2$	F d -3 m S	a = 7.509	52.9	a = 7.432	51.3

Table D.3: Calculated structural parameters for all proposed CTMHs using the more strict convergence criteria for Round 2 phonon calculations. Also included are Sr, Tc, and SrH_2 compounds that are new additions to the materials library of Round 2 calculations. lattice constants *a,b,c* (Å), volume *V* ($Å^3$ f.u.$^{-1}$) . Experimental data are shown in parentheses.

material	lattice parameters	*V*
Cs_2PdH_2_p	*a* = 4.532, *c* = 13.499	138.6
Cs_2PdH4_p	*a* = 6.394, *c* = 8.597	175.8
Cs_2PtH_2_p	*a* = 4.492, *b* = 4.503, *c* = 13.401	136.1
Cs_2PtH4_p	*a* = 6.306, *c* = 8.693	172.8
Cs_2ReH9_p	*a* = 10.428, *c* = 6.067	190.4
Cs_2TcH9_p	*a* = 10.478, *c* = 6.113	193.7
Cs3IrH6_p	*a* = 22.681, *b* = 12.749, *c* = 23.713	214.3
Cs3OsH7_p	*a* = 11.830, *c* = 6.305	220.6
Cs3ReH6_p	*a* = 9.302	201.2
Cs3RhH4_p	*a* = 5.712, *b* = 11.809, *c* = 11.94	201.3
Cs3RhH6_p	*a* = 11.354, *b* = 6.38, *c* = 11.861	214.8
Cs_3RuH_7_p	*a* = 11.823, *c* = 6.312	220.6
Cs_4RhH_4_p	*a* = 12.662, *c* = 4.565	366.0
Cs_4RuH_6_p	*a* = 11.107, *c* = 14.384	256.1
$Cs_5Pt_2H_9$_p	*a* = 9.959, *c* = 9.959 α = 104.21°, β = γ =112.17°	377.8
$CsPd_3H_2$_p	*a* = 3.086, *c* = 5.675	88.9
Eu_2OsH_6_p	*a* = 7.375, β = 110.15°	100.3
K_2PdH_2_p	*a* = 4.133, *c* = 12.398	105.9
K_2PdH_4_p	*a* = 5.611, *c* = 8.314	130.9
K_2PtH_2_p	*a* = 4.156, *b* = 4.157, *c* = 12.169	105.1
K_2PtH_4_p	*a* = 5.798, *c* = 7.765	130.5
K_3IrH_6_p	*a* = 10.379, *b* = 5.836, *c* = 10.803	163.6
K_3OsH_7_p	*a* = 10.771, *c* = 5.795	168.1
K_3RhH_4_p	*a* = 5.208, *b* = 10.895, *c* = 10.943	92.7
K_3RhH_6_p	*a* = 10.378, *b* = 5.833, *c* = 10.814	163.6
K_3RuH_7_p	*a* = 10.759, *c* = 5.803	167.9
K_4OsH_6_p	*a* = 10.235, *c* = 13.002	196.6
K_4RhH_4_p	*a* = 8.461, *c* = 5.324	190.8
K_4RuH_6_p	*a* = 10.222, *c* = 12.937	195.1
$K_5Pt_2H_9$_p	*a* = 9.044, *c* = 9.044 α = 105.99°, β = γ =111.24°	284.0
KPd_3H_2_p	*a* = 2.873, *c* = 5.477	77.9
Na_2PtH_2_p	*a* = 3.629, *b* = 3.629, *c* = 11.069	72.9
Na_2PtH_4__p	*a* = 4.941, *c* = 7.511	91.7
Na_2ReH_9_p	*a* = 8.658, *c* = 5.081	109.9

Table D.3. (Continued)

$Na_3PtH_{5\_p}$	a = 6.504, c = 5.263	111.3
$Na_3ReH_{6\_p}$	a = 7.754	116.5
$Na_4OsH_{6\_p}$	a = 9.117, c = 11.444	137.3
$Na_5Pt_2H_{9\_p}$	a = 8.064, b = 8.064, c = 8.064 α = 107.31°, β = γ =110.56°	201.6
$Rb_2PdH_{2\_p}$	a = 4.336, c = 12.895	121.2
$Rb_2PdH_{4\_p}$	a = 6.115, c = 8.093	151.3
$Rb_2PtH_{2\_p}$	a = 4.340, b = 4.340, c = 12.703	119.7
$Rb_2PtH_{4\_p}$	a = 6.035, c = 8.193	149.2
$Rb_2ReH_{9\_p}$	a = 9.927, c = 5.784	164.7
$Rb_2TcH_{9\_p}$	a = 9.918, c = 5.805	165.0
$Rb_3CdH_{5\_p}$	a = 7.985, c = 8.297	193.8
$Rb_3IrH_{6\_p}$	a = 10.823, b = 6.092, c = 11.297	186.2
$Rb_3OsH_{7\_p}$	a = 11.267, c = 6.036	191.6
$Rb_3ReH_{6\_p}$	a = 8.911	176.9
$Rb_3RhH_{4\_p}$	a = 5.457, b = 11.361, c = 11.413	22.1
$Rb_3RhH_{6\_p}$	a = 10.83, b = 6.092, c = 11.308	186.5
$Rb_3RuH_{7\_p}$	a = 11.256, c = 6.048	191.6
$Rb_4RhH_{4\_p}$	a = 9.017, c = 5.498	292.7
$Rb_4RuH_{6\_p}$	a = 10.671, b = 10.671, c = 13.629	224.0
$Rb_5Pt_2H_{9\_p}$	a = 9.460, b = 9.460, c = 9.460 α = 105.34°, β = γ =111.58°	324.6
$RbPd_3H_{2\_p}$	a = 2.933, c = 5.585	82.3
$Sr_2NiH_{4\_p}$	a = 16.026, b = 7.452, c = 7.563	106.0
$SrNiH_{3\_p}$	a = 3.668	49.4
$Yb_2OsH_{6\_p}$	a = 7.122	90.3
Sr (FM3M)	a = 6.005 (a = 6.085)	54.1 (56.3)
Tc (P63MMC)	a = 2.758, c = 4.409 (a = 2.741, c = 4.398)	14.5 (14.3)
SrH_2 (PNMA)	a = 6.325, b = 7.272, c =3.841 (a = 6.377, b = 7.358, c = 3.883)	44.2 (45.6)

APPENDIX E

PHASE DIAGRAMS OF MOST THERMODYNAMICALLY STABLE CTMHS BASED ON ROUND 2 LEVEL OF SCREENING*

Predicted isobaric *T*-composition phase diagrams (not drawn to scale) at 1 bar H_2 for the *M*−*Tr*−H (*M* = cation, *Tr* = transition metal) elemental systems, including phonon corrections to the free energies of the condensed phases. The horizontal axis represents the molar ratio of metals for a given composition with the pure cation species on the far left and the pure transition metal on the far right. Each box that makes up a given phase diagram describes a unique mixture of stable compounds for a particular hydrogen chemical potential range. The stable mix of compounds for a given *T* can be read from the intersection of a horizontal line drawn at that *T* with the vertical lines, which represent the stoichiometric compounds.

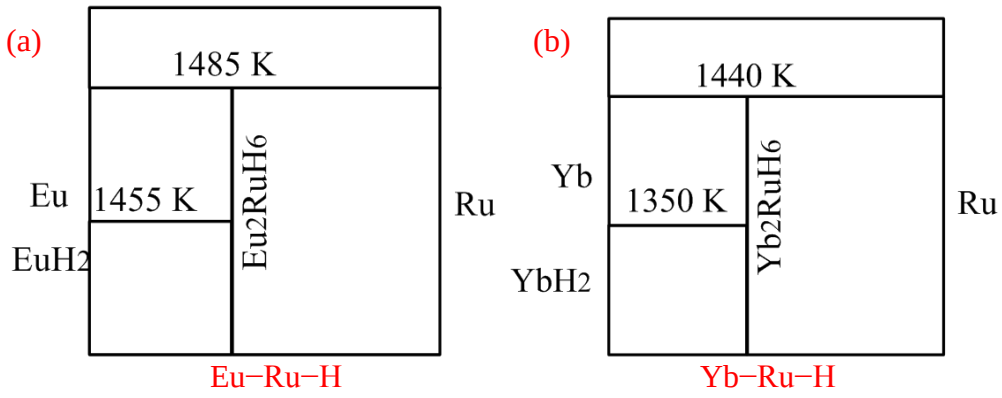

Figure E.1: Phase diagram predictions for element spaces containing Round 2 final candidates for *P* = 1 bar H_2 between $0 \leq T\,(\mathrm{K}) \leq 2000$, including vibrational contributions for condensed phases

* Reproduced in part with permission from Inorg. Chem., submitted for publication. Unpublished work copyright 2014 American Chemical Society.

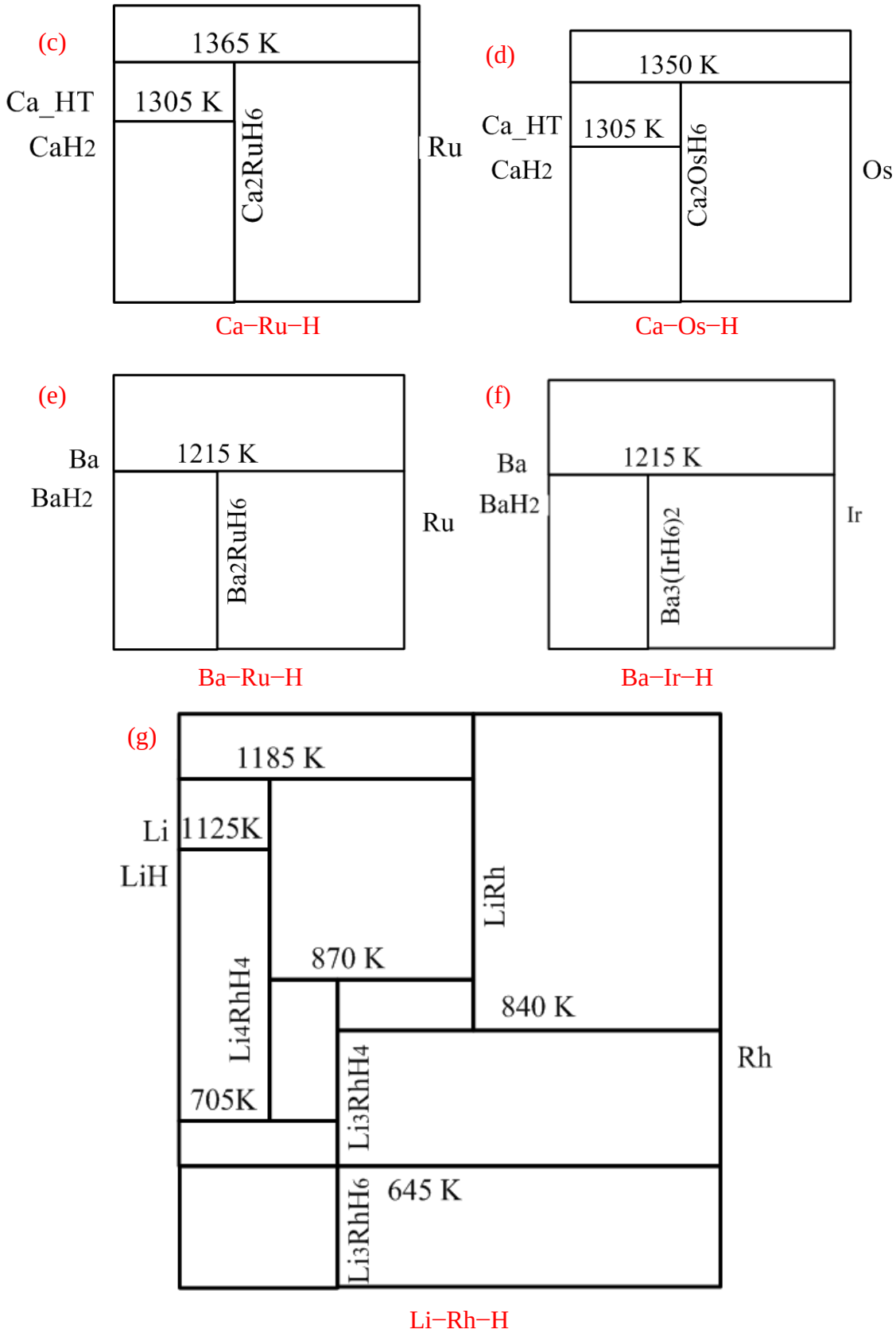

Figure E.1 (Continued)

(h)

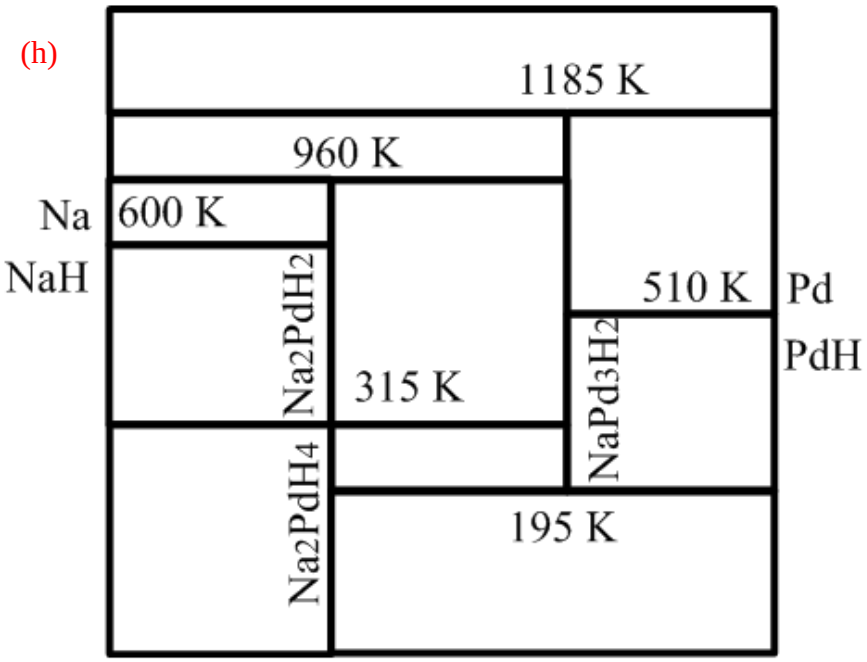

Na–Pd–H

(i)

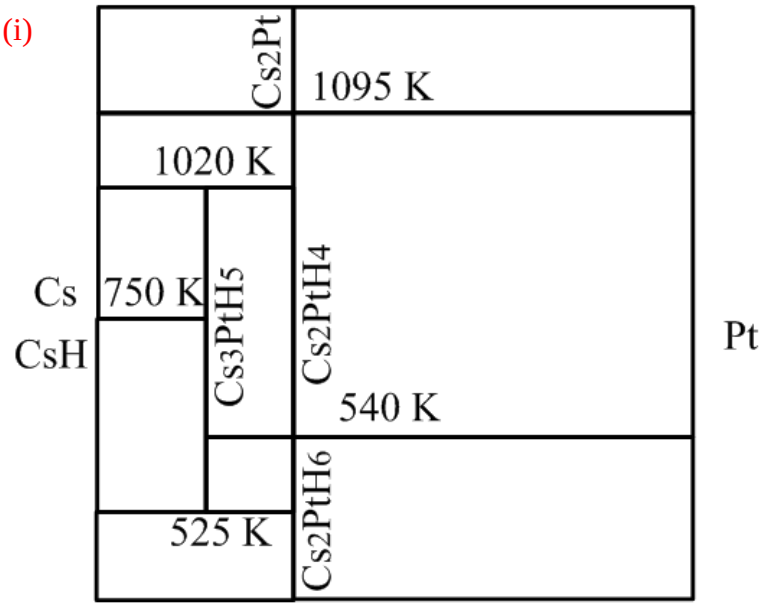

Cs–Pt–H

Figure E.1 (Continued)

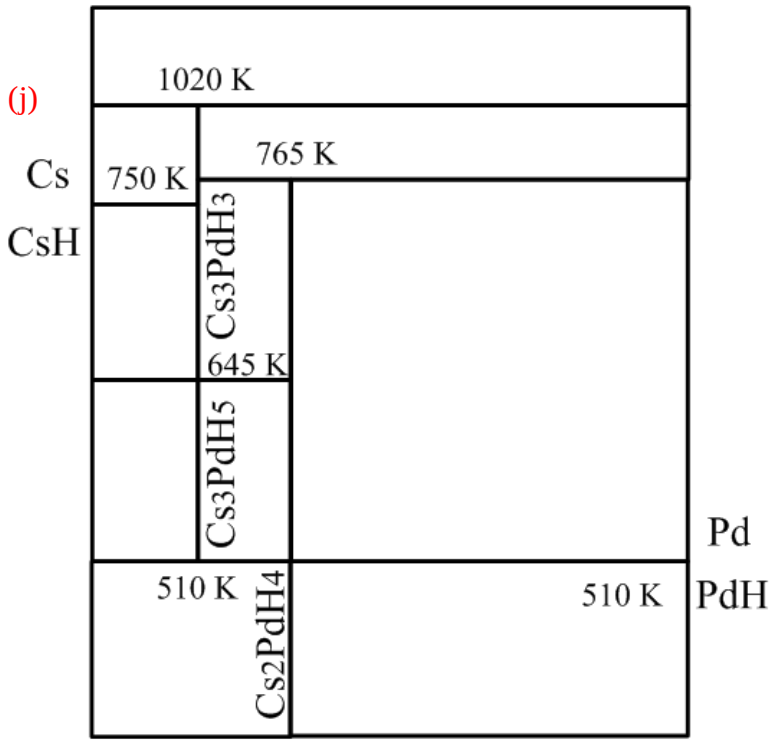

Cs–Pd–H

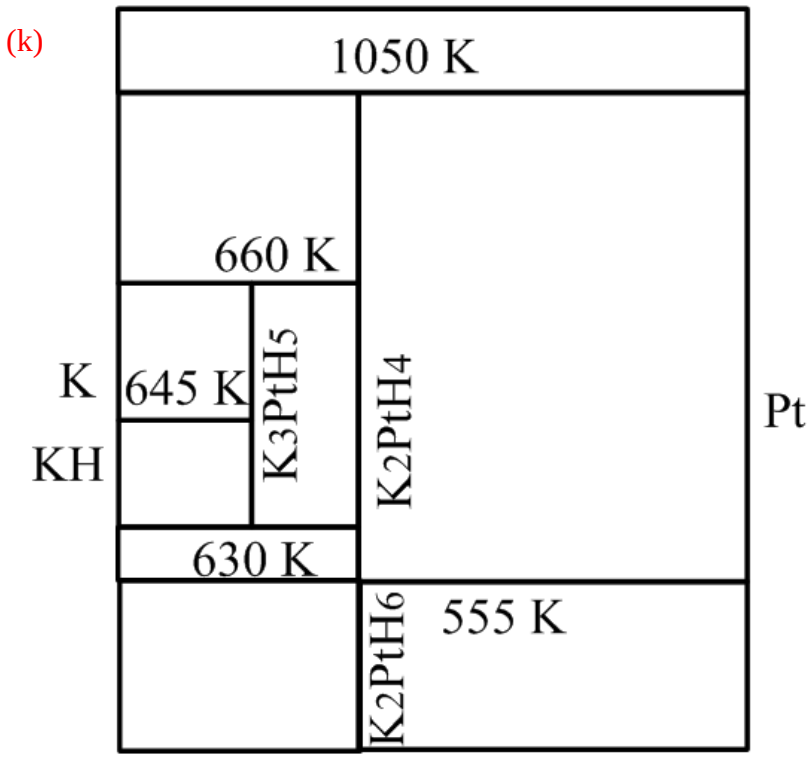

K–Pt–H

Figure E.1 (Continued)

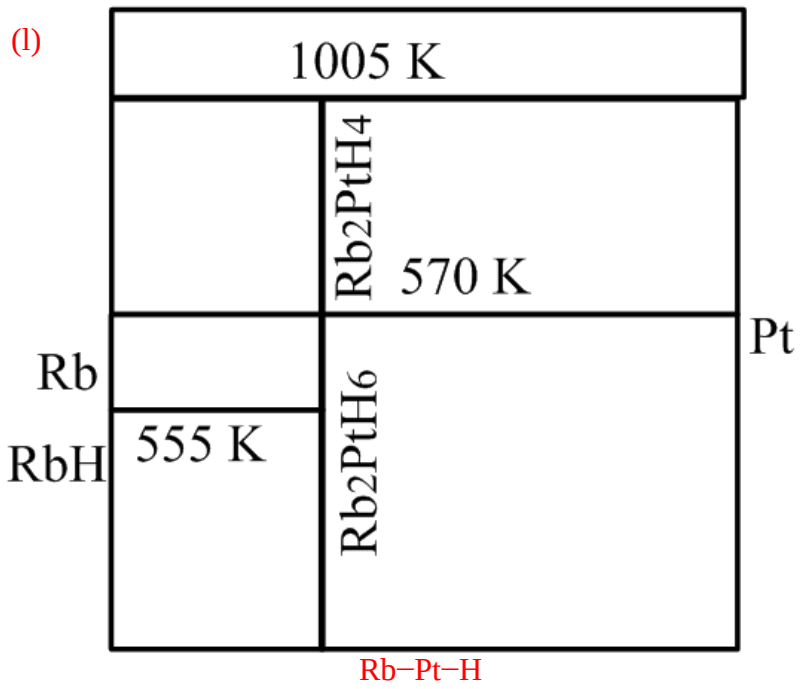

Figure E.1 (Continued)

APPENDIX F

COST ESTIMATION OF METAL HYDRIDES FOR NGNP OPERATION BASED ON PURE METAL COMPONENTS*

The following calculations provide an order of magnitude estimate only of the cost of the base metals required to store tritium in the NGNP application on an annual basis. This is for comparison purposes only and should not be used for systems design without careful consideration of the assumptions. Tables F.1 and F.2 give the elemental molecular weights, costs of bulk metals,[1] hydride gravimetric storage capacities of very stable metal hydrides, and the cost of the base metal for each stoichiometric hydride.

Table F.1: Reference molecular weight and cost of pure bulk metal from Reference 1.

Element	MW (g /mol)	C_i ($/100 g)
Eu	151.96	20000
Yb	173.05	1400
Ca	40.078	20
Os	190.23	7700
Pd	106.42	5833
Ru	101.07	1400
Zr	91.224	157
Ti	47.867	661
Cs	132.91	1100
Y	88.906	430
Protium	1.008	
Tritium	3.016	

* Reproduced in part with permission from Inorg. Chem., submitted for publication. Unpublished work copyright 2014 American Chemical Society.

Table F.2: Reference tritium and protium capacities and metals cost for very stable metal hydrides.

material	$W_{protide}$ g metal/g H	$W_{tritide}$ g metal/g T	Metals Cost ($/100 g metal)
Eu_2OsH_6_p	81.7	27.3	15265
Yb_2OsH_6_p	88.7	29.6	3635
Cs_2PdH_2_p	184.6	61.7	2453
Cs_2PtH_2_p	228.6	76.4	6137
Sr_2NiH_4_p	58.0	19.4	77
K_2PtH_2_p	135.6	45.3	9309
Rb_2PtH_2_p	181.6	60.7	7489
Eu_2RuH_6	67.0	22.4	15358
Yb_2RuH_6	73.9	24.7	1400
Ca_2RuH_6	30.0	10.0	790
Ca_2OsH_6	44.7	14.9	5423
Ba_2RuH_6	62.1	20.8	417
$Ba_3Ir_2H_{12}$	12.0	4.0	2771
CaH_2	19.9	6.6	20
EuH_2	75.4	25.2	20000
YH_2	44.1	14.7	430
ZrH_2	45.3	15.1	157
TiH_2	23.7	7.9	661

The concentration of tritium in the helium coolant at the reactor outlet is assumed to be $P_1 = 10^{-10}$ bar T. The concentration of tritium in a gas stream that can be vented to the atmosphere is less than 1 ppt or $P_2 = 10^{-12}$ bar.[2] To compute the amount of tritium to be removed from the helium coolant on an annual basis, $\Delta\dot{m}_T$, we use Eq. (F.1) derived from Eq. (F.2), assuming ideal gas behavior. In this application, $V_2 = V_1$, $RT_2 = RT_1$, and $\dot{m}_1$ and $\dot{m}_2$ are the flowrates of tritium into and out of the gettering bed, respectively.

$$\Delta\dot{m}_T = \dot{m}_{1,T}\left(\frac{P_2}{P_1} - 1\right) \tag{F.1}$$

$$\frac{P_2 V_2}{P_1 V_1} = \frac{\dot{m}_2 R T_2}{\dot{m}_1 R T_1} \tag{F.2}$$

While the tritium source term for the NGNP reactor has not yet been determined, we estimate it by scaling the total tritium production at past high temperature gas-cooled reactor Fort St. Vrain by the relative size of the nuclear plants using Eq. (F.3). There are approximately 9600 Ci in one gram of tritium.[3]

$$\dot{m}_{1,T} = 3911\ \frac{Ci}{\text{yr}}\left(\frac{600\ \text{MW}_{\text{th}}}{842\ \text{MW}}\right)\left(\frac{1\ \text{g}}{9600\ \text{Ci}}\right) = 0.29\ \frac{\text{g T}}{\text{yr}} \tag{F.3}$$

In order to reduce the concentration of tritium in the helium coolant 100 fold, the metal hydride gettering system should remove $\Delta\dot{m}_T = 0.2874$ grams of T per year. The amount of metal hydride material required to absorb this amount of tritium assuming stoichiometric and compete hydriding depends primarily on the concentration of protium in the helium stream since both tritium and protium will be taken up by the gettering bed. Upon the assumption that all of the protiated hydrogen is taken up by the bed along with the tritium, the cost of the metal for a given metal hydride can be estimated via Eq. (F.4). This equation adds the metals mass required to take up a pure tritium stream and the

metals mass required to take up pure protium and scales the total mass by the cost, C_i, of the stoichiometric bulk metals for a hydride based on values in Table F.2.

$$Cost = \left(\Delta\dot{m}_T W_{\text{tritide}} + \Delta\dot{m}_H W_{\text{protide}}\right) \cdot \sum_i^n C_i \,/100 \tag{F.4}$$

One estimate for the rate of hydrogen release to the primary helium coolant for Japan's 600MW_{th} future very high temperature gas-cooled reactor, the GTHTR300C, gave 2.0 × 10^{-2} m^3 hr^{-1}(STP) based on scale up of a high temperature test reactor.[4] If all of this hydrogen is taken up by the hydride bed then, $\Delta\dot{m}_H$ ~7.884 kg H yr^{-1}. Based on these values, the cost of each metal hydride is listed in Table F.3.

Table F.3: Estimated metals cost for candidate metal hydride systems based on stoichiometric and complete uptake of (1) only tritium and (2) tritium and protium with $\Delta\dot{m}_H$ ~7.884 kg H yr^{-1} and $\Delta\dot{m}_T$ = 0.2874 g T yr^{-1} for the NGNP application.

		(1)		(2)	
material	T_d (K)	metals mass T only (g/yr)	metals cost T only ($/yr)	metals mass T+H (kg/yr)	metals cost T+H ($/yr)
YH_2	> 1500	4.2	18.2	347.7	1,495,068
$Eu_2OsH_6\_p$	1485	6.4	987.8	527.9	81,081,801
Eu_2RuH_6	1485	7.8	1198.0	644.2	98,331,820
EuH_2	1455	7.2	1448.1	594.3	118,855,877
$Yb_2OsH_6\_p$	1440	7.1	99.4	582.9	8,160,952
Yb_2RuH_6	1440	8.5	309.6	699.2	25,410,971
$Cs_2PdH_2\_p$	1395	17.7	435.1	1,455.7	35,711,117
Ca_2RuH_6	1365	2.9	22.7	236.2	1,865,448
$Cs_2PtH_2\_p$	1365	22.0	1347.6	1,802.5	110,613,633
Ca_2OsH_6	1350	4.3	232.9	352.5	19,115,467
$Sr_2NiH_4\_p$	1320	5.6	4.3	457.4	351,498
CaH_2[a]	1305	1.9	0.4	156.7	31,347
Ba_2RuH_6	1215	6.0	24.9	489.8	2,041,474
$Ba_3Ir_2H_{12}$	1215	1.2	31.9	94.6	2,621,183
ZrH_2	1154	4.3	6.8	356.8	560,106
$K_2PtH_2\_p$	1140	13.0	1212.0	1,068.7	99,484,295
$Rb_2PtH_2\_p$	1050	17.4	1306.1	1,431.4	107,200,367
TiH_2	916	2.3	15.1	187.2	1,237,368

[a] melts at 1273 K[5]

F.References

[1] D. Steward, (Chemicool.com, 2012), Vol. 5/19/2014.

[2] S. R. Sherman and T. M. Adams, *Tritium Barrier Materials and Separation Systems for the NGNP*, U. S. DOE Savannah River National Laboratory, Aiken, Nov. 2008.

[3] S. R. Sherman, *A Tritium Research and Collaboration Plan for the NGNP Project*, U. S. DOE Savannah River National Laboratory, Aiken, Aug. 2008.

[4] H. Ohashi, N. Sakaba, T. Nishihara, Y. Tachibana, and K. Kunitomi, *J. Nucl. Sci. Technol.* **45**, 1215 (2008).

[5] "Physical Constants of Inorganic Compounds" in *CRC Handbook of Chemistry and Physics, 88th Edition*.

VITA

Kelly M. Nicholson was born in Louisville, KY, USA, to parents Malinda and Robert Nicholson and elder sister, Lisa. She attended St. Athanasius grade school and graduated from Presentation Academy, a Louisville high school. She was a Kentucky Governor's Scholar and very active in academic competitions, athletics, leadership activities, and musical performances. She attended the University of Louisville (UofL) under a 5 year Hallmark Provost Award scholarship and graduated with a B.S. and M.Eng in Chemical Engineering. Always interested in energy security and energy technologies, Kelly pursued a cumulative year-long engineering co-op with Marathon Petroleum and completed undergraduate biodiesel research and a Masters level thesis related to the performance characterization of a novel vertical axis wind turbine using computational fluid dynamics under Dr. Eric Berson of UofL.

She began her PhD studies with a minor in Public Policy at the Georgia Institute of Technology (GA Tech) in August 2010 in the School of Chemical & Biomolecular Engineering under advisor Dr. David Sholl. While at GA Tech, Kelly participated in the prestigious Sam Nunn Security Program that brings together students, faculty, and policy-makers from multiple disciplines to consider issues critical to U.S. national security. She continues to pursue research with energy applications and hopes to find ways to engage in dialogs with policy makers regarding the future of U.S. energy.